Atom tunneling occurs in many chemical reactions involving hydrogen transfers. Tunneling increases the reaction rate compared to the classical over-the-barrier model especially at low temperature. Computer simulations can directly quantify the effect of tunneling in a reaction by switching it on and off.

The enzyme Glutamate mutase is studied by a multiscale approach combining quantum mechanics with molecular mechanics (QM/MM) and a rigorously improved instanton theory for efficient tunneling rate calculations.

The results of the QM/MM simulations show new details of the catalyzed reaction and lead to a better understanding of the catalysis by glutamate mutase.
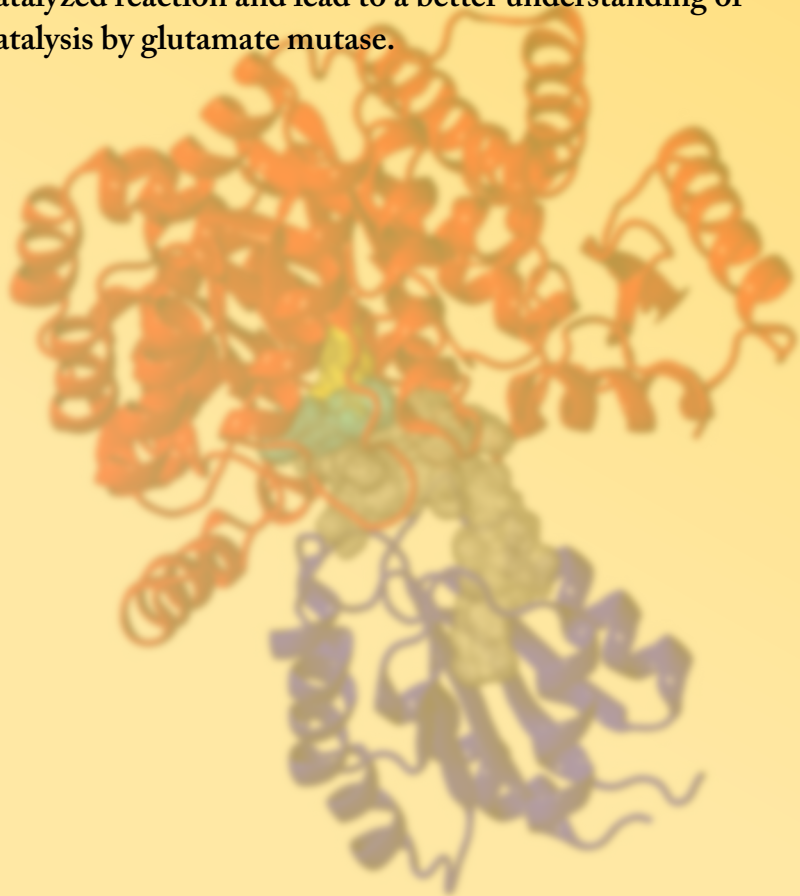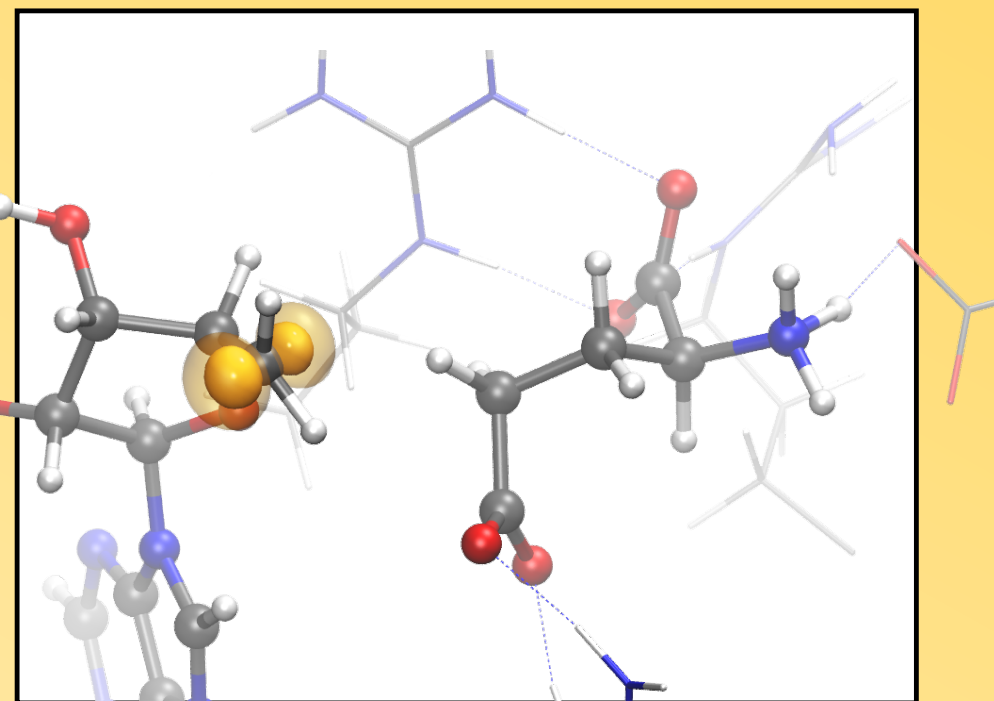
Judith B. Rommel

Improvements to the Instanton Method

Tunnelling in Glutamate Mutase

Improvements to the Instanton Method: Tunneling Rates in the Enzyme Glutamate Mutase

Von der Fakultät Chemie der Universität Stuttgart
zur Erlangung der Würde eines
Doktors der Naturwissenschaften (Dr. rer. nat.)
genehmigte Abhandlung

Vorgelegt von

Judith Barbara Rommel

aus Göppingen

Hauptberichter:	Jun.-Prof. Johannes Kästner
Mitberichter:	Prof. Hannes Jónsson
	Prof. Guntram Rauhut
Prüfungsvorsitzender:	Prof. Bernhard Hauer
Tag der mündlichen Prüfung:	8. Oktober 2012

Institut für Theoretische Chemie
der Universität Stuttgart

2012

"The real voyage of discovery consists not in making new landscapes but in having new eyes."

<div style="text-align: right">

Marcel Proust (1871-1922)

</div>

CONTENTS

LIST OF FIGURES

LIST OF TABLES

Acknowledgments

Stuttgart, June 2012   Judith B. Rommel

ABSTRACT

Motivation: Catalysts for radical reactions are important in industrial processes. The understanding of enzymes catalyzing radical reactions allows to design new biomimetic catalysts. Computational investigations complemented by experiments can provide better insight into the use and the control of radicals by biological systems.

Atom tunneling occurs in many chemical reactions involving hydrogen transfers. Tunneling increases the reaction rate compared to the classical over-the-barrier model especially at low temperature. In many enzymes tunneling of hydrogen atoms influences the reaction rate even at room temperature which can experimentally be observed by unusually high kinetic isotope effects (KIEs). The KIE is the ratio of reaction rates of protium and a heavier isotope, e.g., deuterium or tritium. Computer simulations can directly quantify the effect of tunneling in a reaction by switching it on and off. A high KIE shows that tunneling accelerates the rate limiting step. Whether tunneling is essential for the catalytic effect of some enzymes is part of an ongoing scientific debate. Simulations are a promising tool to gain insights on the level of atoms and electrons to answer that question.

The reaction mechanism of glutamate mutase: The enzyme glutamate mutase catalyzes the radical conversion mechanism of (S)-glutamate to (2S,3S)-3-methylaspartate including two hydrogen transfer steps. Glutamate mutase occurs in many anaerobic bacteria (for example in *Clostridium cochlearium*) that use glutamate as carbon and energy source. The protium/deuterium KIEs measured in glutamate mutase range from 4.1 to 35 at 10°C. Thus, it is unclear whether tunneling is involved or important for the catalytic process. Glutamate mutase is studied by a multiscale approach combining quantum mechanics with molecular mechanics (QM/MM), with quantum mechanical (QM) calculations used for the atoms directly involved in bond rearrangements and force field calculations (MM) for the environment. The QM part is investigated with density functional theory and coupled cluster theory.

The results of the QM/MM simulations show new details of the catalyzed reaction: the conversion of (S)-glutamate to (2S,3S)-3-methylaspartate is found to proceed via a fragmentation–recombination mechanism. The involved hydrogen atom transfer steps exhibit the highest barrier, 101 kJ mol^{-1} (M06 functional). The barriers of the hydrogen transfers match for density functional theory (M06 functional) and coupled cluster (LUCCSD(T)) calculations.

Comparison of the interconversion reaction in the gas phase, water (COSMO), and protein shows that the influence of the enzyme is mainly electrostatical and to a lesser degree sterical. The calculations shed light on the atomistic details of the reaction

mechanism. The well-known arginine claw (Arg 66, Arg 100, and Arg 149) and Glu 171 are found to have the strongest influence on the reaction. The arginine claw keeps the intermediate fragments in place, and is important for the recombination process. However, significant catalytic roles of amino acids close to the active center, e.g., Glu 214, Lys 322, Gln 147, Glu 330, Lys 326, and Met 294 are found as well. These results predict new promising experimental targets.

The role of tunneling in the enzyme glutamate mutase is investigated by QM/MM simulations based on instanton theory with up to 78 atoms allowed to tunnel. Primary protium/deuterium KIEs of hydrogen transfers are in good agreement with experiment. The secondary tritium KIEs hint that coupled motions on a ribose ring of the cofactor are part of the tunneling motions. The enzyme uses both classical and tunneling motions for a successful catalysis.

These simulations lead to an improved understanding of the catalysis by glutamate mutase.

Improvements to the instanton method: To investigate the role of tunneling in glutamate mutase several adaptations of the instanton theory and their implementations are required.

The instanton method (also called *imaginary free energy* method) is based on Feynman's path integral formalism to describe quantities from statistical quantum mechanics. The instanton is the most-likely tunneling path. The instanton is also a first-order saddle point of the Euclidean action. Tunneling rates to calculate KIEs are determined via the second variation of the Euclidean action including the quadratic fluctuations along the instanton path. The problem of finding an instanton is addressed as a saddle-point search problem. Four algorithms implemented to locate instantons are compared: a modified Newton–Raphson method, the partitioned rational function optimization algorithm, the dimer method, and a newly proposed mode-following algorithm. These algorithms are tested on three chemical systems. Overall, the Newton–Raphson turns out to be the most promising method, consistently efficient and stable, with the newly proposed mode-following method being the fall-back option.

Two bottlenecks are challenging in instanton rate calculations:

- Hessian calculations subsequent to the instanton optimization are expensive for large systems like enzymes.

- At lower temperature more and more discretization points (images) on the equidistantly discretized path tend to accumulate at the ends of the instanton path.

Thus, methods that allow to use fewer discretization points for the same quality in the rates are required.

After reviewing the basic concepts of differential geometry necessary for a mathematical formulation, a stringent higher-dimensional derivation of the instanton rate theory is presented. Thereby, a variable step-size discretization of the instanton paths is used. Updating strategies, like for example Bofill updates, increase the efficiency of the rate calculations as well. Another option to save computation time is the fixed-path approximation. The adaptation of the variable step-size to the temperature allows to apply instanton theory at low temperature while avoiding the accumulation of images at the ends of the instanton path observed with the traditional constant step-size discretization. The development of a quadratically convergent optimizer significantly increases the efficiency of instanton optimizations. In combination with a new, flexible, and variable discretization of the integration along the instanton, the computational costs are reduced by one or two orders of magnitude.

ZUSAMMENFASSUNG

Motivation: Die Katalyse von Radikalreaktionen spielt eine wichtige Rolle in industriellen Prozessen. Ein verbessertes Verständnis der Reaktionsmechanismen von Enzymen, die Radikalreaktionen katalysieren, ermöglicht die Herstellung neuer biomimetischer Katalysatoren. Computersimulationen können, ergänzt durch Experimente, besseren Einblick geben, wie biologische Systeme Radikale verwenden und kontrollieren.

Tunneln von Atomen tritt in vielen chemischen Reaktionen auf, vor allem bei solchen, die Wasserstoffatome involvieren. Besonders im Bereich tiefer Temperaturen erhöht der Tunneleffekt die Reaktionsraten im Vergleich zum klassischen Modell, bei dem die Edukte mit genügend Aktivierungsenergie über die Reaktionsbarriere auf die Produktseite gelangen. Bei vielen Enzymen beeinflusst das Tunneln von Wasserstoffatomen sogar bei Raumtemperatur die Reaktionsrate, was sich experimentell in einem ungewöhnlich hohen kinetischen Isotopeneffekt (KIE) zeigt. Der KIE ist das Verhältnis der Reaktionsraten für Protium und eines schwereren Isotops, wie z.B. Deuterium oder Tritium. Computersimulationen können die Bedeutung von Tunneleffekten in der Katalyse direkt zeigen. Der Tunneleffekt kann in Simulationen im Gegensatz zum Experiment an- oder ausgeschaltet werden. Ein hoher KIE zeigt, dass Tunneln den geschwindigkeitsbestimmenden Schritt einer Reaktion beschleunigt. Ob das Tunneln von Atomen essentiell für den katalytischen Effekt einiger Enzyme ist, ist Teil einer aktuellen und aktiven wissenschaftlichen Debatte. Simulationen sind ein vielversprechender Ansatz, um auf Atom- und Elektronenebene zur Klärung dieser Fragestellung beizutragen.

Der Reaktionsmechanismus von Glutamatmutase: Glutamatmutase ist ein Enzym, das die reversible Umlagerung von (S)-Glutamat zu (2S,3S)-3-Methylaspartat über eine Radikalreaktion katalysiert. Es kommt in vielen anaeroben Bakterien (z.B. *Clostridium cochlearium*) vor, die Glutamat als Kohlenstoff- und Energiequelle nutzen. Die für Glutamatmutase gemessenen Protium/Deuterium KIEs reichen von 4.1 bis 35 bei 10°C. Daher ist unklar, ob Tunneln für die Katalyse eine Rolle spielt. Das Enzym Glutamatmutase wird mit einem Multiskalenansatz, einer Kombination aus Quantenmechanik und Molekularmechanik (QM/MM), untersucht. Dabei werden quantenmechanische (QM) Rechnungen für Atome, die direkt an der Umlagerung der Bindungen beteiligt sind, verbunden mit Kraftfeldrechnungen (MM) zur Beschreibung der Umgebung verwendet. Der QM-Teil wird mit Dichtefunktionaltheorie und Coupled Cluster beschrieben.

Die Ergebnisse der QM/MM-Simulationen zeigen neue Details der katalysierten Reaktion auf Atom- und Elektronenebene: Die Umlagerung von Glutamat zu Methylaspartat verläuft über einen Fragmentierungs-Rekombinations-Mechanismus. Die Zwischen-

schritte, in welchen Wasserstoffatome übertragen werden, weisen die höchste Barriere auf, 101 kJ mol^{-1} (M06 Funktional). Für diese Reaktionsschritte stimmen die Barrieren, der Dichtefunktionaltheorie (M06 Funktional) und Coupled Cluster (LUCCSD(T)) Rechnungen überein.

Ein Vergleich der Umlagerungsreaktion in der Gasphase, in Wasser (COSMO) und in der Proteinumgebung zeigt, dass der Einfluss des Enzyms überwiegend elektrostatisch und zu einem geringeren Anteil sterisch bedingt ist. Die Rechnungen demonstrieren Details des Reaktionsmechanismus' auf atomarer Ebene. Die "Argininkralle" (Arg 66, Arg 100, und Arg 149) und die Aminosäure Glu 171 haben den stärksten Einfluss auf die Reaktion. Die Argininkralle hält die Fragmente (Zwischenprodukte der Reaktion) an ihrer Position. Sie spielt eine wichtige Rolle bei der Rekombination der Fragmente. Jedoch haben auch mehrere andere Aminosäuren, z.B. Glu 214, Lys 322, Gln 147, Glu 330, Lys 326 und Met 294, in der Nähe des aktiven Zentrums signifikanten Einfluss auf die Reaktivität des Enzyms.

Die Rolle des Tunneleffekts in Glutamatmutase wird mit QM/MM-Simulationen basierend auf Instantontheorie mit bis zu 78 Atomen, die tunneln dürfen, untersucht. Die primären Protium/Deuterium KIEs der Wasserstoffüberträge stimmen gut mit den experimentellen Ergebnissen überein. Die sekundären Tritium KIEs weisen darauf hin, dass gekoppelte Bewegungen am Ribosering des Kofaktors Teil der Tunnelbewegung sind. Das Enzym verwendet sowohl klassische Bewegungen als auch Tunnelbewegungen für eine erfolgreiche Katalyse.

Diese Simulationen führen zu einem verbesserten Verständis der Katalyse durch Glutamatmutase.

Verbesserungen der Instantonmethode: Um die Rolle des Tunneleffekts in Glutamatmutase zu untersuchen, sind Anpassungen der Instantontheorie und deren Implementierung zur Berechnung von Tunnelraten in großen Systemen notwendig.

Die Instantonmethode (auch *Imaginary F* Methode genannt) basiert auf Feynmans Pfadintegralformalismus zur Beschreibung von Größen der statistischen Quantenmechanik. Das Instanton ist der optimale Tunnelpfad, der den größten Beitrag zur Tunnelrate liefert. Dieser ist ein Sattelpunkt erster Ordnung des euklidischen Wirkungsfunktionals. Tunnelraten zur Berechnung von kinetischen Isotopeneffekten werden über die zweite Variation der euklidischen Wirkung unter Einbeziehung der quadratischen Fluktuationen entlang des Instantonpfades bestimmt. Vier Algorithmen zur Instantonsuche wurden implementiert und verglichen: das Newton–Raphson Verfahren, der *partitioned rational function optimization* Algorithmus, die Dimermethode und eine weitere neu vorgeschlagene auf Gradienten basierende Methode. Die Algorithmen werden an drei chemischen Systemen getestet. Das Newton–Raphson Verfahren zeigte

die beste Stabilität und Effizienz. Die neu vorgeschlagene Methode kann als Alternative dienen.

Zwei Herausforderungen sind bei der Berechnung von Instantonraten zu meistern:

- Die Berechnungen der Hessematrix, die auf die Instantonoptimierungen folgen, sind für große Systeme wie z.B. Enzyme teuer.

- Bei niedriger Temperatur tendieren immer mehr Diskretisierungspunkte (Bilder) auf einem equidistant diskretisierten Pfad dazu, sich an den Enden des Instantonpfades anzuhäufen.

Daher sind Methoden notwendig, die es ermöglichen, weniger Diskretisierungspunkte bei gleicher Qualität der Rate zu verwenden.

Zunächst werden einige grundlegende Konzepte der Differentialgeometrie, die für die mathematische Formulierung notwendig sind, wiederholt. Dann folgt eine konsistente und stringente Herleitung einer Instantonrate für höherdimensionale Systeme. Dabei erfolgt die Diskretisierung entlang der Tunnelpfade mit variabler Schrittweite. Die Verwendung von Hessian-Updates, z.B. Bofill Updates, erhöht die Effizienz der Ratenrechnungen ebenso. Eine weitere Möglichkeit, Rechenzeit zu sparen, ist die Fixed-Path-Näherung. Die Anpassung der variablen Schrittweite an die Temperatur vermeidet eine Anhäufung der Bilder, wie sie bei einer traditionellen Diskretisierung mit konstanter Schrittweite bei niedrigen Temperaturen zu beobachten ist.

Die Entwicklung eines quadratisch konvergenten Optimierers zur Instantonbestimmung steigert die Effizienz der Simulationen signifikant. In Kombination mit einer neuen, flexiblen und variablen Diskretisierung der Integration entlang des Instantons reduziert sich der Rechenaufwand um ein bis zwei Größenordnungen.

GLOSSARY

List of Abbreviations and Acronyms

List of Symbols (Capital Letters)

List of Symbols (Lower Case Letters)

Part I

Introduction and Review

Introduction and Review

Enzymes are very efficient and highly specific biological catalysts occurring in every living organism. They create an environment to enhance the rates of the catalyzed reaction. Understanding the mechanisms they use will help to create new bio-mimetic catalysts with high target specificity. Many catalytic processes also involve tunneling especially at low temperature.

In the following chapter the enzyme glutamate mutase will be introduced and the results of experimental studies with glutamate mutase, especially the kinetic isotope effect measurements will be summarized. Then follows an overview of the basic concepts of two different commonly used rate theories and tunneling. In the last section the computational approaches that have been used by others to study tunneling in enzymes will be discussed. The instanton method and its advantages, which is later on used to study tunneling in glutamate mutase is described in detail in Chapter 3.

1.1 The enzyme glutamate mutase: a radical reaction in biology

Adenosylcobalamin-dependent glutamate mutase (GM), in IUBMB enzyme nomenclature EC: 5.4.99.1, belongs to a group of enzymes that catalyze radical reactions, which is unusual for biological systems. They use 5'-deoxyadenosylcobalamin (AdoCbl), also called coenzyme B_{12}, as a cofactor [1]. GM occurs as a tetramer consisting of two identical $\sigma\varepsilon$-dimers each made up of a σ-subunit and an ε-subunit. One cofactor is bound
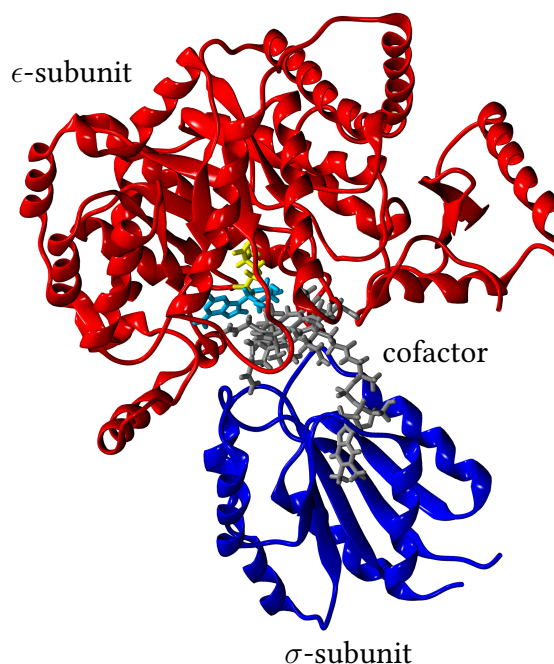
Figure 1.1: Two of the four subunits of GM: a σ-subunit (blue) and an ε-subunit (red). The cofactor AdoCbl homolytically cleaved into cob(II)alamin (gray) and a 5'-deoxyadenosyl radical (blue), state ***A***, and the (S)-glutamate substrate (yellow) are shown as well. The protein consists of two identical $\sigma\varepsilon$-subunits.

to each $\sigma\varepsilon$-interface, see Fig. 1.1. GM is found in anaerobic bacteria, e.g. in *Clostridium spec.* [2]. They use (S)-glutamate as a carbon and energy source and degrade it to butyrate, CO_2, NH_4^+, and H_2 [3]. This work focuses on the first step of glutamate fermentation by those bacteria which starts with a reversible interconversion including a carbon-skeleton rearrangement of (S)-glutamate (Glu) to (2S,3S)-3-methylaspartate (MA, see Fig. 1.2) [4]. This reaction involves radical intermediates. Both, the substrate and the product are small, stable molecules. The reaction is reversible. Thus, glutamate mutase provides a relatively simple system to study enzymatic catalysis using radicals.

The crystal structure of the enzyme in complex with substrate and cofactor has been determined at 1.6 Å and 1.9 Å resolution [5, 6]. NMR structures are available as well [7–10]. Key residues in the vicinity of the active site of GM are, e.g., arginine (Arg) 149, Arg 100, and Arg 66, which form hydrogen bonds to the glutamate substrate. They establish the so-called arginine-'claw' [5]. The amino acid glutamate (Glu) 171 was suggested to act as a a proton acceptor during the reaction [11]. Here and in the following residue numbers refer to GM from *Clostridium cochlearium*. According to
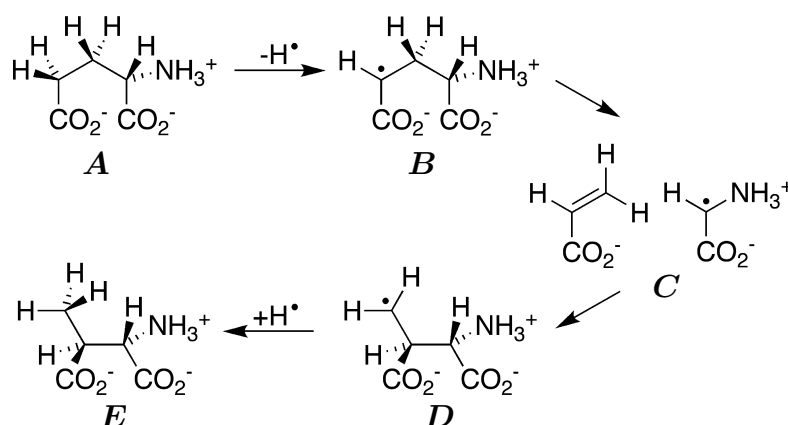
Figure 1.2: The rearrangement of (S)-glutamate (Glu) to (2S,3S)-3-methylaspartate (MA) catalyzed by GM [20] (*A*: 5'-deoxyadenosyl radical (Ado) and glutamate (Glu); *B*: Ado+H and glutamyl radical; *C*: Ado+H, acrylate, and glycyl radical; *D*: Ado+H and methylaspartyl radical; *E*: Ado and methylaspartate)

the bound-free-radical hypothesis, the initial step in coenzyme B12-mediated reactions is the homolytic cleavage of the cobalt-carbon (Co–C) bond of the cofactor, which produces a 5'-deoxyadenosyl radical (Ado) and cob(II)alamin [12, 13]. Compared to the following hydrogen transfer catalyzed by GM, this homolytic cleavage is fast; it is not rate-limiting [14–16]. Therefore it is not considered in our simulations. Several reaction mechanisms have been proposed, e.g., removal of a hydride ion or a not very likely addition–elimination pathway [17]. This study will emphasize on the fragmentation–recombination mechanism proposed based on experimental data [18, 19].

In the following the considered intermediates of the fragmentation–recombination mechanism [18–20] catalyzed by GM are denoted as: the state A_0 is the inactive holoenzyme GM with AdoCbl. The initial step induced by Glu substrate in the binding pocket is the homolytic cleavage of the cobalt-carbon bond of the cofactor, which yields a 5'-deoxyadenosyl radical (Ado) and cob(II)alamin [12, 13], state *A* (see Fig. 1.1 and Fig. 1.2). The transfer of an unpaired electron from Ado to the Glu substrate generates the glutamyl radical and 5'-deoxyadenosine (Ado-H), state *B*. Then follows the fragmentation into acrylate and a glycyl radical, state *C*. Binding of glycyl to acrylate (recombination) results in the methylaspartyl radical, state *D*. The back-transfer of the unpaired electron from the substrate to Ado yields MA, state *E*. The final part of the catalysis in GM is reforming the Co–C bond, resulting in E_0, and product release. From experiment, it is unclear which of the individual steps is rate-limiting. While some studies observed large deuterium Kinetic Isotope Effects (KIEs) [21–23], which indicate the hydrogen-transfer steps to be rate-limiting, more recent work found smaller KIEs and concludes that neither of the hydrogen-transfer steps is

cleanly rate-limiting [24, 25].

1.1.1   Tunneling in the enzyme glutamate mutase?

Atom tunneling is involved in many chemical reactions that include hydrogen transfers. It is a quantum mechanical effect by which a particle can penetrate into classically forbidden regions of coordinate space. Tunneling is also the phenomenon that light particles (e.g. protons) with energies lower than the height of the classical barrier penetrate through the barrier from the reactant to the product side, which is in contradiction to classical mechanics [26].

The probability of tunneling depends on

- the mass of particles that undergo tunneling motions and

- on the shape and

- height of the effective barrier being crossed [27, 28].

It is most important for light particles, in particular hydrogen atoms, and narrow barriers. Tunneling increases the reaction rate compared to the classical over-the-barrier reaction, especially at low temperature. However, in many enzymes tunneling of hydrogen atoms (H^+, H^-, or $H^.$) can contribute to the reaction rate even at room temperature [25, 29–36]. The influence of tunneling and its role in enzyme catalysis is a very controversial topic [37–39]. Kinetic isotope effects are used as indicators to determine the contribution of tunneling [39]. The KIE manifests itself in the ratio of the reaction rates of protium (H=^{1}H) and a heavier isotopologue (containing deuterium: ^{2}H or tritium ^{3}H) in the same reaction. Changing the mass of one or more of the atoms involved in the reaction does not fundamentally change the reacting system. Thus, measurement of KIEs are a powerful tool to study enzymatic reactions [40–45]. The mass-dependence of the tunneling rate gives rise to high KIEs. A high KIE hints that tunneling enhances the rate-limiting step of the reaction. From experiments it is unclear whether tunneling plays a role in the reaction catalyzed by GM. An overview on the experiments will be given in the following section.

1.1.2   Kinetic isotope effect measurements in glutamate mutase

KIEs can experimentally be determined (a) by independently measuring reaction rates, i.e., noncompetitive KIE experiments, or (b) by competitive KIE measurements, i.e., by assessing the isotopic distribution in the substrates and products at the same time. A third option is to determine KIEs (c) by equilibrium perturbation through isotope

Measurement	Substrate	Kinetic parameter	Value (Rate H)	Deuterium isotope effect
Following the kinetics of cob(II)alamin formation				
	trideuterated ($^2H_3$)	Glu	K_{cat}	8.5 ± 0.3 s⁻¹ [46]*	3.9 ± 0.3 [47]
steady state,	trideuterated ($^2H_3$)	Glu	K_m	0.58 ± 0.08 mM [47]	
	trideuterated ($^2H_3$)	Glu	K_{cat}/K_m	(1.5 ± 0.2) × 10⁴ M⁻¹s⁻¹	4.0 ± 1.0 [47]
spectroscopic assay	trideuterated ($^2H_3$)	MA	K_{cat}	7.6 ± 0.2 s⁻¹ [46]*	6.3 ± 0.5 [47]
	trideuterated ($^2H_3$)	MA	K_m	0.14 ± 0.02 mM [47]	
	trideuterated ($^2H_3$)	MA	K_{cat}/K_m	(5.4 ± 0.8) × 10⁴ M⁻¹s⁻¹	3.4 ± 0.7 [47]
	trideuterated ($^2H_3$)	Glu	K_d	0.61 ± 0.07 mM [23]	
stopped flow	trideuterated ($^2H_3$)	MA	K_d	0.037 ± 0.005 mM [23]	
UV-visible	trideuterated ($^2H_3$)	Glu	$K_{obs}(A_0 \to A)$	97 ± 5 s⁻¹	28 [23]
	trideuterated ($^2H_3$)	Glu	$K_{obs}(A_0 \to C)$	35 ± 8 s⁻¹ [23]	
	trideuterated ($^2H_3$)	MA	$K_{obs}(E_0 \to E)$	80 ± 4 s⁻¹	35 [23]
Following the kinetics of Ado-H formation (with rapid quench techniques)				
reverse HPLC to analyze	trideuterated ($^2H_3$)	MA	$K_{obs}(E_0 \to D)$	64 ± 11 s⁻¹ [46]	
reverse HPLC to analyze	trideuterated ($^2H_3$)	Glu	$K_{obs}(A_0 \to B)$	73 ± 8 s⁻¹ [46]	
	perdeuterated ($^2H_5$, $^2H_3$)	Glu (^DV)	$K_{obs}(A_0 \to B)$	73 ± 8 s⁻¹	2.4 ± 0.4 [21]
reverse HPLC to separate,	trideuterated ($^2H_3$)	Glu** (V_{max}/K_m)	$K_{obs}(A_0 \to B)$	73 ± 8 s⁻¹	10 ± 0.4 [21]
electrospray MS to analyse	monodeuterated	MA***	$K_{obs}(E_0 \to D)$		4.1 [25]

*slightly lower values with a coupled assay under slightly different conditions in [47] (see text)
** competitive measurement, both deuterated and unlabeled substrate in the same vessel
*** intramolecular competition experiment between ^1H and ^2H at the same methyl group of the substrate

Table 1.1: Kinetic data for GM at 10°C. The reduced protein consisted of one σ- and one ϵ-subunit. A_0: state before homolytic cobalt-carbon bond cleavage, E_0: inactive enzyme after interconversion (no radical). If not explicitly mentioned the experiments were pre-steady state measurements.

substitution. The noncompetitive measurements (a) are direct methods and include the determination of reaction rates for each isotopologue separately, e.g., with absorption or emission spectroscopy (infrared, ultraviolet-visible, nuclear magnetic resonance, fluorescence, mass spectrometry, etc.) [48]. The competitive KIE experiments (b) start with a mixture of different isotopologues in the same reaction vessel. Then, the reaction mixture is quenched at different points in time, e.g., by mixing with another solution or quickly lowering the temperature. After the quenching the product and substrate are separated. The change of the isotopic ratio in either the substrate(s) or the product(s) relative to the initial ratio in the substrate(s), or final ratio in the product(s) determines the KIEs. The method of equilibrium perturbation (c) starts with adding concentrated enzymes to a reaction mixture that contains the unlabeled (natural) substrates. Then the equilibrium concentrations of the substrates and products are determined. Next, a new reaction mixture of isotopically labeled substrates and unlabeled products at those equilibrium concentrations is prepared. After adding the enzyme the system changes toward a new equilibrium. The rate of change and the final equilibrium constants are determined, e.g., by ultraviolet-visible (UV–visible) spectroscopy and circular dichroism techniques [48].

The experimental intricacy is to measure the rate of the step where tunneling is involved without being affected by any isotopically insensitive steps (e.g. substrate binding, conformational changes, product release).

Experimental measurements of rates and KIEs in GM were conducted with various techniques. The results vary between the different techniques. Here the results of (1) steady state measurements, (2) stopped flow pre-steady state measurements following the kinetics of cob(II)alamin formation, (3) rapid quench pre-steady state measurements following the kinetics of Ado-H formation, and (4) rapid quench secondary KIE measurements will be summarized. An overview of the results for deuterium KIEs determined with (1) to (3) is given in table 1.1. Here the Michaelis–Menten constant [49, 50], i.e., the substrate concentration at which the reaction rate is at half-maximum, is denoted by K_m. The smaller K_m the higher the affinity of the substrate to the enzyme. Reaction rates are the velocity with which a chemical reaction takes place, i.e., how fast or slow the reactants are changed into the products of the reaction. The turnover number K_{cat}, is the number of substrate molecules converted to product by one enzyme active site per second, when the enzyme is fully saturated with substrate. The constant K_{cat}/K_m is a measure of how efficiently an enzyme converts a substrate into product. The higher K_{cat}/K_m the more efficient the enzyme. The turnover numbers $K_{obs}(. \rightarrow .)$, as given in table 1.1, belong to the rates observed for the turnovers with either Glu, $\boldsymbol{A}_0$, or MA, $\boldsymbol{E}_0$, in the binding pocket, starting with the the inactive enzyme (before the homolytic Co–C bond cleavage) and proceeding to different intermediate states. The apparent dissociation constant for the substrate is denoted as K_d. See [39] for more details on these constants and numbers.

Most of the studies mentioned in the following used three times deuterated MA and three times deuterated Glu as substrates to investigate the deuterium rates and KIEs. In two studies [21, 25] perdeuterated Glu and monodeuterated MA were used. A more detailed overview on the results of different measurements in GM can be found in [51].

Steady state measurements (1)

Steady state measurements consider the kinetics of the enzyme in situations, when all state variables are constant despite of ongoing processes trying to change them [52]. With steady state measurements the complete interconversion of MA to Glu was studied with a spectroscopy assay by coupling the formation of Glu to the oxidation of reduced nicotinamide adenine dinucleotide (NADH) [47]. The initial lag phase was about 1 min. The results are given in table 1.1. For the conversion of Glu to MA $k_{cat} = 5.8 \pm 0.3 s^{-1}$ and for the reverse reaction $k_{cat} = 5.8 \pm 0.2 s^{-1}$ [47]. The deuterium isotope effects measured under steady-state conditions are: 3.9 and 6.3 for Glu and MA, respectively. The rates and KIEs obtained form steady state measurements give information about the complete turnover from substrate to product and vice versa. To gain insight on different intermediate steps, for example on the role of tunneling during the two H-transfers, pre-steady state measurements are required.

Stopped-flow pre-steady state measurements (2)

Stopped-flow pre-steady state measurements of GM started with a rapid mixing of the substrate and the enzyme in a chamber, where the reaction could be followed with UV-visible spectroscopy. The disappearance of AdoCbl at 530 nm or the appearance of cobalamin(II) at 470 nm were measured over time [23]. These stopped-flow measurements reported primary deuterium KIEs and rates, see table 1.1, on the H-transfer steps indirectly by following the kinetics of cobalamin(II) formation. The resulting KIEs are large for both substrates, ratios of 28 for $A \to B$ and 35 for $D \to E$. The adenosyl radical (A, E) is a high-energy intermediate that does not accumulate on the enzyme [47]. Thus, the measured KIEs rather belong to the transition from $A \to B$ (or $E \to D$) than to the homolytic cleavage ($A_0 \to A$ or $E_0 \to E$) where an adenosyl radical is formed [23]. The homolysis of AdoCbl with deuterium was found to be biphasic with rate constants differing by 5 to 10-fold [23]. Experiments with rapid quenching techniques showed that these two phases are due to multiple turnovers of deuterium from the substrates to the B_{12}-cofactor, which is undetectable by following the kinetics on cobalamin(II) formation [21]. Then the cofactor is two or more times deuterated. The kinetics are influenced by that. Thus, in further experiments the kinetics of Ado-H formation (intermediate states B to D) was directly followed by using rapid chemical quench techniques.

Rapid quench pre-steady state measurements (3)

Rapid quench pre-steady state measurements helped to identify the intermediates ($\boldsymbol{A}$ to $\boldsymbol{E}$), as well as their kinetics of formation, in the reaction catalyzed by GM [18, 53]. Enzyme, cofactor and substrate were reacted together and then quenched at various times, e.g., between 5–1600 ms [46], with trifluoroacetic acid. Then the components were separated with reverse phase high-performance liquid chromatography (HPLC), which allows to determine a reaction rate. The deuterium content of Ado-H was measured as a function in time by electrospray mass spectrometry. The measurements were all done at T =283.15 K. At a temperature below 283.15 K the multiply deuterated Ado-H contributed negligibly (<1%) to the measured rates [21]. Above 283.15 K the dideuteration increased rapidly to more than 2% of the yield which makes correct measurements of KIEs impossible. With these techniques the observed rates $K_{obs}(\boldsymbol{A}_0 \rightarrow \boldsymbol{B})$ = 73 ± 8 s^{-1} agreed for perdeuterated and trideuterated Glu substrate [21, 46], see table 1.1. The deuterium KIEs were then quite low about 2.4.

When measuring the KIE on the formation of Ado-H directly by a competition experiment with deuterated and unlabeled substrate in the same vessel the primary KIE on Ado-H formation was 10 ± 0.4 [21]. An internal competition experiment was later on designed to measure intrinsic KIEs even if the isotopically sensitive step is not rate-limiting. Protium and deuterium were competing intramolecularly at the same methyl group of the substrate to be transferred to the cofactor. The substrate was monodeuterated MA [24, 25]. The formation of Ado-H over time was followed by radiolabeled [8-^{14}C]-adenosylcobalamin. The resulting KIE was 4.1, at T =283.15 K [24, 25].

An isotopic substitution at an atom directly involved in establishing or breaking bonds during the reaction results in a primary KIE. The measured KIEs reported so far are primary deuterium KIEs. As the primary deuterium KIEs measured in GM range from 4.1 to 35 at T =283.15 K, it is unclear whether tunneling is involved in the catalysis by GM, see Section 1.1.1. Secondary KIEs result from isotopic substitution of atoms which keep their bonds intact during the reaction. Experiments investigating tritium isotope effects, based on rapid quench techniques [21, 54, 55], considered both primary and secondary tritium KIEs.

Tritium isotope effects (4)

Primary tritium isotope effect measurements with rapid-quenching, where tritium was transferred from Ado-H to form either Glu (substrate) or MA (product), resulted for GM in a 1:1 distribution of tritium in the substrate and the product [22]. The primary tritium KIEs were 21 for the transfer to Glu and 19 for the transfer to MA. For the secondary tritium KIEs, also determined with rapid quench methods following the formation

of Ado-H, tri- and perdeuterated substrates were used [21, 54, 55]. An inverse KIE means that deuterium or tritium move faster than protium which leads to a secondary KIE smaller than unity. Experimentally a large inverse secondary tritium KIE of 0.76 ± 0.02 was found with protium in the primary position [54]. With deuterium in the primary position the measured secondary KIE was close to unity, 1.05 ± 0.08 [55]. More details on the interpretation of these measurements in comparison to the calculational results will be given in Section 5.3. Measurements of KIEs in GM are only possible for a temperature less than 283 K, as mentioned above, to prevent the contribution of multiple deuterium transfers to the rate. They are also limited to certain time frames as the threshold in concentration for detecting the substance of interest (e.g. the product) must be exceeded. In experimental investigations the reverse reaction affects the results, as GM catalyzes a reversible conversion. Thus, the measured rates are apparent rates leading to apparent KIEs. The intrinsic KIEs, real KIEs without masking side effects, can be obtained only indirectly by experiment. Experimental results always include the tunneling contributions. In contrast, computational investigations allow to switch tunneling off and on. Direct predictions on the intrinsic, the real, KIEs are possible by computational approaches.

Experiments can indicate the importance of tunneling. However, many difficulties are encountered in studying tunneling effects in enzymes purely by experiments [41, 56]. Experimental studies always measure apparent rates and KIEs that can be masked by experimental side effects, like for example detection methods being insensitive to deuterium content below a certain threshold, see Section 1.1.2. The measurements are also limited to certain time frames as the threshold in concentration for detecting the substance of interest (e.g. the product) must be exceeded. In experimental investigations the reverse reaction can affect the results. Therefore, the measured rates are apparent rates leading to apparent KIEs. The intrinsic KIEs, real KIEs without masking side effects, can be obtained only indirectly by experiment.

Computational approaches allow to predict the intrinsic KIEs. In contrast to experimental measurements which always include tunneling contributions, calculations allow to switch tunneling on and off. Thus, calculations are a promising tool to provide insight into whether tunneling of atoms is crucial for the catalytic effect of some enzymes and whether it is actively promoted by the proteins.

Computational studies can also contribute valuable insights into how enzymes work on the atomic and electronic levels based on high-resolution protein structures. These levels are veiled in experiments due to the large size and complexity of enzymes, and the speed of chemical reactions. Prerequisites to obtain good predictions are models based on the fundamental physics that include the essential details of the enzyme, despite possible simplifications to make calculations feasible. The simulation methods should incorporate multidimensional tunneling and allow quantum simulations of the studied system while taking effects of solvents or protein environment into account.

1.2   Rate theories

The KIEs defined in the previous Section 1.1.1 are based on reaction rates. Several classical rate theories and quantum rate theories have been developed over the last decades, reviewed for example in [57–59]. Methods to calculate tunneling rates in biological systems based on different rate theories will be described in Section 1.3. In the following, a brief overview of some commonly used rate theories will be given.

Classical transition state theory

Classical Transition State Theory (TST) [60–64], strictly based on classical mechanics, assumes:
(1) The Born–Oppenheimer separation of nuclear and electronic motions.
(2) The Boltzmann distribution of energies for reactant molecules.
(3) Molecules pass through the transition state only once while they become products.
(4) The motion along the reaction coordinate in the transition state is separable from other motions.
(5) The use of classical mechanics which includes no tunneling. However, corrections for zero-point energy (ZPE) are possible.

The ZPE originates from Heisenberg's uncertainty principle, which states that, for a moving particle such as an electron, the more precise one measures the position, the less exact is the best possible measurement of its momentum, and vice versa. The least possible uncertainty of position and momentum is specified by Planck's constant, $\hbar$. The zero-point energy is the energy that remains, when all other energies are removed from a system. When considering a one-dimensional quantum mechanical harmonic oscillator the expectation value of its energy at zero temperature is $\langle H \rangle = \hbar\omega/2 \neq 0$, which is the zero-point energy. This behavior is, e.g., demonstrated by liquid helium. When lowering the temperature to absolute zero, helium remains liquid. The irremovable zero-point energy of its atomic motions prevents the helium from freezing to a solid. To freeze it, the pressure has to be increased.

A general transition state in a system with N degrees of freedom is a closed $N-1$ dimensional hypersurface encapsulating the reactant state (dividing surface). Commonly, however, one refers to a (classical) transition state as a first-order saddle point on the potential energy surface. The transition structure (TS) corresponds to the geometry of the transition state.

Let d denote the number of vibrational degrees of freedom, $\omega_{R,i}$ the i-th vibrational frequency of the reactant, $\omega_{T,i}$ the i-th vibrational frequency of the transition state, E_T the potential energy of the transition state, and, E_R the potential energy of the reactant state. With $\Delta E^\dagger = E_T - E_R$, T the temperature, k_B Boltzmann's constant, and

$\beta = 1/k_{\mathrm{B}}T$, the classical TST rate is given as

$$k_{\mathrm{TST}} = \frac{1}{2\pi} \frac{\prod_{i=1}^{d} \omega_{\mathrm{R},i}}{\prod_{i=1}^{d-1} \omega_{\mathrm{T},i}} \exp\left(-\beta\Delta E^{\dagger}\right). \tag{1.1}$$

In order to take the zero-point vibrations into account, the classical partition function of the harmonic oscillator can be replaced by a quantum partition function, which leads to

$$k_{\mathrm{TST}} = \frac{1}{2\pi\beta\hbar} \frac{\prod_{i=1}^{d} 2\sinh(\beta\hbar\omega_{\mathrm{R},i}/2)}{\prod_{i=1}^{d-1} 2\sinh(\beta\hbar\omega_{\mathrm{T},i}/2)} \exp\left(-\beta\Delta E^{\dagger}\right), \tag{1.2}$$

where $\hbar$ denotes the reduced Planck's constant.

Weaknesses of TST are that recrossing of the dividing surface is neglected and that the separability of the motion along the reaction coordinate from the other motions can only be guaranteed in a small range around the TS. In variational TST (VTST) a variationally optimized dividing surface between reactant and product regions is used to minimize the effects of recrossing [65]. There are several applications of (variational) TST approaches in enzymes [66, 67], see also Section 1.3.

Many catalytic processes also involve tunneling. Tunneling is an effect based on wave mechanics. At higher temperature the over-the-barrier model described by classical TST dominates the escape rate from a metastable system. Especially at low temperature tunneling through the barrier is more important, as even the smallest kinetic energy barriers may not be overcome by the particles. Despite the fact that conventional chemical reactions are slowing down as the temperature is lowered, tunneling reactions rarely change at all, which indicates their temperature independence.

Tunneling contributions are disregarded by classical TST, see Fig. 1.3. Quantum rates, taking tunneling into account, are required to find out whether enzymes use tunneling for their catalysis. In the next paragraphs an overview of methods to calculate tunneling rates will be given. Since many methods have appeared over the years, this list is necessarily incomplete.

Quantum corrections to classical TST

In classical TST quantum effects can be included via the vibrations and, thus, the ZPE. However, tunneling is neglected. A schematic comparison of classical, ZPE corrected, and tunneling rates is depicted in Fig. 1.3. Tunneling near the top of the barrier is accounted for by corrections to the classical reaction rate proposed by Wigner [68] and used by Bell [69, 70]. The Wigner correction assumes a one-dimensional reaction coordinate with tunneling occurring through a barrier approximated by a truncated
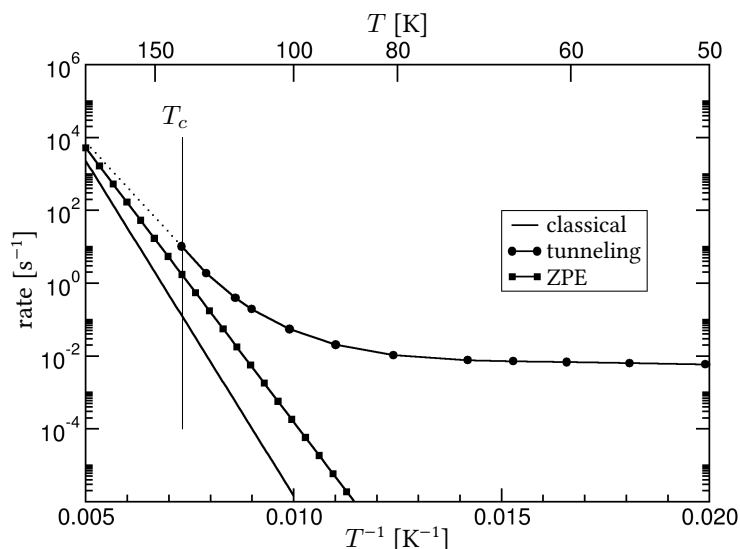
Figure 1.3: Schematic Arrhenius plot as a general example. ZPE denotes the classical rate with zero-point energy corrections.

parabola. The correction $\kappa(T)$ is given as a tunneling enhancement factor:

$$\kappa(T) = \frac{\hbar\omega/(2k_\mathrm{B}T)}{\sin\left(\hbar\omega/(2k_\mathrm{B}T)\right)}, \tag{1.3}$$

where ω denotes the magnitude of the imaginary frequency of the unstable mode at the saddle point. The method is applicable above a crossover temperature T_c [71]:

$$T_\mathrm{c} = \frac{\hbar\,\omega}{2\pi\,k_\mathrm{B}}. \tag{1.4}$$

Above the crossover temperature thermal activation events dominate over tunneling-induced transitions. When going below T_c tunneling through the barrier becomes more and more important. To extend the range of applicability to below T_c, a third-order expansion in $\hbar$ of $\kappa(T)$ was used as correction [72].

Common models based on TST and used for experimental interpretations of enzyme-studies are [48]: the Arrhenius equation [60], the Bigeleisen equation [73], the West-heimer model [74], and the Streitweiser model [75].

Beyond transition state theory

Marcus-like theories have been developed and used for (experimental) studies of enzymes [76–86]. In Marcus theory [76] the electronic transitions occur at solvent

geometries for which the donor and acceptor electronic states are isoenergetic [48, 87, 88]. However, modeling the temperature dependence of KIEs in enzymes with Marcus-like theories gave only moderately satisfying results [41, 42].

An alternative approach is Kramers' rate theory [89] which is, along with some extensions, also used to study enzymatic reactions[32, 90–96]. In Kramers' rate theory the concept of Brownian motion is used to describe the motion of particles over a barrier as a model for chemical reactions in solutions. The basic equation is a Langevin equation describing the classical stochastic dynamics of a particle coupled to a (heat) bath. The bath puts frictional (dissipative) and random forces on the particle.

A representation in Feynman's path integral formalism, see Section 2.5 for details on the formalism, allows to calculate quantum rates. More details on Kramers' rate theory can for example be found in [57, 96–98]. Kramers' approach can be used below the crossover temperature. For reactions above or at the crossover temperature Wolynes corrections [99, 100] have been developed in combination with Kramers' theory. However, the friction term required to describe in an enzyme the interaction between the quantum mechanical system and the bath environment have to be estimated from experiments [96, 101].

Beyond TST, quantum dynamics allows to calculate tunneling rates by solving the time-dependent Schrödinger equation [58]. However, the costs of these methods grow exponentially with the number of degrees of freedom, which makes them difficult to use in high-dimensional systems like enzymes.

1.3 Quantum rate calculations in biological systems

Several methods have been used during the last years to study tunneling in biological systems, which all have strengths and weaknesses. In the following an overview on some of these methods will be given. Among the discussed methods are the variational transition state theory with multidimensional tunneling corrections (VTST/MT) [102, 103], a mixed quantum-classical molecular dynamics approach [104], and a centroid path integral approach [105–107]. The instanton method, implemented and improved [108, 109] to study tunneling in GM, will be presented in more detail in Chapter 3.

Generally methods used to calculate potential energies and methods, based on various rate theories, to calculate reaction rates are distinct. The potential energies can, e.g., be obtained from semiempirical methods like AM1 [110] or from computationally more demanding methods as for example density functional theory or coupled cluster. Expensive methods for rate calculations lead often to the use of less demanding methods to calculate the necessary potential energies.

The semiclassical approximation assumes one main tunneling path rather than taking the whole potential energy surface into account. The zero-curvature tunneling approximation (ZCT) [111] approximates the tunneling path by the intrinsic reaction path (minimum-energy path (MEP) in mass-weighted coordinates). Even at rather high temperature, close to T_c, the most likely tunneling path will deviate from the MEP. The effect is dubbed as corner cutting [112]. Small-curvature tunneling (SCT) [113] assumes a tunneling path in the vicinity of the MEP. SCT can be expected to be a good approximation close to T_c. The other extreme for a choice of a tunneling path is the straight line path in a method known as large curvature tunneling correction (LCT) [114, 115]. While minimizing the tunneling distance, LCT ignores the potential energy in the choice of the path. At low temperature, LCT can be expected to be a better approximation than SCT. It has been proposed [116, 117] to use a linear combination of the SCT and LCT paths by minimizing the tunneling action.

A well-known method to calculate tunneling rates is the Jeffreys–Wentzel–Kramers–Brillouin (JWKB, in some literature also WKB) method [118–121], where the amplitude of the wave function is expanded in powers of $\hbar$. Truncating the expansion (i.e. semiclassical approximation) assumes that either the potential or the amplitude are slowly changing with the position. The JWKB method assumes, like other semiclassical approximations, one main tunneling path rather than taking the whole potential energy surface into account.

The validity of quantum correction to classical TST is limited to tunneling in the close vicinity of the saddle point where the potential energy is approximately quadratic and where all the modes perpendicular to the tunneling path can be assumed to be adiabatic. Methods with a broader range of validity are based on several paths. They employ a transmission coefficient, for example calculated by the SCT, LCT, or ZCT methods mentioned above, to include the quantum and non-separable effects in the rate [102, 103, 122, 123].

Several methods can complement VTST to include tunneling in the calculations [43, 103, 116, 124–128]. In ensemble-averaged variational TST including multi-dimensional tunneling (EA-VTST/MT) a range of different possible tunneling paths, both, close and further away from the classical reaction path at a range of different energies are considered to find the best compromise between path length and effective potential along the path in order to maximize the rate. Several enzymatic reactions have been studied with EA-VTST/MT or with VTST/MT [36, 43, 102, 103, 129–142]. The EA-VTST/MT method is a robust and well tested approach. Tunneling is included in a separate step, which allows to switch the effect on or off. However, most of the current VTST/MT studies used semiempirical electronic structure methods which have a limited accuracy and are not suitable for many important systems. The corrections are typically only calculated for a small number of reaction paths which does not cover the full dynamics of the system. In these QM/MM calculations, quantum mechanical

(QM) calculations for the atoms directly involved in bond rearrangements and force field calculations (MM) for the environment, the geometry optimizations are performed with a frozen MM part. Within the framework of VTST/MT QM/MM calculations most studies focused only on one temperature, with some exceptions [133, 135]. However, to investigate a large temperature range these methods require quite some effort.

Another method based on several paths is mixed quantum-classical molecular dynamics (MD) [40, 104, 143, 144], where the entire solvated enzymatic system is able to move throughout the MD simulation. The dynamics of the entire system can be calculated while the effects of zero-point energy, tunneling and excited vibrational states are included simultaneously. The quantum effects in hydrogen transfer reactions are modeled by numerically solving the vibrational wave function of the transferring hydrogen atom. However, a major limitation is the complexity of the method which prevents its extension to quantize more than one particle.

Statistical Feynman paths [145] can circumvent the exponential growth of computational effort with the number of degrees of freedom when solving the time-dependent Schrödinger equation. They have also been used in simulations to estimate tunneling probabilities either by evaluating a centroid potential of mean force [146−149] or by so-called ring-polymer dynamics [150]. The centroid density method, a quantum transition-state theory (QTST), is a Feynman path integral approach using TST, but not the semiclassical approximation [71, 151, 152]. Another QTST approach is the reversible action-space work QTST (RAW-QTST) [153, 154], which in the harmonic limit reduces to instanton theory, see Chapter 3. As most of the Feynman path integral based methods the centroid path integral approach treats a small number of atoms as ring of quasi-particles (images or beads) each experiencing a fraction of the external potential acting on the real particle. The ring of beads corresponds to the atoms quantized in the simulations, e.g., the transferring hydrogen atom. The quantized classical path method is based on centroid path integral sampling, but is formulated as a correction to the classical potential of mean force [105, 106, 155, 156]. Classical simulations and quantum corrections are fully separated [155]. After the classical trajectories of the beads were run the average over thousands of protein and bead configurations is taken, which provides the difference in the activation free energies including both zero-point energy and tunneling contributions inseparably. By combining the quantized classical path method with bisection sampling [157] the method became applicable to enzymatic systems [107, 158, 159]. However, these QM/MM simulations are limited to semiempirical methods as for example AM1 or PM3 for their QM part. Similar path integral based approaches with and without centroid constraint have also been used to study enzymes [160, 161].

Despite their advantages all the methods described above do not fulfill at least one of the following requirements: a method to efficiently calculate tunneling rates in enzymes should give predictions at various temperatures without much of additional effort. It

should allow a correct description of forming and breaking bonds with reasonable costs and complexity, e.g., density functional theory. The theory behind the method should go beyond corrections to classical TST to circumvent its failures. Finally, the method should also allow tunneling for more than one atom to find out which atoms are additionally involved in the tunneling motion.

In the following, a method will be presented that fulfills these requirements, see Chapter 3 and Chapter 4.

BASICS OF DIFFERENTIAL GEOMETRY AND DEFINITIONS

The aim of the following chapter is to review the definitions necessary in Chapter 3 for the variable step-size tunneling rate formulation. For mathematically rigorous introductions to the field of microlocal analysis, quantum and classical mechanics, and differential geometry see for example [162–166].

The following notation will be used: $\mathbb{R}$ is the set of real numbers, $\mathbb{N} = \{1, 2, \dots\}$ is the set of natural numbers, and $\mathbb{R}^d = \mathbb{R} \times \cdots \times \mathbb{R}$ (d factors) the d-dimensional real space. Let $X \subset \mathbb{R}^d$, $k \in \mathbb{N}$, and $C^k(X)$ denotes the space of k-times continuously differentiable functions $X \to \mathbb{R}$. The space $C^\infty(X) = \bigcap_{k \in \mathbb{N}} C^k(X)$ denotes the space of infinitely (continuously) differentiable functions. i is the imaginary unit, with $i^2 = -1$.

Points in configuration space (d-dimensional for a molecule with d degrees of freedom) will be denoted by bold italic symbols ($\boldsymbol{x}$). Non-bold symbols are used for scalar quantities. Vectors of path dimension ($d(J + 1)$) are denoted as bold upright symbols $\mathbf{x}$.

The chapter is structured as follows: first a short overview on instantons will be given, Section 2.1, then mathematical structures used to describe the theory are introduced. Manifolds and the Euclidean space in Section 2.2, differentiation and derivatives on manifolds in Section 2.3. Lagrangian mechanics is reviewed in Section 2.4 and in Section 2.5 Feynman's path integral formalism is introduced. In the last sections the distributional derivatives of the Euclidean action, Section 2.6, the time slicing approxi-

mation of the stationary-action path, Section 2.7, the use of Fermi local coordinates in connection with the Fourier path integral, Section 2.8, will be discussed.

2.1 Instantons

Instantons are solutions of the Yang-Mills equations [167, 168]. The Yang-Mills theory is a non-abelian gauge theory which describes strong and weak interactions in elementary particles. Strong and weak interactions are two of the four fundamental forces in physics. An example of a non-abelian gauge theory is quantum chromodynamics, whereas quantum electrodynamics is an example of an abelian gauge theory. The instanton solutions are localized in space and (Euclidean) time, which is so to say at a specific instant. They are also called pseudoparticles.

From the huge variety of existing instantons a few examples will be mentioned in the following. There are for example tunneling phenomena in quantum mechanics with a double-well potential as described by the kink, see e.g. [169], or the Yang-Mills instantons in four dimensions [170, 171]. There are also various kinds of instantons in string theory, for example D-instantons [172]. Instantons are also linked to the vacuum structure of quantum chromodynamics [173]. Instantons allow to describe tunneling in quantum mechanics. However, worldsheet instantons lead to many nonperturbative effects in string theory, that go beyond tunneling [173]. More details on field theoretic approaches can, e.g. be found in [168, 174]. A review on instantons from mathematical and physical point of view is given in [175].

Instantons describe tunneling processes in Minkowski space-time from one state to another. Classically, the traveling from one state to another is forbidden for a particle at the tunneling energy. However, quantum mechanically tunneling occurs. After performing a Wick rotation instantons are solutions of equations of motion with a finite, non-zero action in Euclidean space-time. More details on that will be given in the next sections.

2.2 Manifolds and the Euclidean space

Basis to describe physical phenomena are space and time. A $d + 1$-dimensional ($d = 3n$, $n \in \mathbb{N}$ the number of considered atoms or particles) Minkowski space consists of d space-like dimensions and one dimension corresponding to time. In contrast to the Minkowski space the Euclidean space has only space-like dimensions. These two spaces have different metrics. For $d = 3$ the Minkowski metrics is given as

$$ds^2 = -\left(c^2 d\tau^2\right) + dx^2 + dy^2 + dz^2,$$

with τ the time-like, c a unit conversion factor, and x, y, and z space-like coordinates. The four-dimensional Euclidean metric, with $-it := \tau$ is

$$ds^2 = c^2 dt^2 + dx^2 + dy^2 + dz^2.$$

The Minkowski space can be considered as an Euclidean metric with a negative imaginary time coordinate and, thus, become a generalized Euclidean space. This transform is called Wick rotation. The combination of space and time in the Minkowski space forms a $d + 1$-dimensional differentiable (Riemannian) manifold representing a space-time continuum. Manifolds are generalizations of the familiar ideas of lines, planes, and their higher dimensional analogs.

A real $d + 1$-dimensional manifold $\mathcal{M}$ is a space which looks like an Euclidean space $\mathbb{R}^d$ around each point, i.e. it is locally similar to Euclidean space. More precisely, a manifold is defined by introducing a set of neighborhoods U_i, each a subspace of $\mathbb{R}^d$, covering $\mathcal{M}$. Thus, a manifold is constructed by pasting together many pieces of $\mathbb{R}^d$, which motivates the following definition, see also Fig. 2.1:

Definition 1 (Differentiable manifold). *A differentiable manifold is a set $\mathcal{M}$ equipped with the following structure*

1. *A family of coordinate charts, also called an atlas, such that each point $\boldsymbol{x} \in \mathcal{M}$ is represented in at least one chart. A coordinate chart is a subset $U_i \subset \mathcal{M}$ together with a bijective map $\Phi_i : U_i \rightarrow \Phi_i(U_i) \subset \mathbb{R}^{d+1}$.*

2. *For every pair of coordinate charts (U_i, Φ_i) and (U_j, Φ_j) of the atlas, $\Phi_i(U_i \cap U_j)$ and $\Phi_j(U_i \cap U_j)$ are open sets of $\mathbb{R}^d$ and the map*

$$\Phi_j \circ \Phi_i^{-1} : \Phi_i(U_i \cap U_j) \rightarrow \Phi_j(U_i \cap U_j) \tag{2.1}$$

   is smooth (i.e. C^∞).

For every point $\boldsymbol{x}_i \in \mathcal{M}$ there exists a chart $U_i \subset \mathcal{M}$ in which $\boldsymbol{x}_i$ is represented by local coordinates $\boldsymbol{x}_i = (x_i^1, \ldots, x_i^d) = \Phi_i(\boldsymbol{x}_i)$. In the rest of the text the notation $\boldsymbol{x}_i \in \mathcal{M}$, as generally accepted in the literature, will be used to represent local coordinates.

2.3 Differentiation and derivatives on manifolds

To specify the equations of motion of a dynamical system it is necessary to consider derivatives of curves in manifolds. The derivative of a curve in a vector space is again a curve in the vector space. For curves in manifolds this is not generally the case. In the
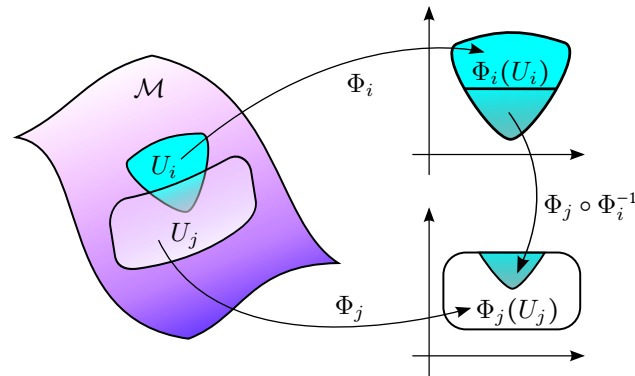
Figure 2.1: Two overlapping coordinate charts on the differentiable manifold $\mathcal{M}$. The map $\Phi_j \circ \Phi_i^{-1} : \Phi_i(U_i \cap U_j) \to \Phi_j(U_i \cap U_j)$ between the overlapping parts is smooth.[1]

following, concepts needed in order to speak of derivatives of maps between manifolds, will be recollected.

By definition the transformation between any two different coordinate representations is smooth, see 1 and Fig. 2.1.

A smooth manifold is, for example, a subset of Euclidean space which is locally the graph of a smooth (vector-valued) function. A line and a circle are one-dimensional manifolds, planes and spheres are two-dimensional manifolds, and so on to high-dimensional spaces. On smooth manifolds each predication about differentiability made in one coordinate representation automatically holds also in other coordinate representations. Because of that ordinary calculus as developed in $\mathbb{R}^d$ may also be used on manifolds. Differentiability of maps between manifolds is defined as follows:

Definition 2 (Differentiability). *Let $\mathcal{M}$ and $\mathcal{R}$ be two differential manifolds of dimension d and m, respectively. A map $\psi : \mathcal{M} \to \mathcal{R}$ is called differentiable at $\boldsymbol{x} \in \mathcal{M}$ if*

$$\Phi_j \circ \psi \circ \Phi_i^{-1} : \mathbb{R}^d \to \mathbb{R}^m \tag{2.2}$$

is differentiable at $\Phi_i(\boldsymbol{x})$ for some coordinate charts (U_i, Φ_i) containing $\boldsymbol{x}$ and (U_j, Φ_j) containing $\Phi_j(\boldsymbol{x})$.

Notice that the definition of differentiability is independent of the coordinate charts used. For more details on the following concepts and a pictorial explanation see for example [165].

Let $\boldsymbol{x}$ be a point in $\mathcal{M} \subset \mathbb{R}^{d+1}$. Then we have a lot of vectors at $\boldsymbol{x}$ in the surrounding space $\mathbb{R}^d$. A vector is characterized by its direction, length, and the point $\boldsymbol{x}$. Thus,

---

[1] Figure inspired by [162]

vectors with different base points $\boldsymbol{x}$ and $\boldsymbol{x}'$ are different even if they have the same length and direction. If considering the vectors at the base point $\boldsymbol{x}$, then not all of them are tangent vectors to the smooth surface $\mathcal{M}$. Let $\gamma(t) : \mathbb{R} \to \mathcal{M}$ be a smooth curve passing through P. Then γ generates a tangent vector at $\boldsymbol{x}$, the velocity vector.

$$\boldsymbol{v}_x = \left. \frac{d\gamma}{dt} \right|_{t=0} .$$ (2.3)

Definition 3 (Tangent vector). *A tangent vector $\boldsymbol{v}_x$ at a point $\boldsymbol{x} \in \mathcal{M}$ is an equivalence class of differentiable curves $\mathbb{R} \to \mathcal{M}$, where the equivalence relation for the two curves γ_1 and γ_2 is given by*

$$\gamma_1(0) = \gamma_2(0) = \boldsymbol{x} \quad \text{and} \quad \left. \frac{d(\Phi_i \circ \gamma_1)(t)}{dt} \right|_{t=0} = \left. \frac{d(\Phi_i \circ \gamma_2)(t)}{dt} \right|_{t=0}$$ (2.4)

for a coordinate chart (U_i, Φ_i) containing $\boldsymbol{x}$.
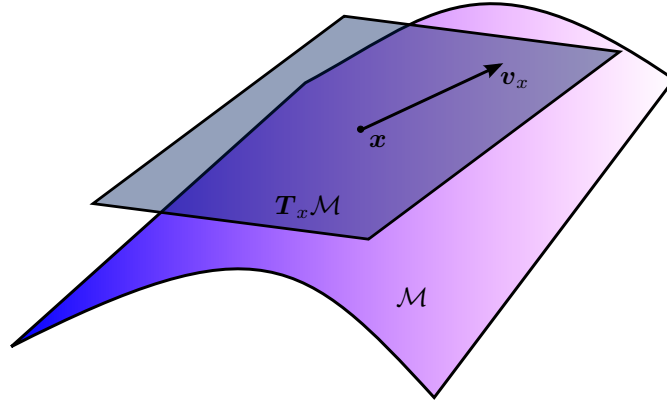
Figure 2.2: The tangent space of $\mathcal{M}$ at $\boldsymbol{x}$, denoted by $\boldsymbol{T}_x\mathcal{M}$, in case of $d = 2$.

Definition 4 (Tangent space). *The tangent space of $\mathcal{M}$ at $\boldsymbol{x}$ is the set of all tangent vectors at $\boldsymbol{x}$, and is denoted as $\boldsymbol{T}_x\mathcal{M}$. It is the linear space of dimension d, where $\alpha\boldsymbol{v}_1 + \beta\boldsymbol{v}_2$ is defined by the equivalence class of curves γ_3 that fulfills*

$$\gamma_3(0) = \boldsymbol{x} \quad \text{and} \quad \left. \frac{d(\Phi \circ \gamma_3)(t)}{dt} \right|_{t=0} = \left. \left(\alpha \frac{d(\Phi \circ \gamma_1)(t)}{dt} + \beta \frac{d(\Phi \circ \gamma_2)(t)}{dt} \right) \right|_{t=0} ,$$ (2.5)

with γ_1 and γ_2 the representatives for v_1 and v_2, respectively.

Definition 5 (Tangent bundle). *The tangent bundle of $\mathcal{M}$ is the union of all tangent spaces, i.e., the set*

$$\boldsymbol{T}\mathcal{M} = \bigcup_{\boldsymbol{x} \in \mathcal{M}} \boldsymbol{T}_x\mathcal{M}.$$ (2.6)

An element in $\boldsymbol{T}\mathcal{M}$ which is in $\boldsymbol{T}_x\mathcal{M}$ is denoted $\boldsymbol{v}_x$. The map $\varPi : \boldsymbol{T}\mathcal{M} \to \mathcal{M}$ which is given by $\varPi : \boldsymbol{v}_x \to \boldsymbol{x}$ is called the natural projection. A C^1 map $X : \mathcal{M} \to \boldsymbol{T}\mathcal{M}$ such that $\varPi \circ X = \mathrm{Id}$ is called a vector field, with Id the identity. Every vector field is intrinsically associated with a differential equation $d\boldsymbol{x}/dt = X(\boldsymbol{x})$. A vector field can be considered as a collection of smoothly varying directional derivatives at each point in $\mathcal{M}$.

Definition 6 (Cotangent space). *The cotangent space of $\mathcal{M}$ at $\boldsymbol{x}$ is the dual space of $\boldsymbol{T}_x\mathcal{M}$, i.e., the space of linear forms on $\boldsymbol{T}_x\mathcal{M}$. It is denoted by $\boldsymbol{T}_x^*\mathcal{M}$.*

Definition 7 (Cotangent bundle). *The cotangent bundle is the union of all cotangent spaces*

$$\boldsymbol{T}^*\mathcal{M} = \bigcup_{\boldsymbol{x} \in \mathcal{M}} \boldsymbol{T}_x^*\mathcal{M}. \tag{2.7}$$

The natural projection $\varPi : \boldsymbol{T}^*\mathcal{M} \to \mathcal{M}$ is defined in line with this.

Both, the tangent bundle $\boldsymbol{T}\mathcal{M}$ and the cotangent bundle $\boldsymbol{T}^*\mathcal{M}$, have the structure of differentiable manifolds of dimension $2d$. Coordinate charts in $\mathcal{M}$ can naturally introduce coordinate charts in $\boldsymbol{T}\mathcal{M}$ and $\boldsymbol{T}^*\mathcal{M}$, see discussion below.

Remark 1. *The set of smooth vector fields on $\mathcal{M}$ is denoted $\mathcal{X}(\mathcal{M})$. This set is an infinite dimensional vector space. The vector space operations are defined by point-wise operations on each tangent space.*

Remark 2. *The set of smooth real-valued functions on $\mathcal{M}$ is denoted $\mathcal{F}(\mathcal{M}) \subset L^2$. This set is an infinite dimensional vector space, with point-wise defined vector space operations.*

Definition 8 (Inner product). *The standard Hilbert space inner product on the function space L^2 is given as*

$$\langle f; g \rangle = \int_a^b f(x)g(x)dx \tag{2.8}$$

for $f, g \in C^2$, will be used for non-discrete functions. The discrete Euclidean inner product is given as

$$\langle \boldsymbol{x}; \boldsymbol{y} \rangle = \boldsymbol{x} \cdot \boldsymbol{y} = \sum_{k=1}^d x_k y_k \tag{2.9}$$

and will be used in the discrete case.

Due to the smooth transition between coordinate charts, the definitions of tangents and cotangents and the corresponding spaces given above are again independent of the choice of the coordinate (U_i, Φ_i), assuming that $\boldsymbol{x} \in U_i$. Therefore, if $\gamma \in \mathcal{F}(\mathcal{M})$ is a C^1 curve, its velocity vector at $\gamma(t)$, denoted by $\gamma'(t)$ or $(\frac{d\gamma}{dt})(t)$, is a tangent vector in $\boldsymbol{T}_{\gamma(t)}\mathcal{M}$. Thus, γ' is a map $t \to \boldsymbol{v}_{\gamma(t)} \in \boldsymbol{T}\mathcal{M}$.

Definition 9 (Derivative). *The derivative of a differential map $\psi : \mathcal{M} \to \mathcal{R}$ is a map $\psi_* : T\mathcal{M} \to T\mathcal{R}$ defined by*

$$\psi_*(\boldsymbol{v}_x) = (\psi \circ \gamma)'(0), \tag{2.10}$$

with $\boldsymbol{v}_x \in T_x\mathcal{M}$ and γ is a representative of $\boldsymbol{v}_x$.

Note that the definition is independent of the representative γ of $\boldsymbol{v}_x$. The derivative ψ_* takes a tangent vector in $T_x\mathcal{M}$ and "pushes it forward", by the map ψ, to a tangent vector in $T_{\psi(x)}\mathcal{M}$. Therefore, ψ_* is sometimes called the push-forward derivative. When expressed in coordinates, ψ_* constitutes the coordinate representation of ψ together with the Jacobian, which is the matrix valued function that gives the directional derivatives.

A vector in $\mathbb{R}^d$ can be viewed as a first order differential operator that acts on real-valued functions on $\mathbb{R}^d$. Thus, the linear space $\mathbb{R}^d$ is equivalent to the linear space of first order differential operators. From that point of view the space $T_x\mathcal{M}$ can be thought of as the linear space of first order differential operators acting on smooth real-valued functions f on $\mathcal{M}$ by taking the derivative of them in some direction. For example, assume γ is a representative of $\boldsymbol{v}_x \in T_x\mathcal{M}$, then the differential operator

$$\boldsymbol{v}_x[f] = \frac{d}{dt}(f \circ \gamma)(t)\Big|_{t=0} \tag{2.11}$$

is well defined. In local coordinates we have

$$\boldsymbol{v}_x[f] = \frac{d}{dt}(f \circ \Phi^{-1} \circ \Phi \circ \gamma)(t)\Big|_{t=0} = \frac{\partial f(\boldsymbol{x})}{\partial \boldsymbol{x}} \cdot \frac{d}{dt}(\Phi \circ \gamma)(t)\Big|_{t=0}. \tag{2.12}$$

Note that here a simplified notation is used: $\partial f(\boldsymbol{x})/\partial \boldsymbol{x}$ really means $\partial(f \circ \Phi^{-1})(\boldsymbol{x})/\partial \boldsymbol{x}$.

A basis in $T_x\mathcal{M}$ is given by $\partial/\partial x^1, \ldots, \partial/\partial x^d$. With (2.12) we see that every element $\boldsymbol{v}_x \in T_x\mathcal{M}$ is uniquely represented in this basis of partial (directional) derivatives

$$\boldsymbol{v}_x = \sum_{i=1}^d \dot{x}^i \frac{\partial}{\partial x^i} = \dot{\boldsymbol{x}} \cdot \frac{\partial}{\partial \boldsymbol{x}}, \tag{2.13}$$

where $\dot{x} = d(\Phi \circ \gamma)(t)/dt|_{t=0}$. Obviously, we have constructed coordinates $\dot{\boldsymbol{x}}$ in $T_x\mathcal{M}$ from coordinates $\boldsymbol{x}$ in $\mathcal{M}$. The pair $(\boldsymbol{x}, \dot{\boldsymbol{x}})$ constitutes local (natural) coordinates for $T\mathcal{M}$. The importance of natural coordinates is given by the fact that if the derivative γ' of a curve is represented in natural coordinates as $(\boldsymbol{x}, \dot{\boldsymbol{x}})$, then holds that $d\boldsymbol{x}(t)/dt = \dot{\boldsymbol{x}}(t)$.

A basis in a vector space induces a dual basis in the dual vector space. Thus, the basis $\{\partial/\partial x^1, \ldots, \partial/\partial x^d\} = \{\boldsymbol{e}_1, \ldots, \boldsymbol{e}_d\}$ in $T_x\mathcal{M}$ induces a dual basis $\boldsymbol{w}_1, \ldots, \boldsymbol{w}_d$ in $T_x^*\mathcal{M}$.

Recall that for a dual basis holds $\langle \boldsymbol{w}_i, \partial/\partial x^j \rangle = \delta_{ij}$, with δ_{ij} the Kronecker delta. From that follows, that $w_i = dx^i$, i.e. the projection of vectors on the x^i-axis. Therefore,

every element $p \in T_x^* \mathcal{M}$ can be written as $\sum_i p_i dx^i = p dx$, and (x, p) constitutes a coordinate chart in $T^* \mathcal{M}$, called canonical coordinates. The cotangent space can also be seen as the space of differentials at p. The general cotangent vector has the form $a_1 dx^1|_p + \cdots + a_d dx^d|_p$.

Definition 10 (Intrinsic coordinates). *Let v_x be a tangent vector generated by γ and let γ have the global coordinate representation $\gamma(t) = (x^1(t), \ldots, x^d(t))$. The numbers $a_i = \frac{dx^i}{dt}$ are called intrinsic coordinates of v_x with respect to the coordinate chart (U_i, Φ_i) containing x.*

The intrinsic coordinates a_i are the components of v_x with respect to the canonical frame $(e_1, \ldots, e_d)$. Any tangent vector $u \in T_u \mathcal{M}$ is a vector spanned by $e_1, \ldots, e_d$, i.e. can be represented as

$$u = a_1 e_1 + \cdots + a_d e_d. \tag{2.14}$$

Intrinsic coordinates to describe the tangent space of a curve γ, will for example be used in the derivations of the rate in Section 3.2.1. The local bases at each point on gamma together form a basis of the tangent bundle. As we are working in a flat space, the coefficients of the orthonormal frames of tangent and cotangent space can be identified with each other, which means that they form a basis and its dual basis at the same time. The coefficients a_i of the tangent space can directly serve as Fourier coefficients in the dual cotangent space, which will be important in Section 2.8.

2.4   Lagrangian mechanics

Recall that a Lagrangian system in classical mechanics consists of a configuration space $\mathcal{Q}$ and a Lagrangian function $L(t, \dot{\gamma}, \gamma)$, with $L : \mathbb{R} \times T\mathcal{M} \times \mathcal{Q} \to \mathbb{R}$ represented by $(t, v_x, x) \mapsto L(t, v_x, x)$. Hamilton's principle states that motions of Lagrangian systems extremize the action integral, see Fig. 2.3. The vector $x_{\text{init}} \in \mathbb{R}^d = \mathcal{Q}$ denotes the initial state of the considered system and $x_{\text{final}} \in \mathbb{R}^d$ the final state. The curve $\gamma : [a, b] \to \mathcal{Q}$, with $\gamma(a) = x_{\text{init}}$ and $\gamma(b) = x_{\text{final}}$, is a trajectory of a Lagrangian system if the action

$$S[\gamma(t)] = \int_a^b L(t, \dot{\gamma}, \gamma) dt \tag{2.15}$$

is extremized, i.e., its differential at γ, see Section 2.6 for the definition, vanishes for variations with fixed end points:

$$\langle S[\gamma], \delta\gamma \rangle = 0, \quad \text{for all } \delta\gamma \in T_\gamma \mathcal{C}_{[a,b]}(\mathcal{Q}), \tag{2.16}$$

where

$$\mathcal{C}_{[a,b]}(\mathcal{Q}) = \{ C^2 \text{ curves } (a, b) \to \mathcal{Q} \text{ with fixed end points } \gamma(a) \text{ and } \gamma(b) \}. \tag{2.17}$$
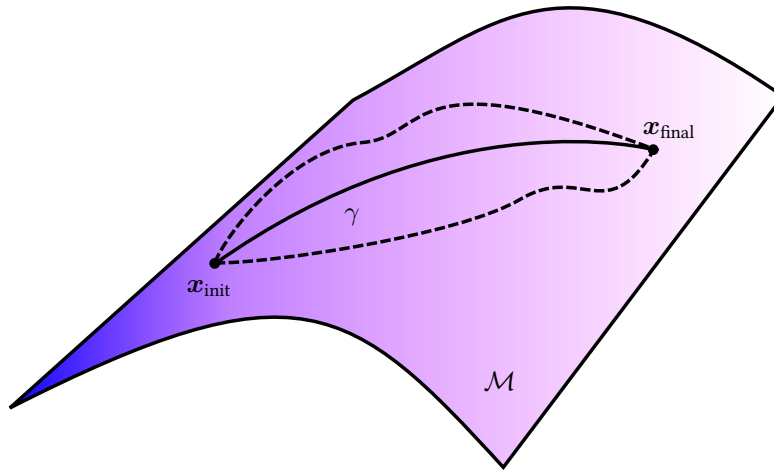
Figure 2.3: Hamiltons principle: variation of the path γ on the manifold $\mathcal{M}$ to find the stationary-action path.

The set $\mathcal{C}(\mathcal{Q})$ is an infinite dimensional differential manifold. However, the space itself is incomplete and, therefore, just a Banach space and not a Hilbert space. An element $\delta\gamma \in \boldsymbol{T}_\gamma\mathcal{C}_{[a,b]}(\mathcal{Q})$ is a curve $(a,b) \to \boldsymbol{T}\mathcal{Q}$ such that $\Pi \circ \delta\gamma(t) = \gamma(t)$.

Hamilton's principle leads to the governing equations, the Euler-Lagrange equations, a system of second order differential equations for the evolution of $\gamma(t)$ expressed in local coordinates

$$\frac{d}{dt}\frac{\partial L}{\partial \dot{\boldsymbol{x}}} - \frac{\partial L}{\partial \boldsymbol{x}} = 0. \tag{2.18}$$

Together with initial conditions $(\boldsymbol{x}_{\text{init}}, \dot{\boldsymbol{x}}_{\text{init}})$ the Euler-Lagrange equations define unique curves of motions. These equations keep their form in all coordinate representations which reflects the fact that Lagrangian mechanics is invariant under the group of diffeomorphisms on $\mathcal{Q}$. The Lagrangian is also invariant with respect to time translation.

A Newtonian potential system with a configuration space $\mathcal{Q} = \mathbb{R}^d$, $d = 3n$ is a special case of a Lagrangian system. The Lagrange function is here defined as the difference between the kinetic and the potential energy

$$L(\boldsymbol{x}, \dot{\boldsymbol{x}}) = \frac{\dot{\boldsymbol{x}} \cdot \mathrm{M}\dot{\boldsymbol{x}}}{2} - V(\boldsymbol{x}), \tag{2.19}$$

where M is the mass matrix, containing the masses of the considered d-body system, and the time independent potential energy function $V : \mathcal{Q} \to \mathbb{R}$, a smooth function, defined on the configuration space. The Euler-Lagrange equations (2.18) of such systems are the classical Newtonian equations of motions. The corresponding action is the classical action.

2.5　Feynman's path integral formalism

Feynman's path integral formalism generalizes the action principle of classical mechanics described in the previous section to quantum mechanics. The Feynman path integral, an integration over all paths γ contained in the path space $\Omega = \mathcal{C}_{[0,\beta\hbar]}(\mathcal{Q}) \subset \mathcal{M}$, can be rigorously defined as [176–178]

$$\int_\Omega \exp\left(\frac{i}{\hbar}S[\gamma(t)]\right) F[\gamma(t)]\mathcal{D}[\gamma(t)] \tag{2.20}$$

with $S[\gamma(t)]$ the classical action functional. The measure $\mathcal{D}[\gamma(t)]$ means the integration over all paths $\gamma(t)$ satisfying the boundary conditions $\boldsymbol{x}_{\text{init}} = \gamma(0) = \gamma(\beta\hbar) = \boldsymbol{x}_{\text{final}}$ weighted with the action $S[\gamma(t)]$. In [176–178] a class of functionals $F[\gamma(t)]$ is provided, such that the path integral (2.20) converges uniformly on any compact subset of the configuration space of the paths $\gamma \in \Omega$. One method to define the path integrals is a time slicing method [176–178], see Section 2.7. In the following the particular case where the functional $F[\gamma(t)] = 1$ for all paths is considered. The variable t parametrizes the arc-length of the path.

Another version of a time slicing approach is obtained by employing Trotter formulas [179]. Further mathematically rigorous approaches to define Feynman's path integrals, e.g., analytic continuation using the Feynman–Kac formula [180, 181] or treating them as oscillatory integrals, are mentioned in [182–187] and references therein. Another approach for a rigorous definition is to form $\mathcal{D}[\gamma(t)]$ into a conditional Wiener measure to give a well-defined formulation of the integral [188].

Now we will have a look at the Wick rotation, a procedure that allows the explicit evaluation of path integrals.

Wick rotation

The basic notion of the Wick rotation is to replace the integration over real time in the classical action with an integration over negative imaginary time when going from the Minkowski space to the Euclidean space. From now on imaginary time will be denoted as t. Then the path $\gamma(t)$ is a continuous or sufficiently smooth map from the inverse imaginary time interval $[0, \beta\hbar]$ to $\mathbb{R}^d = \mathcal{Q}$ in the path space $\mathcal{C}_{[0,\beta\hbar]}(\mathcal{Q})$. Later on we are interested in calculating partition functions via the path integral formalism, therefore, the interval (a, b) is replaced by $[0, \beta\hbar]$.

Also the classical action changes. The new weight function is the Euclidean action functional S_{E}.

$$S_{\text{E}}[\gamma(t)] = \int_0^{\beta\hbar} L(t, \dot{\gamma}, \gamma)dt = \int_0^{\beta\hbar} \frac{1}{2}\dot{\gamma} \cdot \mathrm{M}\dot{\gamma} + V(\gamma(t))dt, \tag{2.21}$$

$\hbar$ reduced Planck's constant, $\beta = 1/k_{\mathrm{B}}T$, T the temperature, k_{B} Boltzmann's constant, and $S_{\mathrm{E}} : C^1\left([0, \beta\hbar]\right) \to \mathbb{R}$. Compared to the classical Lagrangian in (2.19) there is a plus sign instead of a minus in front of the potential function. Therefore, the path γ can also be interpreted as the classical movement on the upside-down potential energy surface $-V(\boldsymbol{x})$ of a chemical system which allows to calculate the transition probability of a particle to tunnel through a classical forbidden region in the Minkowski space (through $V(\boldsymbol{x})$ from the reactant to the product valley). The calculation of the tunneling probability with the Euclidean path integral after the Wick rotation is based on a classically allowed movement on $-V(\boldsymbol{x})$, see Fig. 2.4. For a more detailed explanation of the Euclidean action coming from the classical action see for example [174, 189].
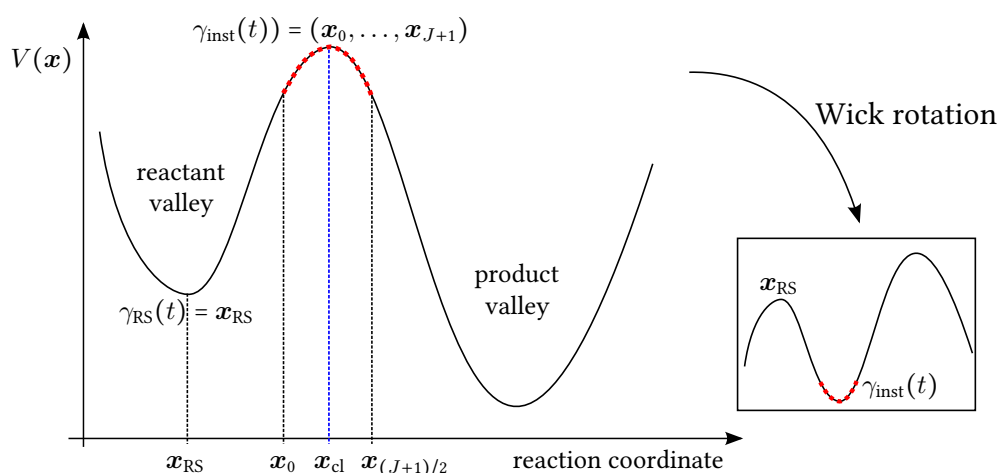
Figure 2.4: Left: The reactant state $\boldsymbol{x}_{\mathrm{RS}}$ and the instanton (red), a special case of $\gamma(t)$, on a one-dimensional potential energy surface, $d = 1$. $\boldsymbol{x}_{\mathrm{cl}}$ is the classical transition state, a first-order saddle point on the potential energy surface. Right: The upside-down potential after the Wick rotation.

The integration over all paths, in equation (2.20), corresponds to all possibilities a particle can take to propagate out of the initial state $\boldsymbol{x}_{\mathrm{init}}$ and go to the final state $\boldsymbol{x}_{\mathrm{final}}$. Thus, the propagator $\langle\boldsymbol{x}_{\mathrm{final}}|\exp\left(-\beta\hat{H}\right)|\boldsymbol{x}_{\mathrm{init}}\rangle$, also called kernel, can be replaced by the integration over all paths and each path has a weight depending on its importance. Here, the Bra-Ket notation is used, the Ket $|\cdot\rangle$ denotes a vector of the Hilbert space L^2 and the Bra $\langle\cdot|$ its dual. $\hat{H}$ is the Hamilton operator. In correspondence to Feynman's derivation of the density matrix [190], where the kernel is expressed in terms of path integrals, the propagator is then given as

$$\langle\boldsymbol{x}_{\mathrm{final}}|\exp\left(-\beta\hat{H}\right)|\boldsymbol{x}_{\mathrm{init}}\rangle = \int_{\gamma(0)=\boldsymbol{x}_{\mathrm{init}}}^{\gamma(\beta\hbar)=\boldsymbol{x}_{\mathrm{final}}} \mathcal{D}[\gamma(t)] \exp\left(-\frac{1}{\hbar}S_{\mathrm{E}}[\gamma(t)]\right), \qquad (2.22)$$

which is also an element of the density matrix.

2.6   Distributional derivatives of the Euclidean action

The formula for the gradient of a functional depends on the chosen inner product. When considering continuous paths, as in the rest of this section, the standard Hilbert space inner product, see (2.8) is used.

In variational calculus the functional (also distributional) derivative arises as generalization of the usual derivative. Instead of differentiating a function with respect to a variable, one differentiates a functional with respect to a function.

Definition 11 (Functional derivative). *Let $\mathcal{M}$ be a differentiable manifold with smooth functions $\gamma(t)$ defined on it and the functional $S[\gamma(t)] : \mathcal{M} \to \mathbb{R}$. The functional derivative of $S[\gamma(t)]$ which is denoted by $\delta S[\gamma(t)]/\delta\gamma(t)$ is a distribution. For all test functions $f(t)$ applied to the distribution holds*

$$\left\langle \frac{\delta S[\gamma(t)]}{\delta\gamma(t)}, f(t) \right\rangle = \int \frac{\delta S[\gamma(t)]}{\delta\gamma(t')} f(t')dt' = \tag{2.23}$$

$$= \lim_{\varepsilon \to 0} \frac{S[\gamma(t) + \varepsilon f(t)] - S[\gamma(t)]}{\varepsilon} \tag{2.24}$$

$$= \frac{d}{d\epsilon} S[\gamma + \epsilon f]\Big|_{\epsilon=0}. \tag{2.25}$$

In a Banach space, e.g., a Hilbert space, the functional derivative is the Fréchet derivative. In general locally convex spaces the Gâteaux derivative is used. The first variation of the action functional $\delta S[\gamma(t)]$ is obtained by replacing $f(t)$ with the first variation $\delta\gamma(t)$ of $\gamma(t)$. Instead of $\delta\gamma(t)$ the Dirac delta function can be used as test function.

First variation

By definition the first variation of the Euclidean action functional (2.21) is then found as

$$\frac{\delta S_{\mathrm{E}}[\gamma(t)]}{\delta\gamma(s)} = \int_0^{\beta\hbar} \frac{\delta}{\delta\gamma(s)} \left[\frac{\mathrm{M}}{2}\left(\frac{d\gamma(t)}{dt}\right)^2 + V(\gamma(t)) \right] dt, \tag{2.26}$$

where the interchangeability of the integral and the variation has been used. With the properties of the delta function (B.4) and $\frac{\delta\gamma(t)}{\delta\gamma(s)} = \delta(t-s)$, see Section B.1, follows

$$\frac{\delta S_{\mathrm{E}}[\gamma(t)]}{\delta\gamma(s)} = \int_0^{\beta\hbar} \left[\frac{\mathrm{M}}{2} 2 \frac{d\gamma(t)}{dt}\frac{d}{dt}\delta(t-s) + \frac{d\gamma(t)}{d\gamma(t)}\frac{\delta V(\gamma(t))}{\delta\gamma(s)} \right] dt. \tag{2.27}$$

By definition of the Delta function and when exchanging the derivative operators in the second term we have

$$\frac{\delta S_{\mathrm{E}}[\gamma(t)]}{\delta\gamma(s)} = \int_0^{\beta\hbar} \left[\mathrm{M}\frac{d\gamma(t)}{dt}\frac{d}{dt}\delta(t-s) - \frac{dV(\gamma(t))}{d\gamma(t)}\delta(t-s) \right] dt. \tag{2.28}$$

With partial integration and evaluating the integration over the delta function

$$\frac{\delta S_{\mathrm{E}}[\gamma(t)]}{\delta\gamma(s)} = \mathrm{M}\left[\frac{d\gamma(t)}{dt}\delta(t-s)\Big|_{-T/2}^{T/2} - \int_0^{\beta\hbar} \frac{d^2\gamma(t)}{dt^2}\delta(t-s)dt \right] - \frac{dV(\gamma(t))}{d\gamma(t)}\Big|_{t=s}, \tag{2.29}$$

if $s \in [0, \beta\hbar]$, else $\int \delta(t-s) = 0$, the first variation of the Euclidean action is

$$\frac{\delta S_{\mathrm{E}}[\gamma(t)]}{\delta\gamma(s)} = -\mathrm{M}\frac{d^2\gamma(t)}{dt^2} - \frac{dV(\gamma(t))}{d\gamma(t)}\Big|_{t=s} \qquad \text{for } s \in [0, \beta\hbar]. \tag{2.30}$$

Second variation

For the second distributional derivative of the action functional holds

$$\frac{\delta^2 S_{\mathrm{E}}[\gamma(t)]}{\delta\gamma(s)\delta\gamma(s')} = \int_0^{\beta\hbar} \frac{\delta^2}{\delta\gamma(s)\delta\gamma(s')} \left[\frac{\mathrm{M}}{2}\left(\frac{d\gamma(t)}{dt}\right)^2 + V(\gamma(t)) \right] dt. \tag{2.31}$$

Here properties of the Dirac delta function are used, see Section B.1, then follows similar to the first variation

$$\frac{\delta^2 S_{\mathrm{E}}[\gamma(t)]}{\delta\gamma(s)\delta\gamma(s')} = \int_0^{\beta\hbar} \frac{1}{\delta\gamma(s)} \left[\frac{\mathrm{M}}{2}\frac{d\gamma(t)}{dt}\frac{d}{dt}\delta(t-s') + \frac{dV(\gamma(t))}{d\gamma(t)}\delta(t-s') \right] dt = \tag{2.32}$$

$$= \int_0^{\beta\hbar} \left[\frac{\mathrm{M}}{2}\frac{d}{dt}\delta(t-s)\frac{d}{dt}\delta(t-s') - \frac{d^2V(\gamma(t))}{dy^2(t)}\delta(t-s)\delta(t-s') \right] dt. \tag{2.33}$$

Partial integration leads to

$$\frac{\delta^2 S_{\mathrm{E}}[\gamma(t)]}{\delta\gamma(s)\delta\gamma(s')} = \frac{\mathrm{M}}{2}\left[\frac{d}{dt}\delta(t-s)\delta(t-s')\Big|_{-T/2}^{T/2} - \right. \tag{2.34}$$

$$\left. \int_0^{\beta\hbar} \delta(t-s)\frac{d^2}{dt^2}\delta(t-s')dt \right] + \frac{d^2V(\gamma(t))}{d^2\gamma(t)}\delta(t-s')\Big|_{t=s} = \tag{2.35}$$

$$= -\frac{\mathrm{M}}{2}\frac{d^2}{dt^2}\delta(t-s')\Big|_{t=s} + \frac{d^2V(\gamma(t))}{d^2\gamma(t)}\delta(t-s')\Big|_{t=s}. \tag{2.36}$$

The last expression (2.36) is the second variation of the Euclidean action. This expression will play a role when deriving the instanton rate formula in the next chapter.

Now the stationary-action paths $\gamma(t)$ with $\delta S_{\mathrm{E}}[\gamma] = 0$ can be determined. The steepest descent evaluation of partition functions in Section 3.1 is based on these paths. The basics for a numerical evaluation are provided in the next section.

2.7   Time slicing approximation of the stationary-action path

To evaluate the path integral formulation of the propagator (2.22) the imaginary time interval $[0, \beta\hbar]$ (of the path $\gamma(t)$, $\gamma : [0, \beta\hbar] \to \mathbb{R}^d \subset \mathcal{M}$) is discretized in $J + 1$ intervals of variable length. A schematic overview of the notation introduced and used in the following is depicted in Fig. 2.5 and Fig. 2.6. The division of $[0, \beta\hbar]$ is

$$\Delta : 0 = t_0 < t_1 < \cdots < t_J < t_{J+1} = \beta\hbar \tag{2.37}$$

and the step-size of each sub interval is $h_j = t_j - t_{j-1}$. Let

$$\tilde{\boldsymbol{x}}_j \in \mathbb{R}^d \subset \mathcal{M}, \quad j = 0, 1, 2, \ldots, J, J + 1 \tag{2.38}$$

be arbitrary $J + 2$ points (coordinate charts) of the configuration space $\mathbb{R}^d = \mathcal{Q} \subset \mathcal{M}$. For sake of simplicity here and in the following mass-weighted coordinates will be used. The mass matrix is then absorbed in the coordinates in configuration space by $\boldsymbol{x}_j = \sqrt{M_j}\tilde{\boldsymbol{x}}_j$, with M_j the mass matrix at t_j.

$$\boldsymbol{x}_j \in \mathbb{R}^d \subset \mathcal{M}, \quad j = 0, 1, 2, \ldots, J, J + 1. \tag{2.39}$$

Each discretization point j of dimension d in the configuration space corresponds to one geometry of the considered molecule. Thus, d and J are independent of each other. The piecewise path $\gamma_\Delta(t) \in \mathcal{C}_{[0,\beta\hbar]}(\mathcal{Q})$ going through $(\boldsymbol{x}_{J+1}, \boldsymbol{x}_J, \ldots, \boldsymbol{x}_1, \boldsymbol{x}_0) \in \mathbb{R}^{d(J+2)} \subset \Omega$ is the broken path satisfying Euler's equation of motion in mass-weighted coordinates

$$-\frac{1}{2}\frac{d^2}{dt^2}\gamma_\Delta(t) - \frac{dV(\gamma_\Delta(t))}{d\gamma_\Delta(t)} = 0, \tag{2.40}$$

for $t_{j-1} \leq t \leq t_j$ $(j = 1, 2, \ldots, J, J + 1)$ with the control points

$$\boldsymbol{x}_j := \boldsymbol{\gamma}_\Delta(t_j), \quad j = 0, 1, 2, \ldots, J, J + 1. \tag{2.41}$$

A path γ_Δ fulfilling condition (2.40) is also called a minimum action path (MAP) that differs from the minimum energy path (MEP).

At each time $0 < t < \beta\hbar$ the path $\gamma_\Delta(t)$ has d components. Thus, after discretization into $J + 1$ intervals the dimension is $d(J + 2)$. When the path is closed, i.e., $t_{J+1} = t_0$, the manifold is of dimension $d(J + 1)$. As we are later on especially interested in calculating partition functions, which are based on closed loops, see (3.5), the following formulations refer to closed paths.

The Euclidean action of the closed and piecewise continuous path is given as

$$S_{\mathrm{E}}^\Delta : \underbrace{\mathbb{R}^d \times \cdots \times \mathbb{R}^d}_{(J+1)\text{-times}} \to \mathbb{R}. \tag{2.42}$$
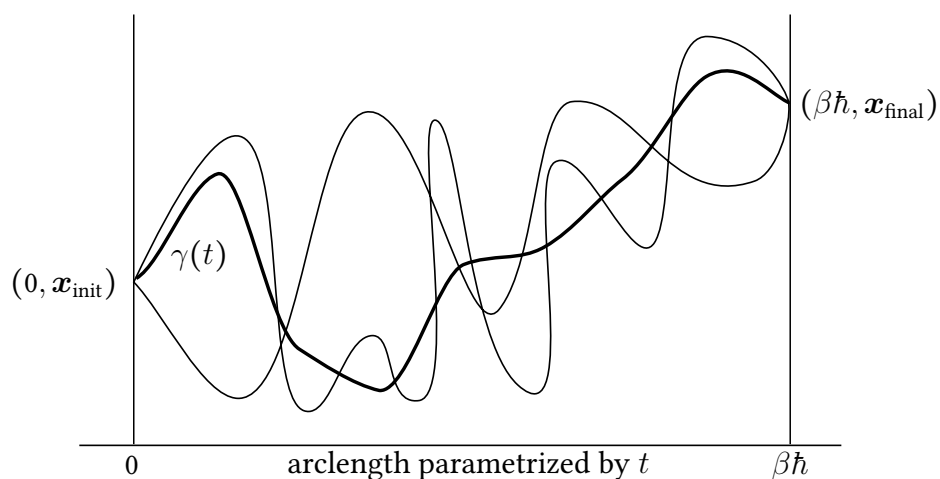
Figure 2.5: Schematic paths fluctuating between $\boldsymbol{x}_{\text{init}} = \gamma(0)$ and $\boldsymbol{x}_{\text{final}} = \gamma(\beta\hbar)$ for $d = 1$.[1]
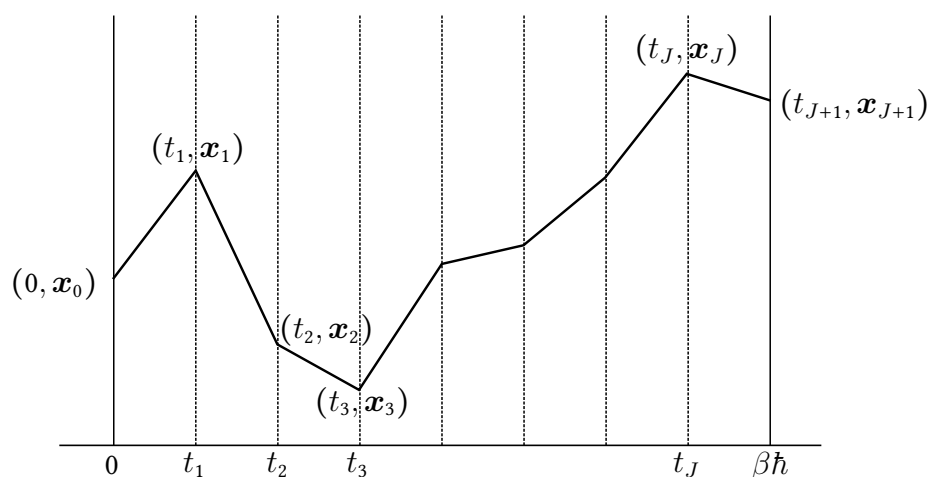
Figure 2.6: The time sliced path $\gamma_\Delta(t)$ for $d = 1$. The connection between the discretization points t_j does not need to be linear. The fluctuations around $\gamma_\Delta(t)$ can have any form, but have to go through the points $(t_j, \boldsymbol{x}_j)$. [1]

---

[1] Figures inspired by [177]

The functional $S_{\mathrm{E}}[\gamma_\Delta]$ becomes in its discrete version the action sum

$$S_E^\Delta(\boldsymbol{x}_{J+1}, \boldsymbol{x}_J, \dots, \boldsymbol{x}_2, \boldsymbol{x}_1) = S_{\mathrm{E}}[\gamma_\Delta] = \int_0^{\beta\hbar} L\left(t, \frac{d}{dt}\gamma_\Delta(t), \gamma_\Delta(t)\right) dt = \quad (2.43)$$

$$= \sum_{j=1}^{J+1} \int_{t_{j-1}}^{t_j} L_d\left(t, \frac{d}{dt}\gamma_\Delta(t), \gamma_\Delta(t)\right) dt = \quad (2.44)$$

$$= \sum_{j=1}^{J+1} S_{\mathrm{E}}^j(\boldsymbol{x}_j, \boldsymbol{x}_{j-1}) = \sum_{j=1}^{J+1} \frac{1}{2} S_0^j + S_{\mathrm{pot}}^j = \quad (2.45)$$

$$=: \frac{1}{2} S_0(\boldsymbol{x}_{J+1}, \dots, \boldsymbol{x}_1) + S_{\mathrm{pot}}(\boldsymbol{x}_{J+1}, \dots, \boldsymbol{x}_1), \quad (2.46)$$

with S_0 the velocity part and S_{pot} the potential energy part of the Euclidean action. For more mathematical details on the symplectic integration on manifolds see for example [191, 192].

This leads to the time sliced flat-space version of path integration. The resulting oscillatory integral, which corresponds to Feynman's definition of path integration in (2.22), has an existing limit [178, 193]

$$\lim_{|\Delta|\to 0} I(\Delta, \boldsymbol{x}_{\mathrm{init}}, \boldsymbol{x}_{\mathrm{final}}) = \lim_{|\Delta|\to 0} \left(\prod_{j=1}^{J+1}\left(\frac{1}{2\pi\hbar h_j}\right)^{d/2}\right) \int_{\mathbb{R}^{dJ}} \exp\left(-\frac{1}{\hbar} S_{\mathrm{E}}[\gamma_\Delta(t)]\right) \prod_{j=1}^{J} d\boldsymbol{x}_j$$

$$(2.47)$$

$$= \int_\Omega \exp\left(-\frac{1}{\hbar} S_{\mathrm{E}}[\gamma(t)]\right) \mathcal{D}[\gamma(t)], \quad (2.48)$$

with $|\Delta| = \max_j\{t_j\}$. Note the meaning of $\int_{\mathbb{R}^d} \dots d\boldsymbol{x} = \int \cdots \int \dots dx^1 dx^2 \cdots dx^d$.

The prefactor $\prod_{j=1}^{J+1}\left(\frac{1}{2\pi\hbar h_j}\right)^{d/2}$, which is important to guarantee the convergence, arises by the free-particle assumption between two time steps. For the kinetic energy part of S_{E}^j denoted by $S_0^j(\boldsymbol{x}_j, \boldsymbol{x}_{j-1})$ holds after discretization (for $d = 1$):

$$\langle \boldsymbol{x}_{j+1}| \exp\left(-\frac{h_j}{\hbar}\frac{d^2}{dt^2}\gamma_\Delta(t_j)\right)|\boldsymbol{x}_j\rangle \quad (2.49)$$

$$= \sqrt{\frac{1}{2\pi\hbar h_j}} \exp\left(-\frac{h_j}{2\hbar}\frac{(\gamma_\Delta(t_{j+1}) - \gamma_\Delta(t_j))^2}{h_j^2}\right). \quad (2.50)$$

2.8   Fermi local coordinates and Fourier path integration

The Fourier path integral approach uses a set of variables which represent the different length scale fluctuations of the quantum path instead of points on the path [194]. The
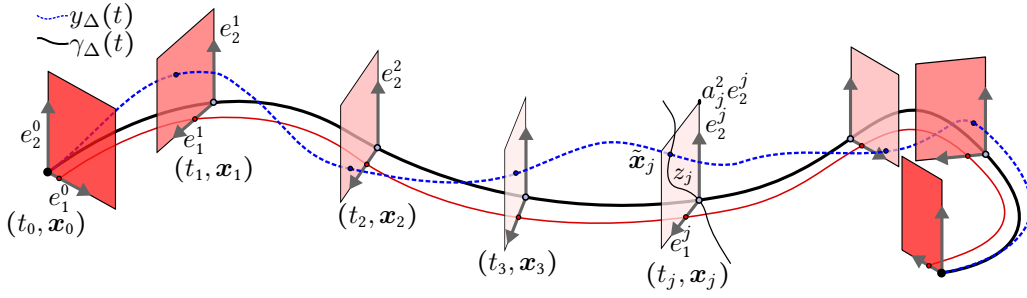
Figure 2.7: black: stationary-action path, blue: fluctuation, red recangles (images along the instanon path): tangent space and Fermi local coordinates for $d = 2$.

paths contributing to a density matrix $\langle x_{\text{final}}|\exp\left(-\beta\hat{H}\right)|x_{\text{init}}\rangle$ have the same initial point x_{init} and final point x_{final}. Thus, it is possible to write the fluctuations with respect to the stationary-action path $\gamma_\Delta(t)$ that fulfills the Euler-Lagrange equation, see equation (2.40). Fermi local coordinates [195] are in Riemannian geometry local coordinates adapted to the stationary-action path $\gamma_\Delta(t)$. They will later on be used for the explicit rate calculations. In global coordinates the stationary-action path is given in discrete form as $\gamma_\Delta \to (x_{J+1}, \ldots, x_1)$. Let $\mathcal{M}$ again be a $d+1$-dimensional Riemannian manifold. The path $\gamma_\Delta(t)$ is the stationary-action path on $\mathcal{M}$ and x_j, $j = 1 \ldots, J+1$ points on $\gamma_\Delta(t)$. Then there exist local coordinates $(t, x_j^1, \ldots, x_j^d)$ around x_j such that (i) for small t_0, $(t_0, 0, \ldots, 0)$ represents the stationary path near x_{init} and (ii) on $\gamma_\Delta(t)$, the metric tensor is the Euclidean metric.

The Fermi local coordinates based on γ_Δ are defined as follows [196, 197]: the coordinates of a point on the curve are $x_j = \gamma_\Delta(t_j) = (t_j, 0, \ldots, 0) \in \mathbb{R}^{d+1}$, where t_j is the proper time (distance) measured along $\gamma_\Delta(t)$ from its origin x_{init} to the point in question. By e_j^0 the tangent to $\gamma_\Delta(t)$ is labeled and $e_j^0 = d\gamma_\Delta/dt_j$.

Pick a vielbein of unit orthonormal vectors e_i^j, $i = 1, \ldots, d$ which are also orthogonal to e_0^j. For these orthonormal vectors holds

$$e_k^j \cdot e_l^j = \delta_{k,l}, \tag{2.51}$$

with $\delta_{k,l}$ the Kronecker Delta. The $\{e_j^k\}_{k=1}^d \in \mathbb{R}^{d+1}$ are similar to the canonical frame vectors of the configuration space defined in definition 10 as intrinsic coordinates. The vectors are given as $e_0^j = (1, 0, \ldots, 0)$, $e_1^j = (0, 1, 0, \ldots, 0)$, and so on until $e_d^j = (0, 0, \ldots, 0, 1)$. This holds for all $j = 1, \ldots, J+1$. Thus, the indices j could in principle be neclegted. These vectors form the rows of the matrices $E^j = (e_0, e_1, \ldots, e_{d-1})^T \in \mathbb{R}^{d \times d}$.

Now we consider a point $\tilde{x}_j$ apart from the curve γ_Δ, see Fig. 2.7. We have a closer look at the curve orthogonal to $\gamma_\Delta(t)$ which goes through $\tilde{x}$ to obtain a coordinate representation of $\tilde{x}$. Let its tangents at the point where it intersects the curve $\gamma_\Delta(t)$ be

expressed as $a_i^j e_i^j \in T_{x_j}\mathcal{M}$. Then $\tilde{\boldsymbol{x}}_j = (t_j, a_1^j z_j, a_2^j z_j, \ldots, a_d^j z_j)$, where t_j is again the proper "time" measured to the foot $(t_0, \boldsymbol{x}_0)$ of $\gamma_\Delta(t)$, while z_j is the proper distance to $\gamma_\Delta(t)$ measured from $\boldsymbol{x}_j$ to $\tilde{\boldsymbol{x}}$. The local Fermi coordinates are well defined in regions, where $\gamma_\Delta(t)$ and its orthogonal curve do not recross.

The paths fluctuating around the stationary-action path $\gamma_\Delta(t)$ are given as

$$\gamma_\Delta^{a_1^1,\ldots,a_d^{J+1}}(t) = \gamma_\Delta(t) + y_\Delta(t), \tag{2.52}$$

with $y_\Delta(0) = 0$ and $y_\Delta(\beta\hbar) = 0$. The full fluctuations around γ_Δ are also represented as

$$\gamma_\Delta^{a_1^1,\ldots,a_d^{J+1}}(t_j) = \tilde{\boldsymbol{x}}_j = \gamma_\Delta(t_j) + \delta\boldsymbol{x}_j = \gamma_\Delta(t_j) + y_\Delta(t_j). \tag{2.53}$$

In general relativity this is also known as the equation of geodesic deviation. The fluctuations can be written in Fermi local coordinates as

$$y_\Delta(t_j) = a_1^j e_1^j + a_2^j e_2^j + \cdots + a_d^j e_d^j. \tag{2.54}$$

However, the boundary conditions for $y_\Delta(t)$ in equation (2.52) indicate that it is possibile to expand the fluctuations in Cartesian coordinates component-wise into a Fourier sine series [182, 198]. The i-th component is (for an equidistant discretization, see [199] for a variable step-size approach) given as

$$y^i(t) = \sum_{l=1}^{\infty} b_l^i \sin\left(\frac{l\pi t}{\beta\hbar}\right). \tag{2.55}$$

The Fourier series can be truncated at some values $l_{\max}$. The $d\,l_{\max}$ Fourier coefficients are the necessary variables to describe the quantum paths contributing to the path integral. Usually, $l_{\max}$ can be chosen to be equal to $J + 1$, the number of discretization points of the interval $[0, \beta\hbar]$. A bijective relation between the b_k^i and the a_k^i can be established. Thus, the b_l^i can as well be considered as local Fermi coordinates, however, in a different representation than in equation (2.54).

Therefore, any $y_\Delta(t) \in T_{\gamma_\Delta}\mathcal{M}$ can be described as

$$y_\Delta(t_j) = a_1^j e_1^j + a_2^j e_2^j + \cdots + a_d^j e_d^j \tag{2.56}$$

$$= \sum_{l=1}^{d(J+1)} b_l \mathbf{u}_l(t_j), \tag{2.57}$$

with orthonormal functions $\mathbf{u}_l(t)$. Their discrete form is given as the vector $\mathbf{u}_l$. The matrix U contains the vectors $\mathbf{u}_l$ as entries of its colums. The functions $\mathbf{u}_l(t)$ are orthonormal with respect to a weighted inner product defined on the Banach space $\mathcal{C}(\mathbb{R}^d)_{[0,\beta\hbar]}$

$$\frac{1}{\beta\hbar}\int_0^{\beta\hbar} dt\, \mathbf{u}_k(t)\mathbf{u}_l(t) = \delta_{kl}. \tag{2.58}$$

In the discrete case the inner product is, analog to definition 8,

$$\langle \mathbf{u}_k, \mathbf{u}_l \rangle = \frac{1}{\beta \hbar} \mathbf{u}_k \mathbf{u}_l = \delta_{kl}. \tag{2.59}$$

The full path y_Δ of a fluctuation is represented as

$$y_\Delta = \begin{pmatrix} y_\Delta(t_1) \\ \vdots \\ y_\Delta(t_{J+1}) \end{pmatrix} = \begin{pmatrix} E^1 & 0 & \cdots & & 0 \\ 0 & E^2 & 0 & \cdots & 0 \\ \vdots & & 0 & \cdots & 0 \\ \vdots & & 0 & \cdots & E^{J+1} \end{pmatrix} \begin{pmatrix} \boldsymbol{a}^1 \\ \vdots \\ \boldsymbol{a}^{J+1} \end{pmatrix} =: E\mathbf{a} = \tag{2.60}$$

$$= (\mathbf{u}_1, \ldots, \mathbf{u}_{J+1}) \begin{pmatrix} \boldsymbol{b}^1 \\ \vdots \\ \boldsymbol{b}^{J+1} \end{pmatrix} =: U\mathbf{b}. \tag{2.61}$$

Here the coefficients of the orthonormal frame vectors are written in vector notation $(\boldsymbol{a}^j)^T = (a_0^j, a_1^j, \ldots, a_{d-1}^j)$. The relation between E and U will become clear on page 56.

For the later derivations of the tunneling rates we are interested in a path integral representation where the integration over the Cartesian coordinates $\boldsymbol{x}_j$ is replaced by the integration over local Fermi coordinates. That includes a transform of the path integral from the time sliced path to a Fourier representation of the path, which are equivalent [200, 201]. The Fourier representation is obtained by a sine transform or an expansion in any complete set of orthonormal functions $\{\mathbf{u}_l(t)\}_{l=0}^{dk_{\max}}$ (normal modes).

The transform from one representation to the other is includes a functional Jacobian determinant N, see page 57. The value of the Jacobian N is connected with the S_0 term of the action. The S_0 term includes the velocity of passing through the path and dominates over the second term S_{pot}. The "Fourier" transform is not a linear transform for time sliced paths.

It turns out, that for small enough step-size the Jacobian N of the sine transform in one-dimension on the interval $[a, b] = [0, 1]$, $d = 1$, and equidistant discretization is [200]:

$$N = \prod_{j=1}^{J+1} \frac{\frac{1}{2}\pi j/(J+2)}{\sin(\frac{1}{2}\pi j/(J+2))} = (J+1)^{1/2} \prod_{j=1}^{J+1} \left(\frac{\pi j}{J+2} \right). \tag{2.62}$$

A similar relation holds for the d-dimensional case. In the limit for $\Delta \to 0$ and $J \to \infty$, N converges to 1. The transformed path integral which needs such an Jacobian will be discussed on page 57.

In the next chapter all the definitions given above will be used to derive a stringent formulation of instanton rate theory.

Part II

Methodological and Technical Improvements and Results

THE VARIABLE STEP-SIZE IMAGINARY F (INSTANTON) METHOD

Instanton rate theory (also called imaginary F method, where F is the free energy) [202–207] is a quantum rate theory based on statistical Feynman path integrals [145], see Section 2.5, incorporating quantum tunneling effects. Adiabatic and non-adiabatic processes can easily be handled while it is a challenge in other rate theories [208]. Central to the instanton method is the optimal tunneling path (the instanton), the path with the highest statistical weight at a certain temperature. The longer the instanton path is, the stronger is the delocalization of the atoms involved thereby indicating tunneling to be important during the reaction. The fluctuations around the instanton tunneling path are taken into account up to second order. The instanton method is, along with some extensions [209, 210], increasingly used to calculate reaction rates in chemical systems [149, 153, 211–226]. In the formulation of a harmonic quantum transition-state theory, many parallels between the classical TST and the instanton method were demonstrated [153, 154, 227].

The aim of the following chapter is a consistent rate formulation with a variable step-size discretization. It will according to my knowledge be the first step-by-step derivation of the imaginary F instanton rate for d-dimensional systems. For an equidistant step-size discretization the rate has been published, see for example [216, 216, 227, 227–229] or for one-dimensional systems [182, 198].

This Chapter is organized as follows: after a short introduction to the imaginary F method, the steepest descent evaluation of path integrals is taken, leading to similar

results as in the JWKB approximation. The next part deals with a consistent and stringent derivation of the more dimensional variable step-size evaluation of the imaginary free energy rate [202–204, 206]. Here the evaluation of partition functions in one- and higher-dimensional systems will be presented. In the final part the variable step-size instanton rate is formulated. Fig. 3.1 contains an overview of the structure of the Chapter as well.

The imaginary free energy method comes from quantum field theory where the squares of the absolute values of the elements of the scattering matrix (S-matrix) [230, 231] describe the probability of a system to pass from a certain initial state to a certain, also predefined, final state. The poles of the S-matrix, its energy eigenvalues, can be complex. Complex S-matrix poles are related to decaying resonances [232]. In analogy to imaginary part of the ground state energy $\mathcal{I}m\ E_0$ of resonances in quantum field theory, the imaginary part of the free energy $\mathcal{I}m\ F$ is related to the decay probability of a metastable system which gives quantum reaction rates (decay rates of a metastable state), k_{inst}, including tunneling [202], see [233] for an overview.

$$k_{\mathrm{inst}} = -\frac{2}{\hbar}\mathcal{I}m\left(F\right), \tag{3.1}$$

with $\hbar$ Planck's constant divided by 2π. This relation, a generalization of equilibrium statistical mechanics, holds for a wide class of models [234] whose dynamics can be described by a Fokker-Planck equation [202]. One of many approaches [234] to calculate $\mathcal{I}m\left(F\right)$ is a field-theoretical approach [206].

Here, the approximation of $\mathcal{I}m\left(F\right)$ is a relation of the partition function of the metastable reactant state Q_{RS} and the imaginary part $\mathcal{I}m\ Q_{\mathrm{inst}}$ of the partition function of the quantum transition state, belonging to γ_{inst}, also called the bounce, see Fig. 2.4. The partition function is $Q = Q_{\mathrm{RS}} + i(\mathcal{I}m\ Q_{\mathrm{inst}})$. Then

$$k_{\mathrm{inst}} = \frac{2}{\beta\hbar}\mathcal{I}m(\ln Q) = \frac{2}{\beta\hbar}\arctan\left(\frac{\mathcal{I}m\ Q}{\mathcal{R}e\ Q}\right) \approx \frac{2}{\beta\hbar}\frac{\mathcal{I}m\ Q_{\mathrm{inst}}}{Q_{\mathrm{RS}}}, \tag{3.2}$$

with $\beta = 1/(k_{\mathrm{B}}T)$, k_{B} Boltzmann's constant, and for temperature $T \le T_{\mathrm{c}}$. The crossover temperature T_{c} is defined in (1.4) on page 14. $\mathcal{I}m\ Q$ denotes the imaginary part of Q and $\mathcal{R}e\ Q$ the real part. The second equality holds as $\mathcal{R}e\ Q = Q_{\mathrm{RS}} > 0$ and the rules for complex functions apply. To evaluate the formula, an analytic continuation of a partition function Q from a stable to a metastable situation is required. The third approximation holds as $\mathcal{I}m\ Q_{\mathrm{inst}} \ll Q_{\mathrm{RS}}$.

In Feynman's path integral formalism the partition function is given as an integration over closed paths (of infinite length, $\beta\hbar \to \infty$ for $T \to 0$). Of course, in calculations the paths are always finite. However, the more the temperature T tends to zero, the longer the paths and the more discretization points are necessary for a sufficient sampling.
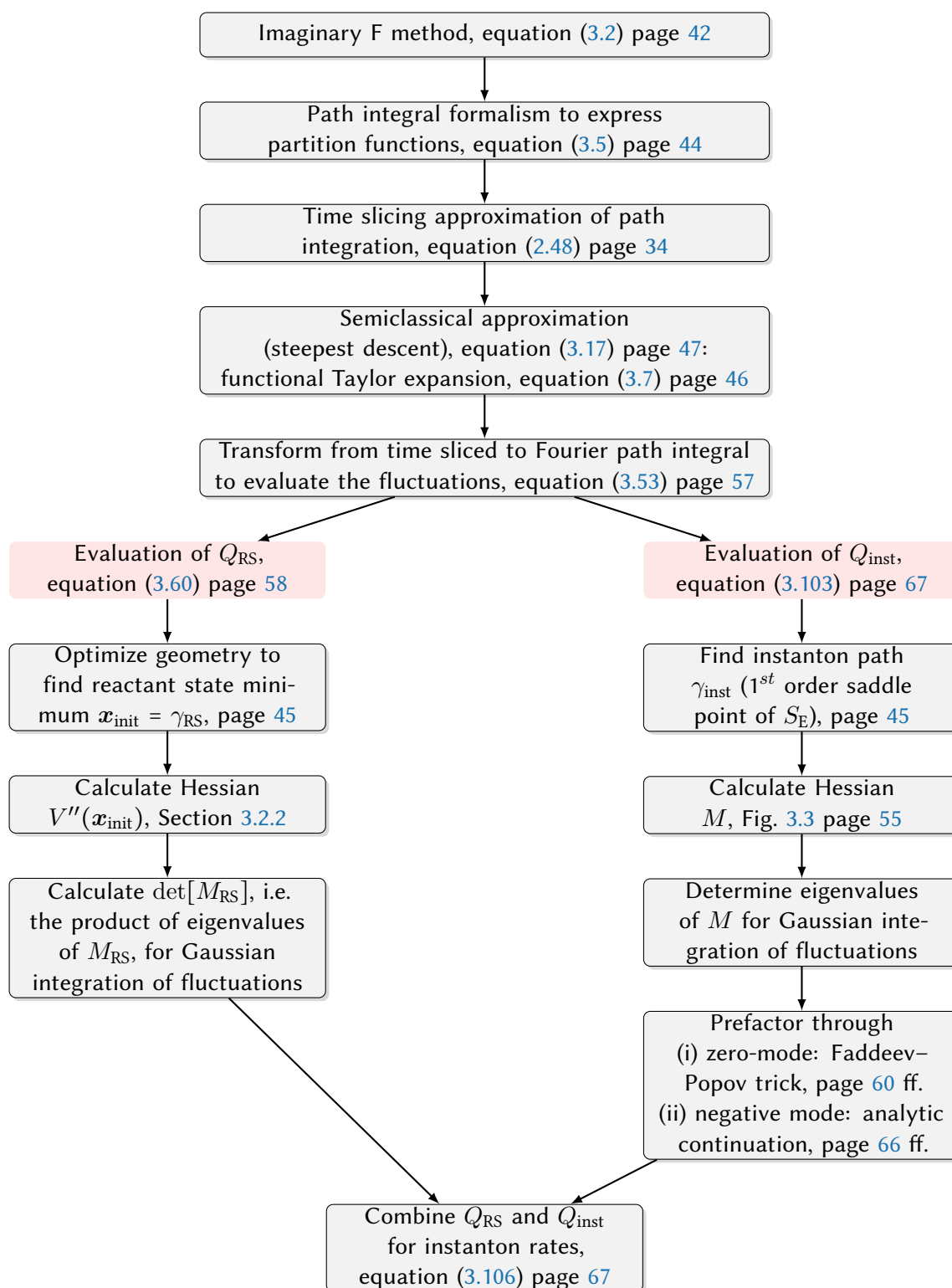
Figure 3.1: Overview of the necessary approximations and single steps to derive and calculate instanton rates.

Here and in the following the definitions and approximations given in Section 2.7 are used. With the kernel of the density operator expressed in Feynman's path integral formalism, see Section 2.5, the partition function reads

$$Q = \text{Tr}\left[\exp\left(-\beta \hat{H}\right)\right] = \tag{3.3}$$

$$= \int_{\mathbb{R}^d} d\boldsymbol{x}_{\text{init}} \langle \boldsymbol{x}_{\text{init}} | \exp\left(-\beta \hat{H}\right) | \boldsymbol{x}_{\text{init}} \rangle = \tag{3.4}$$

$$= \int_{\mathbb{R}^d} d\gamma(0) \int_{\gamma(0)=\gamma(\beta\hbar)} \exp\left(-\frac{1}{\hbar} S_{\text{E}}[\gamma(t)]\right) \mathcal{D}[\gamma(t)]. \tag{3.5}$$

Note, that $\boldsymbol{x}_{\text{init}} = \boldsymbol{x}_{\text{final}}$ as the paths are closed. $\text{Tr}\left[\exp\left(-\beta \hat{H}\right)\right]$ denotes the trace of the density matrix.

The $\mathcal{I}m\, F$ method is applicable when there is thermal equilibrium in the well region. The time scale for relaxation in the well should be short compared to the average time for escape from the well. The advantage of this approach is that no energy and time integrals have to be evaluated. The theory is valid for low temperature as the procedure corresponds to a generalization (extrapolation) of $k(T = 0K) = -\frac{2}{\hbar} \mathcal{I}m\,(E_0)$, which is the ground state decay rate at zero Kelvin where $\beta = \infty$, to finite temperature [98].

To calculate the rate k_{inst} the expression for partition functions given in (3.5) is inserted into (3.2). The next Section deals with a time slicing approximation of the path integrals to derive an explicit formulation of the $\mathcal{I}m\, F$ rate in d-dimensional configuration space and with variable step-size discretization of the path γ. The advantage of the approach used in the following is that the formulation in a variable step-size discretization of the paths is straight forward in each step of the derivation. In contrast to previous derivations, e.g. [182, 198, 206], a more dimensional formulation, i.e. for a path $\gamma \in \mathcal{C}_{[0,\beta\hbar]}(\mathbb{R}^d)$, will be given. This allows the final rate to be easier understood and used for higher dimensional systems. See Fig. 3.1 for an overview of the derivations.

3.1   Semiclassical approximation (steepest descent)

The rate will be evaluated by taking a semiclassical limit, also called steepest descent approximation or stationary path (the instanton) method. Here Feynman's path integral formulation, see (3.5), will be used to express partition functions. When the Euclidean action $S_{\text{E}}[\gamma_\Delta(t)]$ is large compared to the reduced Planck's constant $\hbar$, the path integral in equation (3.5) is dominated by paths which are in the neighborhood of the stationary action paths. The contributions remote from the stationary path cancel out due to oscillations.

Paths extremizing the Euclidean action

The path $\gamma_\Delta(t)$ is a time sliced path defined in Section 2.7. As discussed above, the most important non-vanishing contributions come from the close neighborhood of the stationary action function. The time sliced path γ_Δ satisfying the Euler-Lagrange equation (2.40), which is obtained by the condition that the first variation of the Euclidean action is equal to zero, see Section 2.6, makes the action stationary. Thus, in the following the fluctuations around the path $\gamma_\Delta(t)$ will be of interest. Two possible paths on the potential energy surface that are relevant as $\gamma_\Delta(t)$, see Fig. 2.4 for a schematic overview of the notation.

1. A path that fulfills equation (2.40) is the time-sliced path $\gamma_{RS}(t_j) = \boldsymbol{x}_{RS}$ for all $j = 1, \ldots, J + 1$ collapsed to the geometry of the reactant minimum. From this, the quantum partition function of the reactant state (RS) can be obtained.

2. The non trivial solution of equation (2.40) is the instanton path γ_{inst}. It is the tunneling path with the highest statistical weight at a given temperature.

Here and in the following, the time sliced stationary-action path belonging to the reactant minimum is denoted by $\gamma_{RS}(t)$. It is involved in the calculation of Q_{RS}. The path associated with Q_{inst} is denoted by $\gamma_{inst}(t)$.

The instanton path is obtained by optimizing the action not the energy, thus, it differs from the MEP a classical particle would take to go over the barrier. In contrast to the path corresponding to the reactant minimum, the instanton path $\gamma_{inst}(t)$ is delocalized. In the action sum equation (2.46) the time integration over the interval $[0, \beta\hbar]$ is discretized in $J + 1$ points. Discretizing the integration in the action functional is the same as summing over several images or replicas of the geometry of the particle (or molecule) along the path. That leads to a string of particles (beads) which is the broken time sliced path $(\boldsymbol{x}_1, \ldots, \boldsymbol{x}_{J+1})$ mentioned in Section 2.7. The instanton consisting of this string of beads spreads over the potential energy barrier, as $V(\boldsymbol{x}_j) = V(\gamma_{inst}(t_j))$, $j = 1, \ldots, J + 1$, is part of the integrand of the integral determining S_E. The stronger the tunneling and the lower the temperature, the longer is the path and the stronger will the delocalization during the transition of a particle be.

Fluctuations around the stationary-action paths

In the steepest descent (or stationary phase) method S_E in equation (3.5) is approximated by a second order functional Taylor expansion. The fluctuations, around its stationary path are integrated analytically. The stationary-action path γ_Δ is the most important path of all these tunneling paths. The time-sliced path γ_Δ represents in the following

either γ_{inst} or γ_{RS}, as defined above. The results described for γ_Δ hold for both of these paths.

The fluctuations around the path γ_Δ

$$\gamma_\Delta^{a_1^1,\ldots,a_d^{J+1}} \in \boldsymbol{T}_{\gamma_\Delta} \mathcal{C}_{[0,\beta\hbar]}(\mathbb{R}^d)$$

are part of the tangent space to $\gamma_\Delta \in \mathcal{C}_{[0,\beta\hbar]}(\mathbb{R}^d) \subset \mathcal{M}$, see equation (2.17). Due to the method of geodesic deviation all the full fluctuating paths can be expressed in Fermi local coordinates, see Section 2.8, as the sum of the stationary-action path $\gamma_\Delta(t)$ plus fluctuations $y_\Delta(t)$. The fluctuations satisfy Dirichlet boundary conditions, i.e., $y_\Delta(0) = y_\Delta(\beta\hbar) = 0$. Therefore, the full fluctuating paths

$$\gamma_\Delta^{a_1^1,\ldots,a_d^{J+1}}(t) = \gamma_\Delta(t) + y_\Delta(t) \tag{3.6}$$

will start at $\gamma_\Delta(0)$ and end at $\gamma_\Delta(\beta\hbar)$ for all $y_\Delta(t) \in \boldsymbol{T}_{\gamma_\Delta}\mathcal{M}$, see equation (2.52).

The integration over all paths is in the semiclassical stationary phase method approximated by a second order functional Taylor expansion of S_{E} around the path γ_Δ:

$$S_{\text{E}}\left[\gamma_\Delta + y_\Delta\right] = S_{\text{E}}\left[\gamma_\Delta\right] + \int_0^{\beta\hbar} \frac{\delta S_{\text{E}}}{\delta\gamma_\Delta(t)} y_\Delta(t)dt$$
$$+ \frac{1}{2}\int_0^{\beta\hbar}\int_0^{\beta\hbar} \frac{\delta^2 S_{\text{E}}}{\delta\gamma_\Delta(t)\delta\gamma_\Delta(t')} y_\Delta(t)y_\Delta(t')dtdt' + \mathcal{O}((y_\Delta(t))^3). \tag{3.7}$$

Note that $\frac{\delta}{\delta\gamma_\Delta(t)}$ is meant in a distributional sense (a functional derivative), see Section 2.6. To evaluate the terms included in the functional Taylor expansion the first and second variation of the Euclidean action functional have to be determined, see Section 2.6. The first term on the right hand side is a constant in $\mathbb{R}$ and can be taken out of the integration in (2.48). The second term vanishes as the path γ_Δ fulfills the Euler Lagrange equation, see (2.40).

The functional Taylor expansion is inserted in the time slicing approximation of the partition function, see (2.48), (2.22), and equation (3.5):

$$\int_\Omega \exp\left(-\frac{1}{\hbar} S_{\text{E}}[\gamma(t)]\right)\mathcal{D}[\gamma(t)] \approx \tag{3.8}$$

$$\approx \left(\prod_{j=1}^{J+1}\left(\frac{1}{2\pi\hbar h_j}\right)^{d/2}\right)\int_{\mathbb{R}^{dJ}} \exp\left(-\frac{1}{\hbar}S_{\text{E}}\left[\gamma_\Delta(t) + y_\Delta\right]\right)\prod_{j=1}^{J} d\boldsymbol{x}_j. \tag{3.9}$$

Now let us have a closer look at the third term in equation (3.7) including the second variation of the Euclidean action functional. That term corresponds to a quadratic term in the exponent of an exponential function which becomes a Gaussian integral, see

Appendix B.1 and therein (B.5). The reason for that will become clear in the following. For the third term holds, by evaluating one integration with integration by parts to get rid of the Delta function, see Section 2.6 for more details,

$$\frac{1}{2} \int_0^{\beta\hbar} \int_0^{\beta\hbar} \frac{\delta^2 S_{\mathrm{E}}}{\delta\gamma_\Delta(t)\delta\gamma_\Delta(t')} y_\Delta(t)y_\Delta(t')dtdt' \tag{3.10}$$

$$= \frac{1}{2} \int_0^{\beta\hbar} y_\Delta(t) \cdot \left(-\frac{1}{2}\frac{d^2}{dt^2} + \frac{d^2V(\gamma_\Delta(t))}{d^2\gamma_\Delta(t)} \right) y_\Delta(t)dt \tag{3.11}$$

$$= \frac{1}{2} \int_0^{\beta\hbar} y_\Delta(t) \cdot \mathcal{J} y_\Delta(t)dt \tag{3.12}$$

$$= \frac{1}{2} \left(\int_0^{\beta\hbar} \frac{1}{2}\frac{dy_\Delta(t)}{dt} \cdot \frac{dy_\Delta(t)}{dt} dt + \int_0^{\beta\hbar} y_\Delta(t) \cdot \frac{d^2V(\gamma_\Delta(t))}{d\gamma_\Delta^2(t)} y_\Delta(t)dt \right). \tag{3.13}$$

The operator

$$\mathcal{J} = \left(-\frac{1}{2}\frac{d^2}{dt^2} + \frac{d^2V(\gamma_\Delta(t))}{d\gamma_\Delta^2(t)} \right) \tag{3.14}$$

denotes the Jacobi operator. Expression (3.13) follows by another integration by parts.

The contributions of expression 3.13 can also be considered as spring forces acting on the connection between the different x_j, $j = 1, \ldots, J + 1$ belonging to the path γ_Δ, see Fig. 3.2.

Steepest descent evaluation

The imaginary time interval $[0, \beta\hbar]$ of the integration is discretized as in (2.37), Section 2.7. The $J + 1$ discrete points on the closed time sliced path $\gamma_\Delta(t)$ are denoted by $\{\gamma_\Delta(t_j)\}_{j=1}^{J+1} = \{x_j\}_{j=1}^{J+1} \in \mathbb{R}^d$. The integration over time in (3.12) reduces to a summation due to the discretization of the path.

$$\frac{1}{2} \int_0^{\beta\hbar} y_\Delta(t)\mathcal{J}y_\Delta(t)dt \approx \frac{1}{2}\sum_{j=1}^{J+1} y_\Delta(t_j)\mathcal{J}y_\Delta(t_j)h_j. \tag{3.15}$$

The integrations from minus to plus infinity in (3.9) are then easy to perform. The quadratic form in (3.15) leads in (3.9) to $d(J + 1)$ Gaussian integral evaluations, see Appendix B.1, where each step-size h_j contributes d-times to the product over all eigenvalues of the operator $\mathcal{J}$. The resulting approximation formula based on (3.9) for the partition function reads

$$Q = \int_{\mathbb{R}^d} dx_{\mathrm{init}}\langle x_{\mathrm{init}}|\exp\left(-\beta H\right)|x_{\mathrm{init}}\rangle = \tag{3.16}$$

$$= \left(\prod_{j=1}^{J+1} \left(\frac{1}{2\pi\hbar h_j} \right)^{d/2} \right) \exp\left(-\frac{1}{\hbar}S_{\mathrm{E}}[\gamma_\Delta(t)] \right) \sqrt{\frac{1}{\left(\prod_{j=1}^{J+1}(h_j)^d\right)\det[\mathcal{J}]}} \left(1 + r(\Delta, \hbar, 0, \beta\hbar)\right). \tag{3.17}$$

black: $\gamma_{\text{inst}}(t_j) = \boldsymbol{x}_j,\ j = 1, \ldots, 6$

blue: $\gamma_{\text{inst}}(t_j) + y_\Delta(t_j)$
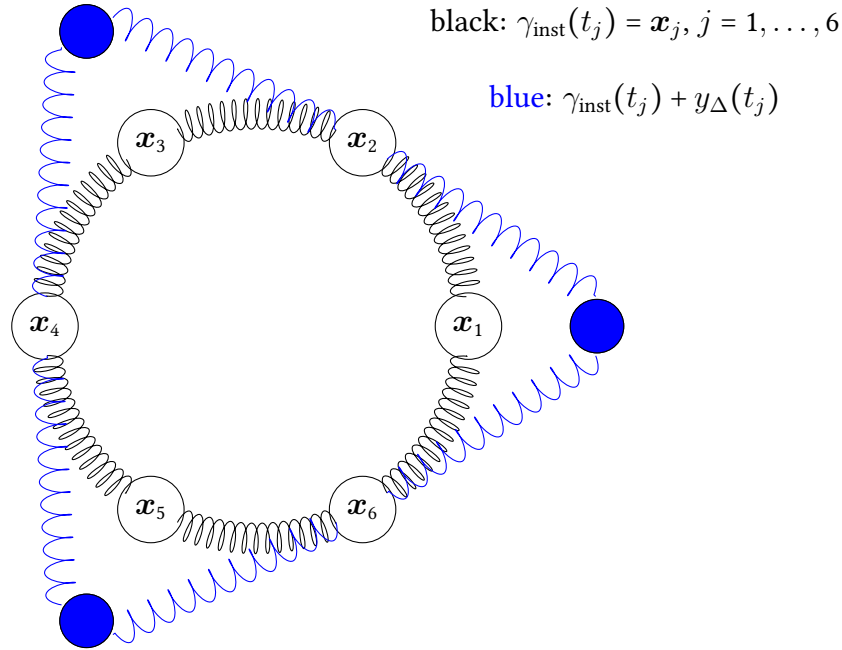
Figure 3.2: The instanton path γ_{inst} and the fluctuations around them connected by springs. The spring constants are temperature dependent.

Formula (3.17) is called the semiclassical or steepest descent approximation of the Feynman path integrals. Δ refers to the divison of the interval $[0, \beta\hbar]$ defined in equation (2.37). More details can be found in, e.g. [182, 185, 235], and references therein. The semiclassical approximation allows to evaluate the partition function in equation (3.5). A more detailed evaluation of this procedure will be given in the next Sections of this Chapter. With the time sliced formulation used above an estimate for the remainder $r(\Delta, \hbar, 0, \beta\hbar)$ of order $\mathcal{O}(\hbar)$ was found, see for example [176–178].

Notes on the determinant of the Jacobi operator

The determinant of the Jacobi operator $\mathcal{J}$ is in discrete form given as:

$$\det[\mathcal{J}] = \det\left[-\frac{1}{2}\frac{d^2}{dt^2} + \frac{d^2 V(\gamma_\Delta(t))}{d^2 \gamma_\Delta(t)}\right] \approx \det[J_\gamma] = \left[\det\frac{\delta^2 S_{\text{E}}(\gamma_\Delta(t))}{\delta\boldsymbol{x}_i \delta\boldsymbol{x}_k}\right]^{-1}, \qquad (3.18)$$

where $\det[J_\gamma] = \det J_{ik}$, i.e., the Jacobi field along the trajectory $\gamma(t) \subset M$ where $J_{ik} = \frac{\delta\gamma_i(t)}{\delta p_k(t)}$ with $i, k = 1, \ldots, d$ and $p_k(t) = m\dot{\gamma}(0)$ different initial momenta of trajectories starting at $\boldsymbol{x}_0 = \gamma(0)$ into different directions, which has been proven several times [174, 182, 236, 237]. Moreover the Jacobi field is related to the second variation of the

Euclidean action functional by $(J_{ik})^{-1} = \frac{\delta^2 S_\mathrm{E}(\gamma_\Delta(t))}{\delta \boldsymbol{x}_i \delta \boldsymbol{x}_k}$. The determinant $\det \left[\frac{\delta^2 S_\mathrm{E}(\gamma_\Delta(t))}{\delta \boldsymbol{x}_i \delta \boldsymbol{x}_k} \right]$ is referred to as the Morette–Van Hove determinant [174, 182, 236–239]. The JWKB approximation [118–121] contains the same determinant as well. So up to now a JWKB-like approach was derived.

The Jacobi field J_{ik} describes the deviation of the stationary phase trajectory γ by a variation through all possible stationary paths. In these paths several conjugate points, i.e., points where two or more paths cross each other at focal points, are possible [174, 182, 240]. The determinant $\det[J_\gamma]$ is also equivalent to the Fredholm determinant $\det_\mathrm{F} \mathcal{J}\mathcal{G}$, where $\mathcal{J} = -\frac{1}{2}\frac{d^2}{ds^2} + \frac{d^2 V(\gamma(s))}{d^2\gamma(s)}$ is the Jacobi operator and $\mathcal{G}$ Feynman's Green function [239]. Sometimes the determinant is also referred to as a regularized zeta-function determinant [166].

In the following Section the results given above are applied to evaluate the partition function at the metastable reactant state Q_RS and the partition function of the quantum transition state Q_inst.

3.2 Evaluation of partition functions

The partition functions Q_RS and Q_inst, we are interested in, see (3.5), are based on loops of closed trajectories γ_Δ. That implies the starting point $\boldsymbol{x}_0$ of a trajectory to be the same as its end point $\boldsymbol{x}_{J+1}$. The trajectories are passed once. To evaluate the partition functions (i) a stationary path has to be located and then (ii) the fluctuations around it are determined. The fluctuations are taken into account by determining the determinant of the operator in (3.17). In the next Sections the first example discussed is always the one dimensional case with $d = 1$. Then follows the higher dimensional case. The final rates will be given in Section 3.3.

The main difference between $\gamma_\mathrm{RS}(t)$ and $\gamma_\mathrm{inst}(t)$, defined on page 45, is their behavior under the displacement along the path. The partition function Q_RS belongs to the metastable system at the reactant minimum. Its path is collapsed to one point, i.e. the displacement along the path $\frac{d\gamma_\mathrm{RS}(t)}{dt} \equiv 0$, see Fig. 2.4.

For the displacement along the instanton path $\frac{d\gamma_\mathrm{inst}(t)}{dt}$ holds, when applying the Jacobi operator

$$\mathcal{J}u(t) = \mathcal{J}\frac{d\gamma_\Delta(t)}{dt} = \left(-\frac{1}{2}\frac{d^2}{dt^2} + V''(\gamma_\Delta(t)) \right)\frac{d\gamma_\Delta(t)}{dt} \tag{3.19}$$

$$= -\frac{d}{dt}\left(\frac{1}{2}\frac{d\gamma_\Delta^2(t)}{dt^2} + V'(\gamma_\Delta(t)) \right) = 0. \tag{3.20}$$

This follows due to the chain rule

$$-\frac{d}{dt}\frac{d}{\gamma_\Delta(t)}V(\gamma_\Delta(t)) = \frac{d}{\gamma_\Delta(t)}\frac{d}{dt}V(\gamma_\Delta(t)) = \frac{d}{\gamma_\Delta(t)}\frac{d}{\gamma_\Delta(t)}V(\gamma_\Delta(t))\frac{d}{dt}\gamma_\Delta(t). \quad (3.21)$$

In (3.19) the trivial solution of the zero-mode $\mathbf{u}(t) := \tilde{\mathbf{u}}_0(t) = \frac{d\gamma_{\mathrm{RS}}(t)}{dt} \equiv 0$ is one of two possible solutions and belongs to Q_{RS}. The second non-trivial solution belongs to displacement along the instanton path γ_{inst}. The zero-mode $\mathbf{u}(t) := \mathbf{u}_0(t) = \frac{d\gamma_{\mathrm{inst}}(t)}{dt} \neq 0$, will be discussed in the Subsection 3.2.1, when evaluating Q_{inst}. The zero-mode makes the matrix representing the Jacobi operator $\mathcal{J}$ at the instanton geometry singular.

3.2.1   Evaluation of Q_{inst}

The closed path $\gamma_{\mathrm{inst}}(t)$ belonging to Q_{inst} has a conjugate point which leads to a determinant of a singular matrix with zero and negative eigenvalues [241, 242]. The discrete Hessian representing equation (3.13), the integration over the second variation of the Euclidean action, exhibits exactly one negative eigenvalue. The eigenvector $\mathbf{u}_{\mathrm{inst}}(t) \in \{\mathbf{u}_k(t)\}_{k=1}^{d(J+1)}$ denotes the unstable mode belonging to the negative eigenvalue which corresponds to a movement of the whole path toward the reactant or the product. The zero-mode corresponds to the arbitrary starting position of the path, i.e., to a reparametrization $t \to t + t_0$ of the path.

The one dimensional case

We consider now a one-dimensional example, where $\gamma_{\mathrm{inst}}(t) : [0, \beta\hbar] \to \mathbb{R}$, i.e., $d = 1$. First of all the stationary path is located by optimizing a discretized version of the first variation of the Euclidean action, see (2.30). The stationary path fulfills equation (2.40). The optimization determines a term equal to zero with $J + 1$ entries each corresponding to one discretization point along the path $\gamma_{\mathrm{inst}}(t)$:

$$0 = \begin{pmatrix} \frac{1}{2}\frac{d^2\gamma_{\mathrm{inst}}(t_1)}{dt_1^2} + V'(\gamma_{\mathrm{inst}}(t_1)) \\ \vdots \\ \frac{1}{2}\frac{d^2\gamma_{\mathrm{inst}}(t_j)}{dt_j^2} + V'(\gamma_{\mathrm{inst}}(t_j)) \\ \vdots \\ \frac{1}{2}\frac{d^2\gamma_{\mathrm{inst}}(t_{J+1})}{dt_{J+1}^2} + V'(\gamma_{\mathrm{inst}}(t_{J+1})) \end{pmatrix}. \quad (3.22)$$

Consider the second order forward finite difference approximation of the j-th component:

$$0 = \frac{1}{2}\frac{d^2\gamma_{\text{inst}}(t_j)}{dt_j^2} + V'(\gamma_{\text{inst}}(t_j)) \tag{3.23}$$

$$\approx \frac{1}{2}\frac{1}{(h_j + h_{j-1})}\left(\frac{\gamma_{\text{inst}}(t_{j+1}) - \gamma_{\text{inst}}(t_j)}{h_j} - \frac{\gamma_{\text{inst}}(t_j) - \gamma_{\text{inst}}(t_{j-1})}{h_{j-1}}\right) + V'(\gamma_{\text{inst}}(t_j)) \tag{3.24}$$

$$= \frac{1}{2}\left(\frac{\gamma_{\text{inst}}(t_{j+1})}{h_j(h_j + h_{j-1})} - \frac{\gamma_{\text{inst}}(t_j)(h_j + h_{j-1})}{h_j h_{j-1}(h_j + h_{j-1})} + \frac{\gamma_{\text{inst}}(t_{j-1})}{h_{j-1}(h_j + h_{j-1})}\right) + V'(\gamma_{\text{inst}}(t_j)). \tag{3.25}$$

The full vector reads in matrix notation

$$0 = \frac{1}{2}\begin{pmatrix} \frac{1}{h_1 h_{J+1}} & -\frac{1}{h_1(h_1+h_{J+1})} & & & -\frac{1}{h_{J+1}(h_1+h_{J+1})} \\ -\frac{1}{h_1(h_2+h_1)} & & & & \\ & & & & \\ & & & & -\frac{1}{h_J(h_J+h_{J-1})} \\ -\frac{1}{h_{J+1}(h_{J+1}+h_J)} & & -\frac{1}{h_J(h_{J+1}+h_J)} & \frac{1}{h_{J+1}h_J} \end{pmatrix}\begin{pmatrix} \gamma_{\text{inst}}(t_1) \\ \vdots \\ \gamma_{\text{inst}}(t_j) \\ \vdots \\ \gamma_{\text{inst}}(t_{J+1}) \end{pmatrix} + \begin{pmatrix} V'(\gamma_{\text{inst}}(t_1)) \\ \vdots \\ V'(\gamma_{\text{inst}}(t_j)) \\ \vdots \\ V'(\gamma_{\text{inst}}(t_{J+1})) \end{pmatrix}. \tag{3.26}$$

The matrix on the right hand side is a band matrix. It contains non-zero entries on the diagonal, the two subdiagonals, here and in the following denoted by a line, and in the outermost subdiagonals. The other entries are equal to zero. The path fulfilling the condition (3.26) is the stationary-action path (MAP), the most probable tunneling path. One possible way to find the path is to optimize the Euclidean action. A detailed discussion and comparison of different optimizers will be given in Chapter 4.

After locating the path its discretized Euclidean action sum, see (2.21) and equation (2.46), has to be evaluated. The discrete action sum reads

$$S_{\text{E}}[\gamma_{\text{inst}}(t)] = \int_0^{\beta\hbar} \frac{1}{2}\left(\frac{d\gamma_{\text{inst}}}{dt}\right)^2 + V(\gamma_{\text{inst}}(t))dt \approx \tag{3.27}$$

$$\approx \sum_{j=1}^{J+1} h_j \frac{1}{2}\left(\frac{\gamma_{\text{inst}}(t_{j+1}) - \gamma_{\text{inst}}(t_j)}{h_j}\right)^2 + h_j V(\gamma_{\text{inst}}(t_j)) = \tag{3.28}$$

$$= \sum_{j=1}^{J+1} \frac{1}{2}\frac{\gamma_{\text{inst}}^2(t_{j+1}) - 2\gamma_{\text{inst}}(t_{j+1})\gamma_{\text{inst}}(t_j) + \gamma_{\text{inst}}^2(t_j)}{h_j} + h_j V(\gamma_{\text{inst}}(t_j)) = \tag{3.29}$$

and in matrix formulation

$$
= \frac{1}{2} \begin{pmatrix} \gamma_{\mathrm{inst}}(t_1) \\ \vdots \\ \gamma_{\mathrm{inst}}(t_j) \\ \vdots \\ \gamma_{\mathrm{inst}}(t_{J+1}) \end{pmatrix}^T \begin{pmatrix} \frac{1}{h_1}+\frac{1}{h_2} & -\frac{1}{h_1} & & & -\frac{1}{h_{J+1}} \\ -\frac{1}{h_1} & \ddots & & & \\ & & \ddots & & \\ & & & \ddots & -\frac{1}{h_J} \\ -\frac{1}{h_{J+1}} & & & -\frac{1}{h_J} & \frac{1}{h_{J+1}}+\frac{1}{h_1} \end{pmatrix} \begin{pmatrix} \gamma_{\mathrm{inst}}(t_1) \\ \vdots \\ \gamma_{\mathrm{inst}}(t_j) \\ \vdots \\ \gamma_{\mathrm{inst}}(t_{J+1}) \end{pmatrix} +
$$

$$
\begin{pmatrix} V(\gamma_{\mathrm{inst}}(t_1)) \\ \vdots \\ V(\gamma_{\mathrm{inst}}(t_j)) \\ \vdots \\ V(\gamma_{\mathrm{inst}}(t_{J+1})) \end{pmatrix}^T \begin{pmatrix} h_1 \\ \vdots \\ h_j \\ \vdots \\ h_{J+1} \end{pmatrix}. \tag{3.30}
$$

The matrix in the first term is again a band matrix with entries on the diagonal, the two subdiagonal and in the outermost subdiagonals. To calculate rates the fluctuations around that path up to second order are considered, as in the discrete equation (3.15), by a functional Taylor expansion. When applying the operator $\mathcal{J}$ to the discrete time sliced path, (3.13) changes to

$$
\frac{1}{2}\int_0^{\beta\hbar}\int_0^{\beta\hbar} \frac{\delta^2 S_E}{\delta\gamma_{\mathrm{inst}}(t)\delta\gamma_{\mathrm{inst}}(t')} y_\Delta(t)y_\Delta(t')dtdt' \approx \tag{3.31}
$$

$$
\frac{1}{2}\left[\sum_{j=1}^{J+1}\frac{1}{2}\left(\frac{y_\Delta(t_{j+1})-y_\Delta(t_j)}{h_j}\right)^2 h_j + \sum_{j=1}^{J+1} y_\Delta(t_j)V''\left(\gamma_{\mathrm{inst}}(t_j)\right)y_\Delta(t_j)h_j\right] = \tag{3.32}
$$

$$
= \frac{1}{2}\left[\sum_{j=1}^{J+1}\frac{1}{2}\frac{y_\Delta^2(t_{j+1})-2y_\Delta(t_{j+1})y_\Delta(t_j)+y_\Delta^2(t_j)}{h_j} + \sum_{j=1}^{J+1} y_\Delta(t_j)V''\left(\gamma_{\mathrm{inst}}(t_j)\right)y_\Delta(t_j)h_j\right] = \tag{3.33}
$$

$$
= \frac{1}{2}\begin{pmatrix} y_\Delta(t_1) \\ \vdots \\ y_\Delta(t_j) \\ \vdots \\ y_\Delta(t_{J+1}) \end{pmatrix}^T \left[\frac{1}{2}\begin{pmatrix} \frac{1}{h_1}+\frac{1}{h_2} & -\frac{1}{h_1} & & & -\frac{1}{h_{J+1}} \\ -\frac{1}{h_1} & \ddots & & & \\ & & \ddots & & \\ & & & \ddots & -\frac{1}{h_J} \\ -\frac{1}{h_{J+1}} & & & -\frac{1}{h_J} & \frac{1}{h_{J+1}}+\frac{1}{h_1} \end{pmatrix}\right.
$$

$$
\left.+ \begin{pmatrix} V''(\gamma_{\mathrm{inst}}(t_1))h_1 & & & \\ & \ddots & & \\ & & \ddots & \\ & & & V''(\gamma_{\mathrm{inst}}(t_{J+1}))h_{J+1} \end{pmatrix}\right]\begin{pmatrix} y_\Delta(t_1) \\ \vdots \\ y_\Delta(t_j) \\ \vdots \\ y_\Delta(t_{J+1}) \end{pmatrix} = \frac{1}{2}\mathbf{y}^T M\mathbf{y}. \tag{3.34}
$$

The y_Δ are the fluctuations around the path $\gamma_{\text{inst}}(t)$ as defined in Section 2.8, see also Fig. 3.2. Thus, to calculate rates first the instanton path has to be optimized and then the second derivative of the potential energies along the path has to be calculated. More details on the evaluation of the Gaussian integrals will be given after the next paragraph concerning the higher dimensional case.

The higher dimensional case

In the higher dimensional case the stationary-action path is given as $\gamma_{\text{inst}}(t) : [0, \beta\hbar] \to \mathbb{R}^d$. The dimension d can be considered as the number of degrees of freedom, i.e., the number of atoms in a system times three as they can move in three directions. For the evaluation of the Euclidean action and its first variation, the matrices in (3.30) and (3.26) will turn into block matrices, when they are treated in the same way as the second variation in the following. The Fermi local coordinates with respect to the classical path $\gamma_{\text{inst}}(t)$ described in Section 2.8 have a local d-dimensional coordinate system at each discrete time point $t_j \in [0, \beta\hbar]$. Inserting the expansion of $y_\Delta(t_j) = \sum_{k=0}^{d-1} a_k^j e_k^j$, which is a representation of the fluctuations in Fermi local coordinates into (3.32) yields

$$\frac{1}{2} \left[\sum_{j=1}^{J+1} \frac{1}{2} \left(\sum_{k=0}^{d-1} a_k^{j+1} e_k^{j+1} - \sum_{k=0}^{d-1} a_k^j e_k^j \right)^2 \frac{1}{h_j} + \right. \tag{3.35}$$

$$\left. \sum_{j=1}^{J+1} \sum_{k=0}^{d-1} a_k^j e_k^j V'' \left(\gamma_{\text{inst}}(t_j) \right) \sum_{l=0}^{d-1} a_l^j e_l h_j \right]. \tag{3.36}$$

Consider the part in the parenthesis taken to the power of two:

$$\left(\sum_{k=0}^{d-1} a_k^{j+1} e_k - \sum_{k=0}^{d-1} a_k^j e_k \right)^2 = \tag{3.37}$$

$$\left(\sum_{k=0}^{d-1} a_k^{j+1} e_k^{j+1} \right)^2 - 2 \sum_{k=0}^{d-1} a_k^{j+1} e_k^{j+1} \sum_{k=0}^{d-1} a_k^j e_k^j + \left(\sum_{k=0}^{d-1} a_k^j e_k^j \right)^2. \tag{3.38}$$

Rewrite the coefficients in vector notation $(\boldsymbol{a}^j)^T = (a_0^j, a_1^j, \ldots, a_{d-1}^j)$ and the d-dimensional orthonormal frame vectors $\boldsymbol{e}_k$ in the rows of a matrix

$$E^j = E^{j+1} = (\boldsymbol{e}_0, \boldsymbol{e}_1, \ldots, \boldsymbol{e}_{d-1})^T \in \mathbb{R}^{d \times d},$$

see page 35. Then the fluctuation reads $y_\Delta(t_j) = E^j \boldsymbol{a}^j$. Then (3.38) reads

$$\left(E^{j+1} \boldsymbol{a}^{j+1} \right)^2 - 2 \left(E^{j+1} \boldsymbol{a}^{j+1} \right)^T E^j \boldsymbol{a}^j + \left(E^j \boldsymbol{a}^j \right)^2 \tag{3.39}$$

$$= (\boldsymbol{a}^{j+1})^T \left(E^{j+1} \right)^T E^{j+1} \boldsymbol{a}^{j+1} - (\boldsymbol{a}^{j+1})^T \left(E^{j+1} \right)^T E^j \boldsymbol{a}^j + (\boldsymbol{a}^j)^T \left(E^j \right)^T E^j \boldsymbol{a}^j. \tag{3.40}$$

The matrices $(E^j)^T E^j$ and $(E^{j+1})^T E^j$ are identity matrices by definition, see page 35. When applying the same step as in (3.34) the result is a block diagonal sparse matrix $M = H + V \in \mathbb{R}^{d(J+1) \times d(J+1)}$. Therefore (3.36) turns into

$$\frac{1}{2} \int_0^{\beta\hbar} \int_0^{\beta\hbar} \frac{\delta^2 S_\mathrm{E}}{\delta\gamma_\mathrm{inst}(t)\delta\gamma_\mathrm{inst}(t')} y_\Delta(t) y_\Delta(t') dt dt' \approx \tag{3.41}$$

$$\approx \frac{1}{2} \begin{pmatrix} \boldsymbol{a}^1 \\ \vdots \\ \boldsymbol{a}^j \\ \vdots \\ \boldsymbol{a}^{J+1} \end{pmatrix}^T \left[\frac{1}{2} \begin{pmatrix} \frac{1}{h_1}+\frac{1}{h_2} & -\frac{1}{h_1} & & & -\frac{1}{h_{J+1}} \\ -\frac{1}{h_1} & & & & \\ & & \ddots & & \\ & & & -\frac{1}{h_J} & \\ -\frac{1}{h_{J+1}} & & & -\frac{1}{h_J} & \frac{1}{h_{J+1}}+\frac{1}{h_1} \end{pmatrix} + \tag{3.42} \right.$$

$$\left. \begin{pmatrix} V''(\gamma_\mathrm{inst}(t_1))h_1 & & \\ & \ddots & \\ & & V''(\gamma_\mathrm{inst}(t_{J+1}))h_{J+1} \end{pmatrix} \right] \begin{pmatrix} \boldsymbol{a}^1 \\ \vdots \\ \boldsymbol{a}^j \\ \vdots \\ \boldsymbol{a}^{J+1} \end{pmatrix} = \frac{1}{2}\mathbf{a}^T M \mathbf{a}, \tag{3.43}$$

where $V''(\boldsymbol{\gamma}_\mathrm{inst}(t_j)) \in \mathbb{R}^{d\times d}$, $\mathbf{a}^T = (\boldsymbol{a}^1, \dots, \boldsymbol{a}^{J+1})$, and each entry of M has become a block diagonal matrix. The matrix $M = H + V$ has the form depicted in Fig. 3.3. It is important to note that the step-size factor h_j which is obtained in equation (3.15) by discretizing the integral is absorbed in the matrices H and V. Thus, the factor $\sqrt{\frac{1}{(h_j)^d \det[\mathcal{J}]}}$ in equation (3.17) becomes $\sqrt{\frac{1}{\det[M]}}$.

To evaluate Q_inst first the optimization of an instanton path $\gamma_\mathrm{inst} \in \mathcal{C}_{[0,\beta\hbar]}(\mathbb{R}^d)$ is required which corresponds to the search of a first order saddle "point" of the Euclidean action. The geometry of the instanton path is then used to setup a matrix in the form of $M \in \mathbb{R}^{d(J+1)\times d(J+1)}$. That matrix can also be considered as a discretized form of the Jacobi operator $\mathcal{J}$. To be able to evaluate the Gaussian integrals in equation (3.9) obtained by the Taylor expansion equation (3.7) analytically, the matrix M is diagonalized:

$$\mathbf{a}^T M \mathbf{a} = \mathbf{a}^T \tilde{U}^T D \tilde{U} \mathbf{a} = \mathbf{b}^T D \mathbf{b}, \tag{3.44}$$

where $\tilde{U}$ is an unitary matrix, $\mathbf{b} := \tilde{U}\mathbf{a}$, and D a diagonal matrix with eigenvalues in the spectrum of M $\sigma(M) := \{\lambda_1^\mathrm{inst}, \dots, \lambda_{d(J+1)}^\mathrm{inst}\}$ on the diagonal.

By diagonalizing the matrix M the local coordinate representation of the fluctuating path changes. The coefficients a_k change to coefficients b_k by

$$\mathbf{b} = \tilde{U}\mathbf{a} \Leftrightarrow \tilde{U}^T \mathbf{b} = \mathbf{a}, \tag{3.45}$$
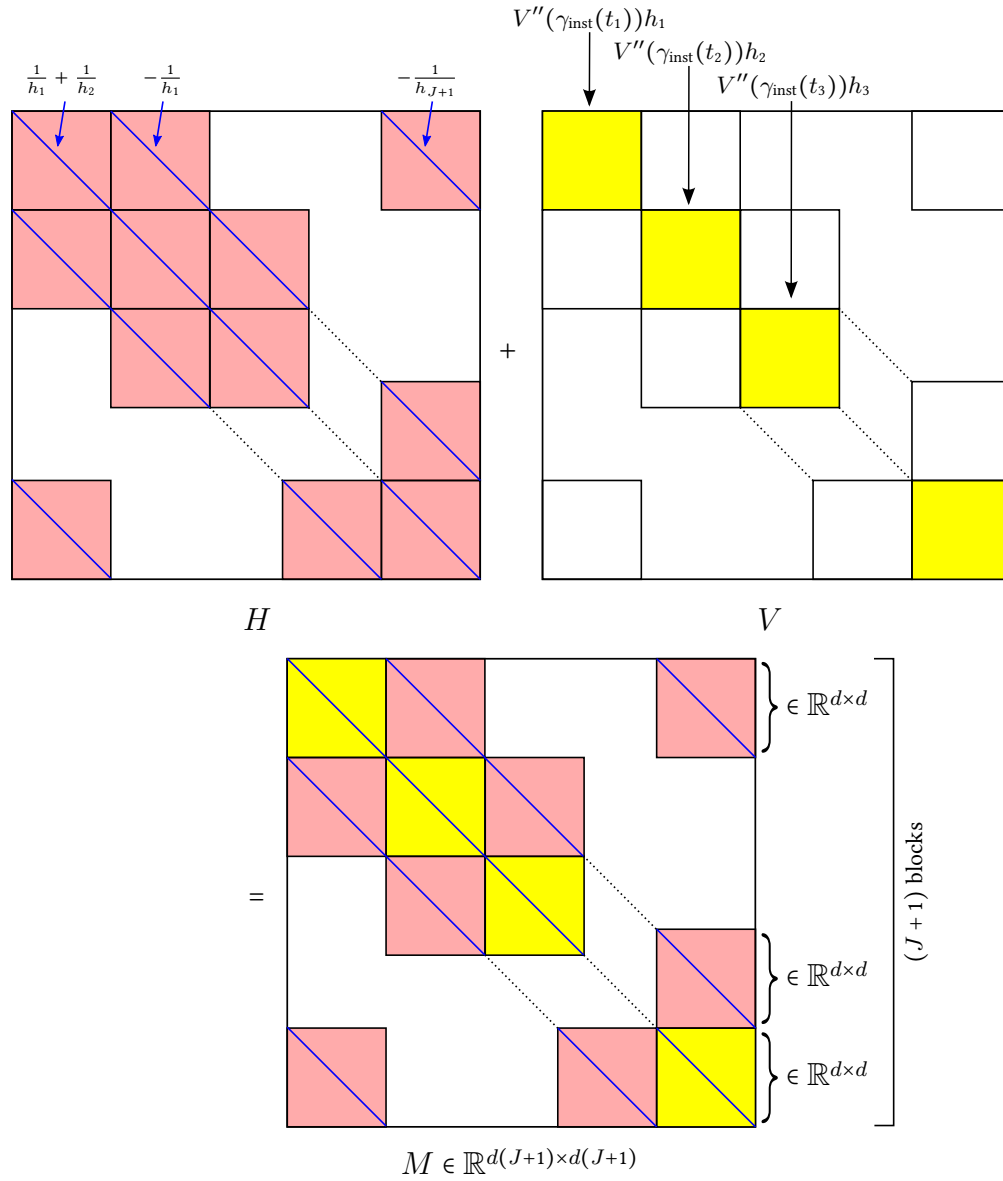
Figure 3.3: The matrices H, V and $M = H + V$ representing the fluctuations up to second order around the instanton path $\gamma_{\text{inst}}(t)$. The eigenvalues of the matrix M are denoted by λ_i^{inst}, $i = 1, \ldots, d(J+1)$. Only the colored blocks contain non-zero entries and the entries of the blocks in H are limited to the diagonal elements (blue lines).

where $\tilde{U}$ is an unitary matrix with eigenvectors of the matrix M in its columns and therefore (2.54) becomes

$$\mathbf{y} = E\tilde{U}^T\mathbf{b} =: U\mathbf{b}. \tag{3.46}$$

The matrix E contains on its diagonal block matrices E^j, which contain the orthonormal frame vectors defined on page 53. The columns $\mathbf{u}_k$ of the matrix U belong to the $d(J+1)$ discrete eigenmodes of the operator $\mathcal{J}$. They constitute a complete orthonormal system spanning the tangent space to γ_Δ. The non-discrete continuous eigenmodes will in the following be denoted as $\mathbf{u}_k(t)$, with $k = 1, \ldots, d(J+1)$. The coefficients b_k determine the amount of contribution of eigenmodes to each fluctuation y_Δ. The entries of U are obtained by solving the equation

$$(M - \lambda_k I)\mathbf{u}_k = 0 \tag{3.47}$$

for each eigenvalue λ_k, $k = 1, \ldots, d(J+1)$ of M with I the unity matrix.

For equation (3.19) is the non-trivial solution after the diagonalization of M given as $\mathbf{u}_0$, the discrete version of $\mathbf{u}_0(t)$. The zero-mode $\mathbf{u}_0$ is the eigenvector belonging to the eigenvalue $\lambda_0 = 0$ in the eigenvalue spectrum of M, $\lambda_0 \in \sigma(M)$:

$$M\mathbf{u}_0 = \lambda_0\mathbf{u}_0 = 0\mathbf{u}_0. \tag{3.48}$$

Changing from time sliced to Fourier path integration

A normal mode expansion of the fluctuations into a complete orthonormal system $y_\Delta(t) = \sum_{k=1}^{d(J+1)} b_k\mathbf{u}_k(t)$ leads to:

$$\frac{1}{2}\int_0^{\beta\hbar}\sum_{k=1}^{d(J+1)} b_k\mathbf{u}_k(t)\left(-\frac{1}{2}\frac{d^2}{dt^2} + V''(\gamma(t))\right)\sum_{l=1}^{d(J+1)} b_l\mathbf{u}_l(t)dt = \tag{3.49}$$

$$\frac{1}{2}\sum_{k,l=1}^{d(J+1)} b_kb_l\lambda_k\int_0^{\beta\hbar}\mathbf{u}_k(t)\mathbf{u}_l(t)dt = \frac{1}{2}\sum_{k=0}^{d(J+1)} b_k^2\lambda_k, \tag{3.50}$$

as $\int_0^{\beta\hbar}\mathbf{u}_k(t)\mathbf{u}_l(t)dt = \delta_{k,l}$, with $\delta_{k,l}$ the Kronecker delta and λ_k the $d(J+1)$ eigenvalues of M. The right-hand side of equation (3.50) depends only on the coefficients b_k. This relation motivates the replacement of the time sliced measure $\mathcal{D}x$ by the normal mode measure $\mathcal{D}b$.

The paths $y_\Delta(t) \subset \boldsymbol{T}_\gamma\mathcal{C}_{[0,\beta\hbar]}(\mathbb{R}^d)$ are characterized by their local coordinates $(a_1^1, \ldots, a_{J+1}^d)$, see Section 2.8. Through the unitary transform in equation (3.45) a bijective correspondence to the coefficients $(b_1^1, \ldots, b_{J+1}^d) \subset \boldsymbol{T}_\gamma^*C_{[0,\beta\hbar]}(\mathbb{R}^d)$ is established. In equation (3.9) after inserting the Taylor expansion equation (3.7) the Euclidean action of the stationary-action path is a constant. The remaining time sliced path integration over the term containing the second variation changes as follows:

$$\left(\prod_{j=1}^{J+1}\left(\frac{1}{2\pi\hbar h_j}\right)^{d/2}\right)\int_{\mathbb{R}}\cdots\int_{\mathbb{R}}\exp\left(-\frac{1}{\hbar}\frac{1}{2}\int_0^{\beta\hbar}\int_0^{\beta\hbar}\frac{\delta^2 S_{\mathrm{E}}}{\delta\gamma_\Delta(t)\delta\gamma_\Delta(t')}\right.$$

$$\left. y_\Delta(t)y_\Delta(t')dtdt'\right)d\boldsymbol{x}_1\ldots d\boldsymbol{x}_{J+1}\approx \tag{3.51}$$

$$\int_{\mathbb{R}}\cdots\int_{\mathbb{R}}\exp\left(-\frac{1}{\hbar}\frac{1}{2}\mathbf{a}^T M\mathbf{a}\right)d\boldsymbol{x}_1\ldots d\boldsymbol{x}_{J+1}= \tag{3.52}$$

$$\left(\prod_{j=1}^{J+1}\left(\frac{1}{2\pi\hbar h_j}\right)^{d/2}\right)N\int_{\mathbb{R}}\cdots\int_{\mathbb{R}}\exp\left(-\frac{1}{\hbar}\frac{1}{2}\mathbf{a}^T M\mathbf{a}\right)da_1^1\ldots da_1^d\ldots da_{J+1}^1\ldots da_{J+1}^d= $$

$$\tag{3.53}$$

$$\left(\prod_{j=1}^{J+1}\left(\frac{1}{2\pi\hbar h_j}\right)^{d/2}\right)N\int_{\mathbb{R}}\cdots\int_{\mathbb{R}}\exp\left(-\frac{1}{\hbar}\frac{1}{2}\mathbf{b}^T D\mathbf{b}\right)$$

$$\det\left[\left(\frac{\partial a_i^k}{\partial b_j^l}\right)_{i,j=1,\ldots,J+1}^{k,l=1,\ldots,d}\right]db_1^1\ldots db_1^d\ldots db_{J+1}^1\ldots db_{J+1}^d= \tag{3.54}$$

$$\left(\prod_{j=1}^{J+1}\left(\frac{1}{2\pi\hbar h_j}\right)^{d/2}\right)N\int_{\mathbb{R}}\cdots\int_{\mathbb{R}}\exp\left(-\frac{1}{\hbar}\frac{1}{2}\sum_{i=1}^{d(J+1)}b_i^2\lambda_i\right)db_0\ldots db_{d(J+1)-1}. \tag{3.55}$$

The normalization factor N accounts for the relation between the time sliced $\mathcal{D}\boldsymbol{x}$ measure and the normal mode measure $\mathcal{D}\mathbf{a}$. It includes a determinant of a Jacobian. Note that this is not a simple linear coordinate transformation [182], see also Section 2.8.

The Jacobian determinant in equation (3.54) is equal to one, as the transform it accounts for is the unitary transform of $\mathcal{D}a$ to $\mathcal{D}b$, see equation (3.44). In the last equation (3.55) the coefficients b_k are just renamed for simpler notation in Section 3.2.3. They are the same $d(J+1)$ coefficients as in equation (3.54).

The value of the constant N will cancel out later in the ratio of $\frac{\mathcal{I}m\ Q_{\mathrm{inst}}}{Q_{\mathrm{RS}}}$ contributing to the instanton rate k_{inst}, as both partition functions are treated in the same way.

3.2.2   Evaluation of Q_{RS}

The evaluation of Q_{RS} follows a similar procedure as the evaluation of Q_{inst}. However, in contrast to $\gamma_{\mathrm{inst}}(t)$ the path $\gamma_{\mathrm{RS}}(t)$ is collapsed to a point. Then, the determinant of the Jacobi operator $\det\{\mathcal{J}\}$ corresponds to the determinant of a non-singular matrix, that has no zero eigenvalues.

To evaluate Q_{RS} first an optimization to find the reactant minimum at $\boldsymbol{x}_{\mathrm{RS}}$ is required. The stationary-action path is then given as $\gamma_{\mathrm{RS}}(t)=\boldsymbol{x}_{\mathrm{RS}}$ for all t. Of course $\gamma_{\mathrm{RS}}(t)$

fulfills $\frac{\delta S_{\mathrm{E}}}{\delta \gamma_{\mathrm{RS}}} = 0$. The Euclidean action function of the stationary path is then

$$S_{\mathrm{E}}[\gamma_{\mathrm{RS}}(t)] = \int_0^{\beta\hbar} \frac{1}{2} \frac{d\gamma_{\mathrm{RS}}(t)}{dt} \cdot \frac{d\gamma_{\mathrm{RS}}(t)}{dt} + V(\gamma_{\mathrm{RS}}(t)) dt = \beta\hbar V(\gamma_{\mathrm{RS}}(t)), \qquad (3.56)$$

as $\gamma_{\mathrm{RS}}(t) = x_{\mathrm{RS}}$ for all t, the first summand $\frac{d\gamma_{\mathrm{RS}}(t)}{dt} = 0$ for all t.

We assume γ_{RS} to have the same discretization as γ_{inst}. Then there are as well $d(J + 1)$ possible fluctuations around γ_{RS}. To find them and then calculate the partition function Q_{RS} the path integral is transformed in the same way as in equation (3.54). The only difference between the calculation of Q_{inst} and Q_{RS} is the form of the matrix V. For γ_{RS} V contains $J + 1$ blocks of $V''(x_{\mathrm{RS}})$ instead of the Hessians at each point x_j on γ_{inst}. Thus, the matrix M_{RS} has different values than M and different eigenvalues, denoted by λ_i^{RS}, $i = 1, \ldots, d(J + 1)$.

To evaluate the partition function Q_{RS} we will now put all together: the path integral expression of the partition function equation (3.5), the semiclassical steepest descent approximation equation (3.17), and the discrete evaluations of the determinant of the Jacobi operator $(h_j)^d \det \mathcal{J}$ which is $\det[M_{\mathrm{RS}}]$.

At first consider the partition function after (i) taking the the fluctuations up to second order into account by a functional Taylor expansion, (ii) transforming from the time sliced to the normal mode measure, and (iii) diagonalizing M_{RS} and transforming from da_j^k to db_j^k:

$$Q_{\mathrm{RS}} \approx \left(\prod_{j=1}^{J+1} \left(\frac{1}{2\pi\hbar h_j} \right)^{d/2} \right) \exp\left(-\frac{1}{\hbar} S_{\mathrm{E}}[\gamma_{\mathrm{RS}}(t)] \right) N$$

$$\int_{\mathbb{R}} \ldots \int_{\mathbb{R}} \exp\left(-\frac{1}{\hbar} \frac{1}{2} \mathbf{b}^T D_{\mathrm{RS}} \mathbf{b} \right) db_1^1 \ldots db_1^d \ldots db_{J+1}^1 \ldots db_{J+1}^d. \qquad (3.57)$$

The relation

$$\mathbf{b}^T D_{\mathrm{RS}} \mathbf{b} = \sum_{i=1}^{d(J+1)} b_i \lambda_i^{\mathrm{RS}} b_i \qquad (3.58)$$

allows to treat the integrals in equation (3.57) as Gaussian integrals, see (B.5). For one integration holds

$$\int_{\mathbb{R}} \exp\left(-\frac{1}{\hbar} \frac{1}{2} b_1 \lambda_1^{\mathrm{RS}} b_1 \right) db_1 = \sqrt{\frac{2\pi\hbar}{\lambda_1^{\mathrm{RS}}}}. \qquad (3.59)$$

Therefore factor $2\pi\hbar$ in the denominator of the first prefactor in (3.57) cancels out against the result of the Gaussian integration. Then the partition function at the reactant minimum is given as

$$Q_{\mathrm{RS}} \approx \left(\prod_{j=1}^{J+1} \left(\frac{1}{h_j} \right)^{d/2} \right) \exp\left(-\frac{1}{\hbar} S_{\mathrm{E}}[\gamma_{\mathrm{RS}}(t)] \right) N \sqrt{\frac{1}{\prod_{i=1}^{d(J+1)} \lambda_i^{\mathrm{RS}}}}. \qquad (3.60)$$

Summarizing, the evaluation of the semiclassical steepest descent approximation (3.17) of Q_{RS} via Gaussian integrals requires

1. to locate the reactant minimum $\boldsymbol{x}_{RS}$,

2. determine the Hessian $V''(\boldsymbol{x}_{RS})$, and

3. calculation of the determinant, possibly by diagonalization of M_{RS}.

3.2.3   Special treatment of Q_{inst}

The normal mode expansion of the fluctuation in terms of $\mathbf{u}_k(t)$ is given as

$$y_\Delta = y^{b_0, b_1, \cdots}(t) = \sum_{k=0}^{d(J+1)-1} b_k \mathbf{u}_k(t), \tag{3.61}$$

with the normal mode functions $\mathbf{u}_k(t) \in C^1(\mathbb{R})$. The powers in the fluctuation $y^{b_0, b_1, \cdots}$ indicate its dependence on the coefficients b_k, see equation (2.52) and equation (3.6). Assume the coefficient b_0, to belong to the direction of the zero-mode. In the discrete case

$$y_\Delta = \begin{pmatrix} y_\Delta(t_1) \\ \vdots \\ y_\Delta(t_{J+1}) \end{pmatrix} = U\mathbf{b}. \tag{3.62}$$

Note that in equation (3.55) the components of $\mathbf{b}$ were renamed with new indices which is used in the following.

Due to two reasons the partition function Q_{inst} based on γ_{RS} can not be calculated in the same way as Q_{RS} in equation (3.60):

1. The Feynman functional integration sums over all possible physical states. However, it is crucial to count equivalent physical states only once. Therefore, in the case where symmetries are present, one has to sum over the orbits of the symmetry group but not over the single points of the orbit which to obtain a finite result. The zero-mode describes the displacement along the instanton path γ_{inst}, which induces a symmetry relation.

   Without loss of generality assume the zero eigenvalue $\lambda_0 = 0$ belonging to the mode $\mathbf{u}_0(t) \propto \frac{d\gamma_{inst}(t)}{dt}$ and $\mathbf{u}_0(t) \in \{\mathbf{u}_k(t)\}_{k=1}^{d(J+1)}$, see equation (3.19) and equation (3.48), which leads to a contribution of

   $$\int_\mathbb{R} \frac{db_0}{\sqrt{2\pi}} \exp\left(-\lambda_0 b_0^2\right) = \int_\mathbb{R} \frac{db_0}{\sqrt{2\pi}} 1 = \infty \tag{3.63}$$

   in equation (3.55). Thus, an eigenvalue $\lambda_0 = 0$ would lead to an infinite contribution to Q_{inst}.

2. In addition to the zero-mode, the negative eigenvalue, caused by $S_{\mathrm{E}}[\gamma_{\mathrm{inst}}(t)]$ being a saddle point, has to be treated separately. The negative eigenvalue leads to a non-Gaussian integral.

A more sophisticated approach to evaluate Q_{inst}, than in equation (3.60), is needed to deal with the negative eigenvalue and the zero eigenvalue. Based on the idea of counting equivalent states only once applying the method developed by Faddeev and Popov to the d-dimensional time sliced formulation will provide a solution [243] for the zero-mode treatment. A more detailed description on the basic notion and the introduction of a delta function in the path integration is given in the Appendix B.2. The non-trivial zero-mode $\frac{d\gamma_{\mathrm{inst}}(t)}{dt}$ belonging to the zero eigenvalue of the operator $\mathcal{J}$ is in the following renormalized and left out in the determinant evaluation. In the procedure proposed by Faddev and Popov the integration over the coefficient b_0 belonging to the zero-mode $\mathbf{u}_0(t)$ is replaced by an integration of a generalized coordinate, t_0, along the instanton trajectory $\gamma_{\mathrm{inst}}(t)$. The parameter $t_0 \in [0, \beta\hbar]$ representing the generalized coordinate varies along the instanton path. At the end a prefactor enters the expression for Q_{inst}, and, thus, the rate, by the renormalization.

The negative eigenvalue of the operator $\mathcal{J}$, $\lambda_1 < 0$, is handled by an analytic continuation into the complex plane. The result is an imaginary partition function $\mathcal{I}m(Q_{\mathrm{inst}}) \neq 0$.

Zero-mode treatment

The functions $\mathbf{u}_k(t)$ satisfy the orthonormality condition for all $k, l = 1 \ldots, d(J + 1)$, see equation (2.58) page 36:

$$\frac{1}{\beta\hbar} \int_0^{\beta\hbar} \mathbf{u}_k(t)\mathbf{u}_l(t)dt = \delta_{kl}, \tag{3.64}$$

where δ_{kl} denotes the Kronecker Delta. For the discretized $\mathbf{u}_k$ obtained from the eigenbasis calculations in (3.47)

$$\langle \mathbf{u}_k, \mathbf{u}_l \rangle = \frac{1}{\beta\hbar} \sum_{i=1}^{d(J+1)} u_k(t_i)u_l(t_i)h_i = \delta_{kl} \tag{3.65}$$

holds for the discrete inner product with $\mathbf{u}_k$ columns of the matrix U which implicates that all vectors $\mathbf{u}_k$ are conjugate (i.e. orthogonal) with respect to the matrix containing the stepsizes h_i on its diagonal. For the definition of the inner products see page 24. The discrete case is in the following marked by a gray bar.

Recover b_0 by forming the inner product of the fluctuation with the zero-mode function $\mathbf{u}_0(t)$

$$b_0 = \frac{1}{\beta\hbar} \int_0^{\beta\hbar} y^{b_0,b_1,\cdots}(t)\mathbf{u}_0(t)dt. \tag{3.66}$$

And in the discrete case

$$b_0 = \langle \mathbf{y}^{b_0,b_1,\cdots}, \mathbf{u}_0 \rangle = \langle U\mathbf{b}, \mathbf{u}_0 \rangle = \frac{1}{\beta\hbar}\mathbf{b}^T U\mathbf{u}_0 = \frac{1}{\beta\hbar}\mathbf{b}^T \begin{pmatrix} 1 \\ 0 \\ \vdots \\ 0 \end{pmatrix}. \tag{3.67}$$

The overlap of the stationary path (the instanton) $\gamma_{\text{inst}}(t)$ and its zero-mode function $\frac{d\gamma_{\text{inst}}(t)}{dt}$ is zero

$$\frac{1}{\beta\hbar} \int_0^{\beta\hbar} \gamma_{\text{inst}}(t-t_0)\mathbf{u}_0(t-t_0)dt$$

$$\propto \frac{1}{\beta\hbar} \int_0^{\beta\hbar} \gamma_{\text{inst}}(t-t_0)\frac{d\gamma_{\text{inst}}(t-t_0)}{dt}dt \propto \left[\frac{1}{2\beta\hbar}(\gamma_{\text{inst}}(t-t_0))^2\right]_0^{\beta\hbar} = 0. \tag{3.68}$$

The equality to zero is given by the fact that the path $\gamma_{\text{inst}}(t)$ is a closed path. Therefore the fluctuations in local coordinate representation can be replaced by by the full fluctuating path $\gamma^{b_0,b_1,\cdots}(t) = \gamma_{\text{inst}}(t) + \boldsymbol{y}^{b_0,b_1,\cdots}(t)$ in general coordinates. Then the coefficient of the zero-mode is given as

$$b_0 = \frac{1}{\beta\hbar} \int_0^{\beta\hbar} \gamma^{b_0,b_1,\cdots}(t)\mathbf{u}_0(t)dt \tag{3.69}$$

and in the discrete case

$$b_0 = \langle \gamma_{\text{inst}} + \mathbf{y}^{b_0,b_1,\cdots}, \mathbf{u}_0 \rangle = \left\langle \begin{pmatrix} \boldsymbol{x}_1 \\ \boldsymbol{x}_2 \\ \vdots \\ \boldsymbol{x}_{J+1} \end{pmatrix} + U\mathbf{b}, \mathbf{u}_0 \right\rangle, \tag{3.70}$$

with $\boldsymbol{x}_i \in \mathbb{R}^d$ the coordinates of the $J+1$ control points belonging to the instanton path determined by the (discrete) Euler-Lagrange equation (2.40).

Let δ denote the Dirac delta function, see Appendix B.1, then

$$\delta(b_0) = \delta\left(\frac{1}{\beta\hbar} \int_0^{\beta\hbar} \gamma_{\text{inst}}^{b_0,b_1,\cdots}(t)\mathbf{u}_0(t)dt\right) \tag{3.71}$$

and discrete

$$\delta\left(b_0\right) = \delta\left(\left\langle\gamma_{\text{inst}} + \mathbf{y}^{b_0,b_1,\cdots}, \mathbf{u}_0\right\rangle\right). \tag{3.72}$$

Now, let t_0 be the generalized coordinate moving along the path $\gamma_{\text{inst}}(t) = \gamma_{\text{inst}}(t - t_0)$. The constant t_0 describes initial positions of the path, in physics literature it is also referred to as kink position [198].

The relation between normal mode coordinate b_0 and t_0 will be established by introducing an alternative parametrization of the path $\gamma_{b_0,b_1,\ldots}(t)$, where b_0 is replaced by t_0:

$$\gamma^{b_0,b_1,\cdots}(t) = \gamma_{\text{inst}}(t) + \sum_{k=0}^{d(J+1)-1} b_k\mathbf{u}_k(t) \tag{3.73}$$

changes to

$$\gamma^{t_0,b_1,\cdots}(t) = \gamma_{\text{inst}}(t) + \sum_{k=1}^{d(J+1)-1} b_k\mathbf{u}_k(t). \tag{3.74}$$

In the discrete case

$$\gamma^{b_0,b_1,\cdots} = \gamma_{\text{inst}} + \mathbf{y}^{b_0,b_1,\cdots} = \begin{pmatrix} \boldsymbol{x}_1 \\ \boldsymbol{x}_2 \\ \vdots \\ \boldsymbol{x}_{J+1} \end{pmatrix} + U\mathbf{b} \tag{3.75}$$

changes to

$$\gamma^{t_0,b_1,\cdots} = \begin{pmatrix} \boldsymbol{x}_1 \\ \boldsymbol{x}_2 \\ \vdots \\ \boldsymbol{x}_{J+1} \end{pmatrix} + \left(\mathbf{u}_1,\ldots,\mathbf{u}_{d(J+1)-1}\right)\begin{pmatrix} b_1 \\ b_2 \\ \vdots \\ b_{d(J+1)-1} \end{pmatrix} =: \gamma_{\text{inst}} + U'\mathbf{b}', \tag{3.76}$$

with $U' \in \mathbb{R}^{(d(J+1)-1)\times d(J+1)}$ and $\mathbf{b}' \in \mathbb{R}^{d(J+1)-1}$. The point $t_0 = 0$ coincides with $b_0 = 0$ by definition. Thus,

$$\delta\left(b_0\right) = \delta\left(\frac{1}{\beta\hbar}\int_0^{\beta\hbar}\left(\gamma_{\text{inst}}(t) + \sum_{k=1}^{d(J+1)-1} b_k\mathbf{u}_k(t)\right)\mathbf{u}_0(t)dt\right) \tag{3.77}$$

and discrete

$$\delta\left(b_0\right) = \delta\left(\left\langle\gamma_{\text{inst}} + U'\mathbf{b}', \mathbf{u}_0\right\rangle\right). \tag{3.78}$$

To apply the transition from expression (3.71) to (3.77) the measure, see (3.55)

$$N \int_{-\infty}^{\infty} \frac{db_0}{\sqrt{2\pi\hbar}} \prod_{k=1}^{d(J+1)-1} \left[\int_{-\infty}^{\infty} \frac{db_k}{\sqrt{2\pi\hbar}}\right] \tag{3.79}$$

has to be transformed into

$$\frac{N}{\sqrt{2\pi\hbar}} \int_{-\infty}^{\infty} dt_0 \prod_{k=1}^{d(J+1)-1} \int_{-\infty}^{\infty} \frac{db_k}{\sqrt{2\pi\hbar}} \det\left[\frac{\partial}{\partial t_0} b_0\left(b_0, b_1, \ldots\right)\right], \tag{3.80}$$

which is achieved by the same trick as in in two dimensions with $d = 1$, see Appendix B.2. Note that the integrals in the last two equations come from the path integration over the whole configuration space not from an inner product. Thus, they range from $-\infty$ to ∞.

Faddeev–Popov trick

To ensure a correct transform (and that the result at $b_0 = t_0 = 0$ stays the same) the Jacobian has to fulfill

$$\int_{-\infty}^{\infty} \delta(b_0) \det\left[\frac{\partial}{\partial t_0} b_0\left(b_0, b_1, \ldots\right)\right] dt_0 = 1. \tag{3.81}$$

The determinant of the Jacobian describes the volume changes caused by the transform of b_0 to t_0. It depends on all paths, i.e., on all coefficients b_k. Inserting (3.77) into (3.81) gives the condition for the Jacobian determinant

$$\int_{-\infty}^{\infty} \delta\left(\frac{1}{\beta\hbar} \int_0^{\beta\hbar} \gamma^{t_0, b_1, \cdots}(t)\mathbf{u}_0(t) dt\right) \det\left[\frac{\partial}{\partial t_0} b_0\left(b_0, b_1, \ldots\right)\right] dt_0 = 1. \tag{3.82}$$

$$\int_{-\infty}^{\infty} \delta\left(\left\langle\gamma_{\text{inst}} + \mathbf{y}^{t_0, b_1, \cdots}, \mathbf{u}_0\right\rangle\right) \det\left[\frac{\partial}{\partial t_0} b_0\left(b_0, b_1, \ldots\right)\right] dt_0 = 1. \tag{3.83}$$

As the δ-function has a vanishing argument at $t_0 = 0$ an expansion in powers of t_0 is possible. When keeping the argument of lowest order the result is

$$\frac{1}{\beta\hbar} \int_0^{\beta\hbar} dt\, \gamma^{t_0,b_1,\cdots}(t)\mathbf{u}_0(t) = \tag{3.84}$$

$$= \frac{-N_0 t_0}{\beta\hbar} \left[\int_0^{\beta\hbar} \left(\frac{d\gamma_{\text{inst}}(t)}{dt} \right)^2 dt + \sum_{k=1}^{d(J+1)-1} b_k \int_0^{\beta\hbar} \frac{d\gamma_{\text{inst}}(t)}{dt} \frac{d\mathbf{u}_k(t)}{dt} dt \right] + \mathcal{O}(t_0^2) = \tag{3.85}$$

$$= \frac{-N_0 t_0}{\beta\hbar} \left[S_0 + \sum_{k=1}^{d(J+1)-1} b_k r_k \right] + \mathcal{O}(t_0^2), \tag{3.86}$$

with the remainder $r_k := \int_0^{\beta\hbar} \frac{d\gamma_{\text{inst}}(t)}{dt} \frac{d\mathbf{u}_k(t)}{dt} dt$, the normalized normal mode $\mathbf{u}_0 := N_0 \frac{d\gamma_{\text{inst}}(t)}{dt}$, and the action $S_0 = \int_0^{\beta\hbar} \left(\frac{d\gamma_{\text{inst}}(t)}{dt} \right)^2 dt$; see also the definition of the action sum in equation (2.46). The normalization constant is given as $N_0 = \sqrt{\frac{\beta\hbar}{S_0}}$, as

$$\frac{1}{\beta\hbar} \int_0^{\beta\hbar} \mathbf{u}_0(t)\mathbf{u}_0(t) dt = \frac{N_0^2}{\beta\hbar} \int_0^{\beta\hbar} \frac{d\gamma_{\text{inst}}(t)}{dt} \frac{d\gamma_{\text{inst}}(t)}{dt} dt = 1 \tag{3.87}$$

$$\Leftrightarrow N_0^2 = \frac{\beta\hbar}{S_0}. \tag{3.88}$$

In the discrete case holds

$$\langle \gamma_{\text{inst}} + \mathbf{y}^{b_0,b_1,\cdots}, \mathbf{u}_0 \rangle = -N_0 t_0 \frac{J+1}{\beta\hbar} \left[S_0 + \sum_{k=1}^{d(J+1)-1} b_k r_k \right] + \mathcal{O}(t_0^2), \tag{3.89}$$

with $N_0 = \sqrt{\beta\hbar/(S_0(J+1))}$. Then follows from (3.82)

$$\int_{-\infty}^{\infty} \delta\left(\frac{-N_0 t_0}{\beta\hbar} \left[S_0 + \sum_{k=1}^{d(J+1)-1} b_k r_k \right] \right) \det\left[\frac{\partial}{\partial t_0} b_0 \left(b_0, b_1, \dots \right) \right] dt_0 = 1. \tag{3.90}$$

Employing the symmetry and the scaling property of the δ-function, see Appendix B.1, yields

$$\int_{-\infty}^{\infty} \sqrt{\frac{\beta\hbar}{S_0}} \frac{\delta(t_0)}{\left[1 + S_0^{-1} \sum_{k=1}^{d(J+1)-1} b_k r_k \right]} \det\left[\frac{\partial}{\partial t_0} b_0 \left(b_0, b_1, \dots \right) \right] dt_0 = 1. \tag{3.91}$$

Using the fact $\int_{-\infty}^{\infty} dt_0 \delta(t_0) = 1$ and rearranging the equation leads to the Jacobian determinant (Faddeev-Popov determinant)

$$\det\left[\frac{\partial}{\partial t_0} b_0\left(b_0, b_1, \dots\right)\right] = \sqrt{\frac{S_0}{\beta\hbar}}\left[1 + S_0^{-1}\sum_{k=1}^{d(J+1)-1} b_k r_k\right]. \tag{3.92}$$

and in the discrete case

$$\det\left[\frac{\partial}{\partial t_0} b_0\left(b_0, b_1, \dots\right)\right] = \sqrt{\frac{S_0(J+1)}{\beta\hbar}}\left[1 + S_0^{-1}\sum_{k=1}^{d(J+1)-1} b_k r_k\right] \tag{3.93}$$

The term $S_0^{-1}\sum_{k=1}^{d(J+1)-1} b_k r_k$ disappears at the level of quadratic fluctuations as they are odd in b_k. Now with the renomalized (gauge fixed) contributions of the zero-mode in (3.80) the fluctuation factor, see also (3.12), (3.17) and (3.50), reads

$$N\frac{1}{\sqrt{2\pi\hbar}}\int_{-\infty}^{\infty} dt_0 \prod_{k=1}^{d(J+1)-1}\int_{-\infty}^{\infty}\frac{db_k}{\sqrt{2\pi\hbar}} \tag{3.94}$$

$$\det\left[\frac{\partial}{\partial t_0} b_0\left(b_0, \dots\right)\right]\exp\left(\frac{1}{2\hbar}\sum_{k=0}^{d(J+1)-1} b_k^2\lambda_k\right) \tag{3.95}$$

$$= N\sqrt{\frac{J+1}{\beta\hbar}}\sqrt{\frac{S_0}{2\pi\hbar}}\sqrt{\frac{1}{\prod_{k=1}^{d(J+1)-1}\lambda_k}}\int_{-\infty}^{\infty} dt_0 \tag{3.96}$$

$$\approx N\left[\frac{1}{2\pi\hbar}\int_0^{\beta\hbar}\left(\frac{d\gamma_{\text{inst}}(t)}{dt}\right)^2 dt\right]^{1/2}\left[\frac{1}{\det'\left[-\frac{1}{2}\frac{d^2}{dt^2} + \frac{d^2 V(\gamma_{\text{inst}}(t))}{d^2\gamma_{\text{inst}}(t)}\right]}\right]^{1/2}\sqrt{\beta\hbar}. \tag{3.97}$$

As $\int_{-\infty}^{\infty} dt_0 = \beta\hbar$ for $t_0 \in [0, \beta\hbar]$ expression (3.96) turns into 3.97 where $\det'$ denotes that the eigenvalue belonging to the zero-mode is omitted. The semiclassical partition partition function Q_{inst} of the quantum transition state is then in analogy to Q_{RS}, see equation (3.60), given as

$$Q_{\text{inst}} \approx \left(\prod_{j=1}^{J+1}\left(\frac{1}{h_j}\right)^{d/2}\right)\exp\left(-\frac{1}{\hbar}S_{\text{E}}[\gamma_{\text{inst}}(t)]\right)\left[\frac{S_0}{2\pi\hbar}\right]^{1/2}\frac{N\sqrt{\beta\hbar}}{\sqrt{\det'\left[-\frac{1}{2}\frac{d^2}{dt^2} + \frac{d^2 V(\gamma_{\text{inst}}(t))}{d^2\gamma_{\text{inst}}(t)}\right]}} \approx \tag{3.98}$$

$$\approx \left(\prod_{j=1}^{J+1} \left(\frac{1}{h_j} \right) \right)^{d/2} \exp\left(-\frac{1}{\hbar} S_E[\gamma_{\mathrm{inst}}(t)] \right) \left[\frac{S_0(J+1)}{2\pi\hbar} \right]^{1/2} \frac{N\sqrt{\beta\hbar}}{\sqrt{\prod_{i=1}^{d(J+1)-1} \lambda_i^{\mathrm{inst}}}}. \qquad (3.99)$$

However, that is not the correct formula as it is still open how to treat the negative eigenvalue which will be discussed in the next paragraph. The evaluation of the negative mode is still an open question.

Negative-mode treatment

Since the zero-mode $\frac{\gamma_{\mathrm{inst}}(t)}{dt}$ has one node and as $\gamma_{\mathrm{inst}}(t)$ lies at a saddle point, one eigenvalue of M (contributing to the discrete version of $\det \mathcal{J}$) is negative [242]. The negative eigenvalue is without loss of generality denoted by $\lambda_1 < 0$, $\lambda_1 \in \sigma(M) \setminus \lambda_0$ and the coefficient of the corresponding mode by b_1. It was shown that the distortion of the integration contour along b_1 into the complex plane enables a Gaussian integration of the negative eigenvalue [202]. The negative eigenvalue λ_1 of the fluctuation is proportional to the negative curvature at the maximum of $\gamma_{\mathrm{inst}}(t)$. There exists only one negative mode [241]. Thus, the remaining modes are not involved in the analytic continuation. A simple approach would be to evaluate the integration over b_1 with $|\lambda_1| = \tilde{\lambda}_1 > 0$ which results in

$$\int \frac{db_1}{\sqrt{2\pi\hbar}} \exp\left(-\frac{1}{2\hbar} b_1 \tilde{\lambda}_1 b_1 \right) = \frac{1}{\sqrt{\tilde{\lambda}_1}} . \qquad (3.100)$$

Then after the analytical continuation the right hand side would read

$$\int \frac{db_1}{\sqrt{2\pi\hbar}} \exp\left(-\frac{1}{2\hbar} b_1 \lambda_1 b_1 \right) = \pm \frac{i}{\sqrt{\lambda_1}} . \qquad (3.101)$$

However, there is a factor $\frac{1}{2}$ missing in the resulting formula (3.101) [202]. The factor $\frac{1}{2}$ is due to the equal probability of the moving particle to return back to the reactant valley or proceed forward to the lower product valley, see Fig. 2.4. Only those paths going forward to the product valley count to the reaction rate. The detailed derivation of this factor can be found in [198] and the integration of the negative eigenvalue results in:

$$\int \frac{db_1}{\sqrt{2\pi\hbar}} \exp\left(-\frac{1}{2\hbar} (b_1)^2 \lambda_1 \right) = \frac{i}{2\sqrt{|\lambda_1|}}. \qquad (3.102)$$

Then the final result for the partition function Q_{inst} is

$$Q_{\text{inst}} \approx \left(\prod_{j=1}^{J+1} \left(\frac{1}{h_j} \right)^{d/2} \right) \exp\left(-\frac{1}{\hbar} S_{\text{E}}[\gamma_{\text{inst}}(t)] \right) \left[\frac{S_0(J+1)}{2\pi\hbar} \right]^{1/2} \frac{i}{2} \frac{N\sqrt{\beta\hbar}}{\sqrt{\prod_{i=1}^{d(J+1)-1} |\lambda_i^{\text{inst}}|}}.$$

(3.103)

This form contains the absolute values, denoted by $|\cdot|$, of all eigenvalues in the second factor (except the one equal to zero) and an additional factor $i/2$ that makes the partition function imaginary. Additionally, the zero-mode ($\mathbf{u}_0(t)$ or discretized $\mathbf{u}_0$) in the integration over the zero-mode coefficient b_0 is by the renormalization discussed in the previous paragraph replaced by an integration over the instanton path. Now we can have a closer look on the resulting rates.

3.3   Instanton rates

Taking the expressions for the partition functions in equation (3.60) and equation (3.103) into account, the result for the $\mathcal{I}m\, F$ instanton rate, see (3.2), as derived in this chapter is:

$$k_{\text{inst}} = \frac{2}{\beta\hbar} \left(\frac{\mathcal{I}m\, Q_{\text{inst}}}{Q_{\text{RS}}} \right) \approx$$

(3.104)

$$\approx \frac{2}{\beta\hbar} \left(\prod_{j=1}^{J+1} \left(\frac{1}{h_j} \right)^{d/2} \right) \exp\left(-\frac{1}{\hbar} S_{\text{E}}[\gamma_{\text{inst}}(t)] \right) \left[\frac{S_0}{2\pi\hbar} \right]^{1/2} \frac{1}{2} \frac{N\sqrt{\beta\hbar(J+1)}}{\sqrt{\prod_{i=1}^{d(J+1)-1} |\lambda_i^{\text{inst}}|}}$$

$$\left(\prod_{j=1}^{J+1} \left(\frac{1}{h_j} \right)^{-d/2} \right) \exp\left(-\frac{-1}{\hbar} S_{\text{E}}[\gamma_{\text{RS}}(t)] \right) N^{-1} \sqrt{\prod_{i=0}^{d(J+1)-1} \lambda_i^{\text{RS}}} =$$

(3.105)

$$= \exp\left(-\frac{1}{\hbar} \left(S_{\text{E}}[\gamma_{\text{inst}}(t)] - S_{\text{E}}[\gamma_{\text{RS}}(t)] \right) \right) \left[\frac{S_0}{2\pi\hbar} \right]^{1/2} \sqrt{\frac{J+1}{\beta\hbar}} \sqrt{\frac{\prod_{i=0}^{d(J+1)-1} \lambda_i^{\text{RS}}}{\prod_{i=1}^{d(J+1)-1} |\lambda_i^{\text{inst}}|}}.$$

(3.106)

This is a variable step-size instanton rate. Note that the product in the denominator contains one factor less than the product in the enumerator. The normalization factor N due to the transform from a time sliced to a Fourier path integral and the product over the step-sizes introduced as normalization in the time sliced path integral formulation cancel out in the ratio of the two partition functions. From equation (3.105) to equation (3.106) the factor $\frac{2}{\beta\hbar}$ becomes $\sqrt{1/\beta\hbar}$, which is a factor slightly different

from the previous versions of the rates. It is introduced through the normalization of the functions that play a role in the zero-mode renormalization.

In molecular systems, $V(\gamma_{\text{inst}}(t))$ is invariant under a global rotation and translation. Therefore, N_0 eigenvalues of the V matrix, which contains the Hessians of the potential energies along the path $\gamma_{\text{inst}}(t)$, see Fig. 3.3, are zero. For non-linear molecules without frozen atoms $N_0 = 6$ (5 for linear molecules). The Euclidean action S_{E} is, just like V, invariant under a rotation and translation of the whole paths γ_{inst} or γ_{RS}. Thus, in the instanton rate for molecules additionally to the eigenvalue corresponding to the zero-mode N_0 are zero. The zero-mode eigenvalue has no counterpart in the reactant-state partition function whereas the N_0 additional zero eigenvalues do. The reactant-state partition function can be treated as the quantum mechanical partition function of a harmonic oscillator in $d - N_0$ dimensions, see [109].

Therefore, the following discrete formulation of instanton theory allows to use variable step-sizes along the instanton path. The indices have been renamed starting from 1 instead of 0 compared to equation (3.106).

$$
k_{\text{inst}} \approx \left(\prod_{l=N_0+1}^{d(J+1)} \sqrt{\lambda_l^{\text{RS}}} \right) \left(\prod_{l=N_0+2}^{d(J+1)} \frac{1}{\sqrt{|\lambda_l^{\text{inst}}|}} \right)
$$
$$
\sqrt{\frac{S_0}{2\pi\hbar}} \sqrt{\frac{J+1}{\beta\hbar}} \exp\left(-\frac{1}{\hbar} \left(S_{\text{E}}[\gamma_{\text{inst}}(t)] - S_{\text{E}}[\gamma_{\text{RS}}(t)] \right) \right). \qquad (3.107)
$$

If the potential energy at the reactant state minimum $V(\boldsymbol{x}_{\text{RS}}) = 0$ is chosen to be equal to zero, the action $S_{\text{E}}[\gamma_{\text{RS}}(t)] = 0$ and vanishes in the exponential function. N_0 eigenvalues corresponding to the overall translation and rotation are excluded from the products, the vibrational partition functions. This means, that for the present derivation, changes in the translational and rotational partition function are ignored. These can be covered by the partition function of a rigid rotor and by the classical translational partition function [227].

The rates obtained for an equidistant discretization $h_j = \beta\hbar/(J+1) \ \forall j = 1, \ldots, J+1$, have been published, see [57, 182, 198, 216, 227–229] and references therein.

In this chapter the instanton method was extended to a discretization using a variable step-size along the imaginary time, the parameter of the stationary-action paths. The derivation is slightly different from the one used in [109]. Gradients and Hessians required for locating the instantons were presented. The final instanton reaction rate was derived step-by-step by considering all necessary intermediate steps. In addition to the theoretical derivations in this Chapter the algorithm for a variable step-size discretization is outlined in [109] and in Chapter 4.2.

IMPROVEMENTS IN THE CALCULATION OF INSTANTON RATES

The instanton method [202, 205, 206] described in Chapter 3 is a promising tool to calculate tunneling rates. The instanton itself is the most-likely tunneling path at a given temperature. It is also a first-order saddle point of the Euclidean action in the space of closed Feynman paths. Thus, optimizations can be used to locate instantons.

This chapter will give insights on (1) how to optimize an instanton path, i.e., locate the dominant tunneling path in systems with many degrees of freedom (for example enzymes), and (2) how to efficiently calculate quantum rates and kinetic isotope effects from the optimized instanton, despite some challenges.

Possible techniques to locate instantons are proposed and tested in Section 4.1: the Newton–Raphson method will be compared to the partitioned rational function optimization (P-RFO) algorithm, the dimer method, and a newly proposed mode-following algorithm, where the unstable mode, $\mathbf{u}_{\text{inst}}$, is directly estimated from the instanton path. The instanton method allows efficient calculation of quantum rates at different temperatures using sequential cooling [108, 216, 216–219, 227]. The results of testing these algorithms at different temperature on three chemical systems, each including a

hydrogen transfer, are presented. Then the efficiency of these algorithms and possible issues which may impede instanton optimizations, and ways to avoid them are discussed. In Section 4.2 possible improvements on the efficiency of rate calculations by taking a fixed-path approximation or using an adaptive, variable step-size discretization will be presented.

4.1   Locating instantons in many degrees of freedom

To calculate tunneling rates, see equation (3.2), the partition function of the reactant state Q_{RS} and the the partition function Q_{inst} are necessary. To determine Q_{RS}, see equation (3.60), first the reactant minimum of $V(\boldsymbol{x})$ is determined, then the second derivative $V''(\boldsymbol{x})$ is calculated and to calculate the rate eigenvalues are determined, as described in Section 3.2.2. The evaluation of Q_{inst} is more complicated, see Section 3.2.1.

In general, sequential cooling is used [108, 216, 216–219, 227], i.e., the starting point is at a temperature below T_c and then an instanton and the tunneling rate are calculated. Then the temperature is successfully lowered, starting the search from a converged instanton. Alternative approaches and other starting paths may be used as well.

The problem of finding an instanton has been formulated here, see Section 3.1, as a saddle-point search of a discretized path. This allows to treat a high number of degrees of freedom. Instantons can, however, also be interpreted as unstable periodic orbits on the upside-down potential energy surface $(-V)$, see Section 2.5. Techniques to find periodic orbits [244, 245] have previously been used to find instantons [246, 247]. In practice, these techniques are, however, only applicable to systems with a few degrees of freedom [247].

Reduced path formulation of S_E

The first possible simplification is due to the fact that for molecules the instanton path γ_{inst} is delocalized along one line in the configuration space of the molecule. The path is closed by proceeding along this line forward and backward.

To calculate the Euclidean action of the closed path $\gamma_{inst}(t)$ and, through that Q_{inst}, $\gamma_{inst}(t)$ is again discretized into $J+1$ images, see Section 2.7. Mass-weighted coordinates are used throughout. Choosing an even number of images and starting the index $j = 1$ at an image next to one turning point, the images j and $(J + 1) - j + 1$ have identical coordinates. All images are traversed twice. The turning points themselves are not control points. An example is depicted in Fig. 4.1, where the turning points lie between the images 4 and 5, as well as 8 and 1 of the path. Thus, it is sufficient to sum over half

of the images ($P = (J + 1)/2$) [227]. The action sum reads then

$$S_{\mathrm{E}}[\gamma_{\mathrm{inst}}(t)] \approx \frac{2P}{\beta\hbar} \sum_{j=1}^{P-1} |\gamma_{\mathrm{inst}}(t_{j+1}) - \gamma_{\mathrm{inst}}(t_j)|^2 + \frac{\beta\hbar}{P} \sum_{j=1}^{P} V(\gamma_{\mathrm{inst}}(t_j)), \qquad (4.1)$$

where $|\cdot|$ denotes the absolute value (Euclidean norm). Here an equidistant discretization was chosen, with $h_j = \frac{\beta\hbar}{J+1}$ for all $j = 1, \dots, J + 1$. The equidistant step-size was used throughout the rest of this section. To fulfill equation (2.40), a stationary action path has to be searched for. Since rates are the interesting object, the search is specialized on looking for a first-order saddle point of S_{E}, the instanton $\gamma_{\mathrm{inst}} \in \mathcal{C}(\mathbb{R}^{3n}) \subset \Omega$, see page 32. The reduced path that is searched for is of dimension Pd (for a molecule with $d = 3n$ degrees of freedom) [153].
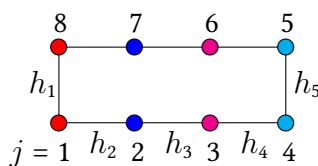
Figure 4.1: Discretization of the instanton path γ_{inst} into $J + 1 = 8$ images. The images (indicated by circles) are numbered by $j = 1$ to 8. The intervals in t between the images are labeled with h_j. Images aligned above each other (1 and 8, 2 and 7, ...) have pairwise identical coordinates.

The collapsed path formulation has a slight impact on the gradient and Hessian formulations which are needed to locate instantons by optimizations. The matrix M belonging to the second variation of S_{E} changes slightly by using the collapsed path. Half of its block entries will be identical. As previously discussed, M (a Hessian) exhibits exactly one negative eigenvalue and a corresponding eigenvector $\mathbf{u}_{\mathrm{inst}}(t) \in \{\mathbf{u}_k(t)\}_{k=1}^{d(J+1)}$ belonging to a movement of the whole path toward the reactant or the product. An example of $\mathbf{u}_{\mathrm{inst}}(t)$ is depicted in Fig. 4.2. The special treatment of the negative mode is discussed on page 66.

The infrastructure to calculate the Euclidean action and all the methods to optimize instantons described in the following were implemented in DL-FIND [248]. They can be used with analytic potentials as well as with electronic structure calculations. Through the interface to ChemShell [249], they can be combined with many quantum chemistry programs as well as classical force fields or QM/MM energy expressions.

4.1.1 Starting path

The instanton optimization starts with an initial guess of a path. The estimation of the starting path should be as close as possible to the final instanton. For temperature

$T \gtrsim T_c$ the instanton is collapsed to $\boldsymbol{x}_{\mathrm{cl}}$, the first-order saddle point on the potential energy surface (classical TS), see Fig. 2.4. As the temperature decreases, the images spread out approximately along the classical unstable mode $\boldsymbol{u}_{\mathrm{cl}}$. In the quadratic region of $V(\boldsymbol{\gamma}_{\mathrm{inst}}(t))$, the images spread on the path reduced to a line like

$$\boldsymbol{\gamma}_{\mathrm{inst}}(t) = \boldsymbol{x}_{\mathrm{cl}} + \Delta r \; \boldsymbol{u}_{\mathrm{cl}} \cos(2\pi \, t/\beta\hbar), \quad 0 \le t \le \beta\hbar \tag{4.2}$$

So, the discretized version for P images was used:

$$\boldsymbol{x}_i = \boldsymbol{x}_{\mathrm{cl}} + \Delta r \; \boldsymbol{u}_{\mathrm{cl}} \cos\left(\frac{j-1/2}{P}\pi\right), \quad 0 < j \le P \tag{4.3}$$

The initial spread Δr is chosen manually. It cannot be estimated from $\boldsymbol{x}_{\mathrm{cl}}$ or its Hessian. If not noted otherwise, $\Delta r = 0.4$ atomic units was used. After optimization and below T_c the instanton path γ_{inst} does not generally pass through the saddle point, $\boldsymbol{x}_{\mathrm{cl}}$, any more.

4.1.2   Mode-following methods

Minimum-mode following is an approach to search for first-order saddle points. The action is minimized in all directions but one, $\mathbf{u}_{\mathrm{inst}}(t)$, see Fig. 4.2. Along $\mathbf{u}_{\mathrm{inst}}(t)$ the action is maximized. If $\mathbf{u}_{\mathrm{inst}}(t)$ is the eigenvector of the Hessian associated with the lowest (the negative) eigenvalue, such an algorithm converges to a first-order saddle point.

The dimer method [250–252] is a minimum-mode-following algorithm with the transition mode recalculated in what is called dimer rotation in each iteration. Converged rotation provides the correct $\mathbf{u}_{\mathrm{inst}}(t)$ without ever requiring the calculation of the Hessian. An improved version of the dimer rotations [253] was implemented. The limited memory version [254, 255] of the Broyden–Fletcher–Goldfarb–Shanno (BFGS) [256–259] optimizer was used for translations and rotations. Dimer rotations were optimized until $\mathbf{u}_{\mathrm{inst}}(t)$ changed by less than 5 degrees in one rotation. This required dimer rotations only at the start of an optimization run. A tighter convergence criterion for the rotations was tried but lead to an increase in the number of energy evaluations (i.e., a possible saving through fewer translations was lost by more rotation steps). An alternative to the dimer method, which also does not require the Hessian, is the Lanczos method [260, 261], which has previously been used to locate instantons [216–219, 227].

For the instanton search problem it turned out that an approximation of $\mathbf{u}_{\mathrm{inst}}(t)$ can easily be obtained

$$\mathbf{u}_{\mathrm{inst}}(t_i) \approx \mathbf{u}_{\mathrm{inst}}^{\mathrm{TM}}(t_i) = \frac{1}{2}\left(\boldsymbol{\gamma}_{\mathrm{inst}}(t_{i+1}) - \boldsymbol{\gamma}_{\mathrm{inst}}(t_{i-1})\right), \tag{4.4}$$

i.e., the transition mode is assumed to be the tangent of the instanton path. Actually, it is the tangent of only half the path and the reversed tangent of the other half. However, as given in equation (4.1), only the points on the first half of the instanton path γ_{inst} are used as active variables in the optimization. The mode $\mathbf{u}_{\text{inst}}(t)$ is recalculated after each optimization step. Calculating it only at the start and keeping it constant resulted in divergence in some cases. Using a $\mathbf{u}_{\text{inst}}$ calculated by equation (4.4) is called "tangent mode" (TM) in the following.

4.1.3 Hessian-based methods

The evaluation of the prefactor of the rate in (3.107) requires to calculate the Hessian of the potential energy surface at each image of the instanton, a computationally demanding task. In sequential cooling it can be used as a good first approximation to the Hessian of the instanton at a lower temperature, which speeds up convergence considerably.

A truncated Newton–Raphson (NR) algorithm and the partitioned-rational function optimizer (P-RFO) [262–265] were tested. NR generally converges quadratically to stationary points. However, it has the disadvantage that it converges to any stationary point, not necessarily to first-order saddle points. This is expected unproblematic since the starting structures are often already quite close to the sought-after saddle point. After convergence is achieved, the Hessian at the new instanton geometry has to be calculated. Its eigenvalue spectrum confirms whether a first-order saddle point was obtained.

The P-RFO method converges to first-order saddle points by construction. It is generally the method of choice to search for classical transition states due to its fast and reliable convergence properties.

Hessians are obtained for the individual images from previous rate calculations. With a changed temperature, they are used for the subsequent optimization. With changes in coordinates, the Hessians of the individual images are updated according to the Bofill scheme [266]. For small steps and a noisy gradient, the update of the Hessian may actually deteriorate it rather than improve it. So the Hessian is kept unmodified if the coordinates of the images change by less than a predefined threshold. Using the initial Hessian without updates results in less stable optimizations.

When the first instanton below T_{c} is calculated, a previous Hessian calculation along the full instanton path is unavailable. However, normally the Hessian of the potential energy surface is evaluated at the classical TS. Here, this Hessian is updated to the initial image positions, again using the Bofill scheme.

4.1.4   Examples and numerical tests
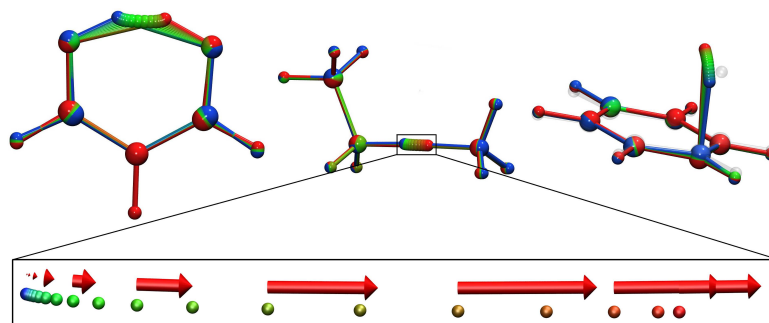
Figure 4.2: top: Instanton geometries of the three test cases: malonaldehyde, ammonium and methylamine, as well as H + benzene. Each calculated at T = 200 K with P = 20 images. Bottom: the transition mode $\mathbf{u}_{\text{inst}}(t)$ indicated as arrows on the hydrogen atom transferred between ammonium and methylamine. For clarity, only the arrows corresponding to every second image are shown. The components of $\mathbf{u}_{\text{inst}}(t)$ on the other atoms are negligibly small on the scale shown.

The performance of the four optimization algorithms was tested on three chemical systems (Fig. 4.3) at various temperature intervals. All systems were described with semiempirical methods. These pose similar challenges to the optimization algorithms, like numeric discontinuities in the potential energy surface due to incomplete self consistent field (SCF) convergence, while being orders of magnitude faster than density functional theory or post-Hartree–Fock methods.

The internal hydrogen transfer in malonaldehyde was simulated with the PM3 Hamiltonian [267]. Since the reactant and product states are chemically indistinguishable, this system has a symmetric barrier. Its tunneling behavior has recently been investigated with a variety of methods [268]. The hydrogen transfer between ammonium and methylamine, also described with PM3, is slightly asymmetric. A very asymmetric barrier is found in the addition of hydrogen to benzene. The latter is a relevant model for the formation of H_2 in space [217, 218]. Here it is described with AM1 [110]. In order to get a more realistic reactant-state geometry (van der Waals complex), an empirical dispersion correction originally designed for higher-order methods [269] was added (prefactor S_6 = 1). Energies and gradients were calculated with MNDO99 [270] interfaced to ChemShell [249] through DL-FIND. It should be emphasized that the aim of this Section is to compare the efficiency of algorithms rather than the reproduction of experimental values. The instantons of the three test cases are depicted in Fig. 4.2. Visualization was done using VMD 1.8.7 [271].
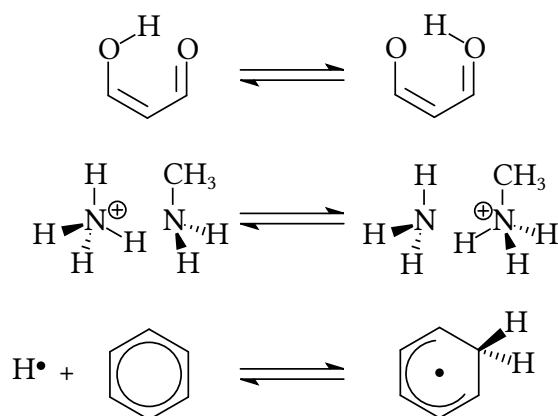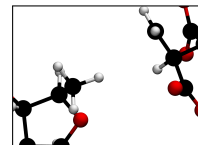
Figure 4.3: The test cases for which the algorithms to locate instantons were tested: malonaldehyde, ammonium and methylamine, and the addition of hydrogen to benzene.

Classical transition states for the three test systems were calculated with the superlinear converging version [253] of the dimer method [250] as implemented in DL-FIND [248]. Mass-scaled coordinates (mass of hydrogen being 1) were used. Convergence was considered to be achieved for the maximum component of the gradient g_{max} of $S_E/(\beta\hbar)$, being below a tolerance value (convergence criterion) of $g_{tol} = 10^{-5}$, the root-mean-square (RMS) of the gradient being below 6.66×10^{-6}, the maximum component of the predicted step being below 4×10^{-5}, the RMS of the predicted step being below 2.66×10^{-5}, and the last change in the energy of the dimer midpoint being below 2.22×10^{-8}, all values in atomic units (a.u.). The dimer direction, which in mass-scaled coordinates converges to $\boldsymbol{u}_{cl}$, was converged in each dimer iteration until it changed by less than one degree.

Hessians were calculated by finite differences of the gradients with two elongations of 2×10^{-3} (mass-scaled atomic units) in each dimension. The crossover temperature T_c was obtained according to equation (1.4), page 14, as 442.3 K, 493.9 K, and 387.2 K for malonaldehyde, ammonium and methylamine, and H + benzene, respectively.

Instanton searches were performed in mass-weighted coordinates with masses consistent with atomic units (electron mass, m_e). That is, the mass of a hydrogen atom (^{1}H) is 1837.15 m_e. This ensures that the masses in equation (3.29) and equation (4.1) really drop out. On the other hand, this scales all distances up by a factor of 42.695 ($= [\text{a.m.u.}/m_e]^{1/2}$), a.m.u. means atomic mass units, compared to mass-scaled coordinates as defined in Section 2.7 on page 32. Thus, g_{tol} has to be smaller by the same factor to achieve equivalent convergence. The convergence criterion for the instanton searches was $g_{tol} = 10^{-7}$ for the maximum component of the gradient of $S_E/(\beta\hbar)$ in mass-weighted coordinates (g_{max}). Suitable choices for g_{tol} will be discussed in
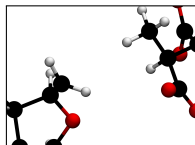
Section 4.1.5

In each case, the first instanton was found for T = 300 K by starting from the classical transition state and distributing the P = 20 images along $\boldsymbol{u}_{\mathrm{cl}}$ using Δr = 0.4 a.u. as described in Section 4.1.1. The numbers of steps needed to reach convergence are given in Table 4.1. In case of malonaldehyde, the instanton search using NR converged back to a state where all images are collapsed to the classical TS. This is obviously a stationary point, but it is not an instanton, i.e., it does not exhibit the correct number of eigenvalues being zero. Using Δr = 0.6, as defined in equation (4.3) leads to convergence to a delocalized Feynman path, the instanton.

system	TM	dimer	P-RFO	NR
Malonal.	114 (2280)	112 (6720)	337 (6726)	64 (1280)
Ammon.	103 (2060)	107 (6420)	338 (6760)	46 (920)
H+Benzene	151 (3020)	355 (19360)	137 (2740)	11 (220)

Table 4.1: Number of steps needed to reach convergence (number of energy and gradient evaluations in parentheses) for finding an instanton at T = 300 K starting from the classical TS. g_{tol} = 10^{-7}, P = 20.

Further instantons at lower temperature were optimized starting from the geometry and the Hessian of the instanton obtained with TM at 300 K. Here the convergence for different temperature intervals was tested rather than using sequential cooling. For T = 200 K an instanton search was additionally performed with more images, P = 77. Geometries and Hessians from the instanton with P = 20 and T = 300 K were interpolated by inserting three extra images in between two consecutive ones.

The number of steps needed to achieve convergence in each case, along with the number of energy and gradient evaluations needed, are given in Table 4.2. The convergence behavior is exemplarily depicted in Fig. 4.4.

In TM, P-RFO, and NR the number of energy evaluations is P times the number of optimization steps. In the dimer method, the rotations require additional energy evaluations. At least two energy and gradient calculations of the full path (dimer mid- and end-points) are required for an estimate of the rotational angle [252]. In most iterations, at least a third calculation (one dimer rotation) was required. Especially at the beginning of an optimization run, more dimer rotations may be necessary. Overall, in the dimer optimizations, the number of energy and gradient evaluations is about $3P$ times the number of optimization steps. This indicates that on average one dimer rotation step per iteration was sufficient.

Those cases for which numbers are given in Table 4.2 converged to the correct instanton within a maximum of 1000 optimization steps and 200000 energy evaluations.
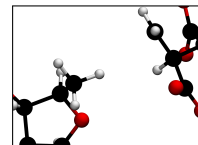
T [K]	P	TM		dimer		P-RFO		NR	
Malonaldehyde									
275	20	81	(1620)	83	(4980)	$—^c$		4	(80)
250	20	75	(1500)	79	(4740)	$—^c$		6	(120)
225	20	72	(1440)	73	(4380)	$—^c$		6	(120)
200	20	70	(1400)	68	(4160)	$—^c$		17	(340)
100	20	75	(1500)	$—^b$		293	(5860)	45	(900)
200	77	275	(21175)	268	(61908)	220	(16940)	7	(539)
Ammonium and Methylamine									
275	20	53	(1060)	66	(3760)	41	(820)	5	(100)
250	20	66	(1320)	67	(4020)	670	(13400)	8	(160)
225	20	114	(2280)	67	(4060)	$—^c$		12	(240)
200	20	111	(2220)	121	(6440)	738	(14760)	18	(360)
100	20	76	(1520)	88	(5160)	$—^c$		100	(2000)
200	77	248	(19096)	$—^c$		$—^c$		16	(1232)
H + Benzene									
275	20	127	(2540)	119	(6080)	263	(5260)	5	(100)
250	20	129	(2580)	123	(6160)	82	(1640)	6	(120)
225	20	142	(2840)	124	(6540)	133	(2660)	10	(200)
200	20	225	(4500)	104	(5480)	258	(5160)	17	(340)
100	20	$—^a$		75	(4080)	652	(13040)	44	(880)
200	77	528	(40656)	463	(106953)	$—^c$		19	(1463)

[a]: Calculation converged to a wrong stationary point
(all images in the reactant minimum).
[b]: Calculation converged to a wrong stationary point
(images interchanged during the optimization).
[c]: not converged

Table 4.2: Number of steps needed to reach convergence (g_{tol} = 10^{-7}, number of energy and gradient evaluations in parentheses) in the different methods at different temperature. All calculations started out from a converged instanton at T = 300 K, P = 20.
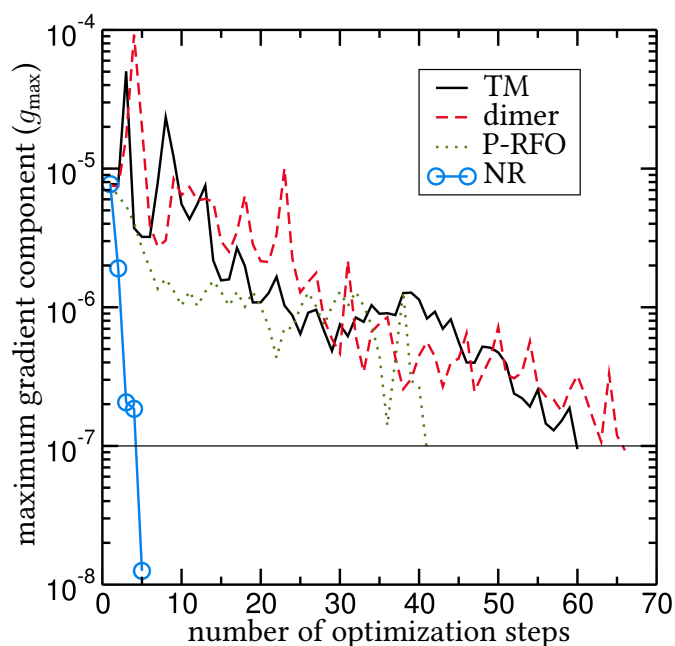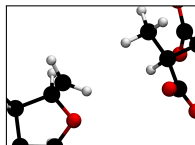
Figure 4.4: Convergence behavior of the four different optimization methods for ammonium and methylamine at T = 275 K. NR converges almost quadratically. The convergence criterion of g_{max} = g_{tol} = 10^{-7} is indicated by a thin horizontal line.

Consistency was checked by comparing S_E, S_0, and k_{inst}, as well as the eigenvalue spectrum between the results of different optimization algorithms.

For the H + benzene case, the initial instanton search for T = 300 K with the TM method resulted in a somewhat problematic starting structure for the following instanton optimizations. The reason being that for this system the potential energy surface is very flat close to the reactant minimum. This results in many of the images accumulating there. A too weak convergence criterion leads to numerical noise in the image positions and, thus, to numerical noise in $\mathbf{u}_{inst}(t)$ in the TM method. Thus, for the TM calculations of this system, the instanton at T = 300 K optimized with NR was used as the starting geometry.

The influence of P and g_{tol} on the vibrational instanton rates ($\log_{10}(k_{inst})$), ignoring changes in the rotational partition function as well as the translational partition function between the reactant and the instanton, is shown in Table 4.3. The error relative to the most accurate value obtained with P = 96 images and g_{tol} = 10^{-9} is given. A difference in the logarithm of 0.1 corresponds to a rate which is off by about 25.9%.

The ammonium and methylamine case raises a particular issue in the rate calculations. The "vibrational" mode in which the two fragments rotate with respect to each other has a very low vibrational frequency of only 11.5 cm^{-1} at the classical TS. Thus, at
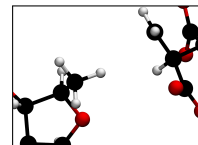
the temperature range considered, this mode would better be described as a hindered rotator than as a harmonic oscillator. Since in this work only the effect of P and g_{tol} on the rates are investigated, in Table 4.3 this mode is ignored just as the other six translational and rotational modes are ignored. If it were included as a vibrational mode in the rate calculations, then its low eigenvalue would cause numerical problems in automatically designating the real zero eigenvalues in the eigenvalue spectrum of the instanton Hessian, thereby compromising the rates. It is worth noting at this point that the additional low mode was handled well by the optimization algorithms.

			g_{tol}		
P	10^{-5}	10^{-6}	10^{-7}	10^{-8}	10^{-9}
Malonaldehyde					
20	−0.05	−0.01	−0.01	0.00	0.00
39	−0.14	−0.15	0.00	0.00	0.00
58	−0.53	−0.00	0.00	0.00	0.00
77	−0.54	−0.10	−0.01	0.00	0.00
96	−0.19	−0.10	−0.01	0.00	0.00
Ammonium and Methylamine					
20	−0.45	−0.01	−0.01	−0.01	−0.01
39	−0.20	−0.01	0.00	0.00	0.00
58	−0.18	−0.27	0.00	0.00	0.00
77	−0.19	−0.41	0.00	0.00	0.00
96	−0.20	−0.40	0.00	0.00	0.00
H + Benzene					
20	0.14	0.25	0.01	0.01	0.01
39	0.18	0.31	0.00	0.00	0.00
58	0.17	−0.05	−0.01	0.00	0.00
77	0.10	0.31	0.00	0.00	0.00
96	0.21	0.29	0.01	0.00	0.00

Table 4.3: Error in the logarithm of the rates compared to the tightest convergence criterion g_{tol} and the largest number of images for each case (T = 200 K, NR).

4.1.5 Comparison of methods for optimizations

Four different algorithms to optimize instantons were compared. The results clearly show that the NR algorithm is the most promising one among those tested. Its near-quadratic convergence results in only few optimization steps necessary to reach tight
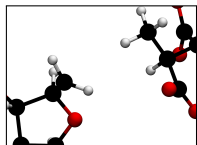
convergence criteria. The convergence behavior is also promising for applications to systems with significantly more degrees of freedom. The methods are not restricted to sequential cooling. Using analytic potentials, convergence was achieved even with the TM method for a straight-line path as starting guess (data not shown). In these cases, a Hessian from previous calculations is not easily available. The results also point out some problems which can be expected in instanton optimizations. These will now be addressed.

It is clear from Table 4.2 that the P-RFO fails to converge in a number of cases. As a fixed-point iteration scheme, it sometimes reaches a periodic cycle rather than actually converging to the desired stationary point. This can be seen by plotting the maximum gradient component against the number of iterations, see Fig. 4.5. In all cases except $T = 100$ K, a cycle is reached rather than the gradient becoming smaller and smaller. This is caused by a strong dependence of the P-RFO algorithm on an accurate Hessian. The Hessians of the individual images are updated rather than recalculating it, which inevitably leads to inaccuracies. Using the Powell update [272] or no update scheme at all leads to an even worse convergence (data not shown). Recalculating the Hessian in each step would of course be prohibitively expensive. Since the other algorithms, in particular NR, generally converge faster and more reliably, instanton optimization with P-RFO is not recommended.
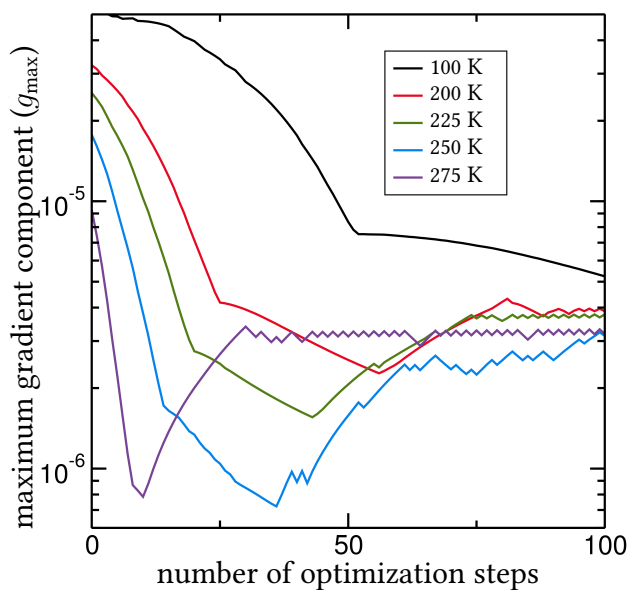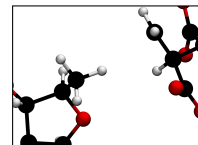

Figure 4.5: Convergence failures of the P-RFO method for malonaldehyde at different temperatures.

NR intrinsically converges to any stationary point, not necessarily first-order saddle

points. While in all results shown here, it actually converged to the sought-after instanton; runs in which NR converged to different states were observed as well. Especially at high temperature, close to T_c, there seems to be a danger of the whole path collapsing to the classical TS. This was observed here when starting from the classical TS and searching for an instanton at T = 300 K in the case of malonaldehyde. A larger Δr for spreading the images in the initial path resolved that problem.

Convergence to a collapsed path can easily be detected during an optimization run by a steadily decreasing value of S_0. According to equation (4.5), S_0 vanishes for any collapsed path. In cases where NR converges to a different stationary point than the instanton, the TM algorithm is recommended as a backup solution.

In two cases, H + benzene at T = 100 K with the TM method and the dimer method, the calculations actually converged to a path collapsed to the reactant state, see Table 4.2. While this is also a stationary point of S_E, it obviously is no instanton. These cases are less worrying, however, because the direct change from T = 300 K (starting point) to T = 100 K is rather extreme. Smaller temperature intervals are recommended. Even at this large temperature interval, however, NR converged well.

Convergence criteria are applied in the present implementation in the same unit system as the optimization being done, i.e., in mass-weighted coordinates with the mass of an electron as unit. To assess which g_{tol} is necessary to obtain the tunneling rate with a given accuracy, the data presented in Table 4.3 were calculated. A criterion of $g_{tol} = 10^{-7}$ seems sufficient to ensure convergence of the logarithm (basis 10) of the rate to within 0.01. For the systems and the temperature (T = 200 K) studied here, P = 20 images are obviously sufficient, as the rate (at sufficiently small g_{tol}) is independent of the number of images. At lower temperature, however, the images become less equally spaced in configuration space. More and more images accumulate close to the minima. In these cases, more images are required to achieve converged rates as found in agreement with previous work [216]. It can also be seen from Table 4.3 that with more and more images, the rate becomes more sensitive to g_{tol}. At 20 images, the rate is already converged if $g_{tol} = 10^{-6}$ is used for malonaldehyde and ammonium and methylamine.

The remaining error at nonperfect convergence can be due to three sources, $k_{inst} = k_{S_0} \cdot k_{harm} \cdot k_{S_E}$: S_0 (entering the rate as $k_{S_0} = \sqrt{S_0/(2\pi\hbar)}$), S_E (entering the rate as $k_{S_E} = \exp(-S_E/\hbar)$), and all terms covering the quadratic expansion of the potential around the stationary paths: $k_{harm} = \frac{1}{Q_{RS}} \frac{J+1}{\beta\hbar} \frac{1}{\sqrt{|\prod_i' \lambda_i|}}$. The latter causes the largest effect. This is somewhat surprising as S_E enters the rate exponentially. The eigenvalues λ_i of the Hessian only enter under the square root. However, numerical noise in the Hessian affects most or all eigenvalues, which together apparently make a noticeable contribution. Thus, it seems important to calculate the Hessians of the images with high accuracy.

Finally, a property of the instanton path itself rather than the optimization of it is
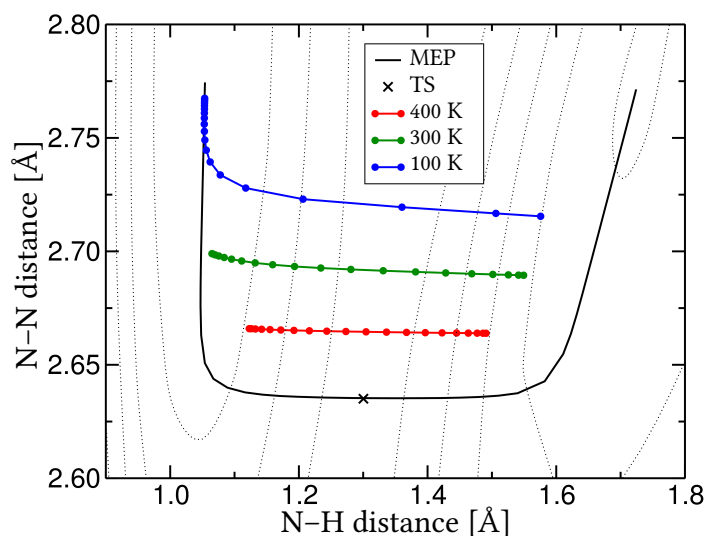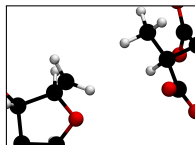
Figure 4.6: The potential energy surface, the MEP, and instantons at three temperatures for the case of ammonium and methylamine, projected onto a plane of two geometric coordinates. The corner cutting shortens the tunneling path by keeping the heavy nitrogen atoms fixed and focusing the movement onto the light hydrogen atom.

discussed, namely corner cutting. Tunneling is more efficient the thinner the barrier is. The relevant width of the barrier is the width in mass-weighted (or any iso-inertial) coordinates. Thus, movement of heavy atoms reduces the tunneling rate more than movement of light atoms. This results in an instanton path which, in many cases, deviates significantly from the MEP, an effect known as corner cutting [112]. An example is demonstrated in Fig. 4.6. The figure shows the N–N distance plotted against one N–H distance of the ammonium and methylamine system used in this work. All numbers are of course calculated with semiempirical methods of limited accuracy. However, the qualitative conclusions also hold with more accurate methods. On the MEP, the nitrogen atoms approach each other significantly (shortening of the N–N distance by 0.14 Å) before the hydrogen atom is transferred. The movement of the heavy atoms is more and more avoided the more important tunneling becomes. At T = 100 K the N–N distance decreases by only 0.06 Å. This shortening of the effective tunneling path comes at the expense of a higher energy of some images along the instanton compared to the classical TS. A similar corner cutting is observed for the instantons in glutamate mutase, see Section 5.3. However, it still results in a larger tunneling rate than tunneling along the MEP.
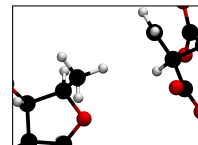
4.2 Instanton tunneling rate calculations

Optimizing an instanton corresponds to finding a first-order saddle point in the space spanned by all coordinates of all images. Efficient optimizers with near-quadratic convergence behavior are available [108], see Sections 4.1.2 and 4.1.2. However, there are several challenges to calculate rates based on the instanton path γ_{inst} located with the methods discussed in the previous section. Two of them are:

1. The temperature dependence of the distribution of images along γ_{inst} (accumulation at the ends of the path), when using an equidistant discretization, see the next paragraph. Calculations of rates become more and more computationally demanding the lower the temperature, as more images are required to calculate rates.

2. The expensive Hessian calculations of $V(\boldsymbol{x}_j)$ at each discretization point (image) $j = 1, \ldots, (J+1)/2$ are challenging for rate calculations in large systems such as enzymes.

Aims of the following section are to improve the efficiency of the instanton rate calculations and to provide a procedure for fast scans of KIEs for different combinations of isotopes.

The temperature dependence of γ_{inst}

In general, the instanton path γ_{inst} shows the following temperature dependence: at temperatures above a crossover temperature T_{c}, defined in (1.4) on page 14, the instanton collapses to, $\boldsymbol{x}_{\text{cl}}$, the saddle point on the potential energy surface [71]. The path spreads out below T_{c}. Then it generally does not pass through the saddle point, $\boldsymbol{x}_{\text{cl}}$, any more. At intermediate temperature below T_{c} the path and the rate vary with T. The path becomes longer and more delocalized, the lower the temperature T becomes. When using an equidistant discretization, $h_j = \beta\hbar/(J+1)$ for all $j = 1, \ldots, J+1$, the distribution of the images (discretization points) along the path changes with T. They accumulate at the ends of the paths. A pictorial understanding for the accumulation of images for a constant step-size in t can be drawn in two ways.

1. The equation (3.7) describes images connected by springs optimized in the potential V, see also Fig. 3.2. The spring constant between the images j and $j-1$ is proportional to $1/h_j^2$. If all the spring constants are equal ($h_j = (\beta\hbar)/(J+1)$ for all j), it is clear that the springs are more stretched in the steep region of the potential (around the barrier) than in the flat region. For low temperature,
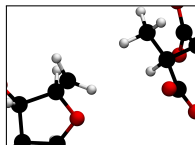
the effective force constants become particularly weak leading to a pronounced effect which is a further spread to accommodate a lower potential energy.

2. The Euclidean action given in (2.21) describes a system in the upside-down potential $-V$ moving according to classical mechanics, see Fig. 2.4. In this interpretation t represents the time and $\beta\hbar$ the period of the closed path (periodic orbit). At low temperature (high β) such a orbit starts close to a stationary point of V, a maximum of $-V$, the reactant state. Close to this maximum the particle moves slowly. In steeper regions of $-V$ it is accelerated, having the largest velocity at the minimum of $-V$ along the path (the barrier) and decelerates as it moves up $-V$ towards the second turning point. The velocity of the particle $(d\gamma_{\text{inst}}(t)/dt)$ directly corresponds to the distance between the images if they are taken at constant intervals in t.

In Fig. 4.7 an example is depicted showing position and energy of the images of a typical instanton at low temperature. 50% of the images end up in only 2% of the length of the path. These numbers get more extreme at even lower temperature. Symmetric barriers lead to accumulations at both ends of the path. Therefore, the region around the top of the barrier is barely sampled, see Fig. 4.7. However, it is the region at the
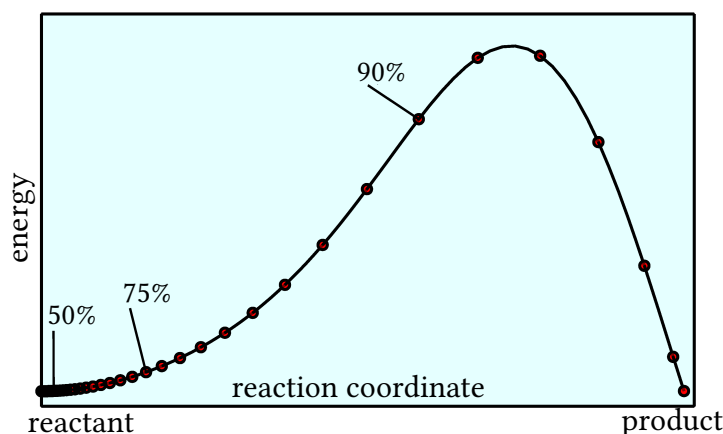
Figure 4.7: Accumulation of images near the end(s) of the instanton path of the Müller–Brown potential at $T = 0.2\,T_{\text{c}}$ for $P = 300$ images (every fifth image is shown by a ring). Percentages of images left of the indicated images are given.

top of the barrier where the kinetic energy and potential energy change most. Thus, a sufficient sampling is required there and along the whole path, for converged rates.

Summarizing, due to the path becoming longer while lowering the temperature more images have to be used to obtain converged rates. Additionally, most of these images accumulate at low temperature close to the end of the instanton path (the one with the
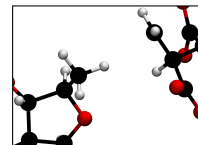
smaller slope of the potential energies surface along the path). Thus, calculations of rates become more and more computationally demanding the lower the temperature, as more images are required to calculate rates.

4.2.1 The fixed-path approximation for the calculation of KIEs

To obtain estimates of KIEs without significant additional computational effort a "fixed-path approximation" (FPA) can be employed [222]. The FPA allows to approximate the instanton path at a given set of atomic masses by the instanton path at the reference masses (generally, the light isotopes), while fixing $\tilde{x}_j$ for all $j = 1, \ldots, J + 1$ and, thus, S_{pot} and the V matrices (part of the Hessian matrix M), but adjusting S_0, λ_l^{RS}, and λ_l^{inst} to the correct masses. The masses would change $\boldsymbol{\gamma}_{\text{inst}}(t_j)$ even though x_j remain fixed. Note that all S_0, λ_l^{RS}, and λ_l^{inst} do depend on the path (i.e., on x_j) as well as on the masses. So, also for these quantities, skipping the re-optimization of FPA while changing the mass is an approximation. Since x_j is kept fixed the recalculation of any potential energies, gradients or V-Hessians, i.e. any quantities which consume significant CPU time, is unnecessary to obtain a KIE. Only the analysis changes and the Hessian has to be diagonalized again. The validity of the FPA has been shown in [222]. Thus, approximations to the KIEs can be calculated with hardly any computational effort, which allows a fast scan of the KIEs for different combinations of isotopes.

4.2.2 Adaptive integration grids: numerical tests

In this section the variable step-size discretization on a collapsed path will be given. Then follows a discussion on how to choose the step-size in order to obtain a roughly uniform distribution of the images in Euclidean space. A short comment on improvements by using updated Hessians is given as well. Finally, the results of testing with different systems are summarized.

By introducing the flexibility of variable step-size discretization of the integral over the instanton path γ_{inst}, instead of a constant step-size the accumulation of images at the turning points of the path can be avoided. Therefore, fewer images are required for an accurate sampling of the path and accurate rates.

A possible approach towards a more uniform distribution of the images based on an extension of the nudged-elastic band method [273] has been derived recently [274, 275]. It requires to set the tunneling energy prior to the calculation. Generally in the application of instanton theory, and also in this work, the temperature is set rather than the tunneling energy. In the following, adaptive step-size of integration will be used to avoid the accumulation of images along the instanton path which will allow to calculate rates with significantly fewer images. The method can be continuously
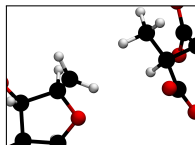
transformed back to the traditional instanton theory with constant step-size, see [109]. The rate will be calculated according to equation (3.107).

Variable step-size discretization on the collapsed path

The variable step-size discretization looks slightly different for the collapsed path than in Chapter 3, for more details see [109]. Another trick for a computable form of the determinant of the second variation of the Euclidean action is to split S_E into its two components, $S_E = S_0/2 + S_{pot}$, see (2.46). The kinetic energy part S_0 is twice the part of the Euclidean action depending on the length of the path:

$$S_0 = \sum_{j=1}^{J+1} \frac{|\gamma_{inst}(t_j) - \gamma_{inst}(t_{j-1})|^2}{h_j} = 2 \sum_{j=2}^{P} \frac{|\gamma_{inst}(t_j) - \gamma_{inst}(t_{j-1})|^2}{h_j}. \tag{4.5}$$

The second equality exploits the fact that each converged instanton path is reduced to one line traversed backwards and forwards. The discretizations of S_0 and S_{pot} into $J+1$ intervals in t can in principle be chosen independently of each other. Here $V(\gamma_{inst}(t_j))$ is chosen to be equally assigned to each neighboring interval.

$$S_{pot} = \sum_{j=1}^{J+1} \frac{h_j + h_{j+1}}{2} V(\gamma_{inst}(t_j)) = \sum_{j=1}^{P}(h_j + h_{j+1})V(\gamma_{inst}(t_j)). \tag{4.6}$$

Finding an instanton path by optimization techniques requires gradients and Hessians of the Euclidean action. The discrete expressions (4.5) and (4.6) can be used to derive the gradient and the Hessian of S_E with respect to the coordinates of the atoms of each image. The result is slightly different from the formulation of the gradients and Hessians presented in Section 3.2.1. For more details see [109]. The variable step-size formulation of the gradients and the Hessians of the Euclidean action can be calculated similarly to the traditional way with constant step size.

Choice of the step-size to obtain a more uniform distribution of the images

By choosing the h_j individually for each interval of the discretization the distribution of images (discretization points) along the instanton path $\gamma_{inst}(t)$ are controlled. There is some freedom for the appropriate choice of h_j. In the following two possibilities to choose the step-size h_j will be presented. These two choices lead to more or less uniform distributions of discretization points along the path.

As the discretization is in $t \in [0, \beta\hbar]$, the condition

$$\sum_{j=1}^{J+1} h_j = \beta\hbar, \quad h_j > 0 \tag{4.7}$$
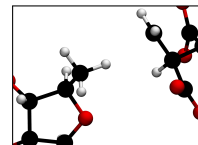
has to hold. With the energy conservation of the system moving on the upside-down potential follows, see [109], one choice for the step-size

$$h_j = \frac{|\boldsymbol{x}_j - \boldsymbol{x}_{j-1}|}{\sqrt{2(V_{[j-1,j]} - V_b)}} \tag{4.8}$$

with V_b being the potential at the turning points of the instanton path, the tunneling energy. And $V_{[j-1,j]}$ indicates a value of the potential in the interval $[t_{j-1}, t_j]$ chosen for $V(t)$. Additionally, $|\boldsymbol{x}_j - \boldsymbol{x}_{j-1}|$ is chosen such that the instanton path has a total length of $\beta\hbar$. For possible choices of V_b and $V_{[j-1,j]}$, e.g., via sequential cooling, see [109]. At low temperature the energy V_b can for example be approximated by its lower bound V_{RS} as there is no need for an exactly equal distribution of images in practical calculations.

Instead of the approximately uniform distribution of images obtained that way by equation (4.8), the images can also be forced to remain exactly uniformly distributed. Start with an equally-spaced initial path and calculate $V'(\boldsymbol{x}_j)$ for all $j = 1, \ldots, P$. The result is then inserted in the formula for the gradient of the action. Setting the gradient equal to zero leads to a nonlinear system of equations for the h_j. These h_j are then used for the instanton path optimizations. An example of the truly uniform distribution of images obtained by that method is depicted in Fig. 4.8 (lower panel) for $T = 0.3\, T_c$. The other paths at the lower panel are calculated based on equation (4.8).

However, the truly equally-spaced discretization leads to a less accurate rate, as the resulting h_j at the end points of the path becomes very large compared to the other step-sizes. This significantly deteriorates the rates and leads to worse results than equation (4.8). Both cases can gradually be converted back to the traditional constant step-size if required, which allows to choose other combinations.

The choice of h_j influences the rate of convergence with the number discretization points, but not the final converged value, see [109]. Independent of the choice of the h_j, as long as they are chosen in an appropriate range, the rates obtained in the limit of many images will be the same.

Updated Hessians for rate calculations

The main aim of this section is to make instanton optimization faster and more efficient also for larger systems by demanding fewer energy and gradient calculations. In the following, the reduction of accuracy by saving explicit evaluations of the Hessians $V''(\boldsymbol{x}_j)$ of the individual images $\boldsymbol{x}_j$, $j = 1, \ldots, P$ will be discussed briefly. These Hessians are blocks of the matrix V, see page 55. They are all used (i) in the Newton–Raphson algorithm to locate instanton paths by optimizations and (ii) to calculate the instanton rate, equation (3.107).
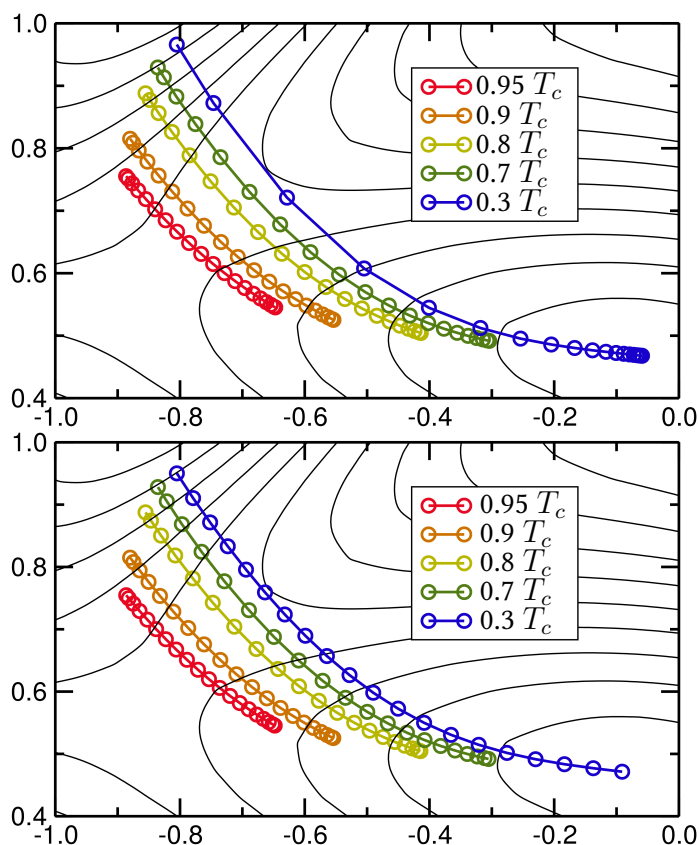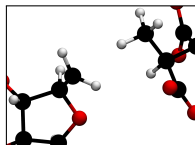
Figure 4.8: Comparison of the traditional discretization with a constant step-size in t (top) and a variable step-size (bottom). Instanton geometries for $P = 20$ images of the Müller–Brown potential are shown. At low temperature (blue curves) images accumulate at the minimum (bottom right corner of each graph) when using a constant step-size, while they keep uniformly distributed with a variable step-size.

After changing the coordinates at one image x_j, the Hessian $V''(x_j)$ can be recalculated or approximated by an update based on the previous Hessian and the gradients at both points [266, 272, 276]. Calculations of potential energies by quantum chemical methods result in computationally expensive Hessians calculations. In that case updating strategies are valuable alternatives. As discussed in Sections 4.1.3 and 4.1.5 the Hessians $V''(x_j)$ are updated during the optimization. However, for rate calculations the Hessians are recalculated to obtain a higher accuracy in the rates. Updated Hessians are certainly less accurate than recalculated ones. However, especially for a QM/MM energy expression, where analytical Hessians are computationally expensive, if available at all, this approximation is advantageous.

In rates estimated from updated Hessians the eigenvalue λ_0 corresponding to the zero-

mode $\mathbf{u}_0(t)$ was frequently found to be significantly different from zero. Therefore, it was problematic to choose which eigenvalues to ignore in the second product of equation (3.107). On the other hand, the eigenvector corresponding to the zero-mode $\mathbf{u}_0$ is just the tangent to the instanton path
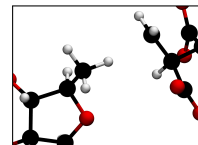
$$\mathbf{u}_0(t) = \frac{d\gamma_{\mathrm{inst}}(t)}{dt} \tag{4.9}$$

which can be approximated by

$$\mathbf{u}_0(t_j) \approx \mathbf{u}_{\mathrm{approx}}(t_j) = \frac{\gamma_{\mathrm{inst}}(t_{j+1}) - \gamma_{\mathrm{inst}}(t_{j-1})}{h_j + h_{j+1}}, \qquad \text{for all } j = 1, \dots, P. \tag{4.10}$$

Thus, the eigenvalue of the matrix M that corresponds to the eigenvector with the largest overlap with $\mathbf{u}_{\mathrm{approx}}$ is ignored in equation (3.107). In addition, the N_0 eigenvectors corresponding to rotation and translation have to be ignored in case of molecules as described in Section 3.3. That procedure lead to improved instanton rates. See [109] for more details. There the results of numerical tests

(a) of the analytic two-dimensional Müller–Brown potential,

(b) of malonaldehyde described by PM3 (same parameters as in Section 4.1.4), and

(c) of the hydrogen addition to benzene described by Density Functional Theory (DFT) can be found as well.

Testing the approaches described above in this Section with (a) to (c) results in a reduction of the computational efforts by more than one order of magnitude in computational time. This benefit is due to three reasons:

1. the improved geometry optimization algorithm (NR vs. mode-following),

2. the reduced number of images (discretization points) due to the variable step-size,

3. the updating strategies for the Hessians instead of their explicit re-evaluation.

Only the third reason leads to a loss in accuracy. The first two reasons save more than a factor of 12 in the number of energy and gradient evaluations in one case [109]. While the computational costs for an analytic Hessian calculation compared to a gradient calculation depends on the details of the implementation and can only with difficulties be compared, the new algorithms result in a speedup of about a factor of 20. The numerical tests of the variable step-size instanton optimization and rate calculation, formulated in Chapter 3, showed that the accumulation of images at the ends of
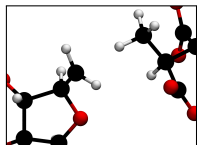
the instanton path observed with the traditional constant step-size discretization are avoided. Additionally, all benefits of the instanton method are retained. For example, the problem of locating the instanton as a saddle point in the space of closed Feynman paths can still be solved with quadratic convergence.
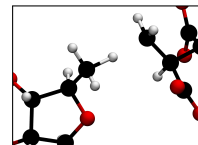
CHAPTER

5

THE REACTION MECHANISM OF THE
ENZYME GLUTAMATE MUTASE

The enzyme glutamate mutase catalyses the reversible interconversion of Glu to MA, as shown in the introduction, see Section 1.1. From experiment, it is unclear which steps is rate-limiting. While some studies observed large ^{1}H/^{2}H KIEs [21–23], which indicate the hydrogen-transfer steps to be rate-limiting, more recent work found smaller KIEs and concludes that neither of the hydrogen-transfer steps is cleanly rate-limiting [24, 25]. Since the measured primary deuterium KIEs range from 4.1 to 35 at 283 K the importance of tunneling during the reaction is unclear, see Sections 1.1.1 and 1.1.2.

To simulate enzymatic reactions the combination of quantum chemical approaches with empiric force fields (QM/MM) [277, 278], reviewed in [249, 279–282], is a promising approach. All previous QM/MM calculations performed on GM considered only the activating, but not rate-limiting, Co–C bond cleavage [14–16]. The dissociation enthalpy for the homolytic cleavage was experimentally estimated in methylmalonyl-CoA mutase, a similar coenzyme B$_{12}$-dependent enzyme, to be about 59 kJ mol^{-1} [283]. Calculations investigating the rearrangement reaction have been done in gas-phase models considering different protonation states [17, 284]. Several reaction mechanisms

have been proposed for GM, e.g., removal of a hydride ion or a not very likely addition–elimination pathway [17]. Experimental and the computational results support the fragmentation–recombination pathway for GM. The following investigations emphasize on the fragmentation–recombination mechanism proposed based on experimental data [18, 19].

The Chapter is organized as follows: in Section 5.1 methodological and technical details for QM/MM simulations of GM, the level of theory, and the method employed to study tunneling in the enzyme based on rates and KIEs are given. In Section 5.2 the computational results concerning the energetics of the rearrangement reaction catalyzed by the enzyme are discussed including a comparison of energies obtained with different functionals used for DFT calculations and coupled cluster. Then a detailed discussion of the enzyme environment and its influence on the reaction follows. Emphasis is given on individual amino acids and their contribution to a productive catalysis. Overall, insights into the reaction mechanism on the level of atoms and electrons will be presented. In Section 5.3 rates based on coupled cluster energy calculations, primary and secondary KIEs will be presented and compared to experimental results. Instanton theory is applicable with any kind of potential energy surface. In the previous Chapter 4 it was be applied to test systems with different methods (for example semiempirical methods, DFT). In this chapter potential energies obtained on the fly from QM/MM calculations will be used to investigate the changes in the active center of GM during the process of tunneling. All atoms included in the optimization of the instanton tunneling path are allowed to tunnel. Thus, the movement of more than one atom is quantized. The relevance of tunneling in GM will be discussed.

5.1   Methods and technical details

5.1.1   System preparation for QM/MM simulations

The enzyme GM from *Clostridium cochlearium* in complex with AdoCbl and substrate was modeled based on X-ray diffraction results at 1.9 Å resolution (PDB entry 1I9C) [6]. The X-ray data include the whole tetramer with two $\sigma\varepsilon$-subunits, and the substrates Glu as well as MA. The enzyme consists of two identical subunits without any covalent connections between them. The reactive parts are remote from each other. Experimental investigations carried out with a mutant containing only one $\sigma\varepsilon$-subunit also show independence of the subunits [285]. Thus, only one $\sigma\varepsilon$-subunit was simulated.

After protonation and solvatization (both with VMD [271] version 1.8.7) in a cubic box of TIP3P [286] water molecules, see Fig. 5.1, the system was extensively equilibrated on an MM-only level. This allows all cavities within the enzyme to be filled with
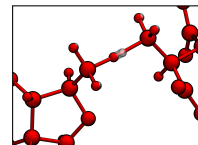
water. Na$^+$ and Cl$^-$ ions (each about 0.05 mol L^{-1}) were added to ensure an overall charge neutrality of the system. The initial size of the rectangular solvent box was 90.5 Å × 80.5 Å × 95 Å.
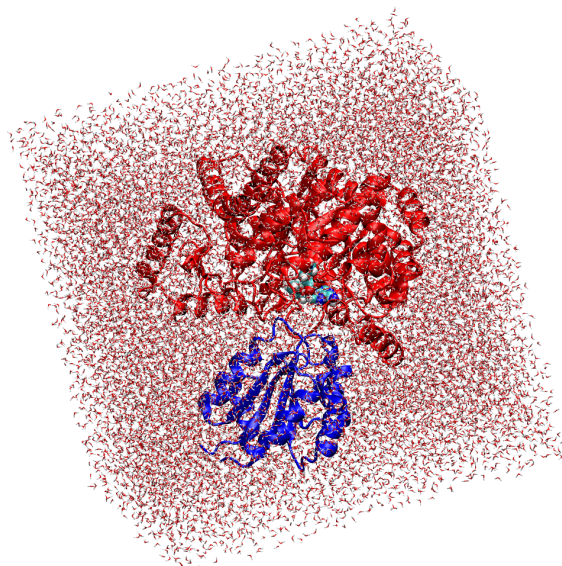
Figure 5.1: The protein GM in a cubic solvent box of water molecules and ions: σ-subunit (blue) and ε-subunit (red).

In the following classical molecular dynamics (MD) simulations with periodic boundary conditions were performed using the CHARMM22 [287–290] force field in the code NAMD, version 2.6 [291]. The Langevin piston Nosé–Hoover method [292, 293] was used to keep the system at 300 K and 1 bar. The time step was 2 fs. Note that the temperature of the MD simulations are independent of the temperature used in the rate calculations later on where optimized geomtries will be used to calculate QM/MM potential energies. In the equilibration phase, constraints followed by position restraints by springs were applied to the whole protein, the cofactor, and the substrate. All water molecules, also those contained in the crystal structure, were unrestrained. The volume was kept constant in the equilibration. At first the solute atoms were completely frozen for 2000 conjugate gradient optimization steps and 0.1 ns of MD simulation. Next, restraints with a force constant of 5.0 kcal mol^{-1} Å^{-2} were applied to the solute again for 2000 optimization steps and 0.1 ns of MD simulation. This was followed by 0.1 ns of MD simulation each with force constants of 2.0 kcal mol^{-1} Å^{-2} and 0.1 kcal mol^{-1} Å^{-2} to gradually relax the protein with the cofactor and the substrate. In one run the binding pocket of the enzyme contained the Glu substrate (50 ns of sampling). Another run was performed for 26 ns for GM containing the product MA in the binding pocket.
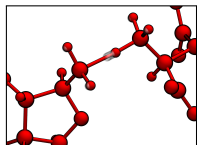
For the MD run with Glu in the binding pocket, the protein in solvent comprised 63 411 atoms, including 17 899 water molecules and 50 Na$^+$ and Cl$^-$ ions. Snapshots were taken from that MD run after 9 ns, 20 ns, 41 ns, 32 ns, 13 ns, and 25 ns of simulation as initial structures for the following QM/MM calculations. They are labeled as SN-Glu-1 to SN-Glu-6. Note that these snapshots were not taken sequentially from the MD trajectory. The snapshots were chosen to cover a range of different C–C-distances (from 3.2 Å to 5.12 Å) for the hydrogen-transfer reaction between the substrate and the cofactor. Aditionally, three snapshots were taken from a separate MD simulation run with MA in the binding pocket (SN-MA-1 to SN-MA-3) after 6 ns, 11 ns, and 15 ns. These snapshots served as starting configurations for the following QM/MM geometry optimizations and transition state searches. Force field parameters for nonstandard residues (cobalamin and MA) were derived by analogy to similar parameterized residues, see Supporting Information of [20]. For the adenosyl part of coenzyme B$_{12}$, which is completely contained in the QM part, the standard adenosyl parameters with the phosphate group deleted were used.
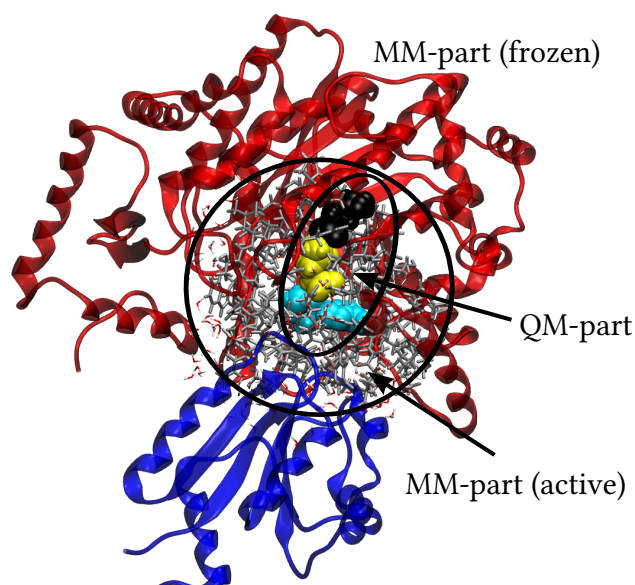
Figure 5.2: The three different regions for QM/MM simulations with GM: in the outer part the frozen MM-region, then the active MM-region, and in the inner part the QM-region consisting of Ado (cyan), the Glu substrate (yellow), and part of Glu 171 (black).

To prepare the snapshots for simulation, all nonprotein atoms having a distance greater than 17 Å from the oxygen atom in the ribose ring of Ado were deleted from the model. This procedure removed the box of water except molecules in the inner part of the enzyme. During the calculations all residues that were entirely outside a
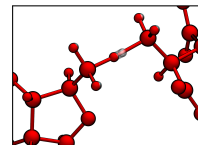
range of 8 Å from any substrate or Ado atom were frozen, see Fig. 5.2. Additionally, all atoms of the adenosyl tail of cobalamin further away than 12 Å from Ado were frozen. That procedure resulted in 96 to 135 water molecules included in the different snapshots. Thus, all residues belonging to the first and the second solvation shells of the environment of the active center were optimized. Additionally, in all snapshots except SN-Glu-1, 14 charged glutamate or aspartate residues on the surface of the protein were protonated to obtain a neutral system. All snapshots comprised about 10,200 atoms in the end. They contained water, protein, cofactor, substrate but no Na^+ and Cl^- ions from the solvatization.

5.1.2 Biochemical multiscale simulations: QM/MM

The chemical steps of the reaction mechanism were investigated using QM/MM [277, 278] geometry optimizations. Moreover to scrutinize the role of tunneling during the catalysis QM/MM instanton geometry optimizations were used, see Chapters 3 and 4. The chemically active center was treated with DFT [294, 295] or with coupled cluster, combined with the environment described by force field calculations. The QM/MM (potential energy) calculations were done with ChemShell [249], using electrostatic embedding, where the MM charges of the force field polarize the QM part. Covalent bonds between the QM part and the MM part were truncated on the QM side by hydrogen link atoms. The charge-shift scheme [249, 296] was employed in order to avoid overpolarization of the QM density near the link. The CHARMM22 force field [287–290] in DL_POLY [297] as included in ChemShell [249] was used for the MM part.

Unless noted otherwise, the QM-region contained the substrate, the Ado radical as part of the cofactor, and the side chain of Glu 171, see Fig. 5.3. The QM part carries a charge of −2 and a spin multiplicity of 2. The truncation of the QM subsystem was done by cutting through the $C\beta$–$C\gamma$ bond of Glu 171. This resulted in a total of 54 QM atoms plus one hydrogen link atom. The choice of the truncation is well justified because only one single bond has been cut, and the distance between the cut and the chemically active atoms is three bonds at the minimum. Any possible charge transfer between the regions designated as QM and MM regions is neglected. In some calculations Glu 171 was left out (48 atoms) or histidine (His) 150 was added (74 atoms) to the QM part to investigate specific effects. The homolytic cleavage in the cofactor is fast compared to the hydrogen-transfer between Ado and Glu substrate; this Co–C bond homolytic cleavage is not rate limiting [14–16]. Thus, cobalamin can be excluded from the QM part.
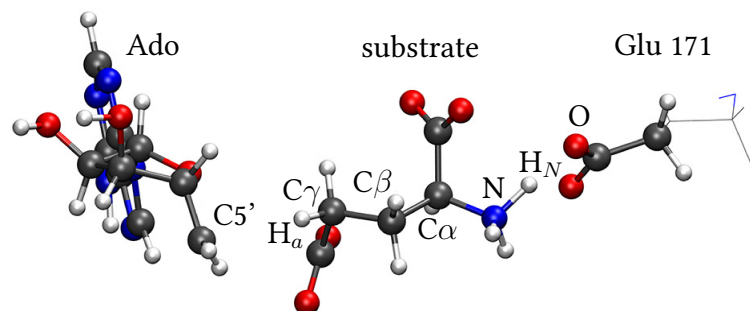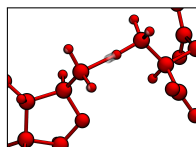
Figure 5.3: The QM region (in ball and stick representation) containing Ado (left), Glu substrate (middle), and the side chain of Glu 171 (right). Carbon is shown in gray, oxygen in red, hydrogen in white, and nitrogen in blue. Atoms mentioned in the text are labeled.

5.1.3   Quantum mechanical methods

The QM region was described with DFT with BP86 [298–302], BP86-D [303], and B3LYP [304] functionals as implemented in TURBOMOLE version 6.0.2 [305]. Density fitting (resolution of the identity [306]) was used throughout. Additionally, the energies on the BP86-optimized geometry were calculated with the M06 functional [307] in NWChem version 5.1.1 [308, 309]. After a comparison of the def2-SVP [310], cc-pVDZ [311], def2-TZVP [312], def2-TZVPP [312], cc-pVTZ [311], aug-cc-pVTZ [311], cc-pVQZ [311], and cc-pV5Z [311] basis sets, all computations were performed with the cc-pVTZ basis set, as larger basis sets led to insignificant changes in the energies. For cc-pVTZ calculations the number of basis functions was 1282. Of the three functionals used, BP86, B3LYP, and M06, the latter can be expected to provide the most accurate results [313]. Additionally, the relative M06 energies were validated against local Coupled Cluster (CC) reference calculations: the energies on the sd-LUCCSD(T) (Local Unrestricted open-shell CC with Single and Double excitations and perturbative treatment of the Triple excitations) level [314, 315] with the aug-cc-pVTZ [311] basis set were calculated. The sd-localization scheme, in which singly occupied and doubly occupied orbital space are treated separately, was used to avoid a mixing of the occupied RHF (Restricted open-shell Hartree Fock) orbital subspaces. The calculations were performed with Molpro version 2010.2 [316]. In local correlation methods a domain error is introduced by restricting the virtual space to the individual localized molecular orbitals. The domain error was determined by the difference between the results for sd-LRMP2 (Local spin Restricted open-shell 2nd order Møller–Plesset perturbation theory) [314, 315] and RMP2 (canonical spin Restricted open-shell 2nd order Møller–Plesset perturbation theory) [317] to the LUCCSD(T) results, see Table 5.1.
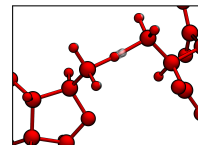
Structure	HF	RMP2	sd-LRMP2	Dom. err.
A	0.00	0.00	0.00	0.00
TS-**AB**	42.20	21.50	19.59	−1.91
B	3.37	2.25	0.10	−2.15
TS-**BC**	30.97	20.81	16.98	−3.83
C	5.90	8.50	5.03	−3.47
TS-**CD**	32.99	18.07	15.25	−2.82
D	5.65	5.39	2.67	−2.71
TS-**DE**	47.93	24.79	22.17	−2.62
E	2.81	3.39	2.18	−1.21

Table 5.1: Relative QM energies (in kcal/mol) obtained with Hartree Fock (HF), RMP2, and sd-LRMP2. The deviations of sd-LRMP2 from RMP2 values are given as domain error, numbers from [314].

Dispersion correction

Table 5.2 compares the empirical dispersion-corrected functional BP86-D to the usual BP86 functional. They differ, apart from **D** and **E**, by less than 3 kJ mol^{-1}. Thus, dispersion within the QM part yields an insignificant influence on the energies.

	BP86-D	BP86	difference
A	0.0	0.0	0.0
TS-**AB**	44.3	44.3	0.0
B	−18.0	−18.9	−0.9
TS-**BC**	64.3	65.6	1.3
C	45.0	42.0	−3.0
TS-**CD**	71.5	69.6	−1.9
D	8.9	1.4	−7.5
TS-**DE**	68.3	64.8	−3.5
E	10.3	4.3	−6.0

Table 5.2: Empiric dispersion corrected BP86-D versus BP86, both with a def2-SVP basis set (relative energies in kJ mol^{-1}, QM-region with 48 atoms).

Basis set comparison

Convergence of the results with respect to the basis set was tested by comparing energy minima obtained with larger basis sets. To test the basis set convergence, energies at
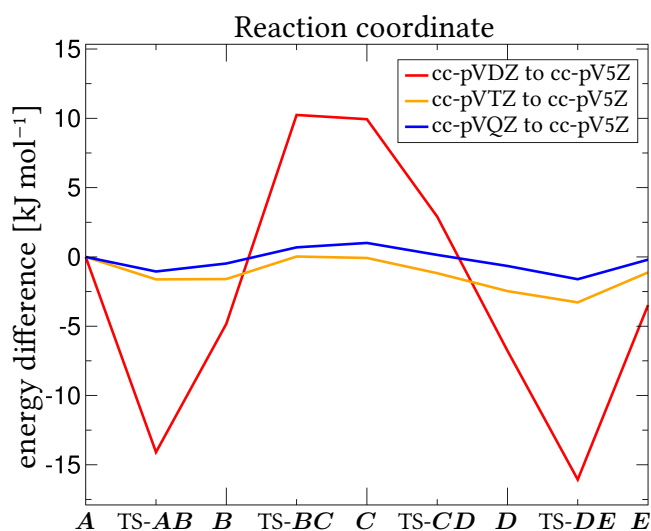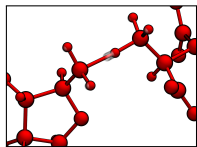
Figure 5.4: Effect of the basis set size: cc-pVDZ, cc-pVTZ, cc-pVQZ compared to cc-pV5Z (QM-region with 48 atoms).
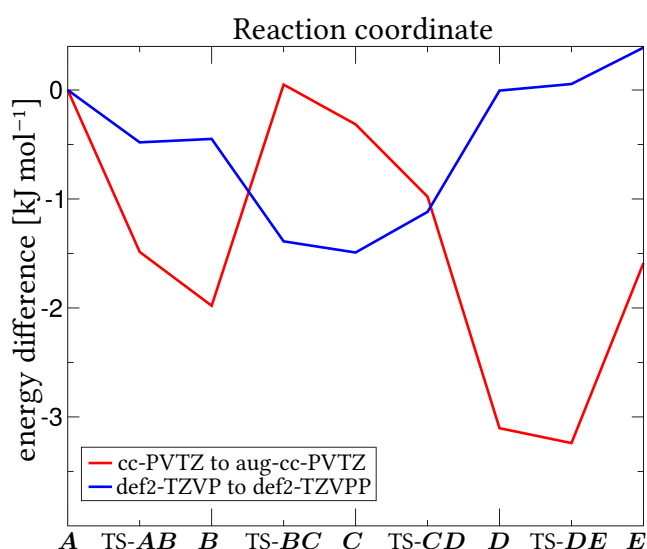
Figure 5.5: Effect of polarization functions: def2-TZVP compared to def2-TZVPP, and effect of augmentation functions: cc-pVTZ compared to aug-cc-pVTZ (QM-region with 48 atoms).

the cc-pVTZ geometry of SN-Glu-1 were calculated with correlation-consistent basis sets of different cardinal numbers. The cc-pVDZ basis set shows a maximum deviation of about $-16 \, \text{kJ} \, \text{mol}^{-1}$, the cc-pVTZ basis set of about $-3 \, \text{kJ} \, \text{mol}^{-1}$, and the cc-pVQZ basis set of about $-1.6 \, \text{kJ} \, \text{mol}^{-1}$ from the cc-pV5Z basis set, see Fig. 5.4. The correlation-

consistent triple-zeta basis was chosen for all further calculations as these results lie well within the accuracy which can be expected from DFT QM/MM calculations.
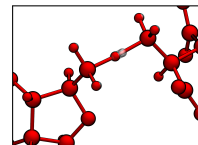
Fig. 5.5 shows energy differences (from energy calculations at the cc-pVTZ geometry of SN-Glu-1) due to augmentation of the cc-pVTZ basis. The maximum error of about -3 kJ mol^{-1} arising from omitting augmentation functions can be neglected. To estimate the importance of polarization functions, def2-TZVP and def2-TZVPP single-point calculations were compared. The results (see Fig. 5.5) indicate that negligence of additional polarization functions contributes only a marginal error of maximal -1.5 kJ mol^{-1}.

5.1.4   Geometry optimizations

Geometries were optimized with DL-FIND [248] in ChemShell [249]. Hybrid delocalized internal coordinates (HDLC) [318] were used throughout the investigations of the fragmentation–recombination mechanism. Minima were located by a quasi-Newton L-BFGS method in ChemShell. This algorithm necessarily converges to minima, as the step is reversed, should it point uphill [248]. Transition states were located with the superlinearly converging variant [253] of the dimer method [250–252]. Scans over bond lengths (for C–C-rearrangement steps) or bond-length differences (for hydrogen-transfer steps) were performed. All other degrees of freedom were relaxed. In each rearrangement step the two structures having the highest energies during the scans were chosen as starting guess for the dimer calculations. The dimer method requires two initial structures. By construction it converges to first-order saddle points. Weights of 1 were used for all atoms in the QM part and weights of 0 for all other atoms in an algorithm described previously [253], which effectively restricts the transition mode to the QM atoms. The energy is minimized with respect to the coordinates of all atoms with weight 0.

5.1.5   Exploring the influence of the protein environment

To investigate the influence of the protein environment on the chemically active center, Conductor-like Screening Model (COSMO) [319] calculations, which model a water environment, were performed in TURBOMOLE [305] (default parameters for COSMO) for the Glu substrate. Additionally, the isolated Glu substrate was investigated in the gas-phase.

To analyze the results of the optimizations, means of the potential energy barriers of the snapshots were calculated by exponential averages [320, 321]:

$$\langle \Delta E \rangle = -k_{\mathrm{B}} T \ln \left\langle \exp \left(-\Delta E \frac{1}{k_{\mathrm{B}} T} \right) \right\rangle \tag{5.1}$$
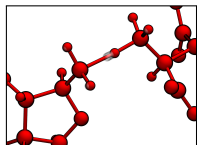
with T = 300 K, and k_B referring to Boltzmann's constant. According to Jarzynski's equation [322], the free energy ΔA of a process equals the exponential average, $\Delta A = -k_B T \ln\langle \exp(-\Delta W/k_B T)\rangle$, of the work ΔW (which can be approximated by potential energy differences ΔE) drawn from a canonical ensemble. Of course, a sample of nine snapshots cannot be expected to provide an accurate average. Taking an exponential average results in a barrier dominated by the smallest barrier which represents the most likely path. Therefore, energies are reported as potential energies rather than free energies.

For further analysis of the reaction mechanism and to investigate the electrostatic influence of each single amino acid on the activation energy, the full QM density of SN-Glu-1 was replaced by electrostatically fitted charges (ESP) [323], which were fitted to reproduce the electrostatic potential of the full DFT (BP86) density polarized by the charges of the MM environment, as these can be expected to result in a quite accurate electrostatic energy at hugely reduced costs compared to the full QM density. The change in the activation energy barrier $\Delta\Delta^{\ddagger}E^i$ due to the charge on residue i can be determined as

$$\Delta\Delta^{\ddagger}E^i = \Delta^{\ddagger}E^0 - \Delta^{\ddagger}E^i. \tag{5.2}$$

where $\Delta^{\ddagger}E^0$ is the electrostatic component of the activation energy (calculated using ESP charges instead of the QM density), and $\Delta^{\ddagger}E^i$ is the electrostatic component of the activation energy with all charges on residue i set to zero. In these calculations, the geometries of both the reactant and the transition state (TS) are kept unchanged. Thus, the self-energy of the QM part is constant and drops out of $\Delta\Delta^{\ddagger}E^i$. Note that $\Delta\Delta^{\ddagger}E^i$ contains contributions from MM–MM interactions as well as from QM–MM interactions. If $\Delta\Delta^{\ddagger}E^i$ is positive, then the atom charges of residue i increase the barrier (destabilize the TS). Otherwise these charges stabilize the TS. $\Delta\Delta^{\ddagger}E^i$ estimated in this way is a semiquantitative measure of the electrostatic influence of individual residues, helpful to determine which residues play a role in the catalytic activity. However, $\Delta\Delta^{\ddagger}E^i$ is certainly a too crude approximation to be compared to the effect of a mutation of the respective residue on the reactivity. Among the effects not covered by $\Delta\Delta^{\ddagger}E^i$ are the substitution of residue i by other moieties and changes in the geometries as well as changes in the polarization of the QM part.

A: Glutamate substrate and Ado   **B**: Glutamyl radical and Ado-H

C: Glycyl radical, acrylate, and Ado-H   **D**: Methylaspartyl radical and Ado-H

E: Methylaspartate and Ado
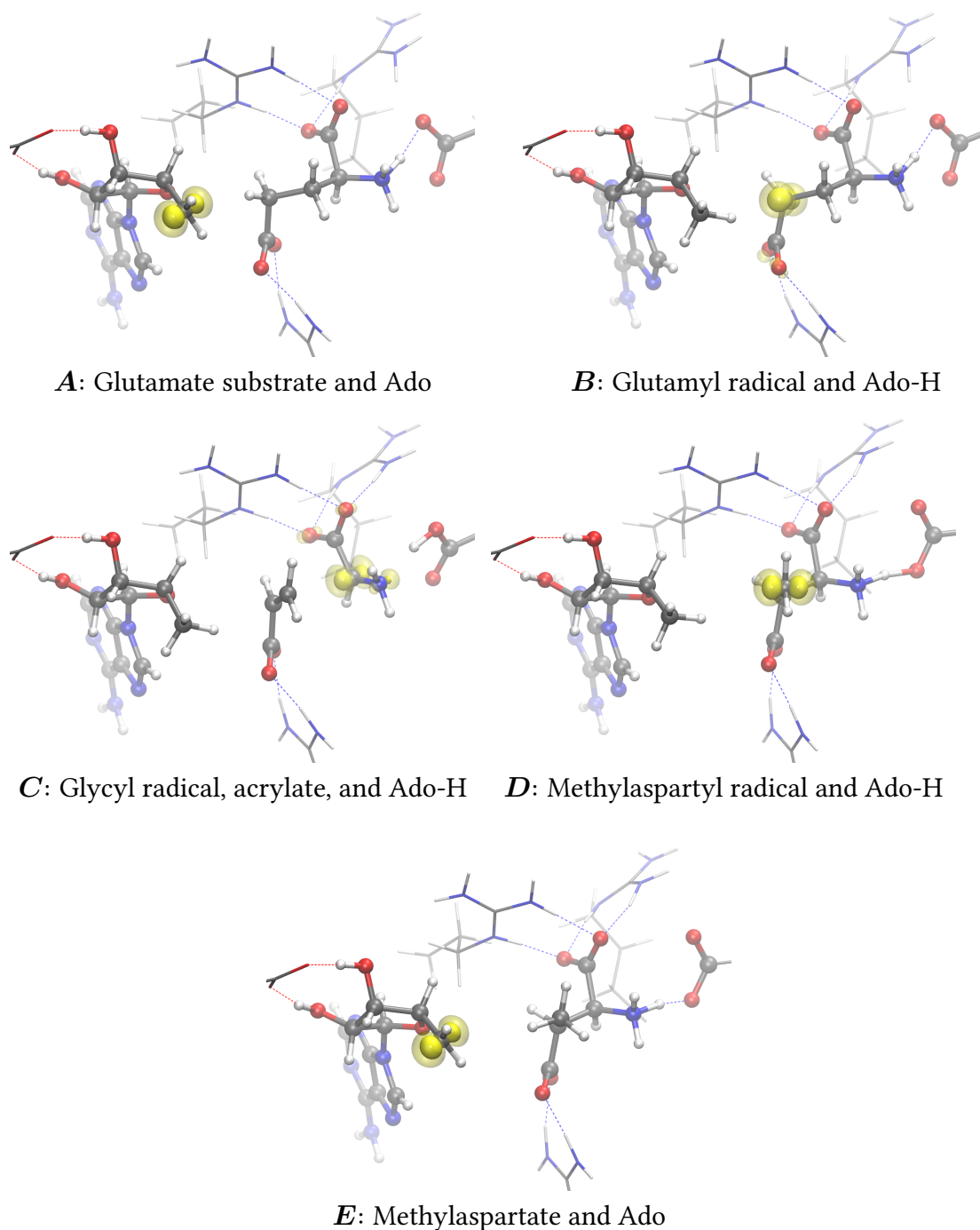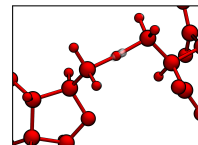
Figure 5.6: The fragmentation–recombination mechanism of GM: intermediates **A** to **E**, QM part (left: Ado, middle: Glu substrate, right: Glu 171) in ball and stick representation with 54 atoms. The yellow blobs denote the spin density. In the background the arginine claw can be seen.
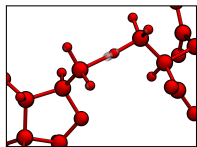
5.2   The fragmentation–recombination mechanism

The mechanism discussed in the following consists of: (1) a hydrogen-transfer from Glu substrate to Ado, (2) a rearrangement of the (S)-glutamyl radical to a (2S,3S)-3-methylaspartyl radical, and (3) a hydrogen-transfer back from Ado to form the MA product, see Fig. 5.6.

The intermediates considered in this study are labeled as follows: homolytic cleavage of the Co–C bond leads to the Ado radical and Glu substrate, state A. Hydrogen transfer generates the glutamyl radical, state B. It fragments into acrylate and a glycyl radical, state C. Glycyl binding to acrylate results in the methylaspartyl radical, state D. At the end, the back transfer of the radical to Ado creates MA, state E, see Fig. 1.2 on page 5 and Fig. 5.6. All transition states between the intermediates are abbreviated by TS, e.g., TS-DE denotes the transition state between D and E.

Energetic data for the different elementary reactions are given in Table 5.5. Energetic data comparing M06 and sd-LUCCSD(T) for the different elementary reactions are given in Fig. 5.11. Relative energies were consistently calculated with respect to the energy of the state A obtained for the same snapshot, unless noted otherwise. Key bond distances which changed during the reaction are given in Table 5.6.

Influence of the density functional on the computational results

The energy profile of the fragmentation–recombination mechanism was validated by performing calculations with the M06 functional as well as the B3LYP functional at geometries optimized with the BP86 functional in the first snapshot (Table 5.3 and Table 5.4). Barriers are generally several kJ mol^{-1} higher with B3LYP and M06 than with BP86, which is in agreement with a generally observed trend caused by the Hartree–Fock exchange in B3LYP and M06 but not in BP86. Table 5.3 and Table 5.4 show negligible influence of B3LYP geometry optimizations. M06 energies at BP86 geometries deviate only by about 1 kJ mol^{-1} from the M06 energies at B3LYP geometries, well within the error bar for QM/MM calculations. The M06 results are shown in Table 5.5 and will be discussed in Section 5.2.1. For technical reasons, calculations with the BP86 functional are much faster than calculations with the B3LYP functional, which are in turn faster than M06 calculations. Thus, BP86 geometries were used throughout, as they hardly differ from those obtained by B3LYP, to calculate QM/MM energies with the M06 functional. In Section 5.2.2 the M06 results will be compared to sd-LUCCSD(T) results at the same geometries.
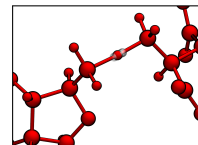
| Energy | M06 | BP86 | B3LYP | B3LYP |
Geometry	BP86	BP86	BP86	B3LYP
SN-Glu-1	79.7	54.2	75.5	74.4
SN-Glu-2	93.0	87.2	110.3	
SN-Glu-3		121.6		
SN-Glu-4		117.8		
SN-Glu-5	98.2	72.6	96.0	95.8
SN-Glu-6		136.0		
SN-MA-1	192.4	165.3	191.5	191.9
SN-MA-2	190.5	147.1	169.8	
SN-MA-3	83.8	56.0	77.9	77.8

Table 5.3: Comparison of different functionals (M06 and B3LYP at BP86 geometry, BP86 and B3LYP after optimizations) for QM/MM energy barriers in kJ mol^{-1} for the reaction $A \to B$ (QM-region with 54 atoms).

| Energy | B3LYP | M06 | M06 |
Geometry	B3LYP	B3LYP	BP86
A	0.0	0.0	0.0
TS-AB	74.4	78.3	79.7
B	−13.8	−22.1	−21.6
TS-BC	59.5	62.4	61.3
C	20.0	21.6	21.7
TS-CD	68.6	70.2	70.9
D	6.1	8.8	9.2
TS-DE	98.6	108.8	110.9
E	5.4	13.1	13.5

Table 5.4: Comparison between M06 and B3LYP functionals: M06 at BP86 and B3LYP geometries of SN-Glu-1 (QM-region with 54 atoms).

5.2.1   Energy profile of the catalytic reaction

The barriers given in Table 5.5 are significantly higher for the hydrogen transfers $A \to B$ and $E \to D$ than for the rearrangement reactions B to D. There is a substantial spread in the hydrogen-transfer barriers between the different snapshots. They range from 79.7 kJ mol^{-1} to 192.4 kJ mol^{-1} in $A \to B$ and from 97.4 kJ mol^{-1} to 192.4 kJ mol^{-1} in $E \to D$. Thus, they show a strong dependence on the environment. The smallest barriers are found in SN-Glu-1 (79.7 kJ mol^{-1} and 97.4 kJ mol^{-1}), suggesting that the reaction will most probably proceed via this path. SN-MA-3 and SN-Glu-1
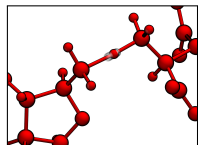
Structure	SN-Glu-1	SN-Glu-2	SN-Glu-5
A	0.0	0.0	0.0
TS-**AB**	79.7	93.0	98.2
B	−21.6	−23.3	−29.7
TS-**BC**	61.3	56.7	51.9
C	21.7	40.7	14.5
TS-**CD**	70.9	78.5	46.1
D	9.2	7.6	−12.3
TS-**DE**	110.9	129.3	153.7
E	13.5	17.9	−1.5

Structure	SN-MA-1	SN-MA-2	SN-MA-3
A	0.0	0.0	0.0
TS-**AB**	192.4	190.5	83.8
B	−37.0	−42.0	−36.9
TS-**BC**	38.9	43.5	43.9
C	−11.4	−19.2	−3.4
TS-**CD**	34.1	15.1	27.2
D	−26.1	−57.2	−49.6
TS-**DE**	110.2	140.1	60.7
E	−14.1	−51.3	−36.7

Table 5.5: Relative QM/MM energies of six snapshots (M06 energies in kJ mol^{-1} at BP86 geometries, QM-region with 54 atoms)

Structure	N–O	N–H$_N$	C5'–Cγ	H$_a$–Cγ	Cβ–Cα	Cγ–Cα
A	2.589	1.145	3.638	1.097	1.540	2.575
TS-**AB**	2.579	1.449	2.746	1.320	1.561	2.563
B	2.552	1.402	3.689	2.718	1.568	2.537
TS-**BC**	2.690	1.651			2.254	2.949
C	2.772	1.760			3.322	3.051
TS-**CD**	2.704	1.661	C5'–Cβ	H$_a$–Cβ	2.849	2.156
D	2.546	1.165	4.105	3.083	2.544	1.571
TS-**DE**	2.594	1.151	2.751	1.360	2.603	1.571
E	2.552	1.160	4.180	1.096	2.578	1.555

Table 5.6: Bond distances in Å during the reaction in SN-Glu-1 (QM-region with 54 atoms)
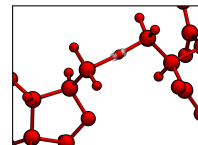
both have a barrier height of 97.4 kJ mol^{-1} for the transition $\boldsymbol{E} \to \boldsymbol{D}$. However, the barrier for $\boldsymbol{A} \to \boldsymbol{B}$ is slightly lower (74.7 kJ mol^{-1}) in SN-Glu-1 than in SN-MA-3 (83.8 kJ mol^{-1}). Accordingly, further investigation of the protein will mainly be performed with SN-Glu-1. The exponentially averaged barrier at T = 300 K is 84.8 kJ mol^{-1} for $\boldsymbol{A} \to \boldsymbol{B}$ and 101.1 kJ mol^{-1} for $\boldsymbol{E} \to \boldsymbol{D}$. The barriers for hydrogen-transfer and
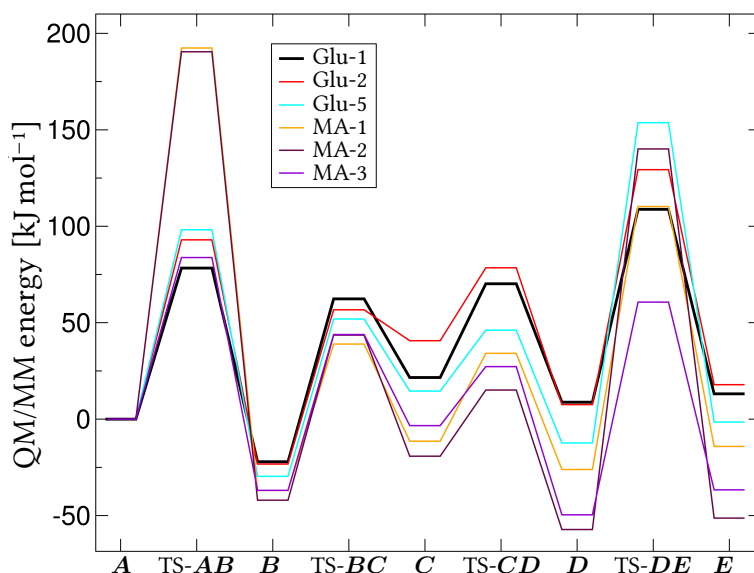
Figure 5.7: Energy profile, M06 at BP86 geometry (relative to $\boldsymbol{A}$); QM-region with 54 atoms.

recombination of the fragments seem to depend stronger on the snapshot than the barriers for the fragmentation (see Fig. 5.7 and Fig. 5.8). Thus, the hydrogen-transfer reactions depend much more on the enzyme environment than the carbon skeleton rearrangement. The exponentially averaged barriers for the hydrogen transfers range from 58.7 kJ mol^{-1} with BP86 over 80.1 kJ mol^{-1} with B3LYP to 84.8 kJ mol^{-1} with M06 for the reaction $\boldsymbol{A} \to \boldsymbol{B}$ and from 73.2 kJ mol^{-1} with BP86 over 93.4 kJ mol^{-1} with B3LYP to 101.1 kJ mol^{-1} with M06 for the transition $\boldsymbol{E} \to \boldsymbol{D}$. All of these results were obtained at BP86 optimized geometries. The exponential average is smaller with 84.8 kJ mol^{-1} for the reaction $\boldsymbol{A} \to \boldsymbol{B}$ than for $\boldsymbol{E} \to \boldsymbol{D}$ with 101.1 kJ mol^{-1}. The lowest barriers contribute most to the exponential average. So, a similar difference is obtained when just comparing the lowest values for the two mechanisms: 79.7 kJ mol^{-1} for the former and 97.4 kJ mol^{-1} for the latter case. For coenzyme B$_{12}$-dependent diol dehydratase, an enzyme similar to GM, the rate-limiting step was predicted [17] to exhibit a barrier between 60 and 75 kJ mol^{-1} based on theoretical and experimental studies [324–326]. In GM, the barrier is found to be about 25 kJ mol^{-1} higher. The wide range of barriers found in the different snapshots is due to the varying geometries of the snapshots.
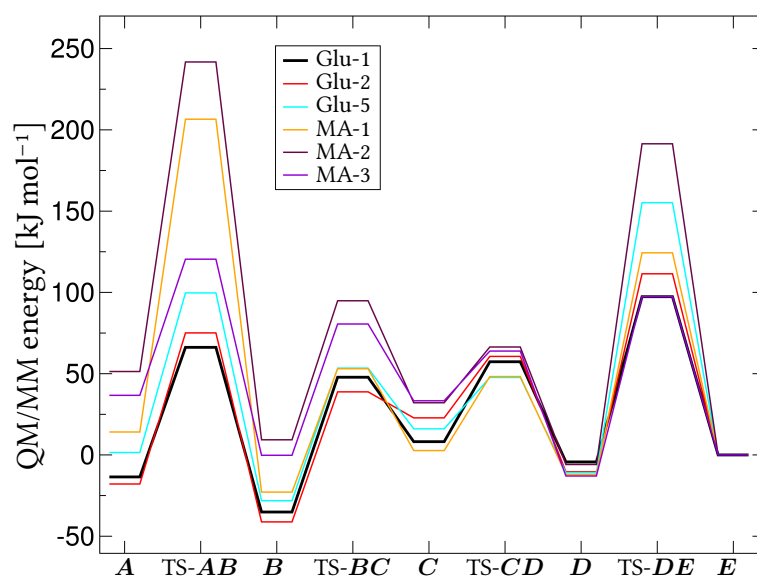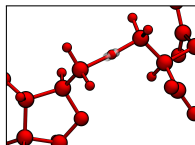
Figure 5.8: Energy profile, M06 at BP86 geometry (relative to E); QM-region with 54 atoms.

Differences will be discussed in more detail in Section 5.2.4. Comparison of the reaction $B \to D$ in Fig. 5.7 and Fig. 5.8 leads to the insight that the barriers from $B \to C$ (average: 80.1 kJ mol^{-1}) as well as the barriers from $D \to C$ (average: 62.4 kJ mol^{-1}) are about the same height in all snapshots. The influence of the protein on the carbon skeleton rearrangement will be discussed in Section 5.2.3.

Hydrogen-transfers and C–C-distance

Fig. 5.9 shows the barriers versus the C–C distance between the hydrogen donor and acceptor in A and E. Independent of the snapshots and of the substrate in the binding pocket at the beginning of the simulations, A tends to have shorter distances than D. Distances refer to the minimized structures. In many cases the distance can be decreased without significantly increasing the energy. Promoting vibrations may lead to shorter hydrogen-transfer distances. The large distances (> 5 Å) are associated with large barriers. The reaction will not proceed via these paths. SN-Glu-3, SN-Glu-4, and SN-Glu-6 show significantly higher barriers than the other snapshots already with the BP86 functional (which underestimates the barrier heights), see Fig. 5.10. Thus, these snapshots have not been investigated in more detail. In one case a large barrier is found for a short distance. In the respective snapshot (SN-Glu-3) one catalytic hydrogen bond is broken, see Section 5.2.4, which causes the large barrier.
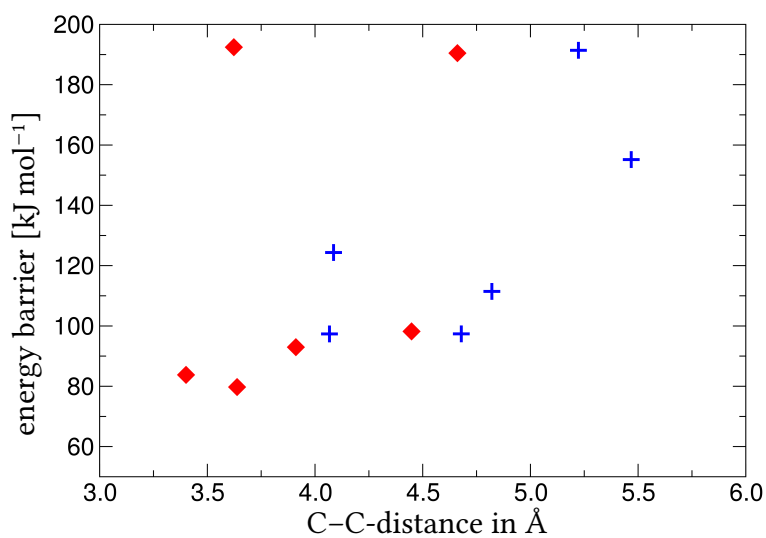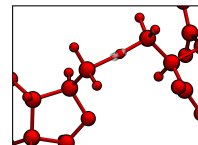
Figure 5.9: Barrier heights of both hydrogen-transfers versus C–C-distance (C5'–Cγ for $\boldsymbol{A}$, red diamonds; C5'–Cβ for $\boldsymbol{E}$, blue plus signs) at energetic minima of Glu and MA substrate (M06); QM-region with 54 atoms.
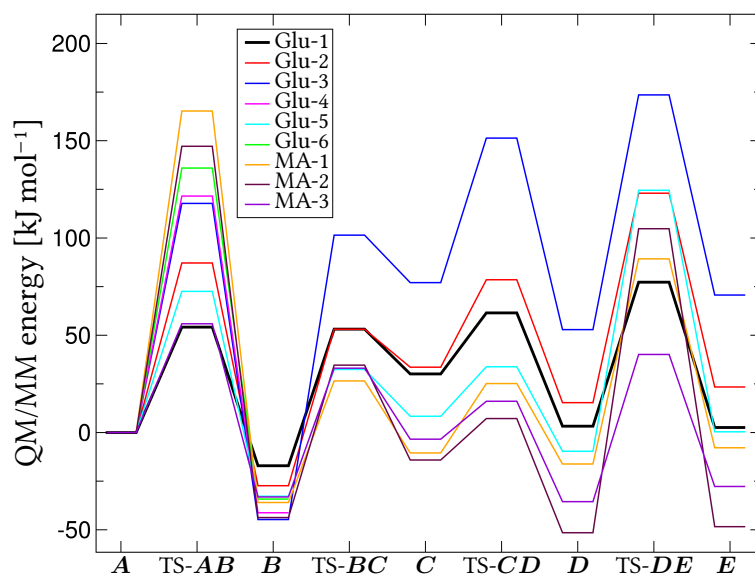
Figure 5.10: Energy profile, BP86 (relative to $\boldsymbol{A}$); QM-region with 54 atoms.
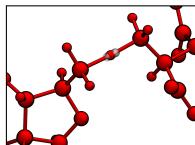
5.2.2 Coupled cluster energies

The H-transfers

The LUCCSD(T)/MM energies are compared to the DFT/MM results for SN-Glu-1 in Fig. 5.11 and Table 5.7. The barriers for the transitions $A \rightarrow B$ and $E \rightarrow D$ remain almost unchanged. They differ by only 1.9 and 1.6 kJ mol^{-1}, respectively, see Table 5.7. Tunneling can play a role during these two isotopically sensitive steps. More details on tunneling will be given in Section 5.3. The hydrogen transfers have the highest barriers, with the transfer $D \rightarrow E$ having a higher barrier than $A \rightarrow B$, see Fig. 5.7. The coupled cluster results yield the same picture. In both cases, DFT and coupled cluster, B is the most stable intermediate, despite an energy difference of 19.3 kJ mol^{-1} between the coupled cluster and DFT results. The coupled cluster barriers for $A \rightarrow B$ and $D \rightarrow E$ differ by 29.4 kJ mol^{-1} whereas the experimental investigations where tritium was transferred from Ado-H to form either Glu (substrate) or MA (product) resulted in a 1:1 distribution of tritium in the substrate and the product which would mean that both barriers for transferring hydrogens are nearly equal [22]. The MD simulations to prepare the QM/MM snapshot used here (SN-Glu-1) contained Glu in the binding pocket, i.e., the QM/MM simulations started at A. The snapshots taken from MD simulations are frozen in the outer part of the enzyme which might cause a bias increasing $D \rightarrow E$ relative to $A \rightarrow B$.
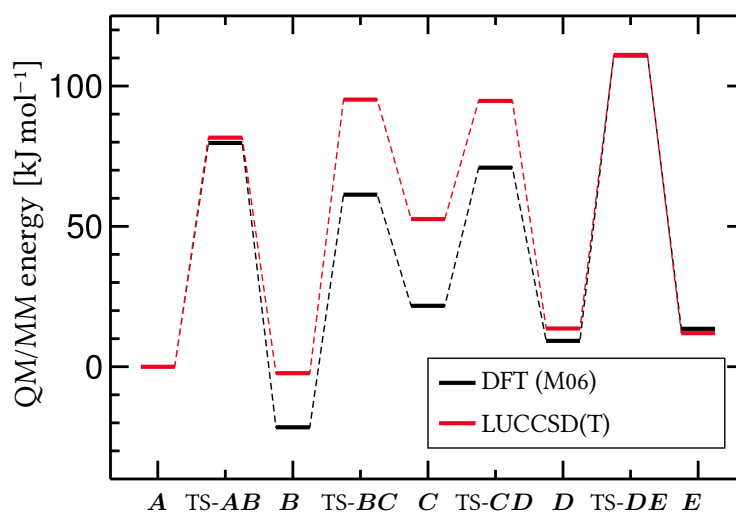
Figure 5.11: Comparison of the QM/MM energy profile with DFT (M06) and LUCCSD(T), SN-Glu-1 (QM-region with 54 atoms).
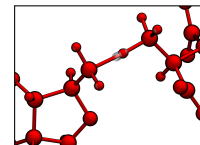
Structure	M06 cc-pVTZ	LUCCSD(T) aug- cc-pVTZ
A	0.0	0.0
TS-**AB**	79.7	81.6
B	−21.6	−2.3
TS-**BC**	61.3	95.1
C	21.7	52.6
TS-**CD**	70.9	94.6
D	9.2	13.6
TS-**DE**	110.9	111.0
E	13.5	12.0

Table 5.7: Comparison of LUCCSD(T) to DFT with M06 functional (QM/MM potential energies in kJ mol^{-1} at BP86 geometries, SN-Glu-1, QM-region with 54 atoms).

The carbon skeleton rearrangement

For the carbon skeleton rearrangement the DFT and coupled cluster energies differ by 19.3 to 33.8 kJ mol^{-1}. The barriers for the fragmentation and recombination are about the same, 95.1 kJ mol^{-1} for $B \to C$ and 94.6 kJ mol^{-1} for $C \to D$. In contrast to the experimental conclusion that "no single step was cleanly rate-limiting" [24, 25], the computed energy differences between the barriers of the hydrogen transfer $D \to E$ and the carbon skeleton rearrangement differ by 15.9 kJ mol^{-1} and 16.4 kJ mol^{-1}.

The differences between DFT and coupled cluster for the potential energies of the carbon skeleton rearrangement are due to different electronic structures as both energies were calculated on BP86 geometries. The similar barrier heights found for all conversions of the intermediates with coupled cluster calculations hint that the enzyme is optimized to lower energy barriers until a threshold of about 80 to 100 kJ mol^{-1} is reached. Lowering barriers below the threshold is then nearly impossible and unfavorable for the enzyme, since it would require to lower several barriers simultaneously.

5.2.3 Catalytic effect of the protein

The catalytic role of Glu 171

The side chain of Glu 171 is positioned next to the ammonium group (NH$_3^+$) of the Glu substrate. During the fragmentation–recombination process a proton is transferred from the ammonium group to Glu 171 in all snapshots, see Fig. 5.3. In the simulations transfer of protons between the QM part and the MM part is impossible. Thus, the
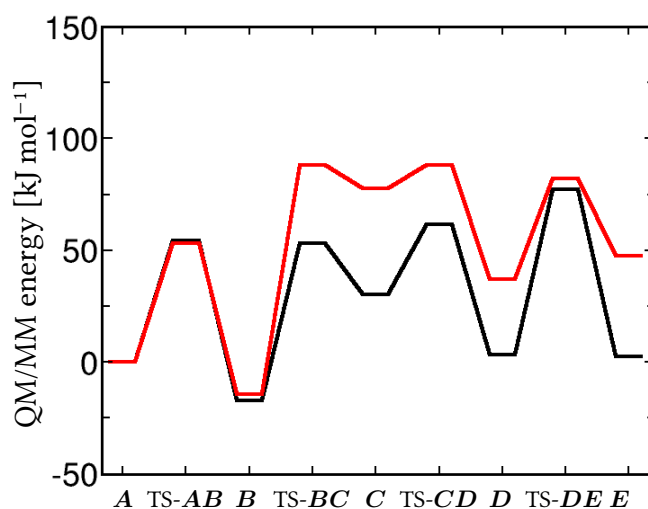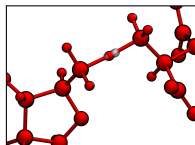
Figure 5.12: Energy profile (BP86) comparing QM parts with (black) and without (red) the inclusion of the neighboring amino acid Glu 171.

inclusion of neighboring amino acids in the QM part allows such acid-base reactions to take place, whereas the exclusion prevents them. The barriers of the rearrangement of the carbon skeleton are about 30 to 40 kJ mol^{-1} higher, see Fig. 5.12, if the proton transfer to Glu 171 is forbidden by the choice of the QM part in SN-Glu-1, which has the lowest hydrogen-transfer barriers, see Table 5.8. This is in agreement with mutation studies in which Glu 171 was replaced by glutamine (Gln) and other amino acids. These show a dramatic decrease in reactivity, and, thus, the importance of Glu 171 [11]. Further investigations including His 150 in the QM part showed that His 150 does not act as a proton acceptor.

A captodative stabilization, i.e., a proton transfer from the ammonium group to the carboxyl group of the glycyl radical in C was proposed by gas-phase calculations [17]. This is energetically unfavorable by about 50, 15, and 60 kJ mol^{-1} for B, C, and D, respectively, in a QM/MM environment (SN-Glu-1), see Table 5.8 columns 2 and 5. The protein stabilizes the zwitterionic state.

Variation of the protein environment

Variation in the protein environment has a significant influence on the energy barriers for the hydrogen-transfers. This causes a large spread in the barriers between the snapshots (Fig. 5.7, Fig. 5.8). The reaction will predominantly proceed via the paths with the lowest barriers. Intermediate B, containing the glutamyl radical, is the most
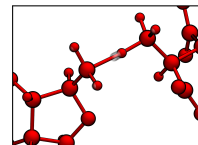
QM part:	substrate + Ado + Glu 171	substrate + Ado	substrate + Ado + Glu 171 + His 150	captodative stabilization (substrate) + Ado + Glu 171)
A	0.0	0.0	0.0	0.0
TS-**AB**	54.2	54.5	52.6	
B	−17.1	−14.4	−18.5	32.3
TS-**BC**	53.2	87.3	49.3	
C	30.1	76.4	28.7	14.4
TS-**CD**	61.5	87.3	61.2	
D	3.3	4.2	4.3	60.4
TS-**DE**	77.3	80.1	77.9	
E	2.6	4.4	3.8	

Table 5.8: Energy profiles of SN-Glu-1 with proton transfer form the substrate to the environment being selectively allowed by the choice of the QM part (BP86 energies in kJ mol^{-1}).

stable structure along the part of the reaction path under study, in agreement with experimental results [22]. In all calculations, in protein as well as in gas-phase and in water, **B** has the lowest energy along the reaction path. The barrier for fragmentation is similar in the gas-phase (69.9 kJ mol^{-1}), in water (69.1 kJ mol^{-1}), Table 5.9, and in the protein (70.1 kJ mol^{-1}) for calculations with BP86 functional, see Fig. 5.13. The rearrangement of the carbon skeleton is less influenced by the protein environment than the hydrogen-transfers. All snapshots show barriers within 75.9 and 82.9 kJ mol^{-1} for the fragmentation (**B** → **C**) and within 30.6 and 49.2 kJ mol^{-1} for the recombination (**C** → **D**), see Table 5.5. The enantioselective catalysis by suppressing the formation of the (R)-enantiomer happens in step **C** → **D**.

The C–C-rearrangement is hardly influenced by a water environment compared to gas-phase calculations. Comparison of the energies of the substrate in the enzyme environment, water (COSMO), and the gas-phase is given in Table 5.9. The enzyme sterically destabilizes the fragments, state **C**. **C** is about as stable as **B** in water or the gas phase, see Table 5.9, while it is 43.3 kJ mol^{-1} (see Table 5.5, which gives the M06 values; the BP86 value is 47.1 kJ mol^{-1}) less stable in the enzyme. **C** is destabilized predominantly sterically. This reduces the barriers to recombine the fragments (**C** → **D**) from 75.2 kJ mol^{-1} in the gas-phase and 80.6 kJ mol^{-1} in water down to 31.4 kJ mol^{-1} (all BP86) in the enzyme environment. In gas-phase and water the fragments lie parallel to each other, while in the enzyme environment they are rotated and in a staggered position. The two fragments are held in place by the enzyme
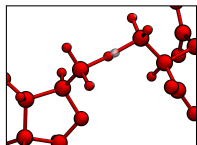
environment: The arginine claw prevents the fragments acrylate and glycyl to move into a parallel position. This raises the energy of the intermediate C but avoids the rotation of the acrylate and, thus, ensures the enantioselectivity. Additionally, the formation of a bond between glycyl and the acrylate is facilitated.

Table 5.9 compares the reaction energies of isolated Glu in the gas-phase and in water (COSMO) at different levels of theory. Compared to the G3(MP2)-RAD(p) level at a different protonation state [17], calculations with BP86 result in a larger barrier. The reaction of the isolated Glu in the gas-phase is overall endothermic (Table 5.9). The enzyme can save this intrinsic energy for the last step of the reaction.

	gas-phase		COSMO
	G3(MP2)–RAD(p)[17]	BP86	BP86
B	0.0	0.0	0.0
TS-BC	59.9	69.9	69.1
C	34.4	2.8	3.6
TS-CD	66.5	78.0	84.2
D	20.3	24.9	31.1

Table 5.9: Relative energies of the isolated substrate radical optimized in the gas-phase and in water (COSMO) (kJ mol^{-1}).
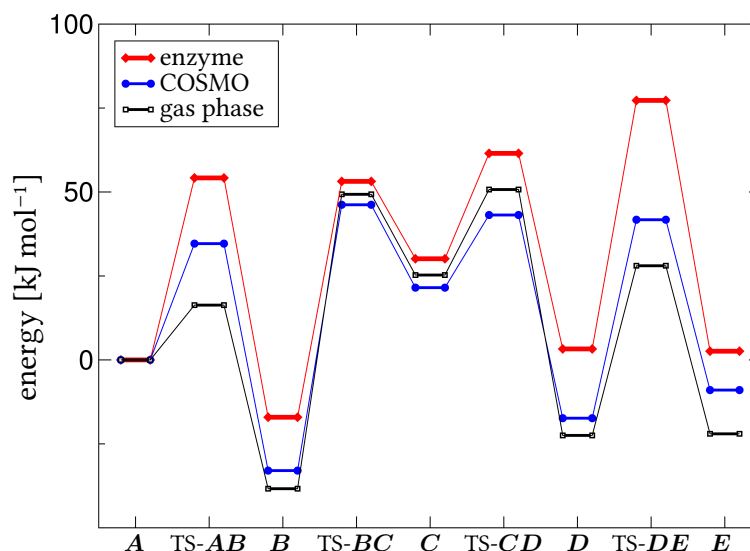
Figure 5.13: Comparison of energy profiles with the QM part in enzyme, water (COSMO), and gas phase environment.
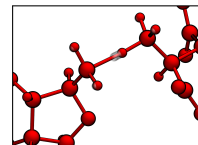
5.2.4 Influence of individual residues on the reactivity

After having located the transition states and the reactant states connected to them, the electrostatic influence of individual residues (neighboring amino acids and water molecules) on the activation barriers using static structures was estimated. The resulting values for $\Delta\Delta^{\ddagger}E^i$ both for the reactions $\boldsymbol{A} \rightarrow \boldsymbol{B}$ and $\boldsymbol{D} \rightarrow \boldsymbol{E}$ are given in Table 5.10. The residues with larger values of $\Delta\Delta^{\ddagger}E^i$ are depicted in Fig. 5.14 to Fig. 5.17. In the following, individual amino acids and their influence on the reactivity will be discussed, first for the reaction $\boldsymbol{A} \rightarrow \boldsymbol{B}$, then for $\boldsymbol{D} \rightarrow \boldsymbol{E}$. In the following, hydrogen bond distances are given between the hydrogen atom and the heavy atom (acceptor).

Arginine claw

Arg 66, 100, and 149 form the arginine claw, see Fig. 5.14. Arg 100 builds a salt bridge to the carboxyl group of the side chain of the Glu substrate, while Arg 66 and Arg 149 are bound to its "backbone" carboxyl group (which is not, in fact, a part of any protein backbone, here it is refered to the carboxyl group bound to the Cα atom). Since each arginine donates two hydrogen bonds, a total of six such bonds make up the arginine claw. Their electrostatic effect on the barriers for hydrogen-transfer is moderate, see Table 5.10. This is mainly due to the fact that the interaction between the substrate and the arginine claw is hardly altered during the mechanism in the snapshot for which the electrostatic contributions were calculated (SN-Glu-1). A slight tightening of the arginine claw is observed during the fragmentation. Qualitatively the same behavior is observed for SN-Glu-2 and SN-Glu-5. During the hydrogen-transfer reactions, the Glu substrate moves slightly toward Ado, which means it moves away from Arg 149. Consequently, in two snapshots (SN-MA-1 and SN-MA-3) Arg 149 forms one hydrogen bond to the carboxyl group of Glu 171, while one to the substrate is absent in the structure derived from the MD simulation ($\boldsymbol{E}$). The other hydrogen bond between Arg 149 is stable in those cases, though. During the reaction mechanism also the second hydrogen bond establishes. In one snapshot (SN-Glu-3), the arginine claw is opened even further. Only one hydrogen bond between Arg 100 and Glu remains stable, the other one is broken. This particular snapshot shows the highest energies of the intermediates TS-$\boldsymbol{BC}$ to $\boldsymbol{E}$, about 50 kJ mol^{-1} higher than in the other snapshots, on a BP86 level. This can be interpreted as a clear indication that an intact arginine claw is crucial for the catalytic activity.
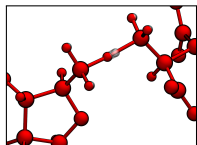
Residue	Charge	$\Delta\Delta^{\ddagger}E^i$ (kJ mol^{-1})	
		$A \rightarrow B$	$D \rightarrow E$
σ−subunit			
Asp 14	−1	0.2	−3.4
His 16	0	−3.7	−8.2
cobalamin	0	−7.0	−6.7
ϵ−subunit			
Arg 66	+1	−3.7	3.2
Arg 100	+1	−4.7	−1.2
Gln 147	0	3.2	0.7
Arg 149	+1	2.4	6.2
His 150	0	10.9	−1.2
Tyr 177	0	10.5	−1.7
Asp 198	−1	−4.9	−1.1
Arg 213	+1	7.3	2.0
Glu 214	−1	−14.5	−5.8
Phe 216	0	4.4	−0.2
Glu 236	−1	−4.8	−1.6
Met 294	0	1.1	3.0
Lys 322	+1	8.4	2.9
Lys 326	+1	−8.2	−2.6
Glu 330	−1	13.9	12.2
water 632	0	3.9	6.0
water 635	0	−0.5	−3.0
water 637	0	−6.6	−6.8
water 642	0	3.4	4.2
water 648	0	3.9	2.5
water 654	0	−5.3	−7.5

Table 5.10: Residues of the environment with an electrostatic influence on the activation barrier of $|\Delta\Delta^{\ddagger}E^i| > 3$ kJ mol^{-1} in either TS-AB or TS-DE (SN-Glu-1).

Environment of the glutamate substrate

Here the residues Arg 213, Glu 214, lysine (Lys) 322, and Gln 147, connected to the Glu substrate via Arg 149 (which is part of the arginine claw) are discussed, see Fig. 5.15. In the reaction from $A \rightarrow B$ a proton is transferred form the Glu substrate to Glu 171. Its charge changes from −1 to zero. The dipole moment of the whole reactive center changes. Thus, negatively charged residues (Glu 214, Glu 236, and aspartic acid (Asp) 198) in the vicinity of Glu 171 stabilize the transition state, while positive ones (Lys 322 and Arg 213) destabilize it. Despite their large distance, these residues seem to have a significant electrostatic influence on the reaction. For example Lys 322 is 8 Å (closest
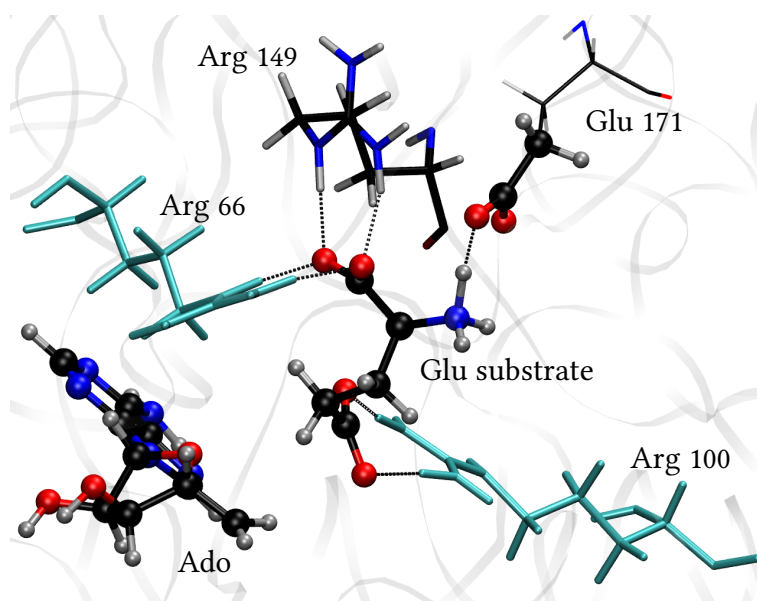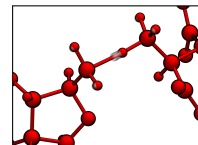
Figure 5.14: Arginine claw of the Glu substrate (intermediate **A**). Residues with $7 > |\Delta\Delta^{\ddagger}E^i| > 3$ kJ mol^{-1} are shown in cyan. They stabilize the transition state. Additionally, the QM part comprising Ado, the Glu substrate, and Glu 171 is shown (ball-and-stick).

atom) away from the transferred proton and increases the barrier by 8.4 kJ mol^{-1}, see Table 5.10. Glu 214 is 5.2 Å away (4.9 Å in TS-**AB**) and decreases the barrier by 14.5 kJ mol^{-1}. In **D** the proton is already back at the substrate, so the above-mentioned residues have a weaker effect on the barrier from **D** → **E**.

Tyrosine (Tyr) 177 provides a hydrogen bond to Glu 171 via its phenol group, see Fig. 5.16. This bond is elongated during the reaction from **A** → **B** which destabilizes the transition state in SN-Glu-1. This is in contrast to the other snapshots where that hydrogen bond is hardly altered in the steps **A** → **B** and **D** → **E**.

His 150 provides a hydrogen bond via its backbone oxygen to a proton of the ammonium group of the Glu substrate, see Fig. 5.16. The bond is present in SN-Glu-1 and SN-MA-2 and absent (>2.2 Å) in the other snapshots. In both, SN-Glu-1 and SN-MA-2, the hydrogen bond elongates during the carbon skeleton rearrangement.

Environment of Ado

Glu 330, Lys 326 and four water molecules change their bonding pattern to Ado during the hydrogen-transfer reactions. The carboxyl side chain of Glu 330 accepts a hydrogen bond from each of the two OH-groups of the ribose ring. In some of the snapshots (SN-
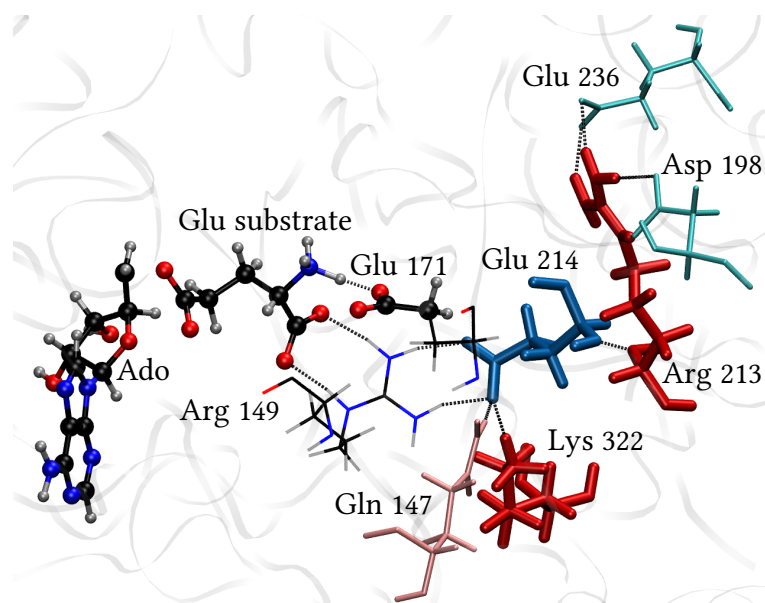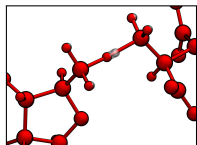
Figure 5.15: Environment of the Glu substrate (intermediate $\boldsymbol{A}$): residues with $\left|\Delta\Delta^{\ddagger}E^i\right| > 7$ kJ mol^{-1} are shown as thicker sticks with darker colors. Thinner sticks and lighter colors denote residues with $7 > \left|\Delta\Delta^{\ddagger}E^i\right| > 3$ kJ mol^{-1}. Additionally, the QM part comprising Ado, the Glu substrate, and Glu 171 is shown (ball-and-stick). Residues shown in blue stabilize the transition state, and residues shown in red destabilize the transition state with respect to the resting state.

MA-2, SN-Glu-2, SN-Glu5) one of these hydrogen bonds opens during the transitions $\boldsymbol{A} \to \boldsymbol{B}$ and $\boldsymbol{D} \to \boldsymbol{E}$. In SN-MA-1 one of the bonds is open in structures $\boldsymbol{A}$ to $\boldsymbol{C}$, resulting in a large barrier (192.4 kJ mol^{-1}) for hydrogen-transfer and closed in the further structures. In summary, in the snapshots with the lowest barriers (SN-Glu-1 and SN-MA-3) both hydrogen bonds between Glu 330 and the ribose ring remain stable.

Glu 330 was found to destabilize TS-$\boldsymbol{AB}$ by 13.9 kJ mol^{-1} and TS-$\boldsymbol{DE}$ by 12.2 kJ mol^{-1}. Lys 326 stabilizes TS-$\boldsymbol{AB}$ by 8.2 kJ mol^{-1} but stabilizes TS-$\boldsymbol{DE}$ by only 2.6 kJ mol^{-1}. Two water molecules (water 654 and 637) stabilize TS-$\boldsymbol{AB}$ by more than 3 kJ mol^{-1} through shortening their hydrogen bonds to Glu 330. Another water molecule (642) increases the barrier by 3.4 kJ mol^{-1} by elongating its hydrogen bond to one OH-group of the ribose ring in Ado.

The amino acid Met 294

The side chain of methionine (Met) 294 has to move to enable the hydrogen-transfer from Ado to the substrate and back, see Fig. 5.16. That requires energy and, thus,
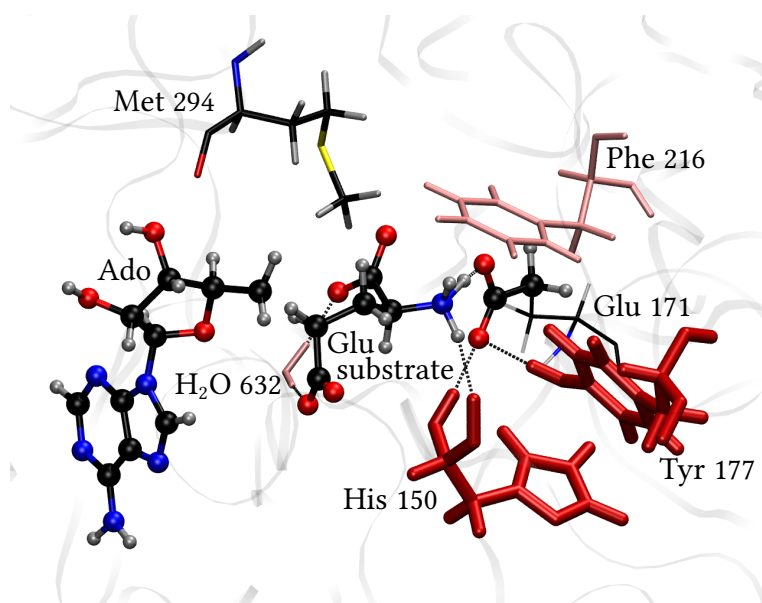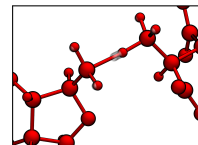
Figure 5.16: Environment of Glu 171 (intermediate $\boldsymbol{A}$): residues with $|\Delta\Delta^{\ddagger}E^i| > 7$ kJ mol^{-1} are shown as thicker sticks with darker colors. Thinner sticks and lighter colors denote residues with $7 > |\Delta\Delta^{\ddagger}E^i| > 3$ kJ mol^{-1}. Additionally, the QM part comprising Ado, the Glu substrate, and Glu 171 is shown (ball-and-stick). Residues shown in red destabilize the transition state with respect to the resting state.

increases the barrier. It plays a more important role in $\boldsymbol{D} \to \boldsymbol{E}$ where it increases the barrier by 3 kJ mol^{-1}, than in $\boldsymbol{A} \to \boldsymbol{B}$. Table 5.11 shows a dihedral angle in Met 294 that indicates the movement of a methyl group located between the substrate and Ado. The strongest movement is found in SN-Glu-1, which has the lowest barriers for the hydrogen-transfers. Noteworthy, Met 294 is not in direct contact with the reactive center, but it influences the reaction barriers.

5.3 Kinetic isotope effects and hydrogen tunneling in glutamate mutase

Here the results of experimental studies of GM are briefly summarized. Experimental measurements of rates and KIEs in GM were conducted with various techniques, see 1.1.2. The rates measured for GM are 5.8 ± 0.3 s^{-1} for the complete interconversion of Glu, $\boldsymbol{A}_0$, to MA, $\boldsymbol{E}_0$ [47]. Measurements considering the hydrogen transfer step separately resulted in uni-molecular rate contributions ranging from 64 ± 11 s^{-1} (for the H-abstraction from Glu substrate) to 97 ± 5 s^{-1} (for the H-abstraction from MA
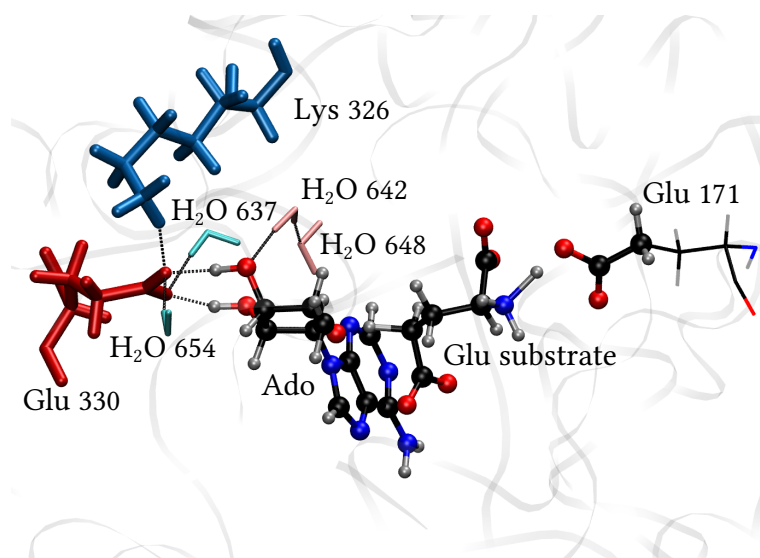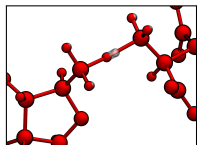
Figure 5.17: Environment of Ado (intermediate $\boldsymbol{A}$): Residues with $|\Delta\Delta^{\ddagger}E^{i}| > 7\,\mathrm{kJ\,mol^{-1}}$ are shown as thicker sticks with darker colors. Thinner sticks and lighter colors denote residues with $7 > |\Delta\Delta^{\ddagger}E^{i}| > 3\ \mathrm{kJ\,mol^{-1}}$. Additionally, the QM part comprising Ado, the Glu substrate, and Glu 171 is shown (ball-and-stick). Residues shown in blue stabilize the transition state, and residues shown in red destabilize the transition state with respect to the resting state.

substrate) [21, 23, 46].

The primary ^{1}H/^{2}H KIEs were measured by different techniques. The deuterium KIE at a temperature of T=283.15 K was measured for the complete interconversion from MA to Glu to be 6.3 ± 0.5 [47]. For the hydrogen abstraction from MA measured with an internal competition experiment it is 4.1 [24, 25]. The KIE of the formation of Ado-H ($\boldsymbol{A_0}$ to $\boldsymbol{B}$) measured directly by a competition experiment with trideuterated and unlabeled substrate in the same vessel was 10 ± 0.4 [21]. However, the formation of cob(II)alamin ($\boldsymbol{E_0}$ to $\boldsymbol{E}$) shows a KIE of 35 at T =283.15 K [23]. As the primary deuterium KIEs measured in GM range from 4.1 to 35 at T =283.15 K, it is unclear whether tunneling is involved in the catalysis by GM. Experiments investigating tritium isotope effects, based on rapid quench techniques [21, 54, 55], considered both primary and secondary tritium KIEs. All variants of experimental KIE measurements described in the introduction will be compared to the calculational results in the following Sections. The calculations are all based on a snapshot taken after 9 ns of classical molecular dynamics [20] with 126 water molecules included in the system.

Experimental studies always measure apparent rates and KIEs that can be masked by experimental side effects, like for example detection methods being insensitive to
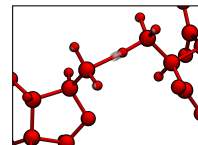
	SN-Glu-1	SN-Glu-2	SN-Glu-3	SN-Glu-5
A	0	0	0	0
TS-AB	7.2	1.2	−2.1	0.4
B	−0.8	0.5	−0.4	−0.2
TS-BC	−2.4	0.9	0.2	2.1
C	−10.4	−0.9	−0.6	1.5
TS-CD	−10.5	−0.3	3.9	2.2
D	−5.0	0.8	3.3	1.8
TS-DE	−2.2	0.4	3.7	3.7
E	−4.3	−0.7	3.4	2.5

	SN-MA-1	SN-MA-2	SN-MA-3
A	0	0	0
TS-AB	−1.0	−0.2	0.9
B	0.5	−0.1	0.7
TS-BC	−0.1	0.0	1.3
C	−0.6	0.8	2.7
TS-CD	−1.1	−0.6	2.6
D	−1.6	−0.1	0.5
TS-DE	−2.6	−5.4	0.3
E	−1.3	0.3	−0.0

Table 5.11: Difference of the dihedral $C\beta-C\gamma-S\delta-C\epsilon$ of Met 294 in different snapshots compared to intermediate A to describe the movement of the methyl group of Met 294 located between Ado and the Glu substrate.

deuterium content below a certain threshold. Artifacts are also caused by multiple transfers of deuterium to the cofactor, which stays undetected when following the formation of cob(II)alamin. At a temperature below 283.15 K the multiply deuterated Ado-H contributed negligibly (<1%) to the measured rates [21]. Above 283.15 K the dideuteration increased rapidly to more than 2% of the yield which makes correct measurements of KIEs impossible. The measurements are also limited to certain time frames as the threshold in concentration for detecting the substance of interest (e.g. the product) must be exceeded. In experimental investigations the reverse reaction affects the results, as GM catalyzes an reversible conversion. Thus, the measured rates are apparent rates leading to apparent KIEs. The intrinsic KIEs, real KIEs without masking side effects, can be obtained only indirectly by experiment.

On the other hand computational approaches allow to predict the intrinsic KIEs. In contrast to experimental measurements which always include tunneling contributions, calculations allow to switch tunneling on and off [35, 36, 96, 327, 328].
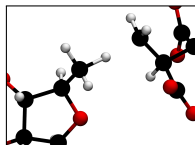
In the following the rates based on both, M06 barriers and coupled cluster barriers will be discussed. Then the primary and secondary KIEs will be presented and compared to experimental results. Then the influence and contributions to a productive catalysis during the tunneling event by the neighboring atoms and amino acids will be discussed. In the last part a speculation about a possible modulation of the rate determining step by the enzyme will be presented.

5.3.1   QM/MM instanton tunneling rate calculations

To calculate instanton rates in enzymes the first step is to optimize an instanton path, i.e., locate the dominant tunneling path [108]. The classical TS served a starting guess. Instanton geometries were optimized using DFT with the BP86 functional. The instanton geometry optimizations were performed at a convergence criterion of 10^{-8} atomic units for the maximum component of the gradient in mass weighted Cartesian coordinates based on the electron mass [108]. The convergence criterion for the SCF calculations with Turbomole was 10^{-9} Hartree and the grid size m4 was used. The subsequent rate calculations require to determine the finite difference QM/MM Hessian of the potential energy at each sampling point (also image or bead) along the path [109].

Rates were calculated at the BP86/MM level with corrections for the barrier height by M06 and coupled cluster, throughout. That is, instanton optimizations, the calculations of Hessians along the instanton path, as well as the harmonic frequencies at the minima and saddle points were calculated by QM/MM based on the BP86 functional. Barrier heights from M06/MM and coupled cluster/MM were used for the rates. KIEs are independent of barrier-height corrections as they cancel out in the ratio. So the KIEs are obtained on the pure BP86/MM level. For the calculations of secondary tritium KIEs the fixed path approximation (FPA) to the instanton rates was used [222]. In the FPA the instanton path is kept fixed at its geometry for protium despite an isotopic substitution to calculate rates, see Section 4.2.1.

It should be noted that the computational treatment of the electrons (atoms in the QM part vs. the MM part) is independent of the computational treatment of the atomic movement (i.e. whether an atom is allowed to contribute to the tunneling). Throughout all the rate calculations the QM part consisted of 54 atoms. However, to allow all atoms involved in the hydrogen transfer to tunnel the number of actively quantized atoms varied during the instanton optimizations and rate calculations. The number of tunneling atoms ranged from one, only the transferred hydrogen atom, to 78 (sets of 1, 7, 11, 23, ,34, 48, 54, 78 active atoms). All these are subsets of the active space of atoms in the geometry optimizations for the QM/MM energy profile calculations. The set of seven active atoms comprised the two carbon atoms between which the
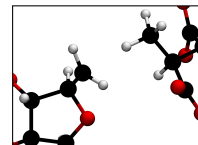
hydrogen atom is transferred and all five hydrogen atoms bound to them. For the calculations with 11 atoms additionally the two neighboring CH-groups at both, the substrate and the adenosyl part of the cofactor, were added. The 23-atom-set contained the complete substrate and the same CH_2CH-group of Ado as the 11-atom-set. The 34-atom-set comprised the substrate and all atoms belonging to the ribose ring of Ado. In the calculations with 48 atoms the active part contained the complete substrate and the complete adenosyl radical as part of the cofactor. In calculations with 54 atoms the active part was extended by the $COO\text{-}CH_2$ sidechain of the neighboring amino acid Glu 171, to match the QM part. Then, after a thorough analysis of the classical transition modes of atoms in the neighborhood of the active center, finally the guanidine part (-$NH\text{-}C\text{-}(NH_2)_2$) of the amino acids Arg 66, Arg 100, Arg 194, and the $COO\text{-}CH_2$ sidechain of Glu 330 were included in the set of 78 active atoms as well, see Fig. 5.21 on page 133.

Technical details on rate calculations

The comparison of the different active subspaces with respect to instanton rates, rates without tunneling corrections, and deuterium KIEs is given in Table 5.15 and Table 5.21. The instanton rates in Table 5.15 are 12.30 to 14.66 times higher than the non-tunneling rates. For active subspaces including 11 and 23 atoms the factor between tunneling rates and non-tunneling rates is much higher (about 14.6) than in the other cases which indicates that the larger active parts are important to ensure good predictions. A similar effect is noticeable in the deuterium KIEs, see Table 5.21. While the smaller active space with 7 atoms still gives reasonably good results it makes investigations of the geometrical changes at the active site during the tunneling process impossible. Thus, the active part consisting of 78 atoms was used for the final rate and KIE calculations. In the following, results for rates and KIEs will refer to an active part consisting of 78 atoms unless stated otherwise.

The instanton method breaks down at the crossover temperature T_c, defined in Section 1.2. T_c can be interpreted as the temperature below which tunneling significantly contributes to the rate. In the following investigations we apply instanton theory for all configurations possible. However, deuterium and tritium transfers have crossover temperatures below the temperatures used in our simulations (273.15 K and 300 K), which makes instanton theory inapplicable in these cases. As mentioned in the introduction, see Section 1.2, there are corrections to incorporate tunneling near the top of the barrier in the classical TST reaction rate, e.g. Wigner corrections [329]. These corrections can also be used above the crossover temperature T_c, where instanton theory breaks down. The full Wigner correction factor which is multiplied with the rate to include tunneling effects is

$$\kappa(T) = \frac{\beta\hbar\omega_b/2}{\sin(\beta\hbar\omega_b/2)}.$$

(5.3)
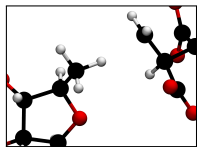
A second-order approximation via a Taylor-expansion in β at $\beta = 0$ reads

$$\kappa(T) = 1 + \frac{1}{24}(\beta\hbar\omega_b)^2 + \mathcal{O}(\beta^4) = 1 + \frac{1}{24}\left(\frac{2\pi T_c}{T}\right)^2 + \mathcal{O}(\beta^4). \tag{5.4}$$

Higher order terms are

$$\kappa(T) = 1 + \frac{1}{6}b^2 + \frac{7}{15}\frac{1}{4!}b^4 + \frac{31}{21}\frac{1}{6!}b^6 + \mathcal{O}(\beta^8), \tag{5.5}$$

where $b = \beta\hbar\omega_b/2$. The full Wigner correction describes the reflection at a barrier exactly for parabolic barriers [329]. When comparing different orders of Wigner corrections to the instanton rates with protium the sixth order approximation turned out to be the best choice to calculate rates above the crossover temperature, see Table 5.12. The rates for deuterium and tritium transfers are given in Table 5.13 and Table 5.14.

In the following tunneling rates refer to instanton rates below the crossover temperature and rates obtained with sixth-order Wigner corrections above the crossover temperature. Non-tunneling rates denote rates by transition state theory with all vibrational modes of the QM/MM system treated as quantum mechanical harmonic oscillators, see equation (1.2) page 13. These account for the zero-point energy, but not for tunneling.

Number of active atoms	Order of approximation: 2nd	4th	6th	8th	Instanton Rate	No Tunneling
1	1.959	2.261	2.483	2.664	2.128	1.467
7	0.873	1.244	1.537	1.793	1.413	0.311
11	0.540	0.909	1.200	1.453	1.145	−0.021
23	0.609	0.979	1.270	1.523	1.213	0.049
34	0.725	1.095	1.386	1.640	1.258	0.164
48	0.817	1.186	1.478	1.732	1.362	0.256
54	0.770	1.140	1.431	1.685	1.300	0.209
78	0.670	1.039	1.331	1.584	1.199	0.109

Table 5.12: Wigner corrected hydrogen transfer rates (BP86/MM) obtained by transition state theory for different active spaces at 273.15 K as $\log_{10}$(rate per second) for the transition form $D \rightarrow E$. "No tunneling" referes to classical TST rates including zero-point vibrations.

5.3.2 Rates

The Section starts with the discussion of the rates for the H-transfers $A \rightarrow B$ and $E \rightarrow D$. The sd-LUCCSD(T) tunneling rate for the transition $E \rightarrow D$ is $3.5 \cdot 10^{-4}$ s^{-1} at
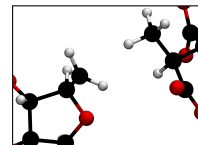
Number of active atoms	Order of approximation:					No tunneling
	2nd	4th	6th	8th	full	
1	0.892	1.031	1.104	1.146	1.212	1.467
7	−0.070	0.140	0.274	0.368	0.819	−0.466
11	−0.402	−0.193	−0.060	0.033	0.466	−0.796
23	−0.332	−0.124	0.009	0.102	1.253	−0.726
34	−0.216	−0.007	0.125	0.219	0.655	−0.611
48	−0.124	0.084	0.217	0.310	0.747	−0.519
54	−0.171	0.038	0.170	0.264	0.700	−0.566
78	−0.272	−0.063	0.070	0.163	0.600	−0.666

Table 5.13: Wigner corrected deuterium rates (BP86/MM) obtained by transition state theory for different active spaces at 273.15 K as $\log_{10}$(rate per second) for the transition from $D \to E$. (deuterium in primary position)

Number of active atoms	Order of approximation:					No tunneling
	2nd	4th	6th	8th	full	
1	0.414	0.495	0.526	0.539	0.549	0.182
7	−0.481	−0.339	−0.263	−0.220	−0.149	−0.797
11	−0.812	−0.670	−0.596	−0.553	−0.484	−1.126
23	−0.742	−0.601	−0.526	−0.484	−0.414	−1.057
34	−0.626	−0.484	−0.410	−0.367	−0.297	−0.941
48	−0.534	−0.392	−0.318	−0.275	−0.205	−0.849
54	−0.581	−0.439	−0.364	−0.322	−0.252	−0.896
78	−0.681	−0.539	−0.465	−0.422	−0.352	−0.996

Table 5.14: Wigner corrected tritium rates (BP86/MM) obtained by transition state theory for different active spaces at 273.15 K as $\log_{10}$(rate per second) for the transition form $D \to E$. (tritium in primary position)

273.15 K. It is 12.3 times larger than the non-tunneling rate. At 300 K these rates differ by a factor of 9.2 and the tunneling rate is $7.8 \cdot 10^{-3}$ s^{-1}, see Table 5.16. Notably, for the transition $A \to B$ tunneling speeds up the reaction only by factors of 5.7 at 273.15 K and by 5.9 at 300 K, see Table 5.17. Thus, tunneling seems to be less important for the hydrogen abstraction from Glu than from MA. Comparing the non-tunneling with the tunneling rates the reaction is enhanced by tunneling in the transition from $E \to D$. However, tunneling is unessential for the reaction to take place at all.

The crossover temperatures T_c for the transitions from $A \to B$ are 307 K for protium, 232 K for deuterium, and 198 K for tritium transfers, consistent with the notion that tunneling is less important for the heavier isotopes. For the transitions form $E \to D$
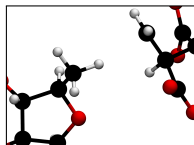
the corresponding crossover temperatures are 346 K, 259 K, and 220 K. For the transition $E \to D$ deuterium rates are increased by tunneling by a factor of 5.4 and tritium rates by a factor of 3.4 at T=273.15 K. A summary of the multiplicative factors between tunneling and non-tunneling rates is given in Table 5.15.

Active atoms	$\log_{10}(k_{\text{tunnel}}(^1\text{H}))$	$\log_{10}(k_{\text{no-tunnel}}(^1\text{H}))$	M_{eff}	$k_{\text{tunnel}}/k_{\text{no-tunnel}}$		
				^1H	^2H	^3H
1	2.128	1.467	1.007825	4.58	3.36	2.21
7	1.413	0.311	1.159765	12.65	5.49	3.42
11	1.145	−0.021	1.160989	14.66	5.44	3.39
23	1.213	0.049	1.159192	14.59	5.44	3.39
34	1.258	0.164	1.163579	12.42	5.44	3.40
48	1.362	0.256	1.163305	12.76	5.44	3.40
54	1.300	0.209	1.163641	12.33	5.45	3.40
78	1.199	0.109	1.163371	12.30	5.45	3.40

Table 5.15: Tunneling rates (BP86/MM) for hydrogen transfer from $E \to D$ at 273.15 K with monodeuterated substrate in comparison to non-tunneling rates (TST rates including zero-point vibrations), rates are given as $\log_{10}$(rate per second). The last three columns contain the multiplicative factor of how much faster the tunneling rates with different isotopologues are compared to the non-tunneling rate. The effective mass for proton tunneling in a.m.u. is M_{eff}.

Considering the rates for the carbon skeleton rearrangement, $B \to D$, the DFT and coupled cluster energies differ by 19.2 to 33.9 kJ mol^{-1}. The energies of the transition states of the fragmentation and the recombination are about the same, 95.1 kJ mol^{-1} for $B \to C$ and 94.6 kJ mol^{-1} for $C \to D$. In contrast to the experimental conclusion that no single step was cleanly rate-limiting [24, 25] the energy differences between the barriers of the hydrogen transfer $E \to D$ and the carbon skeleton rearrangement differ by 15.9 kJ mol^{-1} and 16.4 kJ mol^{-1}. However, the direct reaction $E \to C$, when ignoring the barriers for the hydrogen transfer, has calculated rates based on LUCCSD(T) barriers that are only 15.5 and 16.8 times higher (at 273.15 K and 300 K, respectively) than $E \to D$. Note that rates are measured and calculated in the direction of $E \to D$ and not from $D \to E$. This translates to an energy difference of only 7 kJ mol^{-1} from the Arrhenius factor which is possibly smaller than the accuracy of the QM/MM energies. Noteworthy, a rather large difference of 16.4 kJ mol^{-1} in the potential energies accomplishes the small difference in the rate: the zero-point energy reduces the barrier for $E \to D$ by 12.3 kJ mol^{-1} while it reduces the barrier $D \to C$ by only 3.8 kJ mol^{-1}. The rates, of course, include tunneling additionally to the zero-point energy.

The calculated tunneling rates are higher than the non-tunneling rates, see Table 5.17 and Table 5.16. However, they are very low compared to rates measured experimentally.
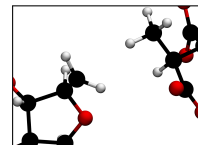
Temperature	BP86	M06	LUCCSDT
$k_{no\text{-}tunnel}$			
300 K	14.81	0.001 659	0.000 845
273.15 K	1.28	0.000 144	0.000 028
k_{tunnel}			
300 K	136.08	0.015 250	0.007 764
273.15 K	15.81	0.001 772	0.000 345
$k_{tunnel}/k_{no\text{-}tunnel}$			
300 K	9.19	9.19	9.19
273.15 K	12.30	12.30	12.30

Table 5.16: QM/MM non-tunneling and instanton tunneling rates (protium transfer) for the transition $E \rightarrow D$ (78 atoms) with different QM energy expressions (DFT and Coupled Cluster) at different temperatures.

Temperature	BP86	M06	sd-LUCCSDT
$k_{no\text{-}tunnel}$			
300 K	550 000	19.64	9.44
273.15 K	120 000	1.54	0.69
k_{tunnel}			
300 K	3 290 000	115.30	55.44
273.15 K	68 000	8.82	3.94
$k_{tunnel}/k_{no\text{-}tunnel}$			
300 K	5.87	5.87	5.87
273.15 K	5.74	5.74	5.74

Table 5.17: QM/MM non-tunneling and instanton tunneling rates (protium transfer) for the transition $A \rightarrow B$ (78 atoms) with different QM energy expressions (DFT and Coupled Cluster) at different temperatures.

The measured rates have a great spread ranging from 5.8 s^{-1} to 97 ± 5 s^{-1} as mentioned in the introduction [21, 23, 46, 47]. The calculated overall rates are smaller than the measured ones by about four orders of magnitude. This translates to an error in the barrier height of about 26 kJ mol^{-1} despite the efforts to use the highest level of theory currently achievable for enzymatic systems. It should be emphasized, however, that inaccuracies in the barrier height cancel when KIEs are calculated, which increases the reliability of the predicted KIEs.
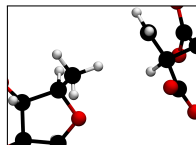
5.3.3 Primary KIEs

Calculations and experimental measurements of KIEs are more accurate than rates. An isotopic substitution at an atom directly involved in establishing or breaking bonds during the reaction results in a primary KIE. In the following the results of primary KIE calculations will be discussed and compared to experiment, for a summary see Table 5.18.

With per- and trideuterated Glu substrate the value of the calculated primary deuterium KIE of 10.3 at 273.15 K for the transition $A \rightarrow B$ is in good agreement with the experimental result of 10 ± 0.4 [21] which was obtained by a competitive measurement (with both deuterated and unlabeled substrate in the same vessel) at 283 K, see Table 5.18. The higher KIE of 16.8 for $E \rightarrow D$ with per- and trideuterated MA substrate supports the notion that tunneling is more important for the hydrogen abstraction from MA.

	This work		Experiment	
Substrate	273.15 K	300 K	283 K	273 K
	Transition $A \rightarrow B$			
^{2}H$_3$-Glu	10.3	11.3	10 ± 0.4 [21] 28[23]	
^{2}H-Glu	9.0	10.0		
	Transition $E \rightarrow D$			
^{2}H$_3$-MA	16.8	14.0	35 [23]	
^{2}H-MA	13.5	11.5	4.1 [24]	6 [25]

Table 5.18: Primary deuterium KIEs for the hydrogen transfers $A \rightarrow B$ and $E \rightarrow D$ on the formation of Ado-H [21, 24, 25] or cob(II)alamin [23], respectively.

	This work		Experiment
	273.15 K	300 K	283 K
$A \rightarrow B$	28.4	27.8	21 [22]
$E \rightarrow D$	46.1	34.7	19 [22]

Table 5.19: Primary tritium KIEs with monotritiated substrate.

The calculated KIEs are somewhat higher than most experimental values, see Table 5.18. The measured rates can be masked by experimental side effects such as undetection through measuring instruments of a deuterium or tritium content below a certain threshold or multiply deuterated substrate. The measured rates and KIEs are always apparent or observed rates under certain conditions without excluding back and forth reactions at the same time. The intrinsic (the true) KIEs are derived from these. The
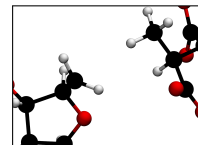
simulations determined intrinsic rates with exactly one deuterium as substitute for one protium. The calculated deuterium KIEs for the transition $E \rightarrow D$ lie between the high and low measured KIEs given in Table 5.18. The large measured KIEs [23] seem to be sensitive to several side effects during the reaction and suffering from systematic error [21].

The primary tritium KIEs are compared to experiment in Table 5.19. Again, the calculated values are slightly higher than the measured ones, which may again be attributed to masking effects. The measurements of primary tritium KIEs used monotritiated AdoCbl and considered the transfer of tritium from Ado-H to Glu or MA substrate. At 283 K the experimental primary tritium KIE for Glu substrate ($A \rightarrow B$) was 21 and for MA substrate 19 ($E \rightarrow D$) [22]. The computational results at 273.15 K are 28 for $A \rightarrow B$ and 46 for $E \rightarrow D$. The results for primary deuterium as well as for tritium KIEs confirm the conclusion drawn from the rates, that tunneling is more important for the transition from $E \rightarrow D$ than for $A \rightarrow B$.

5.3.4 Secondary KIEs
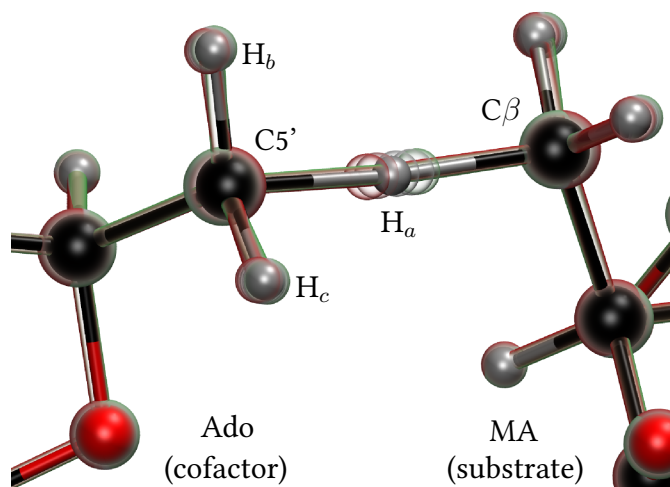
Figure 5.18: The hydrogen transfer between Ado and the MA substrate, $E \rightarrow D$. Atoms mentioned in the text are labeled. The transparent spheres show the instanton indicating the dominant tunneling motion.

Secondary KIEs result from isotopic substitution of atom which keep their bonds intact during the reaction, see Section 1.1.2. These KIEs allow to characterize such coupled motions. Secondary KIEs help to find out whether motions in the neighborhood of the transferred hydrogen atoms mask the primary KIEs and allow to characterize such
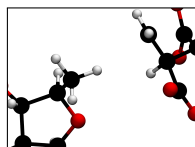
coupled motions. Here computational and experimental results for secondary tritium KIEs will be compared, see Table 5.20. The tritium was placed at the 5'-carbon of the Ado in the calculational and the previous experimental investigations.[21, 54, 55] When replacing two different hydrogen atoms by tritium different KIEs for each of them were obeserved. In Fig. 5.18 the replaced atoms in primary and secondary positions are labeled.

Primary H_a	Secondary	Tunneling 273.15 K	300 K	Non-tunneling 273.15 K	Experiment 283 K
Transition $A \rightarrow B$					
^{1}H	H_b	0.857	0.856		0.76 ± 0.02 [54]
^{1}H	H_c	0.945	0.926		0.76 ± 0.02 [54]
^{2}H	H_b	0.803	0.827	0.818	1.05 ± 0.08 [55]
^{2}H	H_c	0.894	0.910	0.897	1.05 ± 0.08 [55]
Transition $E \rightarrow D$					
^{1}H	H_b	0.978	0.879		
^{1}H	H_c	0.900	0.933		
^{2}H	H_b	0.793	0.819	0.782	
^{2}H	H_c	0.839	0.863	0.822	

Table 5.20: Secondary tritium kinetic isotope effects for the hydrogen transfers $A \rightarrow B$ and $E \rightarrow D$ with monotritiated Ado. The substrate was perdeuterated for investigations of deuterium in primary position. See Fig. 5.18 for atom labeling.

An inverse KIE means that deuterium or tritium increase the reaction rate compared to protium, which leads to a KIE smaller than 1. Replacing H_b with tritium (protium in primary position) results in inverse KIEs. The calculation of secondary KIEs with protium in the primary position (H_a) in principle requires to optimize another instanton – a significant computational demand. It can be avoided by keeping the instanton path fixed despite the substitution of the nucleus, the fixed-path approximation, see Section 4.2.1. The approximation is tested on two secondary KIEs at 273.15 K. Using the FPA the calculated KIEs are 0.857 and 0.978, compared to the KIEs of 0.901 and 0.852 for full instanton optimization ($A \rightarrow B$ and $E \rightarrow D$, respectively). The values are similar, the FPA is a valid approximation and is used in all the following KIEs with protium in primary position. With deuterium in the primary position the inverse KIEs are larger (closer to zero) than with protium, which is in contrast to the experimental results. When substituting H_c instead of H_b with tritium the inverse KIEs with protium and deuterium in the primary position decreases (becomes closer to 1) in the case of $A \rightarrow B$. The same is observed for $E \rightarrow D$ except for the KIE with protium in the primary position at 273.15 K. The experimental values are expected to be an average of both values (H_b and H_c). However, for the secondary tritium KIE with protium in
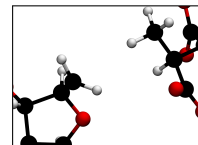
primary position, $A \rightarrow B$, an experimental value of 0.76 ± 0.02 was found [54]. The use of purely non-tunneling rates results in secondary tritium KIEs (H_b replaced) and protium in the primary position at 273.15 K of 0.796 ($A \rightarrow B$) and of 0.782 ($E \rightarrow D$). These values are closer to the experimental results than the KIEs based on tunneling rates. Experimentally, the large inverse secondary tritium kinetic isotope effect of 0.76 ± 0.02[54] was interpreted as the C5′-H bonds becoming stiffer during the reaction from Ado to Ado-H. The secondary tritium KIEs for $A \rightarrow B$ with deuterium in the primary position based on non-tunneling rates at 273.15 K are 0.897 (H_c replaced) and 0.818 (H_b replaced). These and the calculated secondary KIEs for $E \rightarrow D$ with deuterium in primary position remain essentially unchanged when using non-tunneling instead of tunneling rates: 0.782 for $H_b={}^3H$ and 0.822 for $H_c={}^3H$. The experimental measured secondary KIEs for $E \rightarrow D$ include implicitly the effects of the Co–C bond homolysis $E_0 \rightarrow E$ which could cause the difference between calculations and experiments.

The formation of Ado-H is a reversible reaction. Thus, the apparent rate constants measured to determine the secondary isotope effect with deuterium in the primary position include forward and reverse rate constants [54, 55]. However, the KIEs are less error-prone than the apparent rate constant, as some errors cancel in the ratio of the rates. The apparent KIE measured with deuterium in primary position is close to unity, see 5.20, which differs from the calculated KIEs [55]. The differences between experimental and computed results can be due to side effects in measurements, to fitting problems of the experimental data, or geometrical effects of the environment which will be discussed in the next section.

5.3.5 Participation of the environment in the tunneling process

	Number of active atoms							
	1	7	11	23	34	48	54	78
${}^2H$	10.6	13.8	16.1	16.0	13.6	14.0	13.5	13.5
${}^3H$	39.9	47.5	55.1	54.9	46.5	47.9	46.2	46.1

Table 5.21: Deuterium and tritium kinetic isotope effects for the hydrogen transfer from $E \rightarrow D$ at 273.15 K with monodeuterated or -tritiated substrate and different active subspaces.

The instanton optimizations provide the most-likely tunneling path. The most-likely reaction path from a minimum to the start of the tunneling path is provided by the intrinsic reaction coordinate (minimum-energy path) between these points. On average, the system is expected to move classically along the intrinsic reaction coordinate to the first caustic point, the start of the instanton path, tunnel to the second caustic point,
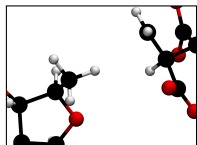
the end of the instanton path, and proceed along the intrinsic reaction coordinate to the product minimum. This combined path is visualized in Fig. 5.19 for $E \to D$ at 273.15 K. The energy profile along that path (BP86/MM level) is illustrated in Fig. 5.20. The heavy atoms dominate the classical movement. The system optimizes the tunneling path to mainly consist of hydrogen-atom movement. In Fig. 5.19 this becomes apparent by the tunneling paths being of significant length only for the transferred hydrogen atom, while the red and green curves (classical paths) are long also for carbon atoms. Fig. 5.20 compares the reaction path for all atoms in Cartesian coordinates to the path in mass-weighted Cartesian coordinates. The fact that the tunneling motion is dominated by hydrogen shortens the section of this motion in the mass-weighted path compared to the Cartesian path length. The mass-weighted path length is the relevant quantity for the reaction rate.

Tunneling is rather weak, only a rather short portion of the reaction path is covered by tunneling motion. Also energetically, the system moves up most of the barrier classically, while only tunneling though the top. At much lower temperature (not accessible by enzymatic reactions) a larger fraction of the path would be covered by tunneling. The instanton path proceeds through a point slightly (1 kJ mol^{-1}) higher than the classical transition state, see Fig. 5.20. This expense comes at the benefit of a shorter tunneling path – an effect known as corner cutting [112].

It should be noted, of course, that what is shown here is only the most-likely reaction path including tunneling. In reality, the path as well as the tunneling energy will fluctuate. The most-likely tunneling energies for deuterium and tritium in the primary position lie above the classical barrier height, which makes instanton theory inapplicable in these cases, see Section 5.3.1.

The atoms in the direct neighborhood of the transferred hydrogen at the Glu substrate and at the ribose ring of the adenosyl radical, and also several hydrogen atoms on Arg 66 are involved in the most likely tunneling process $E \to D$, as illustrated in Fig. 5.21.

The hydrogen atoms H_b and H_c, the secondary hydrogen atoms at the 5'-carbon atom, influence the motions of the transferred primary hydrogen atom H_a. These atoms move from planar sp^2 to tetrahedral sp^3 geometry around the 5'-carbon. Their motions are coupled during the transition, see Fig. 5.21. Such movements increase the effective mass (defined analogously to the effective mass M_{eff} in molecular vibrations, see page 134) and reduce the tunneling efficiency. For the transition $A \to B$ the effective tunneling mass is $M_{\text{eff}} = 1.139$ a.m.u. (instead of $M_H = 1.008$ a.m.u.) and in $E \to D$ it is slightly higher $M_{\text{eff}} = 1.163$ a.m.u. The motions are coupled to all transferred nuclides (protium, deuterium, and tritium), but have the highest effect on protium. The calculations hint that coupled motions are less important during the tunneling motion than previously thought, as the secondary tritium KIEs, see Table 5.20, were found to be about the same irrespectively of protium or deuterium in the primary position.
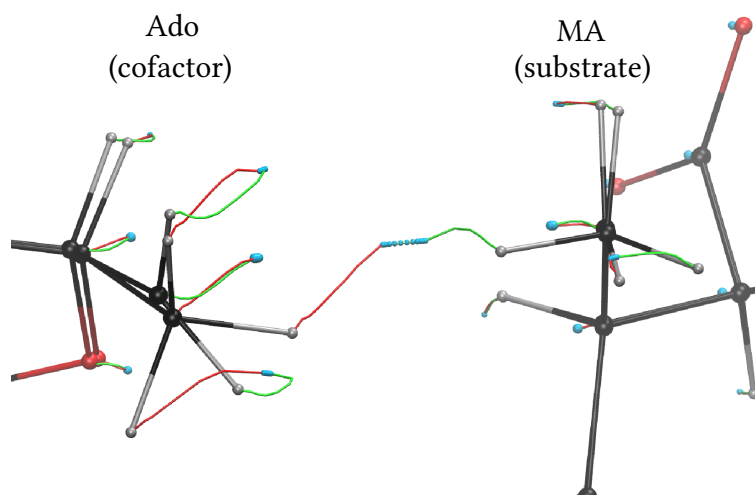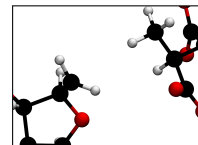
Figure 5.19: The most likely reaction path (intrinsic reaction coordinate and instanton path) of the transition $D \rightarrow E$. The non-tunneling paths are denoted in red (start at D) and green (end at E). The blue balls between the red and green paths denote the instanton tunneling path.

To explore the influence of motions in the direct neighborhood of the active center the tunneling motion was restriced to smaller sets of atoms, see description in Section 5.3.1. The results are summarized in Table 5.15 and Table 5.21. The larger the active subspace the higher the effective mass during the transitions. The primary tritium KIE for $E \rightarrow D$ with only H_a allowed to tunnel is 39.9 at 273.15 K. This KIE is slightly smaller than the KIE of 46.1, see Table 5.19, for 78 tunneling atoms. The multiplicative factors between tunneling and non-tunneling rates with only H_a allowed to tunnel are 3.36 for deuterium and 2.21 for tritium. Much smaller than for the 78-atom-set (with factors of 5.45 for ^{2}H and 3.40 for ^{3}H). Thus, for a successful tunneling contribution the motions of the neighboring atoms are crucial to enhance the deuterium and tritium rates. For these two heavier isotopes the factors between tunneling and non-tunneling rates are the same for all sets of tunneling atoms except for the set with only H_a included. The motions of the neighboring atoms are much more important for protium transfers than for its heavier nuclides. For ^{1}H the tunneling rate for one active atom is 4.58 times faster than the non-tunneling rate. For the large active space with 78 atoms the factor is 12.30. Thus, forbidding coupled motions by restricting the set of tunneling atoms to one atom lowers the tunneling enhancement. On the other hand, this restriction increases the contributions of zero-point vibrations to the tunneling and non-tunneling rates and, therefore, the rates are larger than in the greater set of tunneling atoms. The contributions of zero-point vibrations are larger for one atom,
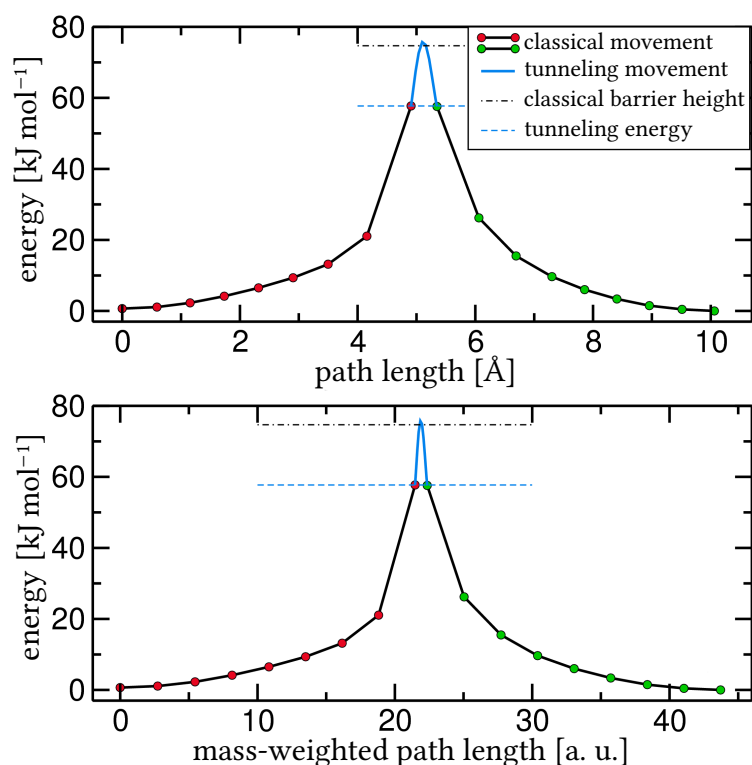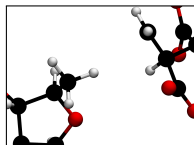
Figure 5.20: Energy profile (BP86/MM) along the most likely reaction path (intrinsic reaction coordinate, red and green dots, and instanton path, blue) of the transition $D \rightarrow E$. The path length covers all atoms.

as the frozen environment is like a rigid wall with a steep potential energy valley in contrast to the softer and more flexible C-H-skeleton environment of the 78-atom-set. Allowing tunneling movements of $C\beta$ and $C5'$, and their hydrogen atoms (active subspace with 7 atoms) results in a tunneling enhancement by a factor of 12.65, similar to the enhancement in the 78-atom-set (factor 12.30). Extending the tunneling region to 11 and 23 atoms increases the enhancement factor to 14.6 and the KIE to about 16 instead of 14, see 5.15. Including the ribose ring of the adenosyl radical to the active subset (34- to 78-atom-sets) yielded smaller enhancement factors and primary KIEs (^{2}H and ^{3}H), all similar to the results of the 78-atom-set. With 34 atoms the effective mass, $M_{eff} = 1.1636$ a.m.u., for the hydrogen transfers is basically the same as with 78 atoms, $M_{eff} = 1.1634$ a.m.u., whereas with 7, 11, and 23 active atoms it is slightly lower ($M_{eff} = 1.1598$ for 7 tunneling atoms). Thus, motions of the ring play a central role during the tunneling of the hydrogen transfers.

These coupled motions can, on the one hand, transfer energy from the atoms moving at the ring into the movements of the transferred hydrogen atom, which would enhance
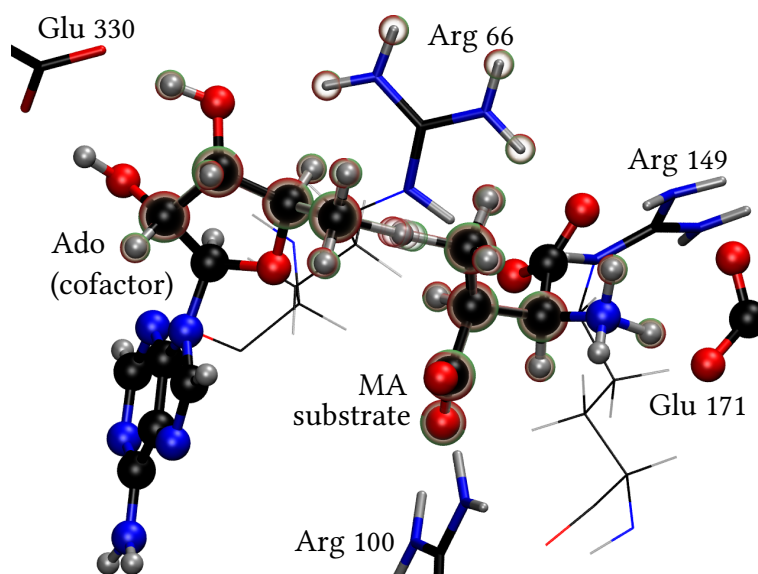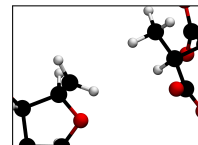
Figure 5.21: The large active region (78 atoms, $E \rightarrow D$) including the QM region (in ball and stick representation) consisting of Ado (left), MA substrate (middle), and the side chain of Glu 171 (right). Carbon is shown in gray, oxygen in red, nitrogen in blue, and hydrogen in white. Transparent spheres denote the movements of tunneling atoms.

the rate, and on the other hand increase the mass and reduce the tunnel rate. Two types of motions are involved in the hydrogen transfers. The classical motions (1) of the heavier carbon and oxygen atoms prepare the tunneling motions of the lighter hydrogen atoms. The larger these classical motions are, the less important is the tunneling effect. The coupled motions (2) of the ribose ring at Ado and the motions of the hydrogen atoms in the neighborhood of H_a which reduce the tunneling rate, see results given above. These motions are coupled in the transition state and part of the tunneling motions.

Another reason for the tunneling enhancement to be smaller with one active atom is that the environment is tensed when the movement of carbon atoms ($C\beta$ and C5′) is forbidden. A highly tensed environment leads to smaller rates for all isotopologues. The rates for 11 and 23 tunneling atoms with the ribose ring excluded from the tunneling motion (the delocalization) are smaller, see Fig. 5.21 and 5.15, than for the larger sets of atoms. Therefore, the tunneling effects dominate over the tensions when the active subspace comprises more than 34 atoms.

The simulations confirm the experimental conclusion from secondary tritium KIE measurements [54], that the rehybridization of the C5′, from planar to tetrahedral, occurs before or during the transition state for the hydrogen abstraction from substrate.
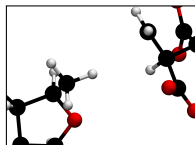
In the transition state both carbon atoms (Cβ and C5′) have a distorted tetrahedral coordination close to sp^3 geometry, see Fig. 5.18, Fig. 5.19, and Fig. 5.22.
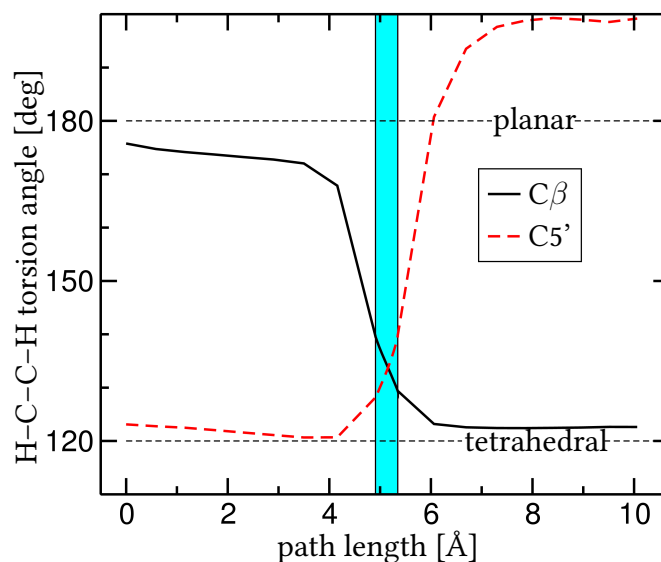
Figure 5.22: Dihedral angles around C5′ and Cβ showing the transition from an almost planar geometry to a distorted tetrahedral geometry during the transition $\boldsymbol{D} \to \boldsymbol{E}$. The segment of the path highlighted with blue background is the tunneling motion. The path length covers all atoms, as in Fig. 5.20.

The effective mass in harmonic vibrations

In this section the effective mass in harmonic vibrations is briefly derived. The effective tunneling mass is defined analogously. Given a one-dimensional system with two atoms of position $\boldsymbol{x}_1$ and $\boldsymbol{x}_2$. The masses of the atoms are M_1 and M_2. Let the potential energy be:

$$V(\boldsymbol{x}_1, \boldsymbol{x}_2) = \frac{k}{2}(\boldsymbol{x}_1 - \boldsymbol{x}_2)^2, \tag{5.6}$$

where k is the spring constant. Mass-weighted coordinates are defined as $\boldsymbol{y}_j = \sqrt{M_j}\boldsymbol{x}_j$. From that one obtains two different Hessians for non-mass-weighted H_x and mass-weighted H_y coordinates:

$$H_x = \begin{pmatrix} k & -k \\ -k & k \end{pmatrix} \qquad H_y = \begin{pmatrix} \frac{k}{M_1} & -\frac{k}{\sqrt{M_1 M_2}} \\ -\frac{k}{\sqrt{M_1 M_2}} & \frac{k}{M_2} \end{pmatrix}. \tag{5.7}$$
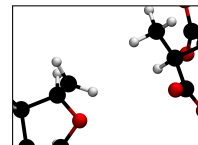
The eigenvectors of H_y are easy to obtain. From the Cartesian eigenvector of the translation $\boldsymbol{t}_x = (11)^T$ follows

$$\boldsymbol{t}_y = \begin{pmatrix} \sqrt{M_1} \\ \sqrt{M_2} \end{pmatrix}. \tag{5.8}$$

The only orthogonal vector to $\boldsymbol{t}_y$ is the eigenvector of the vibration:

$$\boldsymbol{v}_y = \begin{pmatrix} -\sqrt{M_2} \\ \sqrt{M_1} \end{pmatrix} \Rightarrow \boldsymbol{v}_x = \begin{pmatrix} -\sqrt{M_2}/\sqrt{M_1} \\ \sqrt{M_1}/\sqrt{M_2} \end{pmatrix}. \tag{5.9}$$

Elongation along $\boldsymbol{v}_x$ conserves the center of mass: $\boldsymbol{v}_{x,1} M_1 = -\boldsymbol{v}_{x,2} M_2$. The vector $\boldsymbol{v}_x$ can be normalized to $\bar{\boldsymbol{v}}_x$:

$$\bar{\boldsymbol{v}}_x = \frac{1}{\sqrt{M_1^2 + M_2^2}} \begin{pmatrix} -M_2 \\ M_1 \end{pmatrix}. \tag{5.10}$$

The second directional derivative of V in the direction of $\boldsymbol{v}_x$ is the force constant of the vibration k_v. This constant is related to the vibrational frequency ω by $\omega^2 = k_v/M_{\text{eff}}$ which defines the effective mass M_{eff}. k_v is obtained by

$$k_v = \bar{\boldsymbol{v}}_x^T H_x \bar{\boldsymbol{v}}_x = \frac{1}{M_1^2 + M_2^2} \begin{pmatrix} -M_2 \\ M_1 \end{pmatrix}^T \begin{pmatrix} k & -k \\ -k & k \end{pmatrix} \begin{pmatrix} -M_2 \\ M_1 \end{pmatrix} = k \frac{(M_1 + M_2)^2}{M_1^2 + M_2^2}. \tag{5.11}$$

By calculating the eigenvalues of H_y the frequency ω can be obtained:

$$\left(\frac{k}{M_1} - \omega^2 \right) \left(\frac{k}{M_2} - \omega^2 \right) - \frac{k^2}{M_1 M_2} = 0 \Rightarrow \omega^2 = k \frac{(M_1 + M_2)^2}{M_1^2 + M_2^2}. \tag{5.12}$$

The same results yields $\omega^2 = \bar{\boldsymbol{v}}_y^T H_y \bar{\boldsymbol{v}}_y$. Combining the later two equation with $\omega^2 = k_v/M_{\text{eff}}$ results in

$$\bar{\boldsymbol{v}}_y^T H_y \bar{\boldsymbol{v}}_y = \bar{\boldsymbol{v}}_x^T H_x \bar{\boldsymbol{v}}_x / M_{\text{eff}}. \tag{5.13}$$

Thus, the effective mass is given as

$$M_{\text{eff}} = \frac{M_1 M_2 (M_1 + M_2)}{M_1^2 + M_2^2} \tag{5.14}$$

which is different form the general assignment of

$$M_{\text{eff}} = \frac{M_1 M_2}{M_1 + M_2}.$$

The general assignment either neglects the fact that the directional derivative of V is not k or ignores the norm of $\boldsymbol{v}_x$. The extension of equation (5.14) to more dimensions is straightforward. Using $\boldsymbol{v}_y = \text{diag}(\sqrt{M}) \boldsymbol{v}_x$ and equation (5.13) we obtain for a normalized $\boldsymbol{v}_y$, with $\boldsymbol{v}_y^T \boldsymbol{v}_y = 1$:

$$\frac{1}{M_{\text{eff}}} = \boldsymbol{v}_y^T \text{diag}\left(\frac{1}{M} \right) \boldsymbol{v}_y. \tag{5.15}$$

After this short theoretical digression the discussion of the results of the tunneling rate calculations in GM continues.
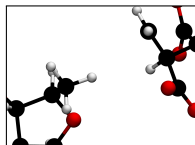
5.3.6   Does a different step become rate-determining through a ^{1}H/^{2}H substitution?

The (measured) primary KIEs can be masked by other intermediate steps, causing the measured KIEs to be smaller than the intrinsic KIEs. A step other than hydrogen transfer could be rate limiting for protium transfer. Substitution of protium by deuterium or tritium could then render the hydrogen transfer rate-limiting. As mentioned in Section 5.3.2, the rate for $\boldsymbol{E} \to \boldsymbol{D}$ is only 16 times lower than for the direct transition $\boldsymbol{E} \to \boldsymbol{C}$, when the hydrogen transfer barrier is ignored. Thus, the carbon skeleton rearrangement would become rate-limiting if the calculations underestimated its barrier by only 7 kJ mol^{-1}. This may well be within the error bar of QM/MM simulations, despite the quite high level of theory (sd-LUCCSD(T)/MM) used to obtain the barriers. Deuterium transfer is slower by another factor of 11.5–16.8. Thus, deuterium transfer is clearly rate-limiting. The isotopically sensitive step not being fully rate-limiting is one form of masking of KIEs. It may explain why the calculated KIEs are generally somewhat larger than the experimental ones.

Despite the frequencies being based on BP86, which underestimates the energy barriers and frequencies compared to the M06 functional or LUCCSD(T), the calculated rates reproduce the qualitative behavior of the system. Higher frequencies would result in a larger rate. Also some rapid quench measurements hint that a slower step could mask the isotopically sensitive step in GM [18, 21, 22, 46, 53], which would reduce the measured KIE from its intrinsic value. The change of the rate limiting step through a conformational change in the protein can be excluded as the protein moves negligibly during the catalytic cycle. The enzyme seems to modulate the transition states for the hydrogen transfers while changing the isotope effect. In the active enzyme the protein is already in a pre-organized form that allows the enzyme to modulate tunneling motions, vibrations, and coupled motions. On the other hand, $\boldsymbol{A}$ is a high energy intermediate not accumulating during the reaction [21, 23]. Therefore it is unlikely that the homolytic cleavage of AdoCbl can become rate-limiting. Further, starting at $\boldsymbol{A_0}$ or $\boldsymbol{E_0}$ could result in a much higher barrier for $\boldsymbol{A_0} \to \boldsymbol{B}$ or $\boldsymbol{E_0} \to \boldsymbol{D}$. Then it would be even less likely that the carbon skeleton rearrangement could become rate-limiting.

The results of all caluclations with GM will be summarized in Chapter 6.

Summary and Conclusions

6.1 Improvements of the instanton technique to calculate tunneling rates in large systems

In instanton theory the main object of interest is the instanton, the most-likely tunneling path at a given temperature solving Euler's equation of motion. The instanton (pseudoparticle) is also a first-order saddle point of the Euclidean action in the space of closed Feynman paths. Due to a mathematical analogy, the so-called Wick rotation from Minkowski space to Euclidean space, see Chapter 2, an instanton can also be considered as an unstable closed orbit of a particle moving on an upside-down potential energy surface in negative imaginary time. The time discretized instanton is represented by a chain of particles (replicas or images). Each discretization point of the imaginary time corresponds to an image of the considered molecule.

In Chapter 3 a stringent formulation of the imaginary F instanton rate theory in variable step-size discretization of the Feynman paths by applying a rigorous time-slicing definition of the path integration was derived. This is to my knowledge the first step-by-step derivation of the instanton rate prefactor with a variable step-size discretization in d dimensions. The basic definitions of the used mathematical objects are presented in Chapter 2. The variable step-size discretization along the imaginary time, presented in Chapter 3 and tested in Section 4.2, is an extension of the existing instanton method.

Chapter 4 starts with a comparison of four algorithms implemented to locate instantons. Instanton theory allows to calculate reaction rates, including atom-tunneling, down to very low temperature. The problem of finding an instanton is adressed as a saddle-point search problem. The Newton–Raphson method was compared to the partitioned rational function optimization (P-RFO) algorithm, the dimer method, and a newly proposed mode-following algorithm, where the unstable mode is directly estimated from the instanton path. The algorithms were tested on three chemical systems, see Section 4.1.4 on page 74, each including a hydrogen transfer, at different temperatures. Overall, the Newton–Raphson turned out to be the most promising method, consistently efficient and stable, with the dimer and the newly proposed mode following, being the fall-back option.

The results of Section 4.1.5, page 80, show that instantons can be optimized rather efficiently. The geometry optimization generally requires fewer evaluations of energy and its gradients than subsequent Hessian calculations at each image, at least if the latter are done by finite-difference calculations of gradients using the two-point formula. Efficiency in the Hessian calculations can of course be improved by using analytic Hessians instead. At lower temperature an additional challenge in instanton theory is that more and more images of the discretized path tend to accumulate at one end of the instanton path (the one with the smaller slope of the energy along the path). Up to some point, this can be accounted for by using more and more images. However, to apply instanton theory to really low temperature, or to calculate the limit at $T \to 0$, methods are required that allow to calculate the rate using the Hessian at fewer points along the instanton.

In Chapter 4 the expressions to locate instantons and calculate reaction rates for instanton paths reduced to a line, as it is the case in molecular systems, are derived. The adaptation of the variable step-size to the temperature is demonstrated which allows to apply instanton theory at low temperature while avoiding the accumulation of images at the ends of the instanton path observed with the traditional constant step-size discretization. The applicability and accuracy of the method was tested, see Section 4.2.2 on page 85. The new algorithms save more than one order of magnitude in CPU time.

The improved instanton method allows efficient calculations of tunneling rates at various temperatures. The combination of Hessian-based instanton optimization with updating strategies, like for example Bofill updates, is the most imporant contribution. The instanton method can be applied in combination with high-level theories, e.g., coupled cluster or density functional theory, to obtain rates based on quantum mechanical energies including a correct description of forming and breaking bonds. It can in principle be used with any potential enery surface. Finally, instanton theory allows to calculate tunneling rates involving several quantized atoms. This is especially interesting in systems like enzymes in order to find out which atoms are involved in

the tunneling motion.

6.2   Application to the enzyme glutamate mutase

I studied the radical conversion mechanism of glutamate to methylaspartate catalyzed by glutamate mutase (GM) in atomistic detail using a QM/MM approach based on DFT and local coupled cluster methods, see Chapter 5. The conversion of glutamate to methylaspartate was found to proceed via a fragmentation–recombination mechanism, see Section 5.2. For a detailed overview of the reaction and the labeling of the different intermediates see Fig. 1.2, page 5 or Fig. 5.6, page 101. The enzymatic reaction was compared to the uncatalyzed reaction in water and in the gas-phase. The hydrogen atom transfer steps exhibit the highest barriers. Here, the transition from an almost planar coordination to a distorted tetrahedral coordination of C5′ and Cβ occurs before and during the transition state. With a barrier of 101.1 kJ mol^{-1} (M06 functional), the transfer $E \rightarrow D$ has the highest barrier. However, the barrier from $A \rightarrow B$ is similar with 84.8 kJ mol^{-1} (M06 functional). The barriers for the hydrogen transfers $A \rightarrow B$ and $E \rightarrow D$ match for DFT (M06 functional) and coupled cluster (LUCCSD(T)) which shows the good predictive value of the results based on the M06 functional, see Section 5.2.1 on page 103.

The thourogh comparison of the reactions in gas phase, water (COSMO), and protein leads to the conclusion that the enzyme environment has a stronger impact on the hydrogen-transfers $A \rightarrow B$ and $E \rightarrow D$ than on the carbon skeleton rearrangement, sturctures B to D. The influence of the enzyme is mostly electrostatical and to a lesser degree sterical, see Section 5.2.3 on page 109.

The calculations shed light on the atomistic details of the reaction mechanism. The well-known arginine claw and Glu 171 are found to have the strongest influence on the reaction. The arginine claw (Arg 66, Arg 100, and Arg 149) keeps the intermediate fragments in place. It raises the energy of intermediate C by steric effects and, thus, facilitates the recombination process. An open arginine claw was found to lead to much higher energies of the intermediates, whereas a closed arginine claw is associated with reaction paths exhibiting the lowest reaction barriers. The arginine claw is crucial for a successful catalysis.

Glu 171, in the vicinity of the glutamate substrate, acts as a catalytic residue by temporarily abstracting a proton from the ammonium group of the substrate. This facilitates the carbon skeleton rearrangement steps (B to D). The proton-transfer changes the dipole moment of the whole active site, an effect being electrostatically buffered by the protein environment.

Careful investigations of the enzyme environment of the active center lead to the identification of additional residues important for the reaction. Significant catalytic roles of Glu 214, Lys 322, Gln 147, Glu 330, Lys 326, and Met 294 are found as well, see Section 5.2.4 on page 113. For example, Glu 330 reduces the barrier of the hydrogen-transfer by establishing stable hydrogen bonds to the ribose ring of Ado. These results highlight new promising experimental targets. Amino acids in considerable distance to the active center were found to have a noticeable influence on the reaction.

The role of tunneling in the enzyme GM was investigated by QM/MM-instanton simulations, see Section 5.3 on page 117. The transition $E \rightarrow D$ has the higher primary KIEs than $A \rightarrow B$. Also the speed-up between non-tunneling and tunneling rates is larger for $E \rightarrow D$. Thus, tunneling is more important in $E \rightarrow D$ than in $A \rightarrow B$. Primary deuterium KIEs are in good agreement with experiment.

The secondary tritium KIEs, see Section 5.3.4 on page 127, hint that coupled motions on the ribose ring of Ado are part of the tunneling motions. Classical movements of the enzyme are important to prepare the system for the tunneling motions. The heavier atoms like oxygen or carbon display small tunneling and large classical motions during the hydrogen transfer $E \rightarrow D$. Allowing tunneling in different sub-sets of the active center showed that the motions at the ribose ring of Ado play a central role during the tunneling enhancement of the hydrogen transfers. The enzyme uses both classical and tunneling motions for a successful catalysis.

These simulations lead to an improved understanding of the catalysis of the carbon skeleton rearrangement of Glu or MA substrate by glutamate mutase.

Part III

Appendix

SUPPORTING MATERIAL: REACTION MECHANISM OF GLUTAMATE MUTASE

Epsilon	infinity	80	10	4
A	0.0	0.0	0.0	0.0
TS-AB	34.6	34.1	30.9	25.3
B	−33.0	−33.3	−35.2	−38.1
TS-BC	46.0	46.1	46.5	46.7
C	21.5	21.5	21.3	20.5
TS-CD	43.0	42.9	42.4	41.7
D	−17.4	−18.0	−21.7	−26.4
TS-DE	41.6	40.9	36.9	31.1
E	−9.0	−9.4	−11.6	−14.1

Table A.1: Different dielectric constants for COSMO calculations with BP86 and cc-pVTZ (relative energies in kJ mol^{-1}).

A.1   Data for all snapshots

Structure	SN-Glu-1	SN-Glu-2	SN-Glu-5
A	−1679.509479	−1681.538948	−1680.388094
TS-**AB**	−1679.479110	−1681.503543	−1680.350696
B	−1679.517693	−1681.547825	−1680.399394
TS-**BC**	−1679.486116	−1681.517351	−1680.368323
C	−1679.501210	−1681.523456	−1680.382552
TS-**CD**	−1679.482484	−1681.509053	−1680.370519
D	−1679.505967	−1681.536070	−1680.392792
TS-**DE**	−1679.467238	−1681.489689	−1680.329563
E	−1679.504325	−1681.532140	−1680.388667

Structure	SN-MA-1	SN-MA-2	SN-MA-3
A	−1680.736409	−1680.403903	−1680.109763
TS-**AB**	−1680.689040	−1680.330998	−1680.072679
B	−1680.740966	−1680.406146	−1680.114692
TS-**BC**	−1680.718030	−1680.378611	−1680.085426
C	−1680.735381	−1680.391672	−1680.097073
TS-**CD**	−1680.716203	−1680.367774	−1680.079078
D	−1680.745113	−1680.400359	−1680.109852
TS-**DE**	−1680.657732	−1680.311812	−1680.063893
E	−1680.731028	−1680.384358	−1680.095796

Table A.2: QM/MM energies of six snapshots (M06 energies in Hartree at BP86 geometries)

Structure	N–O	N–H$_N$	C5'–C$_\gamma$	H$_\gamma$–C$_\gamma$	H$_\gamma$–C$_\beta$	C$_\beta$–C$_\alpha$	C$_\gamma$–C$_\alpha$
A	2.643	1.098	3.911	1.097	2.155	1.541	2.589
TS-**AB**	2.690	1.098	2.772	1.342	2.384	1.561	2.550
B	2.636	1.102	4.120	3.298	4.191	1.559	2.520
TS-**BC**	2.639	1.581	3.902	3.087	3.594	2.217	2.936
C	2.653	1.612	3.923	3.109	2.944	3.235	3.356
TS-**CD**	2.628	1.558	4.518	3.542	3.117	2.839	2.103
D	2.639	1.098	4.820	3.839	3.368	2.538	1.576
TS-**DE**	2.695	1.097	3.774	2.396	1.376	2.606	1.576
E	2.650	1.095	4.821	2.156	1.096	2.573	1.555

Table A.3: Distances in Å changing during the reaction SN-Glu-2

Structure	N–O	N–H$_N$	C5'–C$_\gamma$	H$_\gamma$–C$_\gamma$	H$_\gamma$–C$_\beta$	C$_\beta$–C$_\alpha$	C$_\gamma$–C$_\alpha$
A	2.596	1.115	4.448	1.099	2.148	1.546	2.591
TS-**AB**	2.616	1.117	2.765	1.355	2.322	1.562	2.572
B	2.586	1.125	4.627	3.843	4.219	1.567	2.529
TS-**BC**	2.603	1.528	4.545	3.781	3.788	2.246	2.928
C	2.628	1.568	4.369	3.708	3.088	3.344	3.476
TS-**CD**	2.664	1.614	5.024	4.139	3.261	2.909	2.113
D	2.629	1.110	5.405	4.492	3.568	2.560	1.580
TS-**DE**	2.730	1.097	3.917	2.502	1.410	2.639	1.586
E	2.627	1.107	5.468	2.170	1.097	2.572	1.557

Table A.4: Distances in Å changing during the reaction SN-Glu-5

Structure	N–O	N–H$_N$	C5'–C$_\gamma$	H$_\gamma$–C$_\gamma$	H$_\gamma$–C$_\beta$	C$_\beta$–C$_\alpha$	C$_\gamma$–C$_\alpha$
A	2.660	1.081	4.185	1.100	2.175	1.529	2.616
TS-**AB**	2.667	1.087	2.821	1.407	2.674	1.528	2.726
B	2.656	1.078	4.551	3.741	4.897	1.526	2.572

Table A.5: Distances in Å changing during the reaction SN-Glu-6

Structure	N–O	N–H$_N$	C5'–C$_\gamma$	H$_\gamma$–C$_\gamma$	H$_\gamma$–C$_\beta$	C$_\beta$–C$_\alpha$	C$_\gamma$–C$_\alpha$
A	2.603	1.091	4.420	1.104	2.174	1.529	2.567
TS-**AB**	2.627	1.099	2.761	1.396	2.535	1.530	2.632
B	2.596	1.095	4.472	4.017	4.561	1.529	2.554

Table A.6: Distances in Å changing during the reaction SN-Glu-4

Structure	N–O	N–H$_N$	C5'–C$_\gamma$	H$_\gamma$–C$_\gamma$	H$_\gamma$–C$_\beta$	C$_\beta$–C$_\alpha$	C$_\gamma$–C$_\alpha$
A	2.664	1.079	4.106	1.103	2.179	1.530	2.583
TS-**AB**	2.698	1.083	2.798	1.408	2.580	1.535	2.680
B	2.660	1.082	4.212	3.500	4.428	1.529	2.564
TS-**BC**	2.623	1.566	4.503	3.880	4.593	2.293	3.125
C	2.675	1.642	4.864	4.187	4.927	3.222	3.261
TS-**CD**	2.605	1.514	5.392	4.558	5.279	2.759	2.169
D	2.664	1.097	5.646	4.789	5.373	2.470	1.544
TS-**DE**	2.818	1.065	3.806	2.478	1.379	2.603	1.567
E	2.668	1.095	5.710	2.178	1.091	2.510	1.542

Table A.7: Distances in Å changing during the reaction SN-Glu-3

Structure	N–O	N–H$_N$	C5'–C$_\gamma$	H$_\gamma$–C$_\gamma$	H$_\gamma$–C$_\beta$	C$_\beta$–C$_\alpha$	C$_\gamma$–C$_\alpha$
A	2.552	1.398	5.421	2.406	1.481	3.580	3.737
TS-**AB**	2.627	1.539	5.578	2.498	1.472	3.578	3.758
B	2.580	1.473	5.487	2.424	1.469	3.598	3.792
TS-**BC**	2.711	1.678	5.681	2.456	1.398	3.608	3.986
C	2.790	1.772	5.661	2.417	1.379	3.604	4.096
TS-**CD**	2.732	1.692	5.322	2.465	1.403	3.597	3.951
D	2.699	1.096	4.733	2.094	1.493	3.595	3.610
TS-**DE**	2.727	1.094	4.617	2.083	1.497	3.595	3.602
E	2.695	1.098	4.714	2.097	1.497	3.588	3.593

Table A.8: Distances in Å changing during the reaction SN-MA-1

Structure	N–O	N–H$_N$	C5'–C$_\gamma$	H$_\gamma$–C$_\gamma$	H$_\gamma$–C$_\beta$	C$_\beta$–C$_\alpha$	C$_\gamma$–C$_\alpha$
A	2.526	1.190	3.401	1.097	2.150	1.545	2.519
TS-**AB**	2.561	1.435	2.775	1.339	2.324	1.569	2.495
B	2.525	1.369	3.505	2.759	3.079	1.576	2.461
TS-**BC**	2.628	1.588	3.416	2.709	2.780	2.264	2.805
C	2.663	1.641	3.469	2.840	2.857	3.404	2.845
TS-**CD**	2.616	1.566	3.707	2.922	2.725	2.891	2.156
D	2.622	1.104	4.009	3.158	2.707	2.545	1.565
TS-**DE**	2.653	1.105	3.689	2.371	1.372	2.607	1.566
E	2.616	1.108	4.067	2.161	1.095	2.584	1.553

Table A.9: Distances in Å changing during the reaction SN-MA-3

Structure	N–O	N–H$_N$	C5'–C$_\gamma$	H$_\gamma$–C$_\gamma$	H$_\gamma$–C$_\beta$	C$_\beta$–C$_\alpha$	C$_\gamma$–C$_\alpha$
A	2.624	1.143	4.661	1.102	2.138	1.549	2.632
TS-**AB**	2.603	1.137	2.729	1.408	2.382	1.564	2.649
B	2.622	1.138	4.729	4.246	3.918	1.549	2.569
TS-**BC**	2.624	1.563	4.259	3.706	3.685	2.235	2.805
C	2.736	1.708	4.346	3.823	3.503	3.535	2.880
TS-**CD**	2.657	1.601	4.750	4.127	3.620	2.937	2.193
D	2.605	1.132	5.192	4.515	3.838	2.545	1.563
TS-**DE**	2.633	1.136	3.840	2.454	1.411	2.634	1.572
E	2.600	1.136	5.223	2.161	1.097	2.580	1.552

Table A.10: Distances in Å changing during the reaction SN-MA-2

B

Mathematical Approaches

B.1 Short note on Dirac delta function and Gaussian integration

The Dirac δ-function is given as

$$\delta(x) = \begin{cases} 0 & x \neq 0 \\ +\infty, & x = 0 \end{cases} \tag{B.1}$$

for $x \in \mathbb{R}$ and $\int_{-\infty}^{\infty} \delta(x)dx = 1$. It has the following properties:

1. Scaling property: $\int_{-\infty}^{\infty} \delta(\alpha x)dx = \int_{-\infty}^{\infty} \delta(u)\frac{du}{|\alpha|} = \frac{1}{|\alpha|}$ and thus $\delta(\alpha x) = \frac{\delta(x)}{|\alpha|}$.

2. Symmetry: $\delta(-x) = \delta(x)$.

3. Further defining properties: $y(t) = \int \delta(t-s)y(s)ds$, $\delta y(t) = \int \delta(t-s)\delta y(s)ds$, and $\frac{\delta y(t)}{\delta y(s)} = \delta(t-s)$.

The symbol $\delta'(t)$, which means the derivative of the Dirac delta function with respect to t, is properly defined by its behavior in an integral (with integration by parts)

$$\int_a^b \delta'(t-s)f(s)ds = \int_a^b \frac{d}{dt}\delta(t-s)f(s)ds \tag{B.2}$$

$$= -\int_a^b f(s)\frac{d}{dt}\delta(t-s)ds = \int_a^b f'(s)\delta(t-s)ds = f'(t). \tag{B.3}$$

The manipulations here are purely formal, and serve only to motivate the defining property

$$\int_a^b \delta'(t-s)f(s)ds = f'(t).$$ (B.4)

The determinant in the steepest descent approach is designed in analogy to the evaluation of Gaussian integrals. Consider the following one-dimensional example:

$$\int_{-\infty}^\infty dx \exp(-iax^2) = \sqrt{\frac{\pi}{ia}} = \sqrt{\frac{\pi}{a}} \exp(-i\frac{\pi}{4}).$$ (B.5)

The variable $0 < a \in \mathbb{R}$ is analog to the eigenvalues of the Jacobi operator $\mathcal{J}$, see equation (3.14) page 47, and $x \in \mathbb{C}$ is analog to the fluctuations $y(t)$, see equation (3.15) page 47. Thus, in the result on the right hand side we have the square root over a fraction with the eigenvalues of $\mathcal{J}$ in the denominator, which is equal to $\det \mathcal{J}$.

B.2   The Faddeev-Popov Trick: basic ideas

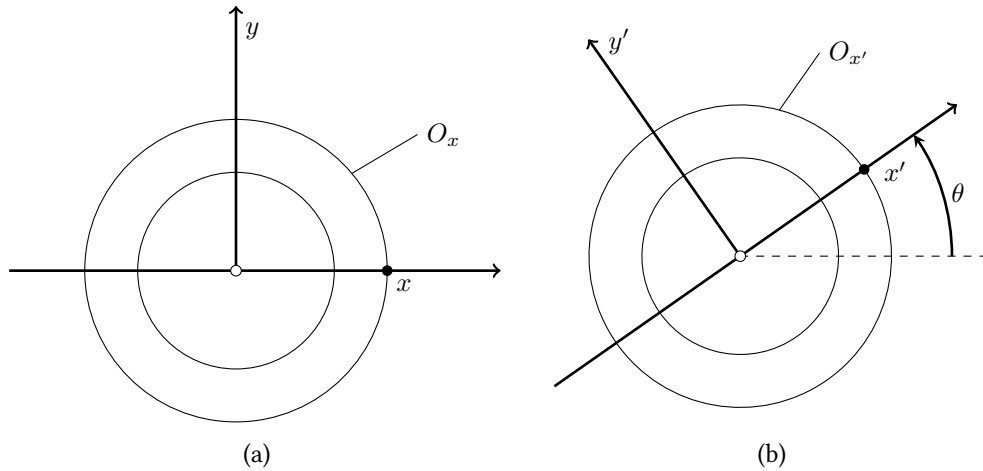(a)   (b)

Figure B.1: Periodic orbits and rotation symmetry

The following example of an simple orbit summation will explain the basic ideas behind the Faddeev-Popov trick for Gauge fixing [243, 330]. The problem is how to simplify the following 2-dimensional integral

$$I = \int_{\mathbb{R}^2} \exp^{-x^2-y^2} dxdy$$ (B.6)

by eliminating the contributions coming from equivalent points. The integrand is invariant under the rotation

$$x' = x \cos \theta + y \sin \theta, \quad y' = y \cos \theta - x \sin \theta \tag{B.7}$$

of the (x, y)-coordinate system. These rotations about the origin are called gauge transformations, which form the group $SO(2)$. An orbit is obtained by rotating a given point $(x, 0)$ in all possible ways. Equivalent points are all points belonging to the same orbit O_x, see Fig. B.1a. In the following the question, how to eliminate these equivalent points, will be discussed more detailed.

Special gauge fixing: Choosing the special gauge angle $\theta := 0$, which plays the role of a generalized coordinate, and using polar coordinates leads to

$$I = \int_0^\infty r \exp^{-r^2} dr \int_{-\pi}^\pi d\theta. \tag{B.8}$$

By writing in terms of orbits the orbit summation is obtained:

$$I = \int_0^\infty \exp^{-x^2} x \left(\int_{O_x} d\theta \right) dx, \tag{B.9}$$

which is equivalent to

$$I = \pi \int_{-\infty}^\infty \exp^{-x^2} |x| \, dx. \tag{B.10}$$

Using the Dirac delta function, having in mind that $\int_{\mathbb{R}} f(x, y) \delta(y) dy = f(x, 0)$, the formula can be rewritten as

$$I = \pi \int_{-\infty}^\infty \int_{-\infty}^\infty \exp^{-x^2 - y^2} \delta(y) |x| \, dx dy. \tag{B.11}$$

General gauge fixing: After fixing the angle θ (see Fig. B.1b) introduce the function

$$y' = f(x, y, \theta) = y \cos \theta - x \sin \theta, \tag{B.12}$$

that describes the periodic orbit O_x. The gauge condition is given as

$$f(x, y, \theta) = 0. \tag{B.13}$$

Thus, the contributions from the periodic orbit are zero. Equivalently, the stationary action path γ_{inst} fulfills the Euler-Lagrange Equation and, thus, the first variation $\delta S_{\text{E}}[\gamma_{\text{inst}}] = 0$. The gauge condition determines the x'-axis. The partial derivative with respect to Θ is

$$\frac{d}{d\theta} y' = f_\theta(x, y, \theta) = -y \sin \theta - x \cos \theta = -x'. \tag{B.14}$$

Then follows analog to equation (B.11)

$$I = \pi \int_{\mathbb{R}^2} \exp^{-(x')^2 - (y')^2} \delta(y') \, |x'| \, dx' dy'. \tag{B.15}$$

Transforming into the variables x, y with the observation that

$$x'^2 + y'^2 = x^2 + y^2, \quad \frac{\partial(x', y')}{\partial(x, y)} = 1 \tag{B.16}$$

leads to $I = \pi \int_0^\infty \exp^{-x^2 - y^2} \delta(y') \, |x'| \, dx dy$.

Thus, the Faddeev-Popov trick results in

$$I = \pi \int_{\mathbb{R}^2} \exp^{-x^2 - y^2} \delta(f(x, y, \theta)) \, |f_\theta(x, y, \theta)| \, dx dy. \tag{B.17}$$

In higher dimensional cases the absolute value in the last equation is replaced by the so-called Faddeev–Popov determinant.

BIBLIOGRAPHY

The numbers in blue behind each reference denote the pages where the entry occurs.

[1] BRUNOLD, T. C., CONRAD, K., LIPTAK, M. D., AND PARK, K. *Coord. Chem. Rev. 253* (2009), 779. 3

[2] GRUBER, K., AND KRATKY, C. *Curr. Opin. Chem. Biol. 6* (2002), 598. 4

[3] BUCKEL, W. *Appl. Microbiol. Biotechnol. 57* (2001), 263. 4

[4] SPRECHER, M., SWITZER, R. L., AND SPRINSON, D. B. *J. Biol. Chem. 241* (1966), 864. 4

[5] REITZER, R., GRUBER, K., JOGL, G., WAGNER, U., BOTHE, H., BUCKEL, W., AND KRATKY, C. *Structure 7* (1999), 891. 4

[6] GRUBER, K., REITZER, R., AND KRATKY, C. *Angew. Chem., Int. Ed. Engl. 40* (2001), 3377. 4, 92

[7] TOLLINGER, M., KONRAT, R., HILBERT, B., MARSH, E. N. G., AND KRÄUTLER, B. *Structure 6* (1998), 1021. 4

[8] HOFFMANN, B., KONRAT, R., BOTHE, H., BUCKEL, W., AND KRÄUTLER, B. *Eur. J. Biochem. 263* (1999), 178. 4

[9] TOLLINGER, M., EICHMÜLLER, C., KONRAT, R., HUHTA, M., MARSH, E. N. G., AND KRÄUTLER, B. *J. Mol. Biol. 309* (2001), 777. 4

[10] HOFFMANN, B., TOLLINGER, M., KONRAT, R., HUHTA, M., MARSH, E. N. G., AND KRÄUTLER, B. *ChemBioChem 2* (2001), 643. 4

[11] MARSH, E. N. G., AND MADHAVAPEDDI, P. *Chem. Biol. 8* (2001), 1143. 4, 110

[12] MARSH, E. N. G. *Bioorg. Chem. 28* (2000), 176. 5

[13] BUCKEL, W., AND GOLDING, B. T. *Chem. Soc. Rev. 25* (1996), 329. 5

[14] JENSEN, K., AND RYDE, U. *Coord. Chem. Rev. 253* (2009), 769. 5, 91, 95

[15] JENSEN, K., AND RYDE, U. *J. Am. Chem. Soc. 127* (2005), 9117. 5, 91, 95

[16] KOZLOWSKI, P. *Curr. Opin. Chem. Biol. 5* (2001), 736. 5, 91, 95

[17] WETMORE, S. D., SMITH, D. M., GOLDING, B. T., AND RADOM, L. *J. Am. Chem. Soc.* *123* (2001), 7963. 5, 91, 92, 105, 110, 112

[18] CHIH, H. W., AND MARSH, E. N. G. *J. Am. Chem. Soc. 122* (2000), 10732. 5, 10, 92, 136

[19] MARSH, E. N. G., AND PATWARDHAN, A. *Arch. Biochem. Biophys. 461* (2007), 194. 5, 92

[20] ROMMEL, J. B., AND KÄSTNER, J. *J. Am. Chem. Soc. 133* (2011), 10195. 5, 91, 94, 118

[21] CHENG, M.-C., AND MARSH, E. N. G. *Biochemistry 44* (2005), 2686. 5, 7, 9, 10, 11, 91, 118, 119, 125, 126, 127, 128, 136

[22] CHIH, H. W., AND MARSH, E. N. G. *Biochemistry 40* (2001), 13060. 5, 11, 91, 108, 111, 126, 127, 136

[23] MARSH, E. N. G., AND BALLOU, D. P. *Biochemistry 37* (1998), 11864. 5, 7, 9, 91, 118, 125, 126, 127, 136

[24] YOON, M., KALLI, A., LEE, H.-Y., HÅKANSSON, K., AND MARSH, E. N. G. *Angew. Chem., Int. Ed. 46* (2007), 8455. 6, 10, 91, 109, 118, 124, 126

[25] YOON, M., SONG, H., HÅKANSSON, K., AND MARSH, E. N. G. *Biochemistry 49* (2010), 3168. 6, 7, 9, 10, 91, 109, 118, 124, 126

[26] BELL, R. P. *Proc. R. Soc. Lond. A 139* (1933), 466. 6

[27] GAMOW, G. *Z. Phys. A 51* (1928), 204. 6

[28] ECKART, C. *Phys. Rev. 35* (1930), 1303. 6

[29] GRANT, K. L., AND KLINMAN, J. P. *Biochemistry 28* (1989), 6597. 6

[30] KOHEN, A., AND KLINMAN, J. P. *Chem. Biol. 6* (1999), R191. 6

[31] KNAPP, M. J., AND KLINMAN, J. P. *Eur. J. Biochem. 269* (2002), 3113. 6

[32] ANTONIOU, D., CARATZOULAS, S., KALYANARAMAN, C., MINCER, J. S., AND SCHWARTZ, S. D. *Eur. J. Biochem. 269* (2002), 3103. 6, 15

[33] LIANG, Z.-X., AND KLINMAN, J. P. *Curr. Opin. Struct. Biol. 14* (2004), 648. 6

[34] KLINMAN, J. P. *J. Biol. Chem. 281* (2006), 3013. 6

[35] BANDARIA, J. N., CHEATUM, C., AND KOHEN, A. *J. Am. Chem. Soc. 131* (2009), 10151. 6, 119

[36] Masgrau, L., Roujeinikova, A., Johannissen, L. O., Hothi, P., Basran, J., Ranaghan, K. E., Mulholland, A. J., Sutcliffe, M. J., Scrutton, N. S., and Leys, D. *Science 312* (2006), 237. 6, 17, 119

[37] Dutton, P. L., Munro, A. W., Scrutton, N. S., and Sutcliffe, M. J. *Philos. Trans. R. Soc. Lond. A 361* (2006), 1293. 6

[38] Williams, I. *J. Phys. Org. Chem. 23* (2010), 685. 6

[39] Allemann, R., and Scrutton, N., Eds. *Quantum tunnelling in enzyme-catalysed reactions.* RSC, Cambridge, UK, 2009. 6, 9

[40] Hammes-Schiffer, S. *Acc. Chem. Res. 39* (2006), 93. 6, 17

[41] Kohen, A. *Isotope Effects in Chemistry and Biology.* Taylor and Francis, Boca Raton, 2006, ch. Kinetic Isotope Effects as Probes for Hydrogen Tunneling in Enzyme Catalysis, p. 759. 6, 11, 15

[42] Nagel, Z. D., and Klinman, J. *Chem. Rev. 106* (2006), 3095. 6, 15

[43] Pu, J., Gao, J., and Truhlar, D. G. *Chem. Rev. 106* (2006), 3140. 6, 16, 17

[44] Warshel, A., Sharma, P. K., Kato, M., Xiang, Y., Liu, H. B., and Olsson, M. H. M. *Chem. Rev. 106* (2006), 3210. 6

[45] Kiefer, P. M., and Hynes, J. T. *Isotope Effects in Chemistry and Biology.* Taylor and Francis, Boca Raton, 2006. 6

[46] Chih, H. W., and Marsh, E. N. G. *Biochemistry 38* (1999), 13684. 7, 10, 118, 125, 136

[47] Chen, H.-P., and Marsh, E. N. G. *Biochemistry 36* (1997), 14939. 7, 9, 117, 118, 125

[48] Kohen, A., Roston, D., Stojković, V., and Wang, Z. *Encyclopedia of Analytical Chemistry,* (2010). 8, 14, 15

[49] Michaelis, L., and Menten, M. L. *Biochem. Z 49* (1913), 333. 8

[50] Johnson, K. A., and Goody, R. S. *Biochemistry 50* (2011), 8264. 8

[51] Marsh, E. N. G. *Biochem. Soc. Trans. 37* (2009), 336. 9

[52] Rice, N. M., Irving, H. M. N. H., and Leonard, M. A. *Pure Appl. Chem. 65* (1993), 2373. 9

[53] Chih, H. W., Roymoulik, I., Huhta, M. S., Madhavapeddi, P., and Marsh, E. N. G. *Methods Enzymol. 354* (2002), 380. 10, 136

[54] CHENG, M.-C., AND MARSH, E. N. G. *Biochemistry 43* (2004), 2155. 10, 11, 118, 128, 129, 133

[55] CHENG, M.-C., AND MARSH, E. N. G. *Biochemistry 46* (2007), 883. 10, 11, 118, 128, 129

[56] KOHEN, A., AND KLINMAN, J. P. *Acc. Chem. Res. 31* (1998), 397. 11

[57] HÄNGGI, P., TALKNER, P., AND BORKOVEC, M. *Rev. Mod. Phys. 62* (1990), 251. 12, 15, 68

[58] POLLAK, E., AND TALKNER, P. *Chaos 15* (2005), 026116. 12, 15

[59] FERNÁNDEZ-RAMOS, A., MILLER, J. A., KLIPPENSTEIN, S. J., AND TRUHLAR, D. G. *Chem. Rev. 106* (2006), 4518. PMID: 17091928. 12

[60] ARRHENIUS, S. *Z. Phys. Chem. (Leipzig) 4* (1889), 226. 12, 14

[61] EYRING, H., AND POLANYI, M. *Z. Phys. Chem. Abt. B B12, 279* (1931), 279. 12

[62] PELZER, H., AND WIGNER, E. *Z. Phys. Chem. B 15* (1932), 445. 12

[63] EYRING, H. *J. Chem. Phys. 3* (1935), 107. 12

[64] POLANYI, M., AND EVANS, M. G. *Trans. Faraday Soc. 31* (1935), 875. 12

[65] KECK, J. C. *Adv. Chem. Phys. 13* (1967), 85. 13

[66] CUI, Q., ELSTNER, M., AND KARPLUS, M. *J. Phys. Chem. B 106* (2002), 2721. 13

[67] KANAAN, N., MARTI, S., MOLINER, V., AND KOHEN, A. *Biochemistry 46* (2007), 3704. 13

[68] WIGNER, E. P. *Z. Phys. Chem. B 19* (1932), 203. 14

[69] BELL, R. P. *Trans. Faraday Soc. 55* (1959), 1. 14

[70] BELL, R. P. *The tunnel effect in chemistry.* Chapman and Hall (London), 1980, ch. The application of tunnel corrections in chemical kinetics, p. 51. 14

[71] GILLAN, M. J. *J. Phys. C: Solid State Physics 20* (1987), 3621. 14, 17, 83

[72] WIGNER, E. *Trans. Faraday Soc. 34* (1938), 29. 14

[73] BIGELEISEN, J. *J. Chem. Phys. 17* (1949), 675. 14

[74] WESTHEIMER, F. *Chem. Rev. 61* (1961), 265. 14

[75] STREITWIESER, A., JAGOW, R. H., FAHEY, R. C., AND SUZUKI, S. *J. Am. Chem. Soc. 80* (1958), 2326. 14

[76] MARCUS, R. A., AND SUTIN, N. *Biochim. Biophys. Acta. 811* (1985), 265. 15

[77] BORGIS, D. C., LEE, S. Y., AND HYNES, J. *Chem. Phys. Lett. 162* (1989), 19. 15

[78] KUZNETSOV, A. M., AND ULSTRUP, J. *Can. J. Chem. 77* (1999), 1085. 15

[79] SCHWARTZ, S. D. *Isotope Effects in Chemistry and Biology.* Taylor and Francis, CRC Press, Boca Raton, FL, 2006, ch. Vibrationally Enhanced Tunneling from the Temperature Dependence of KIE, p. 475. 15

[80] SUTCLIFFE, M. J., MASGRAU, L., ROUJEINIKOVA, A., JOHANNISSEN, L. O., HOTHI, P., BASRAN, J., RANAGHAN, K. E., MULHOLLAND, A. J., LEYS, D., AND SCRUTTON, N. S. *Phil. Trans. R. Soc. B 361* (2006), 1375. 15

[81] MARCUS, R. A. *J. Chem. Phys. 125* (2006), 194504. 15

[82] MARCUS, R. A. *J. Phys. Chem. B 111* (2007), 6643. 15

[83] KNAPP, M., MEYER, M., AND KLINMAN, J. *Hydrogen-Transfer Reactions.* Wiley-VCH Verlag GmbH & Co. KGaA, 2007, ch. Nuclear Tunneling in the Condensed Phase: Hydrogen Transfer in Enzyme Reactions, p. 1241. 15

[84] KOHEN, A. *Hydrogen-Transfer Reactions.* Wiley-VCH, Weinheim, 2007, ch. Probes for Hydrogen Tunneling and Coupled Motion in Enzymatic Systems, p. 1311. 15

[85] NAGEL, Z. D., AND KLINMAN, J. P. *Nat. Chem. Biol. 5* (2009), 543. 15

[86] KLINMAN, J. P. *Chem. Phys. Lett. 471* (2009), 179. 15

[87] PUDNEY, C. R., HAY, S., SUTCLIFFE, M. J., AND SCRUTTON, N. S. *J. Am. Chem. Soc. 128* (2006), 14053. 15

[88] ROSTON, D., AND KOHEN, A. *Proc. Natl.Acad. Sci. U.S.A. 107* (2010), 9572. 15

[89] KRAMERS, H. *Physica 7* (1940), 284–304. 15

[90] ANTONIOU, D., AND SCHWARTZ, S. D. *Proc. Natl. Acad. Sci. U.S.A. 94* (1997), 12360. 15

[91] ANTONIOU, D., AND SCHWARTZ, S. D. *J. Chem. Phys. 110* (1999), 465. 15

[92] SUTCLIFFE, M., AND SCRUTTON, N. *Phil. Trans. Roy. Soc. Ser. A 358* (2000), 367. 15

[93] ANTONIOU, D., AND SCHWARTZ, S. D. *J. Phys. Chem. B 105* (2001), 5553. 15

[94] MINCER, J. S., AND SCHWARTZ, S. D. *J. Chem. Phys. 120* (2004), 7755. 15

[95] ANTONIOU, D., BASNER, J., NÚÑEZ, S., AND SCHWARTZ, S. D. *Chem. Rev. 106* (2006), 3170. 15

[96] BOTHMA, J. P., GILMORE, J. B., AND MCKENZIE, R. H. *New J. Phys. 12* (2010), 055002. 15, 119

[97] TALKNER, P., AND HÄNGGI, P. *New Trends in Kramers' Reaction Rate Theory.* Kluwer, Dordrecht, 1995. 15

[98] WEISS, U. *Quantum dissipative systems.* World Scientific (Singapore and River Edge, NJ), 1993. 15, 44

[99] POLLAK, E. *Chem. Phys. Lett. 127* (1986), 178. 15

[100] WOLYNES, P. G. *Phys. Rev. Lett. 47* (1981), 968. 15

[101] GIESE, K., PETKOVIĆ, M., NAUNDORF, H., AND KÜHN, O. *Phys. rep. 430* (2006), 211. 15

[102] TRUHLAR, D. G., GAO, J., ALHAMBRA, C., GARCIA-VILOCA, M., CORCHADO, J., SÁNCHEZ, M. L., AND VILLÀ, J. *Acc. Chem. Res. 35* (2002), 341. 15, 16, 17

[103] TRUHLAR, D. G., GAO, J., GARCIA-VILOCA, M., ALHAMBRA, C., CORCHADO, J., SÁNCHEZ, M. L., AND POULSEN, T. D. *Int. J. Quantum Chem. 100* (2004), 1136. 15, 16, 17

[104] HAMMES-SCHIFFER, S. *Curr. Opin. Struct. Biol. 14* (2004), 192. 15, 17

[105] HWANG, J. K., CHU, Z. T., YADAV, A., AND WARSHEL, A. *J. Phys. Chem. 95* (1991), 8445. 15, 17

[106] HWANG, K. J., AND WARSHEL, A. *J. Am. Chem. Soc. 118* (1996), 11745. 15, 17

[107] MAJOR, D. T., GARCIA-VILOCA, M., AND GAO, J. *J. Chem. Theory Comput 2* (2006), 236–245. 15, 18

[108] ROMMEL, J. B., GOUMANS, T. P. M., AND KÄSTNER, J. *J. Chem. Theory Comput. 7* (2011), 690. 15, 69, 70, 83, 120

[109] ROMMEL, J. B., AND KÄSTNER, J. *J. Chem. Phys. 134* (2011), 184107. 15, 68, 69, 86, 87, 89, 120

[110] DEWAR, M. J. S., ZOEBISCH, E. G., HEALY, E. F., AND STEWART, J. J. P. *J. Am. Chem. Soc. 107* (1985), 3902. 16, 74

[111] KUPPERMANN, A., AND TRUHLAR, D. G. *J. Am. Chem. Soc. 93* (1971), 1840. 16

[112] MARCUS, R. A., AND COLTRIN, M. E. *J. Chem. Phys. 67* (1977), 2609. 16, 82, 130

[113] SKODJE, R., TRUHLAR, D. G., AND GARRETT, B. C. *J. Phys. Chem. 85* (1981), 3019. 16

[114] GARRETT, B. C., TRUHLAR, D. G., WAGNER, A. F., AND DUNNING JR., T. H. *J. Chem. Phys. 78* (1983), 4400. 16

[115] GARRETT, B. C., ABUSALBI, N., KOURI, D. J., AND TRUHLAR, D. G. *J. Chem. Phys. 83* (1985), 2252. 16

[116] LIU, Y. P., LU, D. H., GONZALEZ-LAFONT, A., TRUHLAR, D. G., AND GARRETT, B. C. *J. Am. Chem. Soc. 115* (1993), 7806. 16

[117] MEANA-PAÑEDA, R., TRUHLAR, D. G., AND FERNÁNDEZ-RAMOS, A. *J. Chem. Theory Comput. 6* (2010), 6. 16

[118] JEFFREYS, H. *Proc. London Math. Soc. 2* (1925), 428. 16, 49

[119] WENTZEL, G. *Z. Physik 38* (1926), 518. 16, 49

[120] KRAMERS, H. A. *Z. Physik 39* (1926), 828. 16, 49

[121] BRILLOUIN, L. *C. R. Acad. Sci. Paris 183* (1926), 24. 16, 49

[122] TRUHLAR, D. G., AND GARRETT, B. C. *Hydrogen Transfer Reactions.* Wiley, Weinheim, 2007. 16

[123] TRUHLAR, D. G. *J. Phys. Org. Chem. 23* (2010), 660. 16

[124] WYATT, R. *J. Chem. Phys. 51* (1969), 3489. 16

[125] LIU, Y. P., LYNCH, G. C., TRUONG, T. N., LU, D. H., TRUHLAR, D. G., AND GARRETT, B. C. *J. Am. Chem. Soc. 115* (1993), 2408. 16

[126] TRUHLAR, D. G., LIU, Y. P., SCHENTER, G. K., AND GARRETT, B. C. *J. Phys. Chem. 98* (1994), 8396. 16

[127] FERNANDEZ-RAMOS, A., AND TRUHLAR, D. G. *J. Chem. Phys. 114* (2001), 1491. 16

[128] TRUHLAR, D. G. *Isotope effects in chemistry and biology.* Marcel Dekker, Inc., New York, 2005. 16

[129] GAO, J., AND TRUHLAR, D. G. *Ann. Rev. Phys. Chem. 53* (2002), 467. 17

[130] TRESADERN, G., MCNAMARA, J. P., MOHR, M., WANG, H., BURTON, N. A., AND HILLIER, I. H. *Chem. Phys. Lett. 358* (2002), 489. 17

[131] GARCIA-VILOCA, M., TRUHLAR, D. G., AND GAO, J. *Biochemistry 42* (2003), 13558. 17

[132] GARCIA-VILOCA, M., ALHAMBRA, C., TRUHLAR, D. G., AND GAO, J. L. *J. Comput. Chem. 24* (2003), 177. 17

[133] PU, J. Z., MA, S. H., GAO, J. L., AND TRUHLAR, D. G. *J. Phys. Chem. B 109* (2005), 8551. 17

[134] GAO, J., MA, S., MAJOR, D. T., NAM, K., PU, J., AND TRUHLAR, D. G. *Chem. Rev. 106* (2006), 3188. 17

[135] PANG, J. Y., PU, J. Z., GAO, J., TRUHLAR, D. G., AND ALLEMANN, R. K. *J. Am. Chem. Soc. 128* (2006), 8015. 17

[136] NUNEZ, S., TRESADERN, G., HILLIER, I. H., AND BURTON, N. A. *Phil. Trans. R. Soc. B 361* (2006), 1387. 17

[137] MASGRAU, L., RANAGHAN, K. E., SCRUTTON, N. S., MULHOLLAND, A. J., AND SUTCLIFFE, M. J. *J. Phys. Chem. B 111* (2007), 3032. 17

[138] RANAGHAN, K. E., MASGRAU, L., SCRUTTON, N. S., SUTCLIFFE, M. J., AND MULHOLLAND, A. J. *ChemPhysChem 8* (2007), 1816. 17

[139] DYBALA-DEFRATYKA, A., PANETH, P., AND TRUHLAR, D. G. *Quantum Tunnelling in Enzyme-Catalysed Reactions*. Royal Society of Chemistry, Cambridge, 2009. 17

[140] GARCIA-VILOCA, M., GAO, J., KARPLUS, M., AND TRUHLAR, D. G. *Science 303* (2004), 186. 17

[141] ALHAMBRA, C., GAO, J., CORCHADO, J. C., VILLÀ, J., AND TRUHLAR, D. G. *J. Am. Chem. Soc. 121* (1999), 2253. 17

[142] ALHAMBRA, C., CORCHADO, J., SÁNCHEZ, M. L., GARCIA-VILOCA, M., GAO, J., AND TRUHLAR, D. G. *J. Phys. Chem. B 105* (2001), 11326. 17

[143] BILLETER, S. R., WEBB, S. P., IORDANOV, T., AGARWAL, P. K., AND HAMMES-SCHIFFER, S. *J. Chem. Phys. 114* (2001), 6925. 17

[144] BILLETER, S. R., WEBB, S. P., AGARWAL, P. K., IORDANOV, T., AND HAMMES-SCHIFFER, S. *J. Am. Chem. Soc. 123* (2001), 11262. 17

[145] FEYNMAN, R. P. *Rev. Mod. Phys. 20* (1948), 367. 17, 41

[146] CAO, J., AND VOTH, G. A. *J. Chem. Phys. 101* (1994), 6157. 17

[147] Voth, G. A. *Adv. Chem. Phys. 93* (1996), 135. 17

[148] Pollak, E., and Liao, J.-L. *J. Chem. Phys. 108* (1998), 2733. 17

[149] Richardson, J. O., and Althorpe, S. C. *J. Chem. Phys. 131* (2009), 214106. 17, 41

[150] Craig, I. R., and Manolopoulos, D. E. *J. Chem. Phys. 122* (2005), 084106. 17

[151] Voth, G. A., Chandler, D., and Miller, W. H. *J. Chem. Phys. 91* (1989), 7749. 17

[152] Voth, G. A. *J. Phys. Chem.* (1993), 8365. 17

[153] Mills, G., Schenter, G. K., Makarov, D. E., and Jónsson, H. *Chem. Phys. Lett. 278* (1997), 91. 17, 41, 71

[154] Mills, G., G. K. Schenter, D. M., and Jónsson, H. *Classical and Quantum Dynamics in Condensed Phase Simulations.* World Scientific, 1998, ch. RAW Quantum Transition State Theory, p. 405. 17, 41

[155] Hwang, J.-K., and Warshel, A. *J. Phys. Chem. 97* (1993), 10053. 17

[156] Sprik, M., Klein, M. L., and Chandler, D. *Phys. Rev. B 31* (Apr 1985), 4234. 17

[157] Pollock, E. L., and Ceperley, D. M. *Phys. Rev. B 30* (Sep 1984), 2555. 18

[158] Major, D. T., and Gao, J. *J. Mol. Graphics Modell. 24* (2005), 121. Biomolecular Recognition and Reactivity Special Issue in honour of the contributions of Professor Ian Hillier. 18

[159] Major, D. T., Heroux, A., Orville, A. M., Valley, M. P., Fitzpatrick, P. F., and Gao, J. *J.Proc. Natl. Acad. Sci. U.S.A 106* (2009), 20734. 18

[160] Gao, J., Wong, K.-Y., Major, D. T., Cembran, A., Song, L., Lin, Y.-L., Fan, Y., and Ma, S. *Quantum Tunnelling in Enzyme-Catalysed Reactions.* Royal Society of Chemistry, Cambridge, 2009, ch. Kinetic Isotope Effects from Hybrid Classical and Quantum Path Integral Computations, p. 105. 18

[161] Wang, Q., and Hammes-Schiffer, S. *J. Chem. Phys. 125* (2006), 184102. 18

[162] Abraham, R., Marsden, J. E., and Ratiu, T. S. *Manifolds, tensor analysis, and applications*, vol. 75. Springer Berlin, Germany, 1988. 19, 22

[163] Arnold, V. I. *Mathematical methods of classical mechanics*, vol. 60. Springer Berlin, Germany, 1989. 19

[164] Grigis, A., and Sjøstrand, J. *Microlocal analysis for differential operators: an introduction*, vol. 196. Cambridge University Press, 1994. 19

[165] FELSAGER, B. *Geometry, particles, and fields.* Springer Berlin, Germany, 1998. 19, 22

[166] TAKHTAJAN, L. *Quantum mechanics for mathematicians.* Am. Math. Soc., Graduate Studies in Mathematics 95, 2008. 19, 49

[167] YANG, C. N., AND MILLS, R. L. *Phys. Rev. 96*, 1 (1954), 191. 20

[168] COLEMAN, S. *Aspects of symmetry.* Cambridge Univ. Press, 1988. 20

[169] GILDENER, E., AND PATRASCIOIU, A. *Phys. Rev. D 16* (1977), 423. 20

[170] BELAVIN, A., POLYAKOV, A., SCHWARTZ, A., AND TYUPKIN, A. *Phys. Lett. B 59* (1975), 85. 20

[171] 'T HOOFT, G. *Phys. Rev. D 14* (1976), 3432. 20

[172] BELITSKY, A. V., VANDOREN, S., AND NIEUWENHUIZEN, P. *Class. Quant. Grav. 17* (2000), 3521. 20

[173] DUNAJSKI, M. *Solitons, instantons, and twistors*, vol. 19. Oxford Univ. Press, 2010. 20

[174] SCHULMAN, L. S. *Techniques and Applications of Path Integration.* Wiley Classics Library (New York), 1996. 20, 29, 48, 49

[175] EGUCHI, T., GILKEY, P. B., AND HANSON, A. J. *Phys. rep. 66* (1980), 213. 20

[176] FUJIWARA, D. *Nagoya Math. J. 124* (1991), 61. 28, 48

[177] KUMANO-GO, N., AND FUJIWARA, D. *RIMS Kôkyûroku Bessatsu, B 5* (2008), 241. 28, 33, 48

[178] FUJIWARA, D., AND KUMANO-GO, N. *Funkcialaj Ekvacioj 49* (2006), 59. 28, 34, 48

[179] TROTTER, H. F. *Proc. Amer. Math. Soc. 10* (1959), 545. 28

[180] KAC, M. *Trans. Amer. Math. Soc. 65* (1949), 1. 28

[181] CAMERON, R. H. *J. Math. Phys. 39* (1960), 126. 28

[182] GROSCHE, C., AND STEINER, F. *Handbook of Feynman path integrals.* Springer Tracts in Modern Physics 145, Springer Berlin, Germany, 1998. 28, 36, 41, 44, 48, 49, 57, 68

[183] ZINN-JUSTIN, J. *Quantum Field Theory and Critical Phenomena.* Clarendon Press, Oxford, 1993. 28

[184] JOHNSON, G., AND LAPIDUS, M. *The Feynman integral and Feynman's operational calculus.* Oxford University Press, USA, 2002. 28

[185] ALBEVERIO, S., AND MAZZUCCHI, S. *A Survey on Mathematical Feynman Path Integrals: Construction, Asymptotics, Applications.* Birkhäuser Basel, 2009. 28, 48

[186] ZINN-JUSTIN, J. *Scholarpedia 4* (2009), 8674. 28

[187] ALBEVERIO, S., AND MAZZUCCHI, S. *Scholarpedia 6* (2011), 8832. 28

[188] SIMON, B. *Functional integration and quantum physics.* Academic Press, New York, 1979. 28

[189] ARISUE, H., FUJIWARA, T., INOUE, T., AND OGAWA, K. *J. Math. Phys. 22* (1981), 2055. 29

[190] FEYNMAN, R. P. *Statistical Mechanics, A set of lectures.* Frontiers in Physics, WA Benjamin, Inc., Reading, Massachusetts, 1972. 29

[191] MODIN, K. *Adaptive geometric numerical integration of mechanical systems.* PhD thesis, 2009. 34

[192] MARSDEN, J. E., AND WEST, M. *Acta Numer. 10*, 357 (2001), 514. 34

[193] FUJIWARA, D., AND KUMANO-GO, N. *J. Math. Soc. Japan 58* (2006), 837. 34

[194] DOLL, J. D., FREEMAN, D. L., AND BECK, T. L. *Equilibrium and dynamical Fourier path integral methods.* Wiley Online Library, 1990. 34

[195] FERMI, E. *Atti R. Accad Lincei Rend., Cl. Sci. Fis. Mat. Nat. 31* (1922), 21. 35

[196] MANASSE, F. K., AND MISNER, C. W. *J. Math. Phys. 4* (1963), 735. 35

[197] BEKENSTEIN, J., AND PARKER, L. *Phys. Rev. D 23*, 12 (1981), 2850. 35

[198] KLEINERT, H. *Path Integrals.* World Scientific, Singapore, 2009. 36, 41, 44, 62, 66, 68

[199] POTTS, D. *Schnelle Fourier-Transformationen für nichtäquidistante Daten und Anwendungen, Habilitationsschrift.* University of Lübeck, 2003. 36

[200] ROYER, A. *J. Math. Phys. 25* (1984), 2873. 37

[201] DAVISON, B. *Proc. Royal Soc. London. Series A. Math. Phys. Sci. 225*, 1161 (1954), 252. 37

[202] LANGER, J. S. *Ann. Phys. (N.Y.) 41* (1967), 108. 41, 42, 66, 69

[203] LANGER, J. S. *Phys. Rev. Lett. 21*, 14 (1968), 973. 41, 42

[204] LANGER, J. S. *Ann. Phys. 54*, 2 (1969), 258. 41, 42

[205] CALLAN JR., C. G., AND COLEMAN, S. *Phys. Rev. D 16* (1977), 1762. 41, 69

[206] COLEMAN, S. *Phys. Rev. D 15* (1977), 2929. 41, 42, 44, 69

[207] MILLER, W. H. *J. Chem. Phys. 62* (1975), 1899. 41

[208] KLINMAN, J. P. *J. Phys. Org. Chem. 23* (2010), 606. 41

[209] MILLER, W. H., ZHAO, Y., CEOTTO, M., AND YANG, S. *J. Chem. Phys. 119* (2003), 1329. 41

[210] VANÍČEK, J., MILLER, W. H., CASTILLO, J. F., AND AOIZ, F. J. *J. Chem. Phys. 123* (2005), 054108. 41

[211] CHAPMAN, S., GARRETT, B. C., AND MILLER, W. H. *J. Chem. Phys. 63* (1975), 2710. 41

[212] MILLS, G., AND JÓNSSON, H. *Phys. Rev. Lett. 72* (1994), 1124. 41

[213] MILLS, G., JÓNSSON, H., AND SCHENTER, G. K. *Surf. Sci. 324* (1995), 305. 41

[214] SIEBRAND, W., SMEDARCHINA, Z., ZGIERSKI, M. Z., AND FERNÁNDEZ-RAMOS, A. *Int. Rev. Phys. Chem. 18* (1999), 5. 41

[215] SMEDARCHINA, Z., SIEBRAND, W., FERNÁNDEZ-RAMOS, A., AND CUI, Q. *J. Am. Chem. Soc. 125* (2003), 243. 41

[216] ANDERSSON, S., NYMAN, G., ARNALDSSON, A., MANTHE, U., AND JÓNSSON, H. *J. Phys. Chem. A 113* (2009), 4468. 41, 68, 69, 70, 72, 81

[217] GOUMANS, T. P. M., AND KÄSTNER, J. *Angew. Chem. Int. Ed. 49* (2010), 7350. 41, 69, 70, 72, 74

[218] GOUMANS, T. P. M., AND KÄSTNER, J. *Angew. Chem. 122* (2010), 7508. 41, 69, 70, 72, 74

[219] GOUMANS, T. P. M., AND ANDERSSON, S. *Mon. Not. R. Astron. Soc. 406* (2010), 2213. 41, 69, 70, 72

[220] RICHARDSON, J. O., ALTHORPE, S. C., AND WALES, D. J. *J. Chem. Phys. 135* (2011), 124109. 41

[221] RICHARDSON, J. O., AND ALTHORPE, S. C. *J. Chem. Phys. 134* (2011), 054109. 41

[222] MEISNER, J., ROMMEL, J. B., AND KÄSTNER, J. *J. Comput. Chem. 32* (2011), 3456. 41, 85, 120

[223] ANDERSSON, S., GOUMANS, T. P. M., AND ARNALDSSON, A. *Chem. Phys. Lett. 513* (2011), 31. 41

[224] GOUMANS, T. P. M. *Mon. Not. Royal Astron. Soc. 413* (2011), 2615. 41

[225] GOUMANS, T. P. M. *Mon. Not. Royal Astron. Soc. 415* (2011), 3129. 41

[226] GOUMANS, T. P. M., AND KÄSTNER, J. *J. Phys Chem. A 115* (2011), 10767. 41

[227] ARNALDSSON, A. *Calculation of quantum mechanical rate constants directly from ab initio atomic forces.* PhD thesis, University of Washington, 2007. 41, 68, 69, 70, 71, 72

[228] MESSINA, M., SCHENTER, G. K., AND GARRETT, B. C. *J. Chem. Phys. 103* (1995), 3430. 41, 68

[229] KÄSTNER, J., AND GOUMANS, T. P. M. *Angewandte Chemie International Edition* (2010). 41, 68

[230] HEISENBERG, W. K. *Z. Phys. 123* (1944), 93. 42

[231] WHEELER, J. A. *Phys. Rev. 52* (1937), 1107. 42

[232] LANDAU, L. D., AND LIFSHITZ, E. M., Eds. *Quantum Mechanics: Non-Relativistic Theory.* Pergamon Press., 1977, p. 502. 42

[233] ZWERGER, W. *J. Phys. A: Math. Gen. 18* (1985), 2079. 42

[234] RIKVOLD, P., AND GORMAN, B. *Ann. Rev. Comput. Phys. 1* (1994), 194. 42

[235] BOROVIKOV, V. *Uniform stationary phase method.* Institution of Electrical Engineers, 1994. 48

[236] GEL'FAND, I. M., AND YAGLOM, A. M. *J. Math. Phys. 1* (1960), 48. 48, 49

[237] CHOQUARD, P. *Helv. Phys. Acta 69* (1996), 636. 48, 49

[238] MORETTE, C. *Phys. Rev. 81* (1951), 848. 49

[239] DEWITT-MORETTE, C. *Ann. Phys. 97* (1976), 367. 49

[240] MORSE, M. *Variational analysis; critical extremals and Sturmian extensions*, vol. 28. Wiley, New York, 1973. 49

[241] COLEMAN, S. *Nucl. Phys. B 298* (1988), 178. 50, 66

[242] AFFLECK, I. *Nucl. Phys. B 191* (1981), 429. 50, 66

[243] FADDEEV, L. D., AND POPOV, V. N. *Phys. Lett. B 25* (1967), 29. 60, 150

[244] MESTELA, B., AND PERCIVAL, I. *Physica D 24* (1987), 172. 70

[245] BARANGER, M., DAVIES, K. T. R., AND MAHONEY, J. H. *Ann. Phys. (N.Y.) 186* (1988), 95. 70

[246] GROBGELD, D., POLLAK, E., AND ZAKRZEWSKI, J. *Physica D 56* (1992), 368. 70

[247] MARCINEK, R., AND POLLAK, E. *J. Chem. Phys. 100* (1994), 5894. 70

[248] KÄSTNER, J., CARR, J. M., KEAL, T. W., THIEL, W., WANDER, A., AND SHERWOOD, P. *J. Phys. Chem. A 113* (2009), 11856. 71, 75, 99

[249] SHERWOOD, P., DE VRIES, A. H., GUEST, M. F., SCHRECKENBACH, G., CATLOW, C. R. A., FRENCH, S. A., SOKOL, A. A., BROMLEY, S. T., THIEL, W., TURNER, A. J., BILLETER, S., TERSTEGEN, F., THIEL, S., KENDRICK, J., ROGERS, S. C., CASCI, J., WATSON, M., KING, F., KARLSEN, E., SJØVOLL, M., FAHMI, A., SCHÄFER, A., AND LENNARTZ, C. *J. Mol. Struct. (Theochem.) 632* (2003), 1. 71, 75, 91, 95, 99

[250] HENKELMAN, G., AND JÓNSSON, H. *J. Chem. Phys. 111* (1999), 7010. 72, 75, 99

[251] OLSEN, R. A., KROES, G. J., HENKELMAN, G., ARNALDSSON, A., AND JÓNSSON, H. *J. Chem. Phys. 121* (2004), 9776. 72, 99

[252] HEYDEN, A., BELL, A. T., AND KEIL, F. J. *J. Chem. Phys. 123* (2005), 224101. 72, 76, 99

[253] KÄSTNER, J., AND SHERWOOD, P. *J. Chem. Phys. 128* (2008), 014106. 72, 75, 99

[254] LIU, D. C., AND NOCEDAL, J. *Math. Program. 45* (1989), 503. 72

[255] NOCEDAL, J. *Math. Comp. 35* (1980), 773. 72

[256] BROYDEN, C. G. *IMA J. Appl. Math. 6* (1970), 76. 72

[257] FLETCHER, R. *Comput. J. 13* (1970), 317. 72

[258] GOLDFARB, D. *Math. Comp. 24* (1970), 23. 72

[259] SHANNO, D. F. *Math. Comp. 24* (1970), 647. 72

[260] LANCZOS, C. *J. Res. Nat. Bur. Stand. 45* (1951), 255. 72

[261] MALEK, R.; MOUSSEAU, N. *Phys. Rev. E 62* (2000), 7723. 72

[262] CERJAN, C. J., AND MILLER, W. H. *J. Chem. Phys. 75* (1981), 2800. 73

[263] SIMONS, J., JØRGENSEN, P., TAYLOR, H., AND OZMENT, J. *J. Phys. Chem. 87* (1983), 2745. 73

[264] BANERJEE, A., ADAMS, N., SIMONS, J., AND SHEPARD, R. *J. Phys. Chem. 89* (1985), 52. 73

[265] BAKER, J. *J. Comput. Chem. 7* (1986), 385. 73

[266] BOFILL, J. M. *J. Comput. Chem. 15* (1994). 73, 88

[267] STEWART, J. J. P. *J. Comput. Chem. 10* (1989), 209. 74

[268] WONG, K. F., SONNENBERG, J. L., PAESANI, F., YAMAMOTO, T., VANÍČEK, J., ZHANG, W., SCHLEGEL, H. B., CASE, D. A., CHEATHAM III, T. E., MILLER, W. H., AND VOTH, G. A. *J. Chem. Theory Comput. 6* (2010), 2566. 74

[269] GRIMME, S. *J. Comput. Chem. 27* (2006), 1787. 74

[270] THIEL, W. MNDO99, V. 6.1; Max-Planck-Institut für Kohlenforschung: Mülheim an der Ruhr, Germany, 2004. 75

[271] HUMPHREY, W., DALKE, A., AND SCHULTEN, K. *J. Molec. Graphics 14* (1996), 33. 75, 92

[272] POWELL, M. J. D. *Math. Prog. 26* (1971). 80, 88

[273] JÓNSSON, H., MILLS, G., AND JACOBSEN, K. W. *Classical and Quantum Dynamics in Condensed Phase Simulations.* World Scientific, 1998, ch. Nudged Elastic Band Method for Finding Minimum Energy Paths of Transitions, p. 385. 85

[274] JÓNSSON, H. *Proc. Nat. Acad. Sci. U.S.A. 108* (2010), 944. 85

[275] EINARSDÓTTIR, D., ARNALDSSON, A., ÓSKARSSON, F., AND JÓNSSON, H. Path optimization with application to tunneling. In *Applied Parallel and Scientific Computing*, K. Jónasson, Ed., vol. 7134 of *Lect. Notes in Comput. Sci.* Springer Berlin, Germany, 2012, p. 45. 85

[276] MURTAGH, B. A., AND SARGENT, R. W. H. *Comput. J. 13* (1970), 185. 88

[277] WARSHEL, A., AND KARPLUS, M. *J. Am. Chem. Soc. 94* (1972), 5612. 91, 95

[278] WARSHEL, A., AND LEVITT, M. *J. Mol. Biol. 103* (1976), 227. 91, 95

[279] SENN, H. M., AND THIEL, W. *Topics in Current Chemistry*, vol. 268. Springer Berlin, Germany, 2007. 91

[280] SENN, H. M., AND THIEL, W. *Curr. Opin. Chem. Biol. 11* (2007), 182. 91

[281] LIN, H., AND TRUHLAR, D. G. *Theor. Chem. Acc. 117* (2007), 185. 91

[282] RICCARDI, D., SCHAEFER, P., YANG, Y., YU, H., GHOSH, N., PRAT-RESINA, X., KNIG, P., LI, G., XU, D., GUO, H., ELSTNER, M., AND CUI, Q. *J. Phys. Chem. B 110* (2006), 6458. 91

[283] CHOWDHURY, S., AND BANERJEE, R. *Biochemistry 39* (2000), 7998. 91

[284] SANDALA, G. M., SMITH, D. M., MARSH, E. N. G., AND RADOM, L. *J. Am. Chem. Soc. 129* (2007), 1623. 91

[285] CHEN, H.-P., AND MARSH, E. N. G. *Biochemistry 36* (1997), 14939. 92

[286] JORGENSEN, W., CHANDRASEKHAR, J., MADURA, J., IMPEY, R., AND KLEIN, M. *J. Chem. Phys. 79* (1983), 926. 92

[287] MACKERELL JR., A. D., BASHFORD, D., BELLOTT, R. L., DUNBRACK JR., R. L., EVANSECK, J. D., FIELD, M. J., FISCHER, S., GAO, J., GUO, H., HA, S., JOSEPH-MCCARTHY, D., KUCHNIR, L., KUCZERA, K., LAU, F. T. K., MATTOS, C., MICHNICK, S., NGO, T., NGUYEN, D. T., PRODHOM, B., REIHER III, W. E., ROUX, B., SCHLENKRICH, M., SMITH, J. C., STOTE, R., STRAUB, J., WATANABE, M., WIORKIEWICZ-KUCZERA, J., YIN, D., AND KARPLUS, M. *J. Phys. Chem. B 102* (1998), 3586. 93, 95

[288] MACKERELL JR., A. D., FEIG, M., AND BROOKS III, C. L. *J. Comput. Chem. 25* (2004), 1400. 93, 95

[289] FOLOPPE, N., AND MACKERELL JR, A. D. *J. Comput. Chem. 21* (2000), 86. 93, 95

[290] MACKERELL JR, A., AND BANAVALI, N. *J. Comput. Chem. 21* (2000), 105. 93, 95

[291] PHILLIPS, J., BRAUN, R., WANG, W., GUMBART, J., TAJKHORSHID, E., VILLA, E., CHIPOT, C., SKEEL, R., KALE, L., AND SCHULTEN, K. *J. Comput. Chem. 26* (2005), 1781. 93

[292] TUCKERMAN, M. E., BERNE, B. J., MARTYNA, G. J., AND L., K. M. *J. Chem. Phys. 99* (1993), 2796. 93

[293] FELLER, S., ZHANG, Y., PASTOR, R., AND BROOKS, B. *J. Chem. Phys. 103* (1995), 4613. 93

[294] HOHENBERG, P., AND KOHN, W. *Phys. Rev. B 136* (1964), 864. 95

[295] KOHN, W., AND SHAM, L. *Phys. Rev. A 140* (1965), 1133. 95

[296] DE VRIES, A. H., SHERWOOD, P., COLLINS, S. J., RIGBY, A. M., RIGUTTO, M., AND KRAMER, G. J. *J. Phys. Chem. B 103* (1999), 6133. 95

[297] SMITH, W., YONG, C. W., AND RODGER, P. M. *Mol. Simul. 28* (2002), 385. 95

[298] DIRAC, P. A. M. *Proc. R. Soc. London, Ser. A 123* (1929), 714. 96

[299] SLATER, J. C. *Phys. Rev. 81* (1951), 385. 96

[300] VOSKO, S. H., WILK, L., AND NUSAIR, M. *Can. J. Phys. 58* (1980), 1200. 96

[301] BECKE, A. D. *Phys. Rev. A 38* (1988), 3098. 96

[302] PERDEW, J. P. *Phys. Rev. B 33* (1986), 8822. 96

[303] GRIMME, S. *J. Comput. Chem. 25* (2004), 1463. 96

[304] STEPHENS, P. J., DEVLIN, F. J., CHABALOWSKI, C. F., AND FRISCH, M. J. *J. Phys. Chem. 98* (1994), 11623. 96

[305] TURBOMOLE V6.0.2 2009, a development of University of Karlsruhe and Forschungszentrum Karlsruhe GmbH, 1989-2007, TURBOMOLE GmbH, since 2007; available from http://www.turbomole.com. 96, 99

[306] ARNIM, M. V., AND AHLRICHS, R. *J. Comput. Chem. 19* (1998), 1746. 96

[307] ZHAO, Y., AND TRUHLAR, D. G. *J. Chem. Phys. 125* (2006), 194101. 96

[308] KENDAL, R. A., APRA, E., BERNHOLDT, D. E., BYLASKA, E. J., DUPUIS, M., FANN, G. I., HARRISON, R. J., JU, J., NICHOLS, J. A., NIEPLOCHA, J., STRAATSMA, T. P., WINDUS, T. L., AND WONG, A. T. *Comput. Phys. Commun. 128* (2000), 260. 96

[309] BYLASKA, E. J., JONG, W. A., GOVIND, N., KOWALSKI, K., STRAATSMA, T. P., VALIEV, M., WANG, D., APRA, E., WINDUS, T. L., HAMMOND, J., NICHOLS, P., HIRATA, S., HACKLER, M. T., ZHAO, Y., FAN, P.-D., HARRISON, R. J., DUPUIS, M., SMITH, D. M. A., NIEPLOCHA, J., TIPPARAJU, V., KRISHNAN, M., WU, Q., V. VOORHIS, T., AUER, A. A., NOOIJEN, M., BROWN, E., CISNEROS, G., FANN, G. I., FRUCHTL, H., GARZA, J., HIRAO, K., KENDALL, R., NICHOLS, J. A., TSEMEKHMAN, K., WOLINSKI, K., ANCHELL, J., BERNHOLDT, D., BOROWSKI, P., CLARK, T., CLERC, D., DACHSEL, H., DEEGAN, M., DYALL, K., ELWOOD, D., GLENDENING, E., GUTOWSKI, M., HESS, A., JAFFE, J., JOHNSON, B., JU, J., KOBAYASHI, R., KUTTEH, R., LIN, Z., LITTLEFIELD, R., LONG, X., MENG, B., NAKAJIMA, T., NIU, S., POLLACK, L., ROSING, M., SANDRONE, G., STAVE, M., TAYLOR, H., THOMAS, G., V. LENTHE, J., WONG, A., AND ZHANG, Z. NWChem, A Computational Chemistry Package for Parallel Computers, Version 5.1. Tech. rep., Pacific Northwest National Laboratory, Richland, Washington 99352-0999, USA, 2007. 96

[310] SCHÄFER, A., HORN, H., AND AHLRICHS, R. *J. Chem. Phys. 97* (1992), 2571. 96

[311] DUNNING, T. H. *J. Chem. Phys. 90* (1989), 1007. 96

[312] WEIGEND, F., HÄSER, M., PATZELT, H., AND AHLRICHS, R. *Chem. Phys. Lett. 294* (1998), 143. 96

[313] ZHAO, Y., AND TRUHLAR, D. G. *Theor. Chem. Acc. 120* (2008), 215. 96

[314] LIU, Y. *Linear scaling high-spin open-shell local correlation methods.* PhD thesis, Universität Stuttgart, 2011. 96, 97

[315] LIU, Y., AND WERNER, H.-J. to be published. 96

[316] WERNER, H.-J., KNOWLES, P. J., MANBY, F. R., SCHÜTZ, M., CELANI, P., KNIZIA, G., KORONA, T., LINDH, R., MITRUSHENKOV, A., RAUHUT, G., ADLER, T. B., AMOS, R. D., BERNHARDSSON, A., BERNING, A., COOPER, D. L., DEEGAN, M. J. O., DOBBYN, A. J., ECKERT, F., GOLL, E., HAMPEL, C., HESSELMANN, A., HETZER, G., HRENAR, T., JANSEN, G., KÖPPL, C., LIU, Y., LLOYD, A. W., MATA, R. A., MAY, A. J., MCNICHOLAS, S. J., MEYER, W., MURA, M. E., NICKLASS, A., PALMIERI, P., PFLÜGER, K., PITZER, R., REIHER, M., SHIOZAKI, T., STOLL, H., STONE, A. J., TARRONI, R., THORSTEINSSON, T., WANG, M., AND WOLF, A. Molpro, version 2010.2, a package of ab initio programs, 2010. see www.molpro.net. 96

[317] AMOS, R. D., ANDREWS, J. S., HANDY, N. C., AND KNOWLES, P. J. *Chem. Phys. Lett. 185* (1991), 256. 96

[318] BILLETER, S. R., TURNER, A. J., AND THIEL, W. *Phys. Chem. Chem. Phys. 2* (2000), 2177. 99

[319] KLAMT, A., AND SCHÜÜRMANN, G. *J. Chem. Soc., Perkin Trans. 2* (1993), 799. 99

[320] KÄSTNER, J., AND SHERWOOD, P. *Mol. Phys. 108* (2010), 293. 99

[321] LONSDALE, R., HARVEY, J. N., AND MULHOLLAND, A. J. *J. Phys. Chem. B 114* (2010), 1156. 99

[322] JARZYNSKI, C. *Phys. Rev. Lett. 78* (1997), 2690. 100

[323] BAYLY, C., CIEPLAK, P., CORNELL, W., AND KOLLMAN, P. *J. Phys. Chem. 97* (1993), 10269. 100

[324] SMITH, D. M., GOLDING, B. T., AND RADOM, L. *J. Am. Chem. Soc. 121* (1999), 1383. 105

[325] SMITH, D. M., GOLDING, B. T., AND RADOM, L. *J. Am. Chem. Soc. 123* (2001), 1664. 105

[326] GEORGE, P., GLUSKER, J., AND BOCK, C. *J. Am. Chem. Soc. 119* (1997), 7065. 105

[327] SUTCLIFFE, M. J., AND SCRUTTON, N. S. *Eur. J. Biochem. 269* (2002), 3096. 119

[328] WANG, M., LU, Z., AND YANG, W. *J. Chem. Phys. 124* (2006), 124516. 119

[329] WIGNER, E. *Phys. Rev. 40* (1932), 749. 121, 122

[330] ZEIDLER, E. *Quantum field theory*, vol. 1. Springer Berlin, Germany, 2008. 150